UNIVERSITÀ
DEGLI STUDI
DI PADOVA

UNIVERSITA' DEGLI STUDI DI PADOVA

Dipartimento di Ingegneria Industriale DII

Corso di Laurea Magistrale in Ingegneria dell'Energia Elettrica

Study of RF generators based on solid-state amplifiers for ion sources of Neutral Beam Injectors

Relatore: Prof. Paolo Bettini
Correlatori: Alberto Maistrello
Mauro Recchia

Studente: Marco De Nardi 1182676

Anno Accademico 2020/2021.

Ai miei genitori
e alla mia fidanzata.

Index

Figures index

Tables index

Abstract

Neutral Beam Injectors (NBI) are fundamental devices in nuclear fusion experiments based on magnetic plasma confinement systems, and their purpose is creating a beam of high energy neutral particles to heat the fusion plasma. They represent one of the main additional heating systems of the ITER experiment, the first fusion device designed for producing 500 MW of fusion power for proving the feasibility of fusion as energy source, with an overall power of 33 MW delivered with two injectors. Other two heating systems exploiting ECRH (Electron Cyclotron Resonance Heating) and ICRH (Ion Cyclotron Resonance Heating) mechanisms provide both 20 MW power. A key component of the NBI is the ion source, where a Hydrogen or Deuterium plasma is generated. The plasma of the ion source of ITER NBI is foreseen to be driven by Radiofrequency (RF) power with 800 kW power at 1MHz frequency (nominal frequency range of 900÷1100 kHz), through 4 RF circuits, by using proper antennas and matching networks, where the RF power is provided by tetrodes oscillators.

Recently, several issues related to the exploitation of this RF power generation technology for ion sources have been highlighted, thus questioning about the implementation of this solution in the ITER NBI. The most critical one observed is the occurrence of a frequency jump (known as Frequency Flip phenomenon) during the tuning of the operating frequency of the RF system that ultimately prevents the RF oscillator working at the optimal frequency and delivering the rated output power to the load. Such behavior is also seen in SPIDER experiment, the prototype of the ion source of ITER NBI, which is hosted in the Neutral Beam Test Facility, in Padua. Furthermore, during SPIDER experimental campaign, another issues, not related to the RF power generation technology, has been faced: the flowing of RF common mode currents at the operating frequency (~1 MHz) in the whole SPIDER ion source power circuit. The circulation of these currents is a crucial topic of the integration process of different power supply systems working in the same circuit and highlights that the proper design of single power unit has to take into account its operating environment, and not view as a standalone system. In SPIDER this phenomena was observed with degradation of signal to noise ratio of measurement systems and with overheating of power components.

This thesis work is on the RF PS of SPIDER and aims to propose a conceptual design based on solid-state RF amplifier technology. It provides a solution for the frequency jump issue, providing frequency stability, and allows the exploitation of the ratings of this system. This technology is under investigation in several test facilities and is based on solid-state generators similar to those currently adopted in broadcasting applications, which are typically constituted by many power amplifier modules based on MOSFETs. The thesis is discussing in particular the RF power generation stage and RF power and frequency control systems.

In addition the work presents the analyses of the integration of the solid state solution in the peculiar SPIDER PS system, discussing the merit of 2 identified circuital solutions of its power supply system and comparing them from the point of view of the RF common mode currents generated.

In chapter 1, a brief analysis of the actual energy problem followed by an introduction to nuclear fusion and fusion experimental power plant based on magnetic confinement are given. In chapter 2, the description of the ITER NBI and its neutral beam test facility in Padua are presented, focusing on the SPIDER experiment and its power supply system. Chapter 3 is focused on the analysis of the actual configuration of the ion source RF power supply of SPIDER, based on tetrodes oscillators. In this section, a description of the RF circuit components is provided, (oscillator, transmission line, matching network and antennas). After that, an analysis of the issues related to the operation of the system is presented. Chapter 4 is dedicated to the characterization of the load of the RF circuit through analytical calculations

and simulations. The goal of this chapter is to understand the influences of the load components on its equivalent impedance as it seen by the RF generator. This is fundamental in order to understand the behavior of the load against frequency for defining the requirements of the RF amplifier. Starting from the model of a single RF circuit, it is analyzed a model with two circuits in order to evaluate the effects of the mutual coupling between them. Then, the voltage and current analysis on the components of the RF circuits is provided, followed by the evaluation of the effects of the error components on the measurement of the antennas parameters. In chapter 5, the evaluation of the RF common mode current in the SPIDER ion source PS circuit is given: the analysis is realized through electrical models in order to obtain the current values in frequency and time domains. Finally, in chapter 6 the proposal for the conceptual design of a solid-state RF amplifier is given. The study starts with the definition of the requirements of the amplifier and the identification of the number of power modules. After that, the conceptual design of the amplifier, its control system and its interfacing with the SPIDER system are provided and summarized through a conceptual block diagram. Then, a section is dedicated to the voltage insulation requirements for the RF generator and the proposal of two different schemes for the power supply system of the RF amplifier. These solutions will be studied through circuital simulations in order to identify the RF common mode current, in the perspective of defining the optimal circuital configuration for the RF amplifier power supply which minimizes them.

Sommario

Gli iniettori di fasci neutri (Neutral Beam Injectors, NBI) sono dispositivi fondamentali negli esperimenti di fusione nucleare basati su sistemi di confinamento magnetico del plasma, e il loro obiettivo è quello di creare un fascio di particelle neutre ad alta energia per il riscaldamento del plasma per fusione. Essi rappresentano uno dei principali sistemi di riscaldamento addizionale dell'esperimento ITER, il primo reattore a fusione progettato per produrre 500 MW di potenza da fusione con l'obiettivo di dimostrare la fattibilità della fusione come fonte di energia, per un totale di 33 MW forniti per mezzo di due iniettori. Altri sistemi di riscaldamento forniscono 20 MW con ECRH (Electron Cyclotron Resonance Heating) e 20 MW con ICRH (Ion Cyclotron Resonance Heating). Un componente chiave del NBI è la sorgente di ioni, dove il plasma viene generato a partire da Idrogeno o Deuterio. E' previsto che il plasma della sorgente di ioni del NBI di ITER sia alimentato in Radiofrequenza (RF) con 800 kW di potenza a 1 MHz di frequenza (intervallo di frequenza nominale di 900÷1100 kHz), attraverso 4 circuiti RF, per mezzo di opportune antenne e matching network, dove la potenza RF viene fornita per mezzo di oscillatori a terodi.

Recentemente, sono stati evidenziati diversi problemi relativi allo sfruttamento di questa tecnologia per la produzione di potenza RF, mettendo in dubbio l'impiego di tale soluzione nel NBI di ITER. Il problema più critico osservato è il verificarsi di un salto in frequenza (noto come fenomeno del Frequency Flip) durante la fase di sintonizzazione della frequenza operativa del sistema RF che in definitiva impedisce all'oscillatore RF di lavorare alla frequenza ottimale e di fornire la potenza di uscita nominale al carico. Tale comportamento è stato osservato anche nell'impianto sperimentale di SPIDER, il prototipo della sorgente di ioni del NBI di ITER, che è ospitato all'interno del Neutral Beam Test Facility, a Padova. Inoltre, durante la campagna sperimentale di SPIDER, è stato affrontato un ulteriore problema, non collegato direttamente alla tecnologia per la generazione della potenza RF: la circolazione, alla frequenza operativa (~1 MHz), di correnti di modo comune RF nell'intero circuito in potenza della sorgente di ioni di SPIDER. La circolazione di tali correnti è un tema cruciale del processo di integrazione di diversi sistemi di alimentazione operanti nello stesso circuito e mette in evidenza che la struttura specifica di una singola unità di potenza deve tenere in considerazione il suo intero ambiente di funzionamento, e non deve quindi essere vista come un sistema isolato. In SPIDER questo fenomeno è stato individuato attraverso il peggioramento del rapporto segnale-rumore dei sistemi di misura e dal surriscaldamento dei componenti di potenza.

Questo lavoro di tesi è incentrato sul sistema di alimentazione a radiofrequenza (RF PS) di SPIDER e mira a proporre un design concettuale basato sulla tecnologia dell'amplificatore RF allo stato solido. Esso fornisce una soluzione al problema del salto di frequenza, garantendo stabilità in frequenza, e permette lo sfruttamento dei rating del sistema. Questa tecnologia è in fase di studio in diversi impianti sperimentali ed è basata su generatori allo stato solido simili a quelli attualmente impiegati in applicazioni broadcasting, che sono tipicamente costituite da diversi moduli amplificatori di potenza basati su MOSFETs. La tesi si sofferma in particolare sullo stadio di generazione di potenza RF e sui sistemi di controllo di potenza RF e frequenza.

In aggiunta, il lavoro presenta le analisi dell'integrazione della soluzione allo stato solido nello specifico sistema di alimentazione di SPIDER (SPIDER PS), discutendo il merito di 2 soluzioni circuitali identificate e confrontandole dal punto di vista delle correnti di modo comune RF prodotte.

Nel Capitolo 1, sarà fornita una breve analisi dell'attuale problema energetico, seguita da un'introduzione alla fusione nucleare e alle caratteristiche di un impianto sperimentale a fusione basato sul confinamento magnetico. Nel Capitolo 2, sono presentate la descrizione del NBI di ITER e del relativo Neutral Beam Test Facility a Padova, concentrandosi sull'esperimento SPIDER e sul suo sistema di alimentazione. Il

Capitolo 3 è focalizzato sull'analisi dell'attuale configurazione del sistema di alimentazione RF della sorgente di ioni di SPIDER, basata su oscillatori a tetrodi. In questa sezione, viene fornita una descrizione dei componenti del circuito RF (oscillatore, linea di trasmissione, matching network e antenne). Dopodichè, viene presentata un'analisi dei problemi relativi al funzionamento del sistema. Il Capitolo 4 è dedicato alla caratterizzazione del carico del circuito RF attraverso calcoli analitici e simulazioni. L'obiettivo del capitolo è capire le influenze dei componenti del carico sulla sua impedenza equivalente, così come viene vista dal generatore RF. Ciò è fondamentale al fine di capire il comportamento del carico al variare della frequenza per la definizione dei requisiti dell'amplificatore RF. A partire dal modello di un singolo circuito RF, viene analizzato un modello con due circuiti al fine di valutare gli effetti del mutuo accoppiamento tra gli stessi. Poi, viene fornita l'analisi della distribizione di tensione e corrente sui componenti del circuito RF, seguita dalla valutazione degli effetti dei diversi componenti di errore sulla misura dei parametri delle antenne. Nel Capitolo 5 viene fornita la valutazione delle correnti di modo comune RF nel circuito del sistema di alimentazione della sorgente di ioni di SPIDER: l'analisi è stata realizzata attraverso modelli elettrici al fine di ottenere i valori di corrente sia nel dominio della frequenza che nel dominio del tempo. Infine, nel Capitolo 6 viene fornita la proposta per il design concettuale di un amplificatore RF allo stato solido. Lo studio comincia a partire dalla definizione dei requisiti dell' amplificatore e sull'identificazione del numero di moduli di potenza. Dopodichè, il design concettuale dell'amplificatore, il suo sistema di controllo e il suo interfacciamento con il sistema di SPIDER sono presentati e riassunti all'interno di uno schema a blocchi. In seguito, viene dedicata una sezione ai requisiti di isolamento in tensione dei generatori RF e alla proposta di due diversi schemi per il sistema di alimentazione dell'amplificatore RF. Queste soluzioni saranno studiate attraverso simulazioni circuitali al fine di identificare le correnti di modo comune RF, con l'obiettivo di definire la configurazione circuitale ottimale per l'alimentazione dell'amplificatore RF, che sia tale da minimizzarle.

1 Introduction to thermonuclear fusion and experimental power plants

1.1 Global challenges and perspectives of fusion energy

One of the greatest problems of the 21st century is finding an efficient way to cover the increasing global energy demand. This challenge is driven by the fast demographic growth, which is expected to increase of about two billion until 2050, from the actual 7.7 billion to 9.7 billion, and by the strong economic growth of the developing countries. Figure 1. 1shows the world energy consumption foreseen until 2050, according to the Reference scenario of the International Energy Outlook 2019[1], which corresponds to the baseline scenario for which the current trends and relationships among supply, demand and prices are assumed.

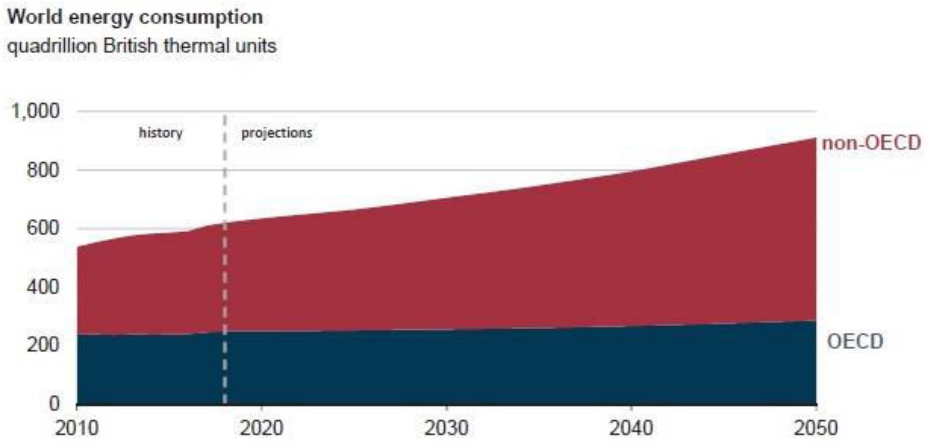

Figure 1. 1 *World energy consumption for OECD and non-OECD countries over year* [1]

The total energy consumption is shown for OECD and non-OECD countries, where OECD stands for Organization for Economic Co-operation and Development. Today there are 37 member countries of the OECD and they include countries like Japan, Italy, France and United States, which share high standards based on market economy and democracy. Non-OECD countries include developing countries with growing economy which do not meet the requirements of the OECD, such as China, India and Brazil. It is clear that the highest share of energy consumption is due to non-OECD countries with an increase of about 70% between 2018 and 2050. Meanwhile, for the OECD countries, the increment of the energy consumption is reduced to 15%. This may be justified, for example, by a slower population and economic growth and improvements in the energy efficiency.

The strong energy demand is not the only topic to deal with: the politics of environmental protection to mitigate the climate change issue, limiting greenhouse gases (GHG) emission, have assumed an increasingly pivotal role in the world stage considering that fossil fuels represent the largest share of the current primary energy consumption mix as it is shown in Figure 1. 2.

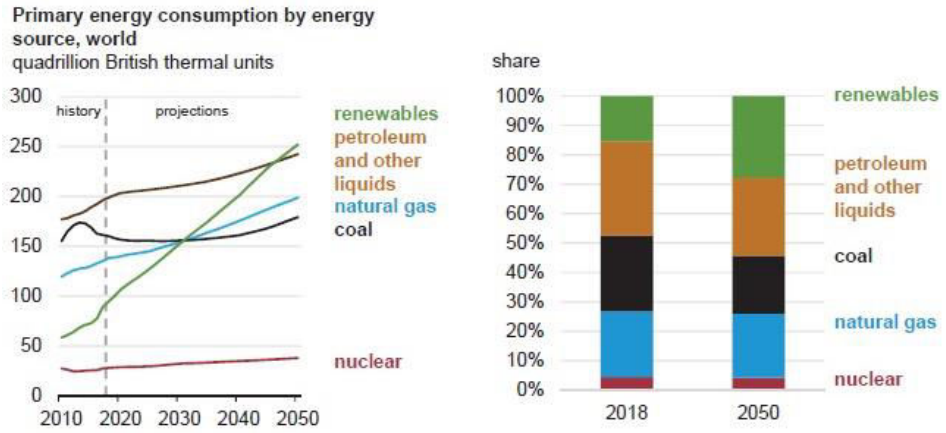

Figure 1. 2 *Global primary energy consumption by energy source* [1]

Despite the decline expected in the growing rate of fossil fuels towards 2050, they will account for almost 70% of the total primary energy consumption. Moreover, the projections to 2050 highlight that renewable energies will have the largest growing rate among the energy sources due essentially to the strong electricity demand and to economic and policy drivers [1].

Renewable energies, such as wind power, hydro power and solar, will play a crucial role in the perspective of a low-carbon scenario and their further developments in terms of energy efficiency and energy storage would strengthen their share within the energy mix. However, due to their intrinsic nature, renewable energies are not suitable to totally replace fossil fuels: low-density power plants, which require wide area for their allocation, the reliance on the environmental conditions and the intermittent nature highlight the limits of renewable energies that prevent them from becoming the reference base-load energy source. However, the exploitation of fossil fuels must be reduced in the short time, both for their reducing expected availability and in order to limit the impact of the climate change. Actually, the energy sector, alone, is responsible for a large share of the total GHG emissions, as it is shown in Figure 1. 3 [2].

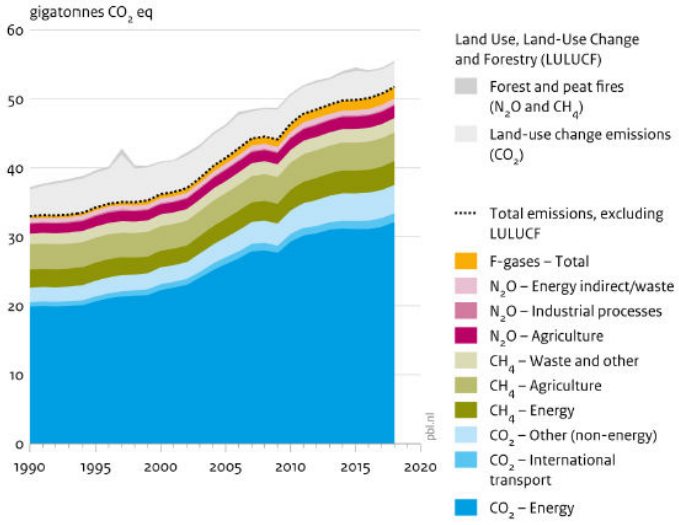

Figure 1. 3 *GHG emission by sector* [2]

It is precisely in this context of high energy demand and need to greenhouse gasses emissions reduction that the request for alternative energy sources able to meet these challenges emerges. Nuclear

energy sources are the only zero-emissions power supply capable of competing with fossil fuels for large-scale electricity production. Nuclear power plants currently in operation are fission-based power plants and, although they can guarantee the aforementioned advantages, they have also to face several issues like the management, transportation and disposal of radioactive waste and meet social acceptance, which is increasingly undermined by the fear of possible nuclear accidents, such as Chernobyl and Fukushima. For these reasons the global amount of primary energy consumption by nuclear fission, projected to 2050, will show a lower growth than the others energy sources as it is seen in Figure 1. 2, following the current phase-out policies.

As a result, many efforts are devoted to find another method to exploit nuclear energy: several research and development projects, focused on nuclear energy production based on nuclear fusion, has been started in the last decades. A fusion power plant could meet both the issues of high energy demand and environmental protection: the former because Deuterium-Tritium fusion reaction can release over 4 million times the energy of a chemical reaction, such as coal burning, and over 4 times the energy produced by a fission reaction (at equal mass), with a potentially inexhaustible and easy to obtain fuel supplies; the latter guaranteeing to avoid GHG emissions, because no fossil fuels are involved in the process, and the major product of the fusion reaction is helium. Other advantages rely on a secure and safe operation, no long-lived radioactive waste, a limited risk of proliferation and no risk of meltdowns. In fact there are no risks of chain reaction, as in a fission-based power plant, because if any disturbance modifies the fusion's conditions, the reaction will stops in few seconds. Unlike a traditional fission-based power plant, these features could help the social acceptance towards a future fusion energy production.

However, the feasibility of a controlled nuclear fusion reactor is opposed by strict requirements to obtain a controlled and continuous operation and none of the experimental reactors designed since 1960 was able to produce higher output power than the one needed for their operation until now.

1.2 Introduction to nuclear fusion

Fusion reaction is a process that occurs spontaneously within the core of stars and releases huge amount of energy that is transmitted through electromagnetic radiations; this is possible thanks to their specific condition of temperature and gravity. Considering the sun, the conditions of high core temperature (15.6 MK), high core pressure (250 billions of atm) and high density of the gasses inside the core (1.5×105 kg/m^3) allow the atoms of hydrogen to merge, releasing high energy and atoms of helium. The idea behind a nuclear fusion-based reactor is trying to reproduce the natural fusion conditions existing within the sun in an artificial, controlled way on the earth. Fusion reaction requires extremely high temperature heating of several tens of keV[1] (of about 10÷20 keV for D-T reaction) to allow for the reaction occurrence. At these temperatures the matter passes from gas to plasma state. Plasma is a quasi-neutral gas ($n_e \approx n_i$ where n_e and n_i are respectively the electron and ion density) of charged particles displaying collective behavior and it behaves like a conductor. It is recognized as the 4th state of matter. A fundamental parameter to describe the features of plasma is the Debye length λ_D. It is the spatial distance, in m, whithin which the moving charged particles shield the electric field inside plasma, and it is defined as

[1]The electronvolt (eV) is the unit of energy usually adopted in nuclear physics and it corresponds to the amount of energy gained or lost by a single electron accelerating from rest through a potential difference of 1 V in vacuum (1 eV=1.6*10^{-19} J).

$$\lambda_D = \sqrt{\frac{k_B T_e \varepsilon_0}{n_e {q_e}^2}},$$

where k_B=1.38×10^{-23} J/K is the Boltzmann constant, T_e is the electron temperature in K, n_e is the electron density in m^{-3} and q_e is the electron charge in C. It provides fundamental evidences to prove the properties of quasi-neutrality and low recombination probability of plasma: the former is verified when $L \gg \lambda_D$, where L is the characteristic dimension of the vessel, and according to this condition, the plasma is screened from charge imbalances and there are not any macroscopic concentration of charge; the latter is verified when $\frac{4}{3}\pi {\lambda_D}^3 n \gg 1$, where n is the particle's charge density, meaning that there are many charges inside a sphere with the radius equals to the Debye length. The key point towards the scientific feasibility of the nuclear fusion is the confinement of plasma at these thermonuclear temperatures, in order to ensure a continuous fusion reaction. This can be done through different confinement system: inertial confinement [3], gravitational confinement [4] and magnetic confinement. In this thesis work, it will be considered only the magnetic confinement and its configuration will be described in 1.3.

1.2.1 The concepts of mass defect and binding energy

Before discussing the fusion reaction, it is necessary to introduce the structure of the atom and the concepts of mass defect and binding energy. The atom consists of three elementary particles: protons and neutrons, which shape the atomic nucleus, and the electrons, which are forming a cloud around it with an approximate diameter of about 1000 times higher than the nucleus one (ϕ_{core} = 10^{-13} m, ϕ_{atom} = 10^{-8} m). The mass of the atom is concentrated to the nucleus, as protons and neutrons have a nearly equivalent mass, much higher than the electrons one.

$m_p = 1.673 * 10^{-27}\ kg$ Mass of the proton

$m_n = 1.675 * 10^{-27}\ kg$ Mass of the neutron

$m_{e-} = 9.101 * 10^{-31}\ kg$ Mass of the electron

An element can be represented as

$$^{A}_{Z}X$$

where X is the chemical symbol, which identifies the element, Z is the atomic number and it is equal to the number of protons and A is the mass number and it is equal to the sum of the number of protons and neutrons. While Z uniquely identifies the chemical elements, A could change as the number of neutrons changes. Two atoms with the same number of protons but a different number of neutrons are defined isotopes and even if they show the same chemical behavior, their physical behavior will be different, with the possibility of being stable or unstable, and then radioactive.

Inside atoms there are two types of forces that act between elementary particles: the Coulomb repulsion and the nuclear force. The protons inside the atomic nucleus are charged particle and for this reason they interact each other by coulomb repulsion forces, which are acting to reject them according to

$$F_{Coulomb} = \frac{1}{4\pi\varepsilon}\frac{Q_1 Q_2}{d^2},$$

where $Q_1$and $Q_2$are the charges of the two interacting particles, d is the distance between them and ε is the dielectric constant. However, at a distance approximately equal to 1 fm (1 fm=1.0×10^{-15} m, corresponding to the proton's radius), nuclear forces between protons and neutrons emerge and they are opposed to coulomb repulsion forces, preventing protons from leaving the nucleus. These forces decrease steadily exiting the nucleus, where coulomb repulsion forces prevail.

Recalling the concept of isotopes, it is possible to introduce another fundamental concept to comprehend the principles of fusion reaction: the mass defect. Hydrogen ($^1_1$H), the lighter element of the periodic table, has only one proton within its atomic nucleus, while one of its isotopes, Deuterium, ($^2_1$H or D), has one proton and one neutron. For the analysis, it is important to introduce the molar massM_x as

$$M_x = \left(\frac{m_x}{1\ Da}\right) M_u$$

where M_x is expressed in g/mol, m_x is the atomic mass in kg, 1 Da is the unified atomic mass unit or Dalton, which is equal to 1/12 of the mass of an unbound neutral atom of carbon-12 (1 Da is equal to 1,66054×10^{-27}kg) and M_u~1 g/mol is the molar mass constant. Hence, the molar mass of H and D are:

$$M_H = M_p = 1.00728 \text{ g/mol}$$

$$M_D = 2.01355 \text{ g/mol}$$

Considering that the molar mass of the neutron is equal to M_n = 1.00867 g/mol, and since the atom of D has one proton and one neutron, it is possible to calculate the molar mass of deuterium as

$$M_p + M_n = 2.01595 \text{ g/mol} \neq 2.01355 \text{ g/mol} = M_D$$

The difference between the molar mass of the original nucleons (neutron and proton) and the molar mass of D, experimentally observed, is the mass defect, and in this specific case, it is equal to

$$\Delta m = M_D - (M_p + M_n) = -0.0024 \text{ g/mol}.$$

Introducing the mass-energy equivalence,

$$E_b = \Delta m c^2$$

where c = 299 792 458 m/s, it is possible to highlight that the mass defect is converted into *binding energy*, which corresponds to the energy to be provided to the atom to dissociate its bonds. The presence of an energy defect is a fundamental behavior that can be analyzed by the ratio between the *binding energy* and A providing the mean value of the *binding energy per nucleon* as

$$E_{b/nucl} = \frac{E_b}{A}.$$

Applying this relation to all the chemical elements of the periodic table, Figure 1. 4 is obtained, which shows the variation of the mean value of the *binding energy per nucleon* (here it is expressed in MeV unit), for the nuclei known until now, against the mass number A .

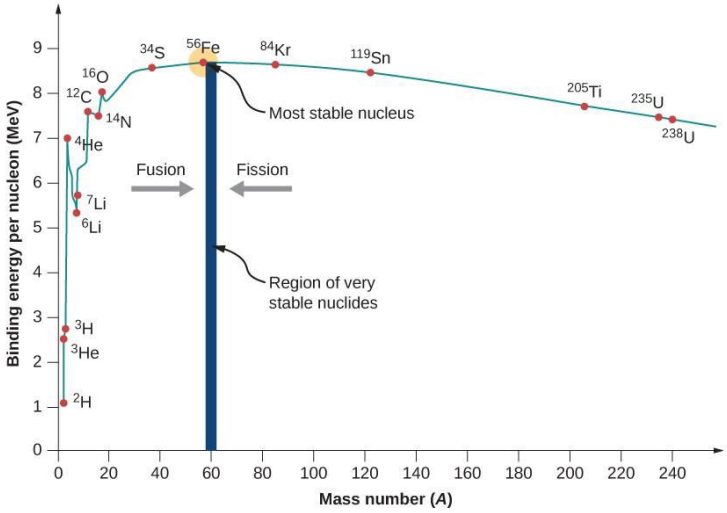

Figure 1. 4 *Binding energy per nucleon*

The graph highlights a peak, corresponding to $^{56}_{26}$Fe which is the most stable nucleus in nature, and the largest values of *binding energy per nucleon* are near it. Starting from the most stable point, the graph shows a strong decrease towards lower A and a slighter decrease towards higher A and this is explained due to the competing forces inside the nucleus: for lower A, nuclear force prevails, holding nucleons together in more strongly way, while for higher A, coulomb repulsion force prevails, tending to break apart the nucleus. Furthermore, focusing on the differential *binding energy per nucleon* among neighboring atoms, it is possible to derive indicative information about the sign of the potential energy released by fusion reaction (positive by increasing A) or by fission reaction (positive by decreasing A).This is a fundamental aspect in nuclear reactions because only heavier nuclei, such as $^{235}_{92}$U and $^{239}_{94}$Pu, which can be easily separate, are suitable for fission reactions while only lighter nuclei, are suitable for fusion reactions. The lighter nuclei suitable for fusion reactions are: the aforementioned deuterium D, tritium T, another hydrogen isotope ($^{3}_{1}$H), and even helium He. The different magnitude in the *binding energy per nucleons*, shown in Figure 1. 4, proves that the amount of energy released in a fusion reaction is higher than the fission reaction's one [5].

1.2.2 The fusion reaction

At this point it is possible to analyze the fusion reaction. Unlike fission reaction, which provides for the breach of the nucleus of heavy atoms through neutrons bombing to obtain as result high energy and lighter nuclei, fusion reaction requires to merge two lighter nuclei to obtain a heavier nucleus and a high amount of energy. There are three relevant fusion reactions which are advantageous for the application in energy production, involving D, T, $^{3}_{2}$He:

- **D - D reaction** (with two equally possible branches)

$$D + D \rightarrow {}^{3}_{2}He + n + 3.27\ MeV$$

$$D + D \rightarrow T + p + 4.03\ MeV$$

- **D - $^3_2$He reaction**

$$D + {}^3_2He \rightarrow \alpha + p + 18.3\ MeV$$

- **D - T reaction**

$$D + T \rightarrow \alpha + n + 17.6\ MeV$$

Between all of these alternatives, the D-T reaction is the central focus of worldwide fusion research. This reaction requires a steady supply of tritium for continuous operation, which is an artificial and radioactive hydrogen isotope that need to be properly produced from lithium (called tritium breeding), while D-D reaction can benefit from a potentially inexhaustible deuterium supply, easily obtained from the ocean it produces a lower amount of energy, compared to D-$^3_2$He reaction, and it produces high-energy neutrons as product, thus requiring adequate solution in order to handle material activation and radiation damage. Nevertheless, the D-T is the easiest fusion reaction to initiate and this is the reason why, despite its issues, it has been adopted as the reference reaction [6]. The concept of "reaction easy to initiate" can be explained thanks to the introduction of the concept of cross section σ: it quantifies the probability that two nuclei will undergo a nuclear fusion reaction. It can be visualized, considering the "hard-sphere" model, as the projection of the nuclear attractive field produced by the target particle on the plane perpendicular to the trajectory of the impinging particle. If the latter transits through σ and the field is sufficiently strong, a fusion reaction can occur. Figure 1. 5 shows the experimental cross sections, in m^2, for the three fusion reactions described against the deuterium energy in keV, highlighting that the largest σ is the D-T reaction one.

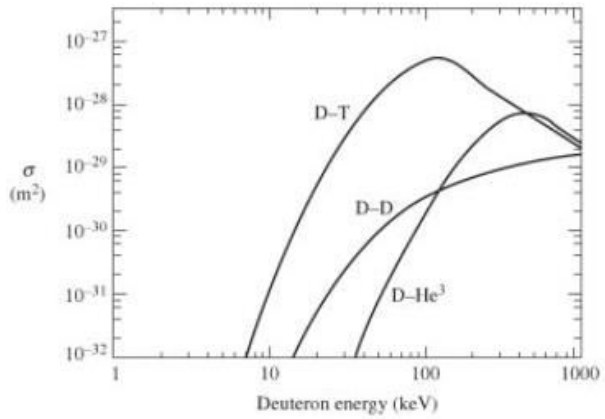

Figure 1. 5 *Experimental cross sections for relevant fusion reactions*

To produce the aforementioned D-T fusion reaction, but the statement is valid for each fusion reactions mentioned, D and T nuclei must be merged together. Nevertheless, since they are positively charged, it is necessary to force them to come very close to each others, within a distance of the magnitude of 1 fm, by providing them an adequate kinetic energy to overcome the so-called coulomb barrier. There is a sort of energy limit beyond which the nuclear attractive forces exceed the coulomb repulsion forces. The coulomb barrier is defined as

$$W = \frac{Z_1 Z_2 e^2}{4\pi\varepsilon_0 r_m},$$

where Z_1 and Z_2 are the atomic number of the interacting nuclei, e is the elementary charge and it is equal to 1.602×10^{-19} C, and r_m is the gap between the centers of the interacting nuclei. Figure 1. 6 shows the behavior of the potential energy and coulomb barrier for a D-T reaction, where W = $\frac{e^2}{4\pi\varepsilon_0 r_m}$ = 288 keV, because in this case Z_1=Z_2=1 and $r_m\approx5\times10^{-15}$ m.

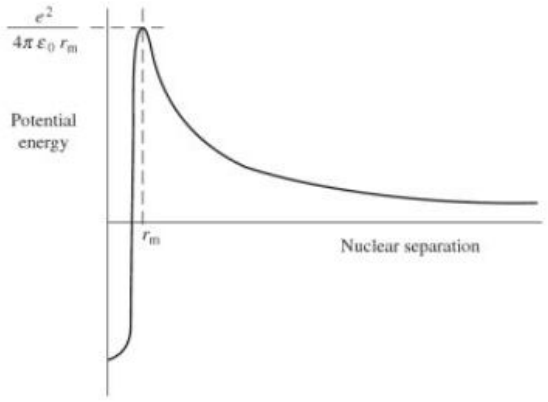

Figure 1. 6 *Coulomb barrier for D-T system*

According to these assumptions, if D and T nuclei are provided with energy over 288 keV and the nucleus of D intercepts the σ of the nucleus of T, the fusion reaction can occur. However this is a too much simplified model, and for a correct analysis the wavelike properties of the system must be taken into account. This new model, based on the nuclear quantum mechanical effects, implies three fundamental modifications:

1. Even for kinetic energies below 288 keV there is still a finite probability of interaction.

2. At nuclear distances two nuclei can pass through one another.

3. Under specific condition of relative velocity, the combined potential energies of the interacting nuclei can show a resonance, increasing the nuclear reaction probability.

The final step in the analysis of fusion reaction is the introduction of the fusion reaction rateR_{12}. Differently from the concept of cross section, which refers to the nuclear collision between individual particles, the reaction rate represents the number of particles having collision per unit volume per unit time. Indeed, the system is characterized by a gas of interacting particles (D-T in this case), which are moving within a specific volume at specific velocities. The number of particles per unit volume having the velocity space v_x, v_y, v_z and the position x, y, z, at time t, can be described through a particle distribution function (pdf) which can be written as

$$f(t, x, y, z, v_x, v_y, v_z).$$

Single species of particles, in thermal equilibrium with itself, with no time variations, no gradients and no accelerations can be described by the Maxwell-Boltzmann distribution function, depending only on the velocity space, as

$$f(v_x, v_y, v_z) = n\left(\frac{m}{2\pi k_B T}\right)^{\frac{3}{2}} exp\left(-\frac{m\left({v_x}^2 + {v_y}^2 + {v_z}^2\right)}{2k_B T}\right)$$

which can be rewrite as a function of modulus velocity by transforming from rectangular to spherical co-ordinates ($dxdydz \rightarrow r^2 \sin\vartheta \, drd\vartheta d\varphi$) and then integrating over ϑ and φ, thus obtaining

$$f(v) = 4\pi v^2 n\left(\frac{m}{2\pi k_B T}\right)^{\frac{3}{2}} \exp\left(-\frac{mv^2}{2k_B T}\right)$$

where n is the particles density, m is the mass of the particles and $k_B T$is the thermal energy.Thanks to this assumption, it is possible to evaluate the reaction rate, R_{12}, taking into account that both incident and target particles have a distribution of random velocities, thus obtaining [6]

$$R_{12} = \int f_1(v_1)\, f_2(v_2)\sigma(|v_2 - v_1|)|v_2 - v_1| dv_1 dv_2$$

where $f_k(v_k)$ is the Maxwell-Boltzmann distribution function for the k specie. It is possible to rewrite this relation in a more compact form as

$$R_{12} = < \sigma v > n_1 n_2$$

where <σv> is the *reactivity*, which is the product of the fusion cross section σ and the relative velocity of the two interacting nuclei v, averaged over the Maxwellian distribution function of nuclei's velocities, while n_1 and $n_2$are the ion densities of the two species (in this case D and T).By multiplying the fusion reaction rate by the energy produced in the fusion reaction,E, (which for a D-T reaction is17.6 MeV), the thermonuclear power P_{th} is obtained as[7]

$$P_{th} = R_{12} E.$$

Since the task is to maximize P_{th}, the maximum reaction rate between different fusion reactions must be considered. Figure 1. 7 shows the behavior of the reactivity of several fusion reactions against the temperature in keV. It highlights that the maximum value of R_{12} obtainable is the D-T reaction one, remarking why this is the reaction on which the experimentations are focused on. It shows a peak at ~100 keV, which corresponds to a temperature of two order of magnitude higher than the temperature at the center of the sun [8].

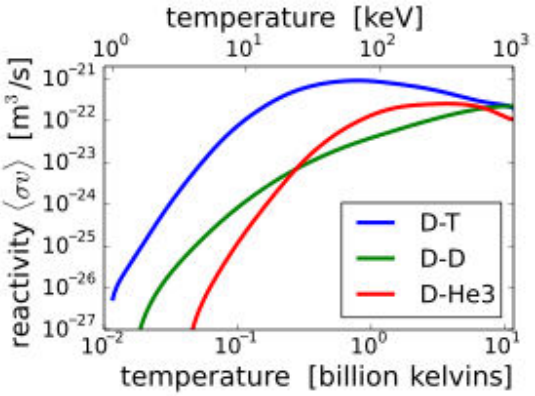

Figure 1. 7 *Reactivity for several fusion reactions*

1.3 Key components of a fusion experimental power plant based on magnetic confinement

The heart of a fusion experimental power plant based on magnetic confinement is the magnetic confinement system and the heating and current drive (H&CD) systems. These specific systems have to guarantee the adequate plasma heating and confinement in order to sustain fusion reaction for energy production in the perspective of a continuous operation. Indeed, energy production through fusion reaction is not an easy task and there are several conditions that must be achieved for a correct and controlled operation, requiring adequate technologies and knowledge. Plasma needs to be constantly maintained at high temperature preserving the continuity of the fusion reaction. For this reason, it must be properly controlled, preventing it from touching the walls of the vessel in which it is produced, otherwise it cools down and the fusion reaction stops. The amount of time the energy confined within the plasma is called *confinement time* (τ_e) and, in the perspective of a continuous operation, it should be sufficiently long (the values obtained so far are in the order of seconds).Furthermore, since the interacting particles (D-T in this case) are moving really fast within plasma, in order to allow the fusion reactions to occur, the magnetic confinement system, thanks to specific magnetic configuration, has the task to keep the plasma density sufficiently high, thus ensuring collisions do actually occur.

1.3.1 Tokamak

The plasma magnetic confinement, in order to obtain sufficiently high values of plasma density and confinement time, is studied in three different magnetic configurations: stellarator, reversed field pinch and tokamak [6]. The latter is the reference configuration since it provided the best technological results. The tokamak has a toroidal, ring-shaped vacuum vessel in which plasma is produced and confined through a specific design of magnetic fields configuration. It is equipped with three different magnetic field sources:

- a toroidal field coils system: it is characterized by several D-shaped toroidal field magnets placed around the vacuum vessel and producing the toroidal magnetic field which force particles to move following helicoidal trajectories along the field line;

- a inner poloidal fields coils system: it is characterized by a central solenoid which acts as the primary winding of a transformer, whose secondary winding is the plasma itself. This solenoid induces a current inside the plasma that both heat the plasma itself (by ohmic heating) and produces a poloidal magnetic field;

- an outer poloidal field coils system: it is characterized by several ring-shaped poloidal field coils, which are placed outwards the toroidal field coils system. They have the task to provide a vertical magnetic field.

The toroidal field provides the guiding centre for the electrons and ions helicoidal trajectories. The poloidal field prevents particles from drifting in the vertical direction and escaping outwards the confinement region. Finally the vertical field, interacting with the current induced to the plasma, is opposed to the expansion of plasma towards the inner walls of the ring-shaped vacuum vessel, providing also plasma positioning and shaping. Figure 1. 8 shows the structure of a tokamak highlighting the different magnetic fields and their sources.

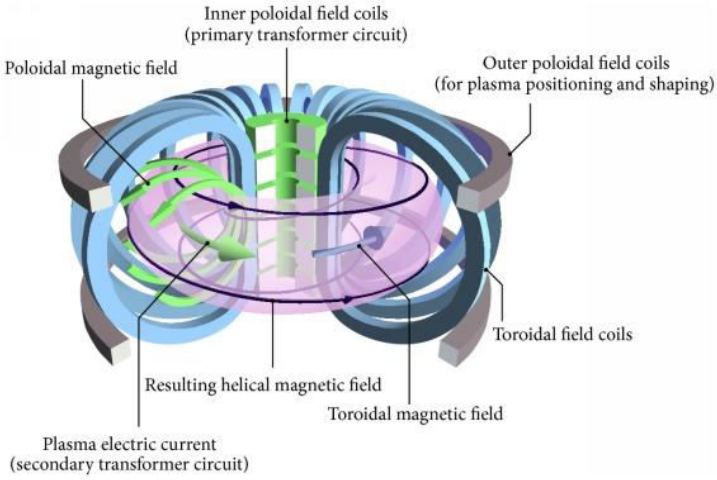

Figure 1. 8 *Principle's scheme of a tokamak magnetic confinement system*

1.3.2 Heating &Current Drive systems

Besides the magnetic confinement, in order to sustain a continuous fusion reaction for energy production, a sufficient temperature level for plasma is required. A useful parameter to evaluate the feasibility of a controlled fusion reaction is the energy gain factor Q, which is the ratio of fusion power produced in a fusion reactor P_{th}[2] to the external power required to sustain the plasma P_{ext} as

$$Q = \frac{P_{th}}{P_{ext}}.$$

[2]The thermonuclear power for a D-T fusion reaction can be define as $P_{th} = n_D n_T \langle \sigma v \rangle E$, where E is the overall energy released during the reaction (17.6 MeV), which is consisting of 3.5 MeV associated to the α particle and 14.1 MeV associated to the neutron, and $R_{D-T} = n_D n_T \langle \sigma v \rangle$ is the reaction rate. R_{D-T} is maximum when $n_D = n_T = \frac{n}{2}$ and P_{th} is equal to $P_{th} = \frac{n^2}{4} \langle \sigma v \rangle (E_\alpha + E_n) = P_\alpha + P_n$[6].

Until now, the best result for a fusion experimental power plant was Q = 0.67, obtained through a D-T reaction at Joint European Torus project (JET) in 1997, with a P_{th}= 16 MW and a P_{ext} = 24 MW highligthing that even the equilibrium condition for which P_{th}=P_{ext}, the*breakeven condition*, has never been reached[9]. The ideal and most desirable condition for a continuous production of fusion energy is the so-called *ignition condition*, which foresees to reach $Q = \infty$, condition at which a nuclear fusion reaction is self-sustaining, without requiring any external heating. The *ignition condition* can be express through Lawson criteria considering only the power losses related to transport (energy lost in τ_e by conduction and convection) and Bremsstrahlung (radiation losses), the confinement of the α particles and that no power is delivered to the grid. Hence it is possible to analyze a simplified 0D power balance inside plasma, which is outlined in Figure 1. 9. Since P_{ext} is assumed equal to zero in this condition, the input is associated to the alpha power,P_α, and the neutron power, P_n, which are related to the kinetic energy of the α particle and the neutron produced by a fusion reaction (see D-T reaction in 1.2.2),while the output is associated to power related to the neutrons, P_n, which are not confined within plasma, and to the transport and Bremsstrahlung losses, respectivelyP_T and P_B.Hence, the power balance can be express as,

$$P_\alpha + P_n = P_n + P_T + P_B$$

where, considering $n_D = n_T = \frac{n}{2}$, $P_T = \frac{3nk_BT}{\tau_e}$ and $P_B = bn^2\sqrt{T}$ where b is a proportionality constant experimentally determined and equal to 5.35×10^{-37} [7].

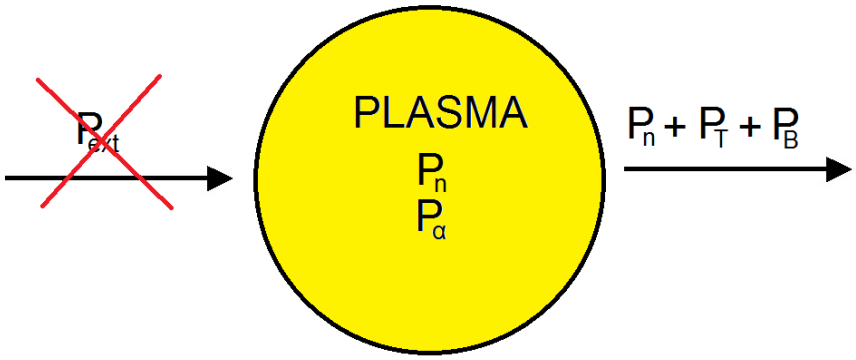

Figure 1. 9 *Simplified 0D power balance inside plasma*

By deleting P_n, since it is on both side of the equivalence, the resulting equation is equal to$P_\alpha = P_T + P_B$and solving the latter equation, it is possible to obtain a fundamental result:

$$n\tau_e = \frac{3k_BT}{\frac{1}{20}\langle\sigma v\rangle E - b\sqrt{T}}.$$

By plotting this equation against temperature (in keV), Figure 1. 10 is obtained: the minimum of the curve corresponds to the *ignition condition* and it is achievable only for $n\tau_e$ = 1.5×10^{20} m^3/s, which is obtainable only for a temperature of 20 keV.

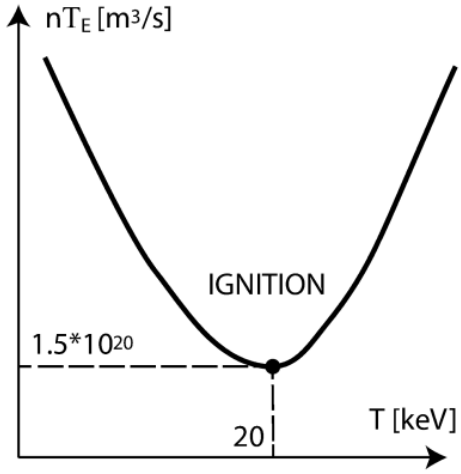

Figure 1. 10 *Value of $n\tau_e$ against temperature in order to reach the ignition condition*

This result is crucial since the combination of temperature, confinement time and plasma density has a fundamental role within fusion research: the product of these three parameters, the so-called *triple product*, provides a convenient form to define the *ignition condition*. In this specific case, for a D-T reaction, this condition corresponds to

$$nT\tau_e > 3 \times 10^{21} \text{ m}^{-3}\text{keVs}.$$

In order to reach such temperature, an adequate heating system is required. Plasma, within the tokamak, acts like a conductor and it is characterized by an internal ohmic resistance. For this reason, ohmic heating (P_{ohm}) can be provided by producing a high plasma current. However, for a typical tokamak configuration, P_{ohm} can reach the maximum temperature of $\sim$3 keV since the electrical resistance of plasma decreases as the temperature increases, following the *Spritzer conductivity* relation for which the resistance decreases in proportion to $T_e^{-\frac{3}{2}}$, where T_e is the electron temperature [10]. Furthermore, alpha power (P_α) becomes relevant from temperature higher than 5÷7 keV and then ohmic heating alone is not sufficient to reach these temperature values. For this reason, an external additional power must be provided, and this need is fulfilled by the Heating & Current Drive (H&CD) systems, which structure is shown in Figure 1. 11.

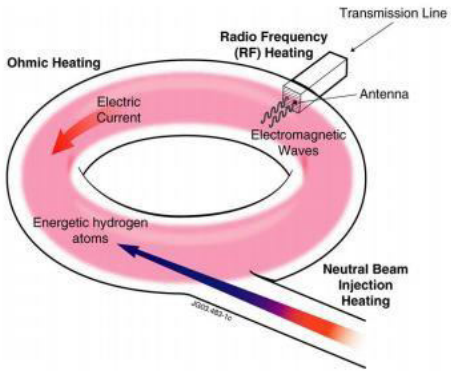

Figure 1. 11 *Principle's scheme of H&CD systems*

The H&CDsystems has the dual task of heating plasma and driving plasma current by means of two different systems, which can provide several MW of additional power: a Radio Frequency (RF) system and a Neutral Beam Injection (NBI) system.

The former is based on coupling of resonant RF electromagnetic waves to the plasma and it has to drive plasma current by accelerating a plasma species. Since the cyclotron frequency of a specie is

$$\omega = \frac{qB}{m}$$

where q is the charge of the specie, B is the magnetic field and m is the mass of the specie, and it is different between ionsand electrons, two diffferent systems are used: an Electron Cyclotron Resonance Heating (ECRH) for a frequency range of 50-170 GHz and an Ion Cyclotron Resonance Heating (ICRH) for a frequency range of 30-100 MHz. There is also a third system for a small middle frequency range (1-10 GHz) called Lower Hybrid (LH) system [9].

The NBI system provides to heat plasma by injecting high energy neutral particles inside plasma, which are forcibly directed along specific straight lines, until they are ionized by plasma, becoming confined fast ions. Hence, their energy is transferred to plasma through Coulomb collision and this process is called *slow down process*. Moreover, by varying the toroidal direction of the velocity of the injected particles, realizing a tangential injection, it is possible to drive plasma current. The NBI is characterized by 4 different stages: a positive or negative-ion source, where ions are generated; an acceleration grids system through which ions are accelerated to the required energy level, obtaining fast ions beamlets; a neutralizer where the accelerated ions are neutralized, obtaining fast neutral particle beamlets travelling through the NBI duct; a residual ion dump where the ions survived from the neutralization process are collected, thanks to the deflection produced by electric or magnetic fields configurations. The NBI will be analyzed more in detail in chapter2, focusing deeper on the ion source and its power supply system.

1.4 ITER project and planned fusion experimental power plants

The roadmap towards the realization of a fusion experimental power plant able to achieve the breakeven condition, and even overcome it, is complex and several projects have been carried out since the second half of the 20th century, such as the aforementioned JET project. The most ambitious fusion energy project in the world today is ITER.

ITER is an international project involving 35 nations in order to build the world's largest tokamak, of about 23000 tons, to prove the feasibility of net fusion energy production. ITER is under construction in Saint Paul-lez-Durance, southern France. The idea for a collaborative international project to develop fusion energy for peaceful purpose was firstly proposed at Geneva Superpower Summit in November 1985, and the next year an agreement between European Union (EURATOM), Japan, Soviet Union and United States for the realization of the design of a large international fusion facility was concluded. After several years of project proposals and design variations, the final design of ITER was approved by members in 2001. In the following years the number of members of the ITER project grows and on 24 October 2007, the ITER Agreement was officially established between China, the European Union, India, Japan, Korea, Russia and the United States. This experimental project has been designed with the ambitious goal to reach a gain factor equals to 10 (Q=10), producing 500 MW of fusion power with 50 MW of input heating power. To obtain such thermonuclear power value, plasma volume inside the tokamak must be of 840 m^3, with a major plasma radius of 6.2 m and a minor plasma radius of 2 m,

and a plasma temperature of 1.5×10^8 K is required. Moreover, ITER project has other fundamental goals: demonstrate the integrated operation of the specific technologies and components of a fusion power plant (such as NBI, magnetic confinement components, cryogenics and so on); achieve a D-T plasma in which the reaction is sustained thanks to internal heating, obtaining the so-called burning plasma, which could avoid external heating; test tritium breeding in order to prove the feasibility of a tritium production inside the vacuum vessel through a breeding blankets solution; demonstrate the safety characteristics of a fusion device, proving fusion reaction control with no environmental consequences. The timeline of ITER foresees the first plasma in 2025 and the start of the D-T operation in 2035.For a complete support to ITER project, every member of the ITER Agreement has founded its own domestic agency to fulfill its procurement responsibilities, coordinating the interactions and contracts with industry. It is important to highlight that ITER is not the final step in fusion energy research, but it is only part of the roadmap towards the commercial feasibility of fusion energy production[11].

The next step will be DEMO project, proposed by the EUROfusion consortium, which will have the task to prove the feasibility of commercial electricity production for a future fusion power plant. DEMO (DEMOnstration power plant), besides the knowhow obtained thanks to ITER campaign, will aim to set a transition from a science-driven, lab-based exercise to an industry-driven and technology driven programme. The project is planned to deliver from 300 MW to 500 MW of net electricity to the European grid. Besides this goal, it has the task to verify the feasibility of an operation with a closed fuel-cycle, reprocessing the tritium spent inside the system to sustain the fusion reaction [12].

Another project, proposed by ENEA and approved by EUROfusion, is the Divertor Tokamak Test facility (DTT), which aims to be the link between ITER and DEMO, providing a testbed for specific components that will be crucial in DEMO operation, such as the divertor that is a direct plasma facing component and part of the system deputed to convey out of the vessel the “dust” of the fusion reactions and that is stressed by extremely high heat loads technologically challenging. It will be realized in Frascati, Italy, and its first experimental plasma is foreseen for 2026 [13].

2 ITER Neutral Beam Injector and test facility

The ITER NBI system is foreseen to deliver an overall of 33MW to the plasma thanks to two neutral beam injectors each delivering 16.5 MW of 1 MeV D^0 for a beam pulse length up to 3600 s (it has been foreseen also the space for a third optional NBI). Furthermore, ITER design allows the integration of a smaller NBI which will be used for the plasma diagnostic [11]. Figure 2. 1 shows the structure and the components of the ITER NBI.

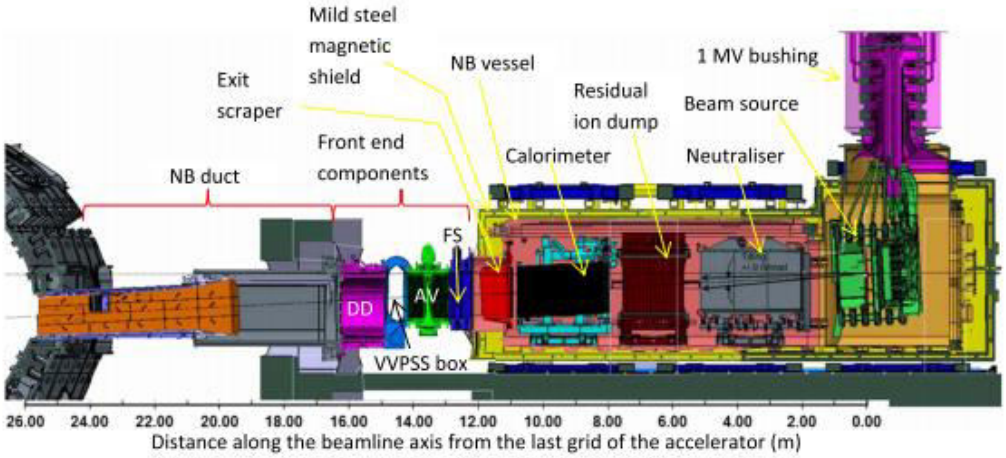

Figure 2. 1 *Design of the ITER NBI* [14]

ITER NBI is foreseen to be supplied by a high pressure SF_6insulated high-voltage (1 MV DC) transmission line, separated by the vacuum in the vessel by a 1 MV bushing. Downstream, there is the beam source, which includes the ion source for the production of the plasma through specific RF sources (the RF circuits of the ion source will be described in chapter 3) and the extraction and acceleration grids system for the extraction and acceleration of the negative ions (it will be described in detail in 2.1.2). Then, there is the neutralizer, where the fast negative-ions obtained in the beam source become neutrals, and the Residual Ion Dump (RID) towards which the surviving deuterium ions, D^- and D^+, are deflected and collected. Downstream the RID, the resulting neutral beamlets reach the calorimeter, which is made by two panels either in a V shape. It intercepts the beam during commissioning and when it is open the beam is allowed passing through. The vacuum vessel, is linked to the front-end component through an exit scraper made by water cooled copper panels, to prevent the direct beam interception on the vessel. Downstream there are the front-end components, including a Fast Shutter (FS), whose primary task is to minimize the transport contamination from tokamak to the vacuum vessel, an Absolute Valve (AV), which is able to isolate the upstream parts of the vacuum vessel to the Drift Duct (DD), the NB duct and the tokamak vessel. The DD provide a flexible connection between the vacuum vessel and the NB duct, which is part of the primary confinement barrier and its left-end is attached to the tokamak vessel. The NB duct consists of a rectangular SS duct, which forms the vacuum barrier, equipped in the internal left wall with a high water cooled Cu panel as protection system for the duct wall from re-ionized beam particles. Between DD and AV, there is a Vacuum Vessel Pressure Suppression System (VVPSS) which must to keep the overpressure resulting from tokamak's events to < 0.15 MPa and a VVPSS box which has to deflect the hot gases entering the NB duct from the tokamak to the VVPSS expansion tanks [14].

To reach the planned output power, as aforementioned, deuterium atoms must be accelerated inside the beam source to 1 MeV through the application of a specific electric field. For this reason they must be converted to ions before accelerating them, and then they must be neutralized to penetrate into

ITER plasma. Since particles must be accelerated to 1 MeV, a positive ion source would be critical for the operation of ITER. This is due to the fact that positive ions are hard to neutralize at this high kinetic energy levels, showing prohibitive low neutralization efficiency. Meanwhile, negative ions allow to obtain an acceptable neutralization efficiency of ~60% at the required energy of 1 MeV/nucleon, showing a nearly independent behaviour from 100 keV/nucleon onwards, as it is highlighted in Figure 2. 2 [15].

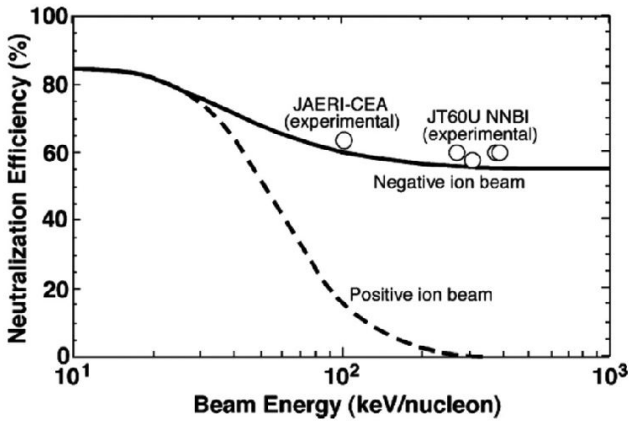

Figure 2. 2 *Neutralization efficiency for positive and negative ion beams against beam energy* [15]

However, even if a negative ion source is necessary for ITER requirements, producing and handling negative ions is more difficult than positive ions, especially as regards managing the co-extracted electrons from the source, which produce high heat loads by impinging on the grids. Hence, it implies that a strong R&D and testing programme is needed to support the ITER NBI project.

2.1 ITER Neutral Beam Test Facility (NBTF): PRIMA

Since the operating conditions of 16.5 MW of 1 MeV D^0 beam for beam pulse length up to 3600 s has never been reached jointly, in 2010, ITER Council decided to build a test facility for the realization and test of the prototype of the ITER NBI. The designated location was Consorzio RFX in Padua, Italy, a research laboratory involved in plasma physics and controlled nuclear fusion since 1996. In 2012, building work of the ITER NBTF, called PRIMA (Padova Research on ITER Megavolt Accelerator), has started with a programme of support and collaboration between Consorzio RFX, European, Japanese and Indian Domestic Agencies, the ITER Organization and several European laboratories. PRIMA test facility, which is shown in Figure 2. 3, comprehends a total area of 17.500 m^2 where two different experiments are hosted: MITICA (Megavolt ITER Injector & Concept Advancement), the full-scale prototype of the ITER heating neutral beam injector, and SPIDER (Source for Production of Ion of Deuterium Extracted from RF plasma), the full-size RF negative-ion source.

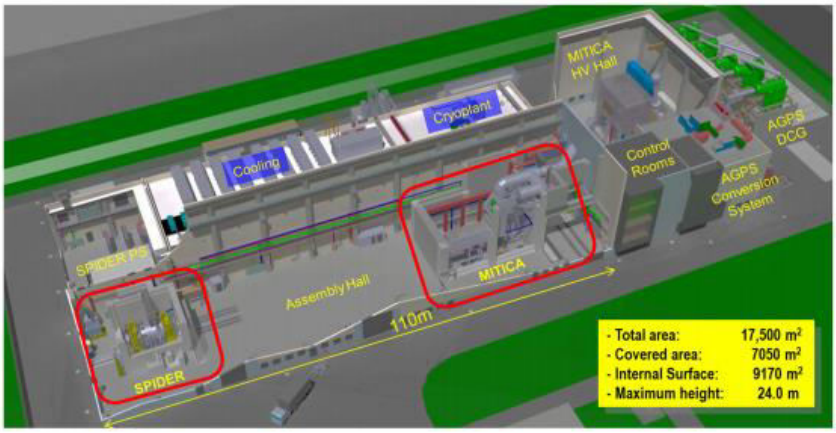

Figure 2. 3 *Structure of PRIMA test facility* [16]

2.1.1 MITICA

MITICA experiment, as the prototype of the NBI that will be installed on ITER, has the task to achieve the full performances and requirements of the future ITER NBI. Moreover MITICA will be equipped with additional diagnostics devices, which may not be used inside ITER NBI during operation, providing further possibilities of analysis and monitoring of the behavior of the system. The primary goals of the MITICA experiment can be summarized as:

- improving high voltage holding capability to reach 1 MeV of particle energy;
- maximize the ion beam current produced and minimize transmission losses in order to reach the required 16.5 MW of neutral beam power delivered;
- minimize heat loads and thermo-mechanical stresses on beamline components to reach the requirements of fatigue lifetime.

MITICA is currently under construction and the first plasma, according to ITER schedule, is expected to be in 2025 [16]. ITER Japan Domestic Agency (JADA), in collaboration with the National Institutes for Quantum and Radiological Science and Technology (QST) and Hitachi ltd., has already procured and installed the SF_6 insulated transmission line and the 1 MV high voltage bushing for MITICA experiment.

2.1.2 SPIDER: design and power supplies

SPIDER, the ITER-scale negative-ion source, which started operation from 2018, has a fundamental role within the programme of the NBTF. Its design, is based on the concept developed at Max-Planck-Institut für Plasmaphysik (IPP) in Garching, Germany, thanks to the expertise obtained through the negative-ion source testbed BATMAN (BAvarian Test MAchine for Negative ions). Hence, a cooperation programme between Consorzio RFX and IPP-Garching started. At present a half ITER-size test facility called ELISE (Extraction from a Large Ion Source Experiment) is in operation at IPP. SPIDER is a crucial step towards the NBTF schedule: the RF driven negative-ion source, which comprehends the plasma source and the extractor, has the same topological design to those that will be provided to ITER NBI and even MITICA. Hence, SPIDER campaign will grant huge benefits to MITICA experiment, allowing it to be mainly

focused on 1 MeV beam. SPIDER experiment has the goal to reach the challenging target requirements summarized in Table 2. 1.

Table 2. 1 *SPIDER target requirements* [16]

	Unit	H	D
Beam energy	keV	100	100
Max beam source filling pressure	Pa	0.3	0.3
Max deviation from uniformity	%	±10	±10
Current density of ions extracted from the plasma	A m^{-2}	>355	>285
Beam on time	s	3600	3600
Co-extracted electron fraction (e^-/H^-) and (e^-/D^-)		<0.5	<1

Figure 2. 4 shows the section of the internal structure of SPIDER.

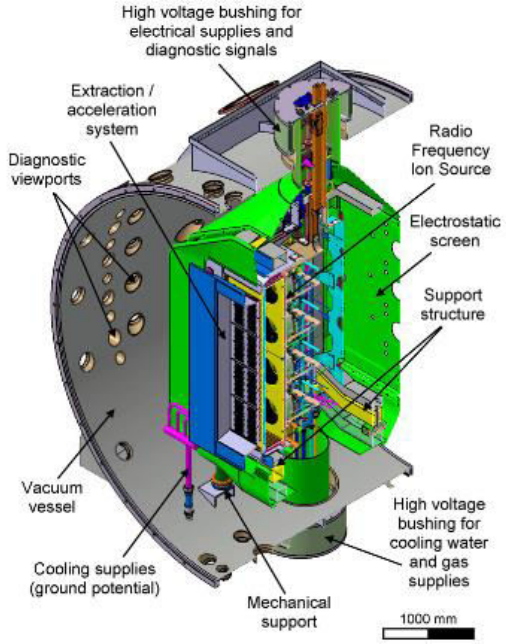

Figure 2. 4 *Section of the internal structure of SPIDER* [17]

SPIDER is characterized by an AISI 304 stainless steel cylindrical vessel of 4 m diameter and 6 m length, the Vacuum Vessel (VV), which is equipped with three 100 kV ceramic bushing for the service line feedthrough (power and signal, hydraulic injection, gas injection). Inside the VV is contained the SPIDER Beam Source (BS), which is designed to produce and accelerate the negative-ion beam to 100 keV. The plasma source, which is shown in Figure 2. 5 is characterized by eight cylindrical chambers, called drivers, mounted on the backplate of the source along with their matching networks (see 3.1.2). To produce plasma, deuterium or hydrogen gas at 0.3 Pa is injected into them. Each one of these drivers has coils wound around itself to transfer RF power, thus heating gas until it reaches the plasma-state. Thanks to the series connection of these coils, the overall eight drivers are grouped into 4 driver pairs, arranged in rows.

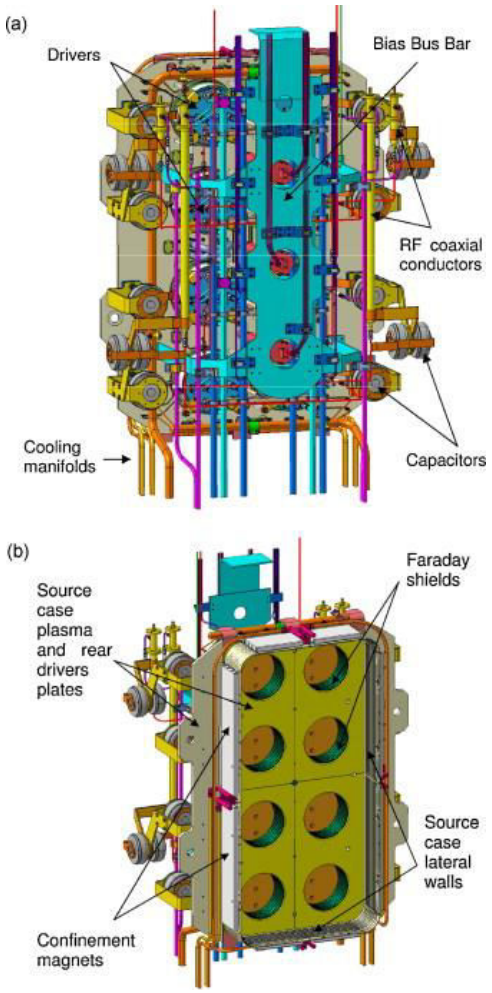

Figure 2. 5 *Rear view (a) and front view (b) of the ion source of SPIDER* [17]

2.1.2.1 The design of the beam source of SPIDER

Then plasma diffuses into an expansion chamber where it encounters a multiaperture grids system (each grid of about 2 m^2 wide with 1280 apertures) of the beam source. Figure 2. 6 shows the exploded view of the SPIDER beam source, which is consisting of:

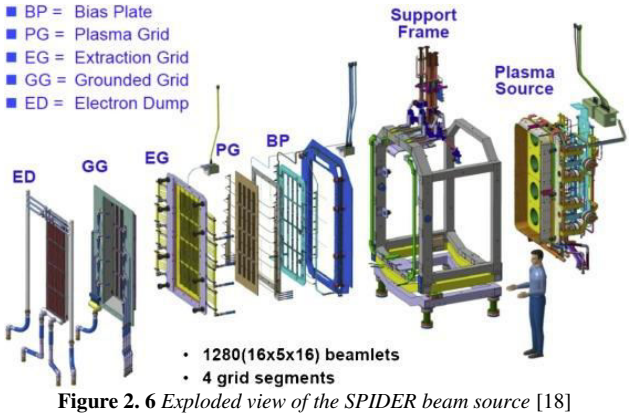

Figure 2. 6 *Exploded view of the SPIDER beam source* [18]

- Plasma Grid (PG): the first grid facing the plasma at (almost) the potential of the plasma source (-112 kV DC); it is made by four segments, which are caesiated during plasma pulses by evaporating caesium within the source in order to reduce the work function, thus facilitating the D/H atoms conversion to negative-ions. Moreover a 5 kA current flows in vertical direction through the PG producing a horizontal magnetic field to reduce electron temperature near the grid and the number of co-extracted electrons. Upstream the PG there is the Bias Plate (BP) which is divided in 5 segments and it provides an electrostatics barrier for the electrons thus modifying the electric field distribution in the region where the negative ions are produced.

- Extraction Grid (EG): the EG is biased by +12 kV DC with respect to the PG, thus enabling the extraction of D^-/H^- from plasma through the grid apertures, producing negative-ion beamlets, and deflecting the co-extracted electrons towards the EG, thanks to suppression magnets embedded into the grid.

- Grounded Grid (GG): the GG is at ground potential (0 V). Hence, the negative-ion beamlets exiting the EG are accelerated towards the GG by 100 kV, reaching their full energy. Furthermore, the deflection of the beamlets, due to the magnetic field configuration of the EG, is compensated through a second array of permanent magnets housed in the GG and by a ferromagnetic plate just after it. Downstream the GG there is the Electron Dump (ED) which is foreseen for removing the heat power produced by the co-accelerated electrons exiting the GG.

The beam source is surrounded by an electrostatic shield to prevent the risk of electric breakdown between source components and vessel. Moreover SPIDER is equipped with three caesium ovens installed in the beam source and it has several diagnostic devices both inside VV, such as thermocouples and probes, and outside VV, such as source emission spectroscopy and tomography [16].

2.1.2.2 The design of the of SPIDER power supply system

To guarantee the full operation of the components of SPIDER, a specific design for the power supply system is required. The SPIDER Power Supply (PS), which is shown in Figure 2. 8, is split into two parts: the Acceleration Grid Power Supply (AGPS) and the Ion Source and Extraction Power Supply (ISEPS). The former is a power supply rated for 96 kV and 71 A, which, thanks to three-oil insulated multi-secondary transformers and AC/DC converters with 150 switching modules, provides the main acceleration voltage between EG and GG. The latter is installed, along with the front-end of the diagnostic which are mounted on the source, within the High Voltage Deck (HVD), an air-insulated Faraday's cage of 13 m length, 11 m wide and 5 m height, which is at -100 kV respect to ground potential. For this reason it is mounted on a system of supporting insulators and it is connected to ground by an earthing switch. ISEPS three-phase power supply is provided by a -100 kV isolating transformer (ISGT), stepping down from 22 kV, delivered by the distribution system, to 6.6 kV. Then, from the ISGT, the supply line gets inside the HVD reaching a 6.6 kV distribution board (ISGW) from which all the ISEPS systems are supplied. They consist of:

- Extraction grid power supply (ISEG): it has the positive output pole connected to the EG and the negative output pole connected to the PG, thus imposing 12 kV between EG and PG. This DC voltage is obtained from an AC/DC modular converter (ISEG-TE), fed by a three-windings step-down transformer (ISEGT),based on a Pulse Step Modulator (PSM) topology, with 28 chopper modules connected in series, able to produce a DC square wave at 5 kHz. The EG, which is at -100 kV, is electrically connected to the HVD, requiring a set of isolating transformers for the equipment at PG potential (-112 kV).

- Radio Frequency power supply (ISRF): it is the ISEPS system which is responsible for the supply of the four pairs of driver's coils for the generation of plasma inside the plasma source. The ISRF design and the issues linked to its operation are the focus of this thesis work, hence its complete analysis will follow in chapter 3.

- Source support power supplies (ISSS): it brings together the Bias plate power supply (ISBP) and the Source bias power supply (ISBI), respectively needed for polarizing the BP and the source with a low voltage and an high current, the PG filter power supply (ISPG) and other auxiliary power supplies. They are all fed by a low voltage distribution board referred to PG potential, the ISGP.

In order to complete the analysis, Figure 2. 7 has been provided. It summarizes the interconnections between the grids system (on the right side) and their related power supplies (on the left side).

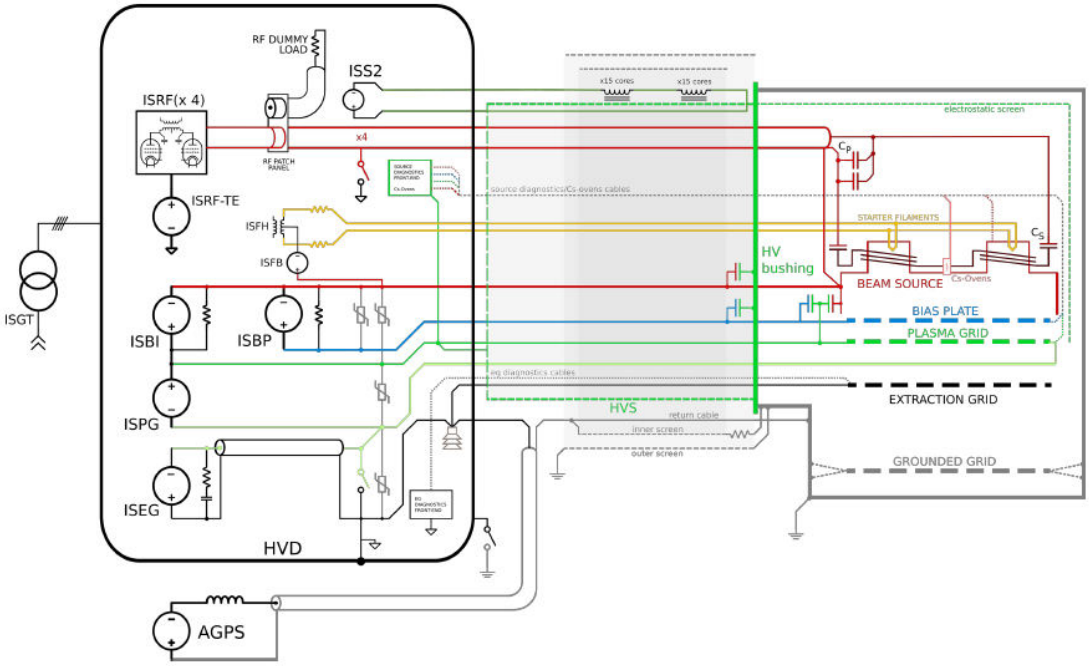

Figure 2. 7 *Conceptual scheme of SPIDER: power supplies (on the left side), transmission line (in the middle) and loads and grids system (on the left side)*

From the 6.6 kV distribution board is derived even the supply for the local control system (ISGN) through a step-down transformer 6.6 kV/400 V (ISGNT). The local control system is dedicated to the monitoring, protection and regulation of all ISEPS systems and the interaction with power supplies and between local and remote control are all realized through optic fibers to ensure the required insulation. Table 2. 2 shows the relevant specifications of ISEPS systems.

Table 2. 2 *ISEPS systems specifications* [19]

Power supply	Output ratings
ISEG	−12 kV ripple < ±1%, 140 A dc
ISRF-TE	12 kV ripple < ±0.25%, 140 A dc
ISRF	4 units, 200 kW each *f*= 1 MHz, 50 Ω load
ISBI	30 V, 600 A dc
ISPG	15 V, 5 kA dc

All the outputs of the ISEPS systems, after reaching the load collector (ISLC) (see Figure 2. 8), and the outputs of the AGPS, both power conductors and signal, are routed to the ion source through a high voltage transmission line (TL). The TL is a 100 kV air-insulated tri-axial line with a high voltage inner conductor with a diameter of 0.5 m inside a double screened structure of 1.2 m×1.2 m, aiming to reduce electromagnetic interferences.

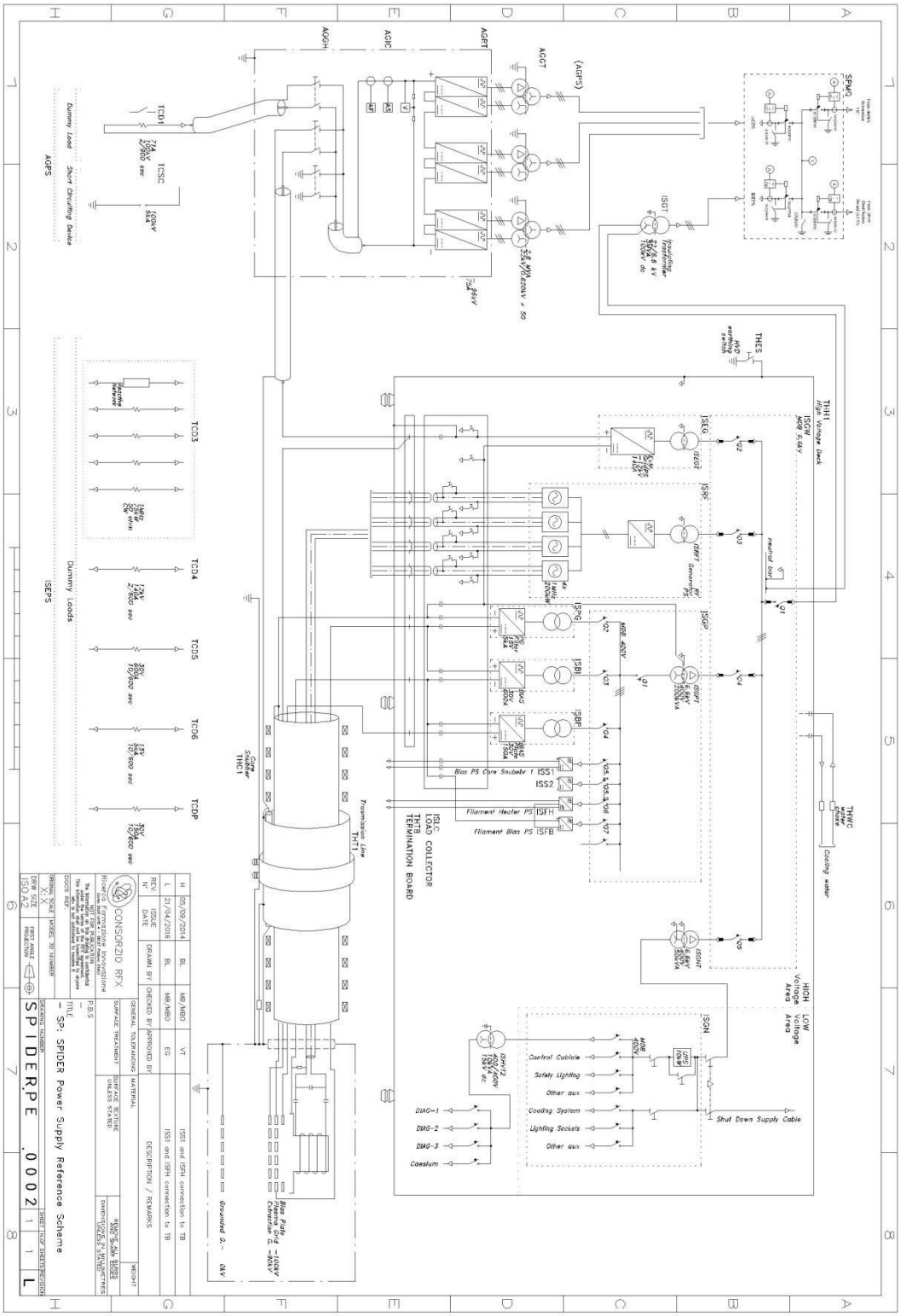

Figure 2. 8 *Reference electrical scheme of ISEPS and AGPS*

3 Ion Source Radio-Frequency Power Supply (ISRF)

The ISRF has the fundamental role of providing the required RF power to the coils wound around the drivers, in order to force D/H gas to plasma-state for the proper operation of the ion source. As aforementioned in 2.1.2, plasma is produced within eight drivers, which are grouped in 4 driver pairs each with series connection of their coils. For this reason, the RF system, as it has been shown in Figure 2. 8, is splitted into four different circuits, each one delivering an active power of 100 kW per driver at 1 MHz. This RF power is applied to the antennas of the driver (i.e. the coils wound around a driver), which are coupled with plasma, through a specific RF circuit, properly designed in order to provide the optimal power transfer. In this chapter the features of the RF circuits and the inherent issues related to its operation and design will be described.

3.1 The components of the RF circuit

The RF circuits are properly designed to guarantee that the required RF power reaches the antennas, allowing the correct operation of the plasma source. A single RF circuit is consisting of:

- a tetrode based self-excited oscillator as RF generator (RF-OSC), rated for operating in class C, in order to obtain an high efficiency (70 %), and delivering an active power of 200 kW on a 50 Ω resistive load;
- a coaxial transmission line;
- a matching network, based on a L-type configuration, consisting of a parallel capacitor (Cp) and series capacitors (Cs), properly designed for reaching the best matching condition with plasma;
- an ohmic-inductive impedance (Zd), representing the equivalent series impedance of the antennas of the two drivers.

The circuit diagram of the RF circuit is shown in Figure 3. 1.

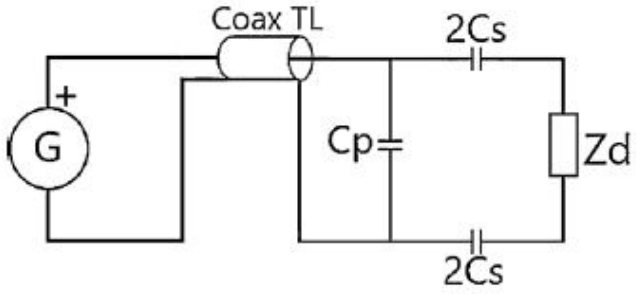

Figure 3. 1 *Design of the RF circuit*

3.1.1 RF-OSC

The RF-OSC is designed to deliver an overall RF active power up to 200 kW to the pairs of drivers (100 kW each), within the operative frequency range of 1 MHz $\pm$ 0.1 MHz. The use of a tetrode based oscillator typology is derived from the expertise obtained at IPP-Garching laboratory. The schematic configuration of the RF-OSC is shown in Figure 3. 2.

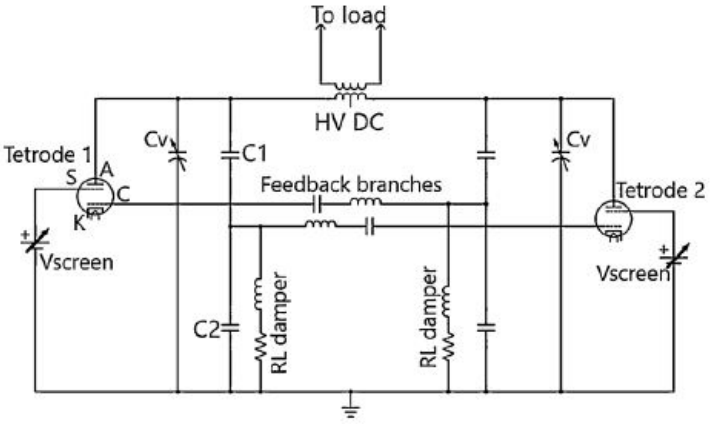

Figure 3. 2 *Circuit diagram of an RF-OSC* [20]

Every ISRF-OSC is tetrode based: tetrodes are four ports non-linear devices belonging to the thermionic vacuum tube device family. The proper operation and control of the oscillators is allowed by an electrode based system where each electrode is connected to a different port of the tetrode. According to Figure 3. 2[20], the cathode (K) is ground connected and it works as an electron source, while the associated anode/plate (A), which is positively biased at high DC voltage with respect to the cathode, has the aim of collecting the emitted electrons. The electron flux towards the anode can be modulated thanks to two grid-like electrodes connected to the remaining two ports of the tetrode: the control grid (C) and the screen grid (S). The former typically carries high frequency voltage signal to be amplified, while the latter is used for the modulation of the amplitude of the oscillation, and then power modulation. In addition, a feedback connection is realized between the two tetrodes and each control grid is fed by a fraction of the plate voltage of the other tetrode, allowing steady state oscillations of the RF-OSC. The screen grid is fed by a DC adjustable voltage (V_{screen}), lower than the anode voltage. The two tetrodes are combined in a Colpitts push-pull configuration: two Colpitts oscillators, which are anti-series connected, work alternatively and 180° phase shifted with each tetrode producing a half current sine wave. Each tank circuit is made by two capacitors (C1 and C2), the LC feedback branch of the control grid, the RL damper and an adjustable capacitor C_v. By varying C_v, it is possible to change the resonance frequency of the RF circuit, thus allowing changing the operating frequency of the RF generator. The variation range of the two C_v, which are regulated simultaneously thanks to controlled stepping motors, is between 0.1 nF and 1.5 nF, ensuring the required operation frequency of 1 MHz $\pm$ 0.1 MHz. The system is interfaced with the RF load thanks to an output transformer whose primary is splitted into two windings, each one connected to the anode of the two tetrodes. The supply voltage of the oscillator is a high DC voltage (HV DC), up to 12 kV DC, which is provided by the ISRF-TE, and it is applied to the anodes of the two tetrodes. The primary winding middle point is clamped to this HV DC. The RF-OSC unit includes also the circuits dedicated to the feedback control of the oscillator, which is portrayed in Figure 3. 3.

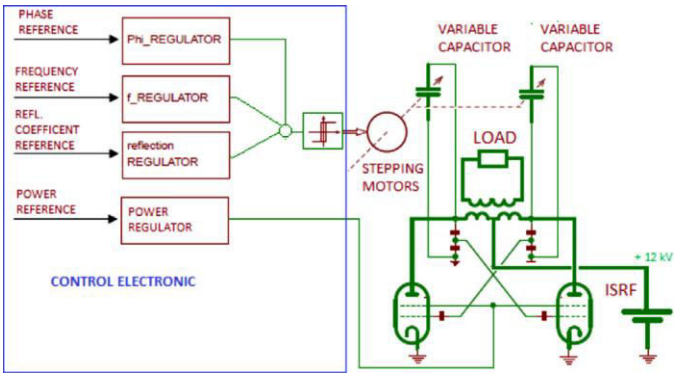

Figure 3. 3 *RF generator functional block diagram* [19]

Thanks to the output transducer of the RF-OSC (a current transformer and a capacitive voltage divider, whose description is postponed in 3.3.1) the measurements of active power, modulus of the reflection coefficient, frequency and phase are compared to their reference value and the resulting errors are employed in order to adjust them. In particular, the output power control loop is based on the variation of V_{screen} thanks to the output power error. Meanwhile, the frequency, the phase and the modulus of the reflection coefficient are regulated by adjusting the two variable capacitors through a stepping motor driven by their specific errors. The specifications of the RF-OSC are shown in Table 3. 1.

Table 3. 1 *Specifications of the RF-OSC* [19]

Item	Features
Frequency range	900–1100 kHz
Tetrode	THALES lQK-35 (two off)
Frequency accuracy	±1 kHz
RF harmonic distortion	<1% at full power on 50 Ω
Rated output	20–200 kW continuous on 50 Ω 160 kW on 50 Ω ± 30°
Power control accuracy	1% of rated power
Output volt. accuracy	±1% of rated voltage
Output curr. accuracy	±1% of rated current
Pulse duration	Continuous
RF decay/rise time	<300 µs
Cooling	Water cooled
Modes of operation	1. Internal tuning in real time 2. Preset freq. (plasma ignition) 3. Fixed preset frequency

3.1.2 RF load

Considering the scheme of Figure 3. 1, the coaxial transmission line, the matching network and the equivalent impedance of the two RF antennas constitute the RF load. It is fed by the RF generator (RF-OSC) and it is referred to the Ion source potential (-112 kV to ground) through a bar. The coaxial transmission line adopted within each RF circuit is a copper air-filled 3" 1/8 rigid transmission line with a characteristic impedance of 50 Ω and length of about 40 m. In order to ensure the maximum power transfer from the RF-OSC to the RF antennas, a matching condition must be achieved. Considering that the characteristic impedance of the coaxial transmission line is equal to 50 Ω, a matching network, properly designed to reach the matching condition with the RF antennas in presence of plasma, has been developed. The equivalent impedance of the antennas of the pairs of drivers series connected has been estimated to have a resistive part (Rd) and an inductive part (Ld). The reference values of the RF antennas parameters which have been estimated in order to dimension the matching network, were Rd = 4÷6 Ω and Ld = 15÷25 µH at 1 MHz [21]. Thanks to these reference values, the components of the capacitive L-type

matching network, which is shown in Figure 3. 1, have been dimensioned as: Cp = 10 nF, for the parallel capacitor, and 2Cs = 3 nF, for each of the two series capacitors, corresponding to an equivalent series capacitor, Cs, of 1.5 nF. The experimental measurements of the RF antennas parameters, without plasma, have provided the values of Rd = 1.9 Ω and Ld = 20.5 μH. The same parameters change once plasma has been initiated within drivers: the ignition of plasma produces an increase in Rd, due to the plasma internal resistance, and a slight decrease in Ld, due to the shielding effect of the plasma. Today, the estimation of Rd and Ld, with plasma, is currently difficult because it derives from measurements which are affected by errors (voltage, current and phase measurements) and uncertainties on the precise values of the line length and on the capacitance of the matching capacitors.

3.1.3 Frequency regulation for the best matching condition

The effects of the matching network can be clearly observed in Figure 3. 4, where the graphs of magnitude and phase of the equivalent impedance of the RF load, evaluated for specific antennas parameters (Rd = 5 Ω and Ld = 18 μH), against the frequency range of the RF-OSC, with plasma, are shown. The RF load is resonant, due to the capacitive nature of the matching network and the inductive nature (with losses) of the antennas. The frequency response of the RF load shows a resonance and an anti-resonance, which correspond to the zero crossing points of the phase curve. These specific points are highlighted in Figure 3. 4: the red circle represents a resonant point at about 1.03 MHz, while the blue triangle represents an anti-resonant point at about 1.05 MHz. Furthermore the resonant and the anti-resonant points do not respectively correspond to the peak and the minimum of the impedance, but they are frequency shifted: the resonant point towards higher frequency and the anti-resonant point towards lower frequency. This is essentially due to damping phenomena of the resistive elements of the circuit.

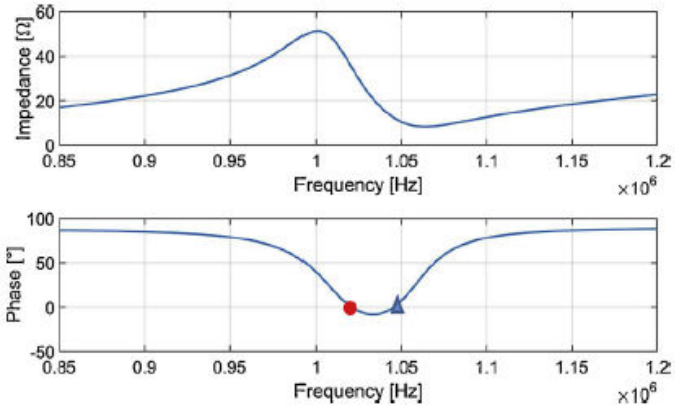

Figure 3. 4 *Magnitude (top) and phase (bottom) of the equivalent impedance of the RF load against the RF-OSC frequency range, with plasma, for Rd = 5 Ω and Ld = 18 μH* [20]

The perfect matching condition imposes that the impedance of the RF load must be equal to a pure resistance of 50 Ω. This condition is verified when the equivalent impedance of the matching network and the antennas is equal to the characteristic impedance of the coaxial transmission line (50 Ω). It implies that the line is perfectly matched and the reflection coefficient (at the output port) of the transmission line is equal to zero, thus allowing the maximum power transfer from the RF-OSC to the antennas. This is possible only in a strict frequency range and for a very small range of the impedance of the antennas of the drivers, coupled with plasma. For this reason, a frequency regulation to reach the matching condition and to cope the variations of the RF load, due to the variations of the plasma parameters, is required. These tasks could be achieved regulating together the adjustable capacitors, C_v, of the RF-OSC. However, approaching the matching frequency, an instability phenomenon, due to the self-

excited nature of the RF-OSC, may occurs, thus preventing to reach the matching condition. This phenomenon is called "frequency flip" and it will be described in 3.2.

3.1.4 Insulation between RF-OSC and RF-load

Since every single RF circuit is extended from the HVD to the ion source, which are referred to different DC potential levels, as it is shown in Figure 3. 5, a suitable insulation system must be adopted to guarantee a proper and safe operation. The RF-OSC, which is part of the ISRF, is referred to -100 kV to ground, which is the reference potential of the HVD. Meanwhile the matching network and the RF antennas are referred to -112 kV to ground, which is the reference potential of the ion source, as aforementioned in 2.1.2. However, thanks to the specific design of the RF generator, the proper insulation within the RF circuit is guaranteed by the output transformer of the RF-OSC.

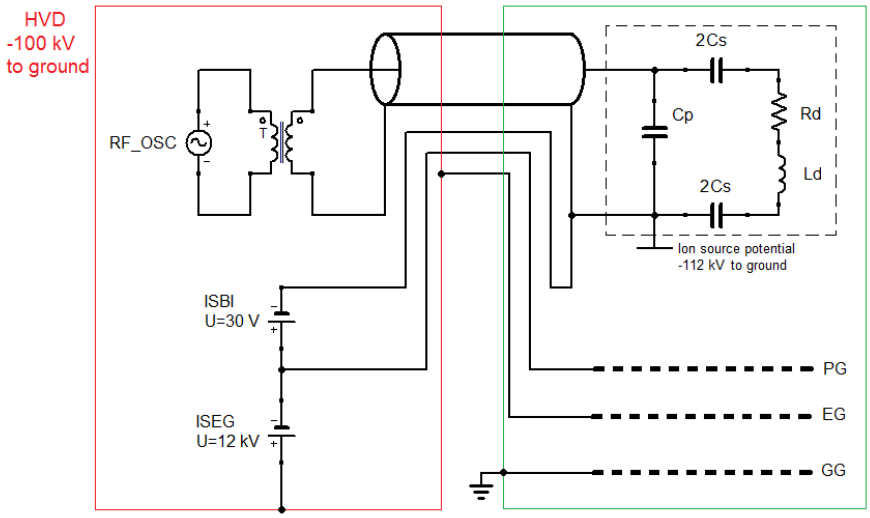

Figure 3. 5 *Simplified scheme of the Ion source and its power supplies (only ISBI and ISEG) with their related reference potentials, for a single RF circuit*

3.2 Issues related to tetrode based oscillators technology

Several issues related to the use of self-excited RF oscillators have been observed, essentially regarding frequency instability, and low efficiency. The RF-OSC of SPIDER has been properly designed to work in class C, in order to reach an electrical nominal efficiency of 70%. However, it is still a low value compared to solid-state solutions, which could guarantee a nominal efficiency of over 90%. Furthermore, future procurements and replacements of high power tubes, which are needed for RF circuits, could be difficult since solid-state components are replacing them in several modern applications. Hence, the production of tetrode and tetrode based components is expected to be reduced in the next decades, undermining the confidence upon the application of this technology, due to the risk of its potential obsolescence. Between all of these issues, the frequency instability during the operation of the tetrodes based oscillators on a resonant load circuit, due to the so-called frequency flip phenomenon, is critical and complex, thus requiring deeper analysis.

3.2.1 Frequency flip phenomenon

The frequency flip phenomenon, which is also observed at IPP-Garching laboratory during BATMAN and ELISE operation, is consisting of a sudden jump in the operating frequency of the oscillators of few tens of kHz. This jump has strong effects on the impedance of the RF load as it is seen by the RF-OSC, producing, consequently, a fast variation of its output voltage and current. This phenomenon, in SPIDER, occurs during frequency regulation, which is achieved thanks to the variations of the adjustable capacitors (Cv) of the RF-OSC, for reaching the matching condition, as aforementioned in 3.1.3. It is exactly next to the matching frequency (f_{match}) that the frequency flip is triggered. Approaching f_{match} from low frequencies, for a specific value of C_v, there is a certain probability that a jump towards frequencies higher than f_{match} can occur. The opposite behaviour can happen approaching f_{match} from higher frequencies. These trends result in a precluded frequency operating region of about 50 kHz that, in a frequency-C_v plane, as it is shown in Figure 3. 6, is represented by a hysteresis relation [20].

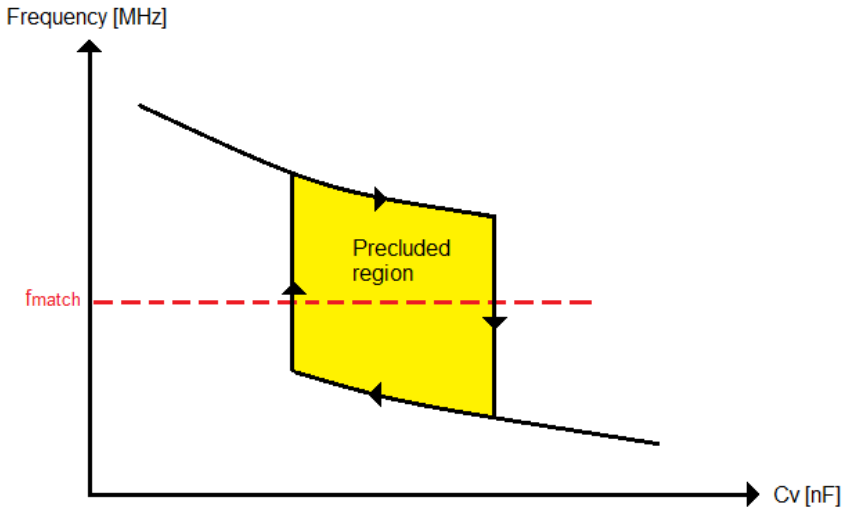

Figure 3. 6 *Hysteresis behavior due to the frequency flip phenomenon, resulting in a precluded region in the frequency-Cv plane*

As a result, the frequency flip phenomenon forces to operate the system mismatched, thus preventing the RF-OSC from delivering the rated power of 200 kW to the antennas because it is bound to work with low power factors. Moreover, the frequency flip implies several additional problems, concerning the operation of the RF circuit. At first, the impedance of the RF load varies suddenly as the frequency flip occurs:

- when $f < f_{match}$ and the flip is triggered, the impedance varies suddenly from a higher value than 50 Ω, near resonance, to a much lower value than 50 Ω, tens kHz higher than f_{match}, near the anti-resonance. This fast decrease in the RF load impedance produces a strong increase in the output current of the RF-OSC, with the same output power.

- when $f > f_{match}$ and the flip is triggered, the impedance change from a lower value than 50 Ω to a higher value than 50 Ω, tens kHz lower than f_{match}. Unlike the previous case, the sudden increase in impedance produces a strong increase in the output voltage of the RF-OSC, with the same output power.

These two consequences of the frequency flip phenomenon produces heavy electrical stresses on the components of the RF circuit, as they have to withstand fast variations of voltage and current, which

can exceed their ratings. It is possible to show numerically the occurrence of these events thanks to Figure 3. 4, considering the rated value of the RF-OSC of 200 kW delivered on 50 Ω. Assuming that the frequency flip could occur at ~1.01 MHz, at this frequency, the impedance is ~55 Ω and the phase is ~25°. In this operating condition the magnitude of the output voltage of the RF-OSC is about 3.32 kV while the magnitude of the output current is about 60.3 A. Hence, assuming that the working point would jump to ~1.06 MHz, due to the flip, where the impedance is ~10 Ω and the phase is ~15°, the output voltage of the generator would be reduced to about 1414 V, while the output current would reach about 141.4 A, more than double the previous output current value.

3.3 Issues related to the RF system

3.3.1 Output power measurement

Beside the issues concerning the operation of the RF-OSC, there are several problems related to its measurement system, which is schematized in Figure 3. 7.

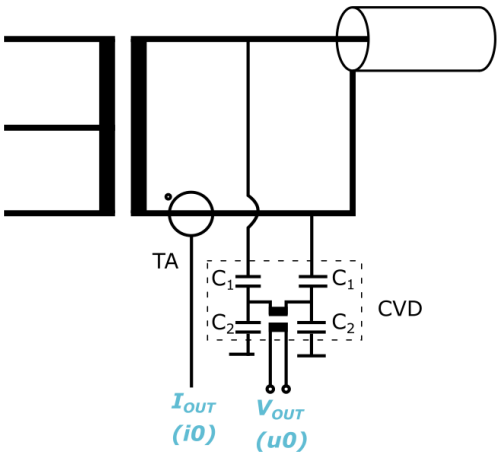

Figure 3. 7 *Measurement system of the RF-OSC based on transducers: a current transformer (TA), for the current measurement, and a capacitive voltage divider (CVD), for the voltage measurement*

It is consisting of a current transformer (TA) and a capacitive voltage divider (CVD) which are installed on the secondary winding of the output transformer of the RF-OSC, upstream the coaxial transmission line, in order to measure the output power of the oscillator for control and measurement purposes. Hence, the output active power, P, is measured by the volt-amperometric method as the integral of the istantaneous values of voltage, $v_M(t)$, and current, $i_M(t)$, as follows

$$P = \frac{1}{t_2 - t_1} \int_{t_1}^{t_2} v_M(t) \cdot i_M(t)\, dt.$$

Hence, thanks to the active power estimation, it is possible to estimate the power factor, $\cos\varphi$, by calculating the apparent power, S, as the product of the RMS values of voltage, V_{RMS}, and current, I_{RMS}, as

$$S = V_{RMS} I_{RMS}$$

and then dividing P by S, thus obtaining

$$\cos\varphi = \frac{P}{S}.$$

However, during SPIDER campaigns, issues were observed regarding the measured RF output power. For example, the derived power factor was sometimes higher than 1, or even the efficiency of the RF-OSC, which was expected to be not higher than 70%, was calculated to be even higher than 100%. After several researches, the cause of these errors on the RF output power evaluation has been discovered: there is a systematic error on the phase shift, variable with frequency, between the TA and the CVD signals not compensated by the RF output power measurement board. For this reason there is the need for substituting this output power measurement system of the RF-OSC with other alternative and independent systems, which can avoid the introduction of this phase displacement, or even compensate it. The possible solution is the use of dual directional couplers (DDC), which are four port devices able of measuring the forward voltage, V_{fwd}, and the reverse voltage, V_{refl}, in the transmission line, and then allowing to evaluate the forward and reflected power, the standing wave ratio (SWR), etc. The DDC measurements are foreseen to be more reliable and not affected by the load and by the upstream circuit.

3.3.2 RF common mode currents

Another problem, strictly related to the CVD and the design of the system, is the circulation of RF common mode currents (CMC). The CVD, which is needed for measuring the output voltage of the RF-OSC, has the high voltage terminals connected to the RF circuit by two vacuum capacitors of 250 pF, and it is bounded to the HVD with its lower end. This feature aims to refer the output signal of the CVD, as well as the control board of the RF-OSC, to the HVD potential. The impedance of the CVD at the operating frequency of the RF-OSC, it is equal to ~600 Ω and it allows the circulation of RF CMC from the ion source to the CVD [22]. Figure 3. 8 shows the scheme of the RF circuit, highlighting the path of the RF CMC, which is represented by the current I_3 (the current probe downstream the CVD is neglected).

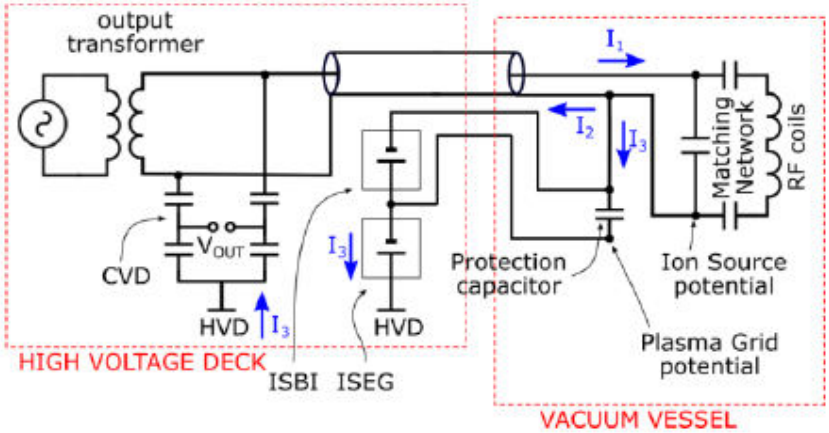

Figure 3. 8 *Single RF circuit for the analysis of the path of the RF CMC*

This RF current pass through a 2 μF protection capacitor, $C_{protect}$, which is connected between the ion source and the negative terminal of ISEG, whose task is to reduce the overvoltages due to possible breakdowns between the grids. Then it circulates across the ISEG filter, reaching the HVD and closing

through the CVD, being able to block the DC voltage components, but not the RF one. The effects of the RF CMC are clearly evident on the ISEG filter, where, with all the four RF-OSC in operation, each delivering 100 kW, a not negligible RF current of about 4 A appears. This current produces issues both on the diagnostic devices, overwhelming the useful signals with noise at RF frequency, and on the ISEG filter causing overheating over the passive components (250°C after 4 minutes) [22]. For these reasons, a proper modification of the design, or the components of the RF circuit is required in order to limit the RF CMC effects. Two different alternatives have been developed:

- the substitution of the CVD with a resistive voltage divider (RVD), connected to the RF circuit through two blocking capacitors of 10 pF, in order to block the DC voltage component of ISEG;

- the connection of the CVD at the primary side of the output transformer of the RF-OSC, thus including within the path of the RF CMC the stray capacitance between the two windings. In this case, the ISEG DC voltage component is blocked thanks to the output transformer. However, the CVD design must be changed, in order to sustain the DC voltage component coming from the ISRF-TE and the higher RF voltage applied.

Both these two alternative solutions are able to strongly reduce the RF CMC and they are currently under investigation. Between them, the latter solution has been chosen to be implemented within SPIDER during 2021 experimental campaign.

4 Characterization of the RF-Load through numerical models

To identify the proper RF amplifier specifications a clear knowledge of the RF load circuits seen at its output is necessary. This includes the coaxial transmission line, the matching network and the Drivers impedance which is affected by the plasma.

This chapter reports a characterization of the RF-Load through simulations obtained by proper numerical models realized with MATLAB scripts [23] run both in absence and in presence of plasma. Then, a peculiar aspect of SPIDER is discussed: the effect on the equivalent RF-Load impedance seen by the RF-Generator of the mutual coupling between two RF circuits in the source. The aim is to clarify whether this has consequences or not on the evaluated impedance and in what measure. After that, it is estimated the voltage and current distributions over the coaxial transmission line and the voltage and current on the Driver of the ion source. Then, an error analyses is presented: it is focused on the driver impedance parameter values that consider the uncertainties on the values of U, I, phase (available from measurements of the RF oscillator) and other RF load parameters like Cs, Cp and the transmission line length. Finally, to study in deep, it is realized a Sensitivity Analysis to find the most influential parameter in the determination of the error.

4.1 RF-Load impedance

The first step of the process of the RF-Load's characterization is the definition of its equivalent impedance. The input parameters of the numerical simulation, based on the RF circuit shown in chapter 2, are:

- a copper air filled 3" 1/8 rigid transmission line 30 m length;
- a capacitive matching network which is realized with a parallel capacitor Cp, having a capacitance of 10 nF, and series capacitors Cs, with an equivalent capacitance of 1.5 nF;
- the equivalent impedance of the series of the two drivers of the ion source Zd, which is an RL impedance.

Since the purpose is to initiate the plasma, it is necessary to analyze the RF load circuit both without plasma and with plasma. Without plasma, the assumption is that Zd is characterized by Rd= 2*Rdriv = 1.9 Ω and Ld = 2*Ldriv = 20.5 μH. With plasma, the resistive and inductive values of the driver impedance depend on the intrinsic nature of plasma, however, the trend with respect to the no plasma conditions shows the resistive part of the impedance increased due to the internal plasma resistance, while the inductive part lightly reduced, as a consequence of the shielding effect of the plasma. These variations are not easy to quantify, especially since the current power measurement systems are not enough reliable. Finally, for the numerical simulation, the estimated values are considered as Rd = 2*Rdriv = 3.5 Ω and Ld = 2*Ldriv =20.2 μH.

In the following each part of the developed electrical model of the RF load and the frequency response of the RF load impedance will be detailed. For the characterization of the RF-Load, it is assumed a frequency range of $0.9 \div 1.1$ MHz. This frequency range is coherent with the one expected to have with the solid-state RF amplifiers. The process of derivation of the RF load impedance is described in appendix

A work and the resulting formula has been implemented in a MATLAB script in order to evaluate the frequency response of the RF load both without plasma and with plasma condition, reported respectively in 4.1.1 and 4.1.2.

4.1.1 Frequency response without plasma

In Figure 4. 1 the magnitude and phase, respectively upper and lower graph, of the RF load frequency response are represented as results of the numerical model without plasma.

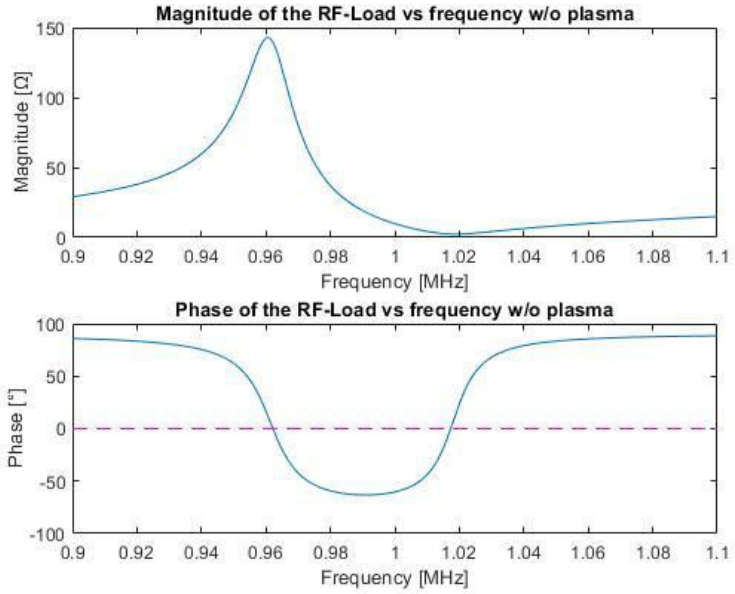

Figure 4. 1 *Graphs of magnitude (top) and phase (bottom) of the RF-Load without plasma*

As expected, the impedance shows a resonant behavior: it is possible to identify two resonant points where the phase crosses the zero value, symbolized by the horizontal magenta dotted line. Confronting the magnitude and the phase graphs it is possible to highlight the presence of a resonance for a frequency value of about 0.962 MHz to which corresponds to a magnitude of about 140 Ω, near the magnitude peak of 142.8 Ω. The second point corresponds to an anti-resonance with a frequency value of about 1.017 MHz and a magnitude of 2.4 Ω, near the minimum of the magnitude value of about 2.3Ω. The magnitude of the impedance at beginning of the frequency range is at 29.2 Ω, with a phase of about 86°. Approaching the resonant frequency, the magnitude grows, it reaches the peak and then it starts to fall, while the phase steadily drops until it reaches the zero value. From the resonance onwards the magnitude decreases and the phase assumes negative values until the minimum value of about -63.2° to which corresponds to a magnitude of about 18.7 Ω. From this point the magnitude continues to decrease, but the phase starts to grow until the anti-resonance frequency. From this point the magnitude of the impedance slightly starts to increase, while the phase continues growing until the right edge of the frequency range, where the magnitude value is of about 14.9 Ω and the phase value is of about 88.5°.

4.1.2 Frequency response with plasma

In Figure 4. 2 the magnitude and phase, respectively upper and lower graph, of the RF load frequency response are represented as results of the numerical model with plasma.

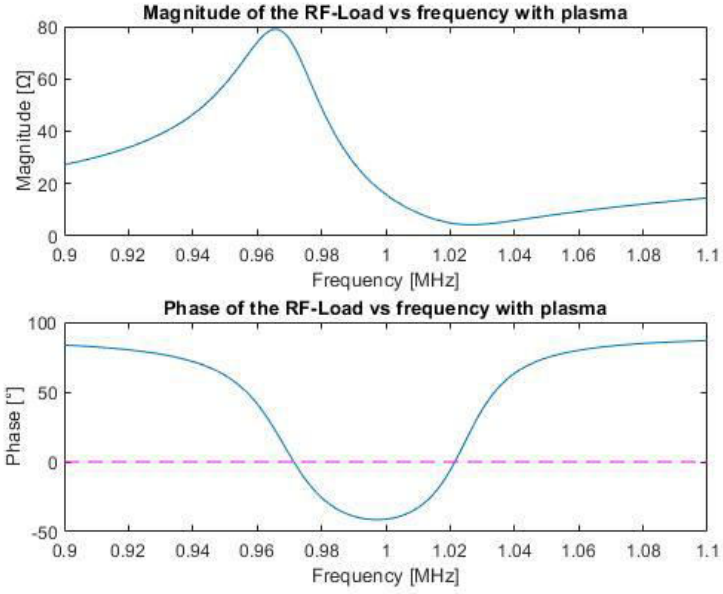

Figure 4. 2 *Graphs of magnitude (top) and phase (bottom) with plasma*

As mentioned before, with the ignition of the plasma, the parameters of the plasma vary as well as the magnitude and the phase of the impedance. It is worth noting that, even with plasma, there are a resonant point and an anti-resonant point: the first one is at about 0.971 MHz with a corresponding magnitude value of about 72.5 Ω; the second one is ∼1.021 MHz with a magnitude of ∼4.8 Ω. The behaviour of the graphs are similar to the no-plasma ones, but it is worth highlighting that the peak value of the magnitude of the impedance is lower than without plasma (∼79 Ω compared to ∼142.8Ω) and the minimum value of the magnitude is bigger than the previous case (∼4.3 Ω compared to ∼2.3Ω). Starting from the left edge of the frequency range, the magnitude of the impedance is of about 27.2 Ω and the phase value is of about 83.7°. The minimum value of the phase is of about -41.37° to which corresponds to a magnitude value of about 18.9 Ω. On the right frequency edge, the magnitude value is ∼14.5 Ω and the phase is ∼86.8°. It is interesting to notice that with plasma the magnitude range is lower than without plasma and the same trend is reflected to the phase range. Furthermore, changing from the case without plasma to the case with plasma, each characteristic slightly shift towards higher frequency.

4.2 Derivation of RF load impedance considering the mutual coupling between RF circuits

The generation of plasma inside the Ion Source is provided by 4 RF circuits each of which is fed by an independent RF-Oscillator, as described in chapter 2. In the previous analysis, the evaluation of the magnitude and the phase of the impedance of the RF-Load were carried out considering a single RF circuit, without any interactions with the others. Instead, in the real case, there is an interaction between the RF circuits due to the proximity of the respective RF connections. Aim of this section is to quantify how this aspect affects the equivalent impedance, in particular its frequency response, as it is seen by the RF-Generator.

For the analysis of the effects of the mutual coupling on the RF-Load impedance it is considered the interaction between only two RF circuits. This is done considering that experimentally the RF circuits are actually coupled in pairs.

Figure 4. 3 represents the reference scheme for the study of the mutual coupling effects: on the left side is considered the reference circuit consisting of the coaxial transmission line, the matching network and the driver, while on the right side it is considered the circuit mutually coupled with the previous one, identified by the impedance of the driver and the matching network (RF line and the equivalent load of the RF generator are not considered). The coupling is realized by two mutually coupled inductors. Estimations provide inductance equal to 1 μH ($L1$) for both circuits, and with a coupling coefficient Kequal to 10%. For this reason, in this specific analysis, the 20 μH inductance of the driver is decreased to 19 μH both without plasma and with plasma.

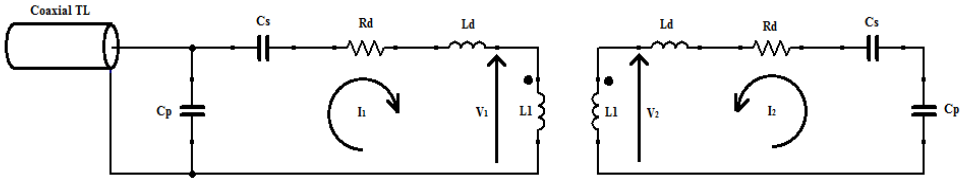

Figure 4. 3 *Scheme of the mutual coupling between two RF circuits*

Assuming linearity and temporal invariance it is possible to introduce the system that defines the mutual coupling between two circuits as

$$\begin{cases} v_1 = L_{11}\dfrac{di_1}{dt} + M_{12}\dfrac{di_2}{dt} \\ v_2 = M_{21}\dfrac{di_1}{dt} + L_{22}\dfrac{di_2}{dt} \end{cases}$$

where L_{11} is the selfinduction coefficient of the primary winding, L_{22} is the selfinduction coefficient of the secondary winding, M_{12} is the mutual coupling coefficient of the secondary winding over the primary one and M_{21} is the mutual coupling coefficient of the primary winding over the secondary one.

For the reciprocity principle it is possible to define

$$M_{12} = M_{21} = M$$

where M, the mutual inductance, is derivable from the coupling coefficient $K = \frac{M}{\sqrt{L_{11}L_{22}}}$ obtaining

$$M = K\sqrt{L_{11}L_{22}}$$

In this specific case, as mentioned before, the same values of inductance for both windings involved in the mutual coupling is assumed, so it is possible to write that $L_{11} = L_{22} = L1$. The mutual inductance, with this assumption becomes

$$M = KL1$$

Considering a sinusoidal regime, the system can be rewrite as

$$\begin{cases} \boldsymbol{V_1} = j\omega L1\boldsymbol{I_1} + j\omega M\boldsymbol{I_2} \\ \boldsymbol{V_2} = j\omega M\boldsymbol{I_1} + j\omega L1\boldsymbol{I_2} \end{cases}$$

The voltage applied to the secondary winding, $\boldsymbol{V_2}$, considering the voltage and current references highligthed in Figure 4. 3, is equal to the voltage drop over the series impedance $\boldsymbol{Z_{series}}$ of R_d, L_d, C_s and C_p

$$\boldsymbol{Z_{series}} = R_d + j\omega L_d + \frac{1}{j\omega C_s} + \frac{1}{j\omega C_p}$$

$$\boldsymbol{V_2} = -\boldsymbol{Z_{series}}\boldsymbol{I_2}$$

Substituting $\boldsymbol{V_2}$inside the system, it is possible to determine $\boldsymbol{I_2}$as

$$\boldsymbol{I_2} = -\frac{j\omega M\boldsymbol{I_1}}{\boldsymbol{Z_{series}} + j\omega L1}$$

and then, substituting it inside the first equation of the system, the relation between $\boldsymbol{V_1}$and $\boldsymbol{I_1}$is defined as

$$\boldsymbol{V_1} = j\omega L1 + \frac{\omega^2 M^2}{\boldsymbol{Z_{series}} + j\omega L1}\boldsymbol{I_1}$$

Hence, writing the ratio between $\boldsymbol{V_1}$and $\boldsymbol{I_1}$, the equivalent impedance $\boldsymbol{Z_{12}}$ at the secondary winding brought back to the primary winding is obtained

$$\boldsymbol{Z_{12}} = \frac{\boldsymbol{V_1}}{\boldsymbol{I_1}} = j\omega L1 + \frac{\omega^2 M^2}{\boldsymbol{Z_{series}} + j\omega L1}$$

Figure 4. 4 highlights the circuital configuration obtained.

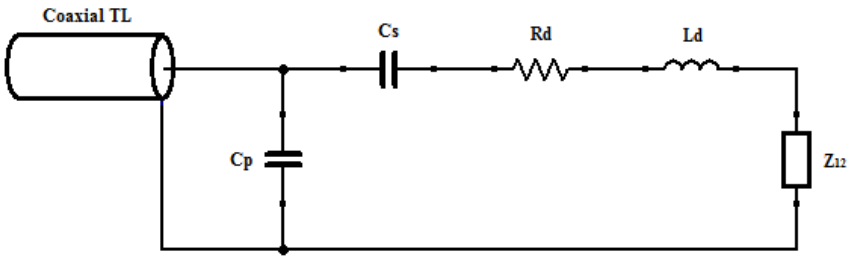

Figure 4. 4 *Scheme of the mutual coupling between two RF circuits, where the equivalent impedance of the secondary winding is brought back to the primary winding*

At this point it is easy to define the impedance of the RF-Load with the same method used in 4.1: defining the equivalent impedance of the series branch as

$$\boldsymbol{Z_{sb}} = \boldsymbol{Z_{12}} + R_d + j\omega L_d + \frac{1}{j\omega C_s}$$

and then the equivalent impedance at the end of the coaxial transmission line as

$$\boldsymbol{Z_{pb}} = \frac{\boldsymbol{Z_{sb}} \frac{1}{j\omega C_p}}{\boldsymbol{Z_{sb}} + \frac{1}{j\omega C_p}}$$

Finally it is possible to evaluate the impedance as it is seen by the RF-Generator as

$$\boldsymbol{Z_{RF-Load\_MC}} = \boldsymbol{z_0} \frac{\boldsymbol{Z_{pb}} \cosh \boldsymbol{k}d + \boldsymbol{z_0} \sinh \boldsymbol{k}d}{\boldsymbol{Z_{pb}} \sinh \boldsymbol{k}d + \boldsymbol{z_0} \cosh \boldsymbol{k}d}$$

The implementation of this formula in a MATLAB script was exploited to evaluate the frequency response of the RF load both without plasma and with plasma condition, reported respectively in 4.2.1 and 4.2.2.

4.2.1 Frequency response without plasma

In Figure 4. 5 the magnitude and phase, respectively upper and lower graph, of the RF load frequency response considering the influence of the mutual coupling without plasma are reported. These graphs are compared to the ones without mutual coupling condition for a further analysis.

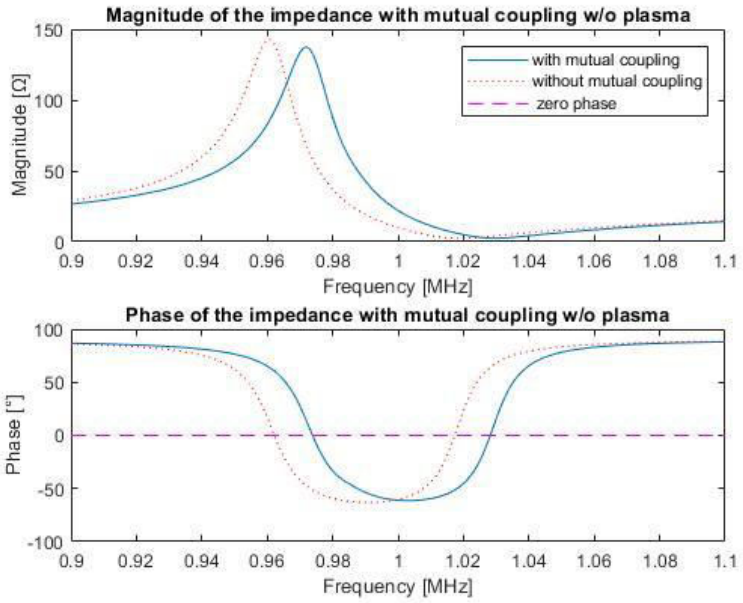

Figure 4. 5 *Graphs of magnitude (top) and phase (bottom) of the mutual coupling without plasma*

Starting from the left side of the frequency range, the magnitude of the impedance is equal to ~26.6 Ω, slightly smaller than the no mutual coupling case one (~29.2Ω). Instead, as regards the phase, in the mutual coupling case it is equal to ~86.8°, slightly bigger than 86° of the other case. Then the behaviour of the impedance and of the phase graphs, at the increasing frequency, is the same of the no mutual coupling, but it is possible to highlight some crucial aspects. At first, the characteristics of the mutual coupling case are shifted towards higher frequencies: the resonance frequency is shifted by 12 kHz

from about 0.962 MHz (which corresponds to a magnitude of ~140 Ω) to 0.974 MHz (~132.5 Ω) and the same happens to the anti-resonance frequency, shifted from about 1.017 MHz (~2.4 Ω) to 1.029 MHz (~2.5 Ω). Furthermore it is possible to observe that the peak of the magnitude of the impedance in the mutual coupling case, which is equal to 137.5Ω, is lower than the no mutual coupling case one (142.8Ω). The two peaks, in turn, are shifted by 12 kHz each other and the same happens to the minimum of the magnitude which reaches, in the mutual coupling case, the value of 2.5 Ω, bigger than the no mutual coupling case (equal to 2.3 Ω). On the right edge of the frequency range, for the mutual coupling case, the magnitude reaches ~14.1 Ω while the phase is equal to 88.1°. Finally the minimum of the phase is equal to -61.4° while in the no mutual coupling case is equal to -63.2°. Hence, considering the mutual coupling case, it can be observed an offset of 12 kHz towards higher frequency, compared to the no mutual coupling case, a little decrease in magnitude and an increase in phase.

4.2.2 Frequency response with plasma

In Figure 4. 6 the magnitude and phase, respectively upper and lower graph, of the RF load frequency response considering the influence of the mutual coupling with plasma are reported. Even under this condition, these graphs are compared to ones without mutual coupling.

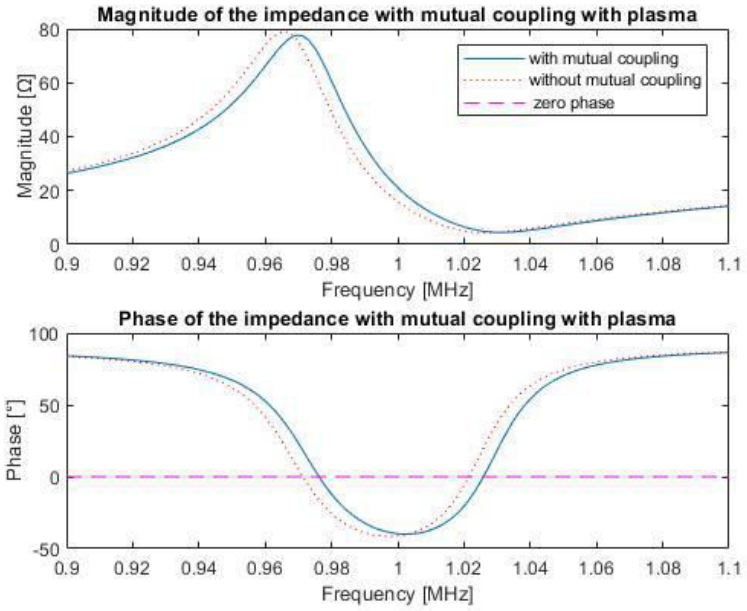

Figure 4. 6 *Graphs of magnitude (top) and phase (bottom) of the mutual coupling with plasma*

Even with plasma, the magnitude and phase graphs show a common behavior between the mutual coupling case and the no mutual coupling case, with an offset of about 5 kHz, lower than without plasma of 12 kHz. Moreover the differences in magnitude of the peak points and the minimum points between the two cases are lower than without plasma: the magnitude's peak point of the mutual coupling case, which is equal to 77.6 Ω, is closer to the no mutual coupling case one of ~79 Ω and the same, on a smaller scale, happens for the minimum point of the magnitude which for the mutual coupling case is ~4.4 Ω, against 4.3 Ω of the no mutual coupling case. The resonance frequency point is shifted from the value of the no mutual coupling case of about 0.971 MHz (to which corresponds to a magnitude of about 72.5 Ω) to ~0.976 MHz (~71 Ω) of the mutual coupling case, while the anti-resonance frequency point is shifted from ~1.021 MHz (~4.8 Ω) to ~1.026 MHz (~4.9 Ω). As regards the phase graph of the impedance, the minimum of the phase for the mutual coupling case, which is equal to -39.9°, is in correspondence of

1.002 MHz, while in the no mutual coupling case it is equal to -41.37°, in correspondance of 0.997 MHz. Moreover, at the left edge of the frequency range the magnitude for the mutual coupling case is equal to ~26.4 Ω and the phase is equal to ~84.2°, while at the right edge the magnitude is equal to ~14.2 Ω and the phase is equal to 86.5°. Finally it is possible to highlight that even with mutual coupling, the behavior in the transition from without plasma case to with plasma case remains similar to the no mutual coupling case. For this reason and since the of the mutual coupling with plasma produces low variation with respect to the no mutual coupling case, in the following analysis the mutual coupling effect has been neglected.

4.3 Voltage and current analysis on the components of the RF circuits

In this section the analysis of the voltage and current distribution along the coaxial transmission line and the voltage and current values on the driver are evaluated. This analysis, which is realized both without plasma and with plasma, aims to verify the value of the voltage applied to the driver RF coil to initiate plasma, which should have a V_{RMS} ranging from 20 kV to 30 kV, under the hypothesis of the series of two driver coils for every RF circuit.

4.3.1 Reflection coefficient

Focusing on the analysis of a single RF circuit, the series of two RF drivers is fed through a tetrode based self-excited oscillator, the aforementioned RF-OSC, with a nominal output power of 200 kW of active power on a 50 Ω resistive load. Based on this specification, it is easy to determine the corresponding nominal values of its output voltage and current through the simple equivalent circuit represented in Figure 4. 7.

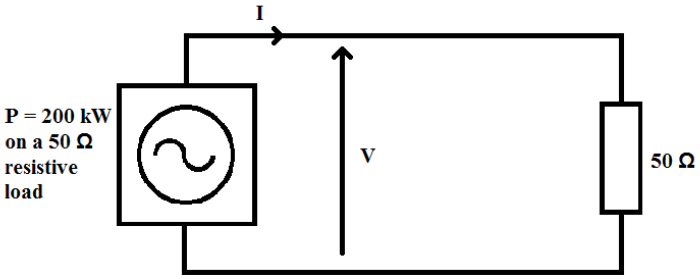

Figure 4. 7 *Reference scheme to obtain the nominal output values of the RF-OSC*

$$V_{nom} = \sqrt{\frac{P}{50}}$$

$$I_{nom} = \frac{V_{nom}}{50}.$$

As it is seen in 4.1, the impedance of the RF-Load assumes different values within the frequency range, and only in a strict frequency range it approaches the value of 50 Ω, which correspond to the matching condition and thus the maximum power transfer. The matching condition is the condition for which the reflection coefficient is at its null value.

In the specific case of the analysis of the RF circuit, the evaluation of the reflection coefficient (see Appendix B) is fundamental to understand the real power transferred from the RF-OSC to the driver coil: the lower the reflection coefficient, the higher is the power transferred to the load. The reflection coefficient is evaluated through a MATLAB script, both without plasma and with plasma, where the impedance at the output port corresponds to the equivalent impedance at the end of the coaxial transmission line $\boldsymbol{Z_a}$, which has been determined in 4.1. The results obtained in each condition are compared to each other to observe the differences with the ignition of plasma. Figure 4. 8 shows the comparison between the reflection coefficient without plasma and with plasma, against frequency.

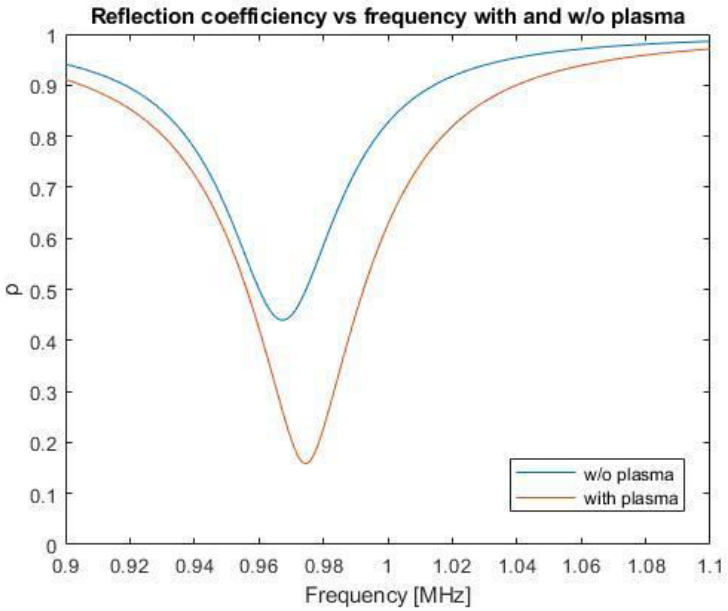

Figure 4. 8 *Reflection coefficient without and with plasma*

Starting from the no-plasma case, at the left edge of the frequency range, the reflection coefficient is equal to ∼0.95, showing a poor matching condition for 0.9 MHz. With increasing frequency, $\boldsymbol{\rho}$ improves, as it decreases until the minimum value of 0.44 at the frequency of about 0.967 MHz. This frequency corresponds to the best obtainable requirement, however pointing out that without plasma the system operates in mismatching condition. From the minimum point, the reflection coefficient starts to grow until it reaches the right edge of the frequency range, showing a value of 0.986 at 1.1 MHz, the maximum value of $\boldsymbol{\rho}$ and the worst.

With plasma, the frequency characteristic of the reflection coefficient maintains the same behavior but it is slightly shifted towards higher frequency and it decreases towards lower $\boldsymbol{\rho}$ values, showing a better matching condition and a strong improvement in the power transferred to the load. The improvement on $\boldsymbol{\rho}$ values, in the transition between no-plasma case and plasma case, is clearly due to the specific design of the matching network: it is properly tuned to reach the best matching condition with plasma. Starting from the frequency 0.9 MHz, which corresponds to a $\boldsymbol{\rho}$ value 0.91, the curve starts to decrease, as well as the without plasma, reaching the minimum value of 0.1594 at 0.975 MHz, highlighting a remarkable reduction in the reflection coefficient, compared to the minimum value without

plasma, and in the maximum gap between the two conditions. Then, with the increase of frequency, $\boldsymbol{\rho}$ increases, thus reducing gradually the gap between the case with plasma and without plasma, until the value of 0.971 at 1.1 MHz. It represents the maximum $\boldsymbol{\rho}$ value and the minimum gap between the two conditions.

4.3.2 Voltage and current distribution over the transmission line

By using the reflection coefficient calculated in the previous section, it is possible evaluate the voltage and current on the components of the RF circuit, starting with the coaxial transmission line. As well discussed in the previous sections, the RF-Load is not a pure resistive impedance of 50 Ω, it varies with the frequency and it has impedance with a real part and an imaginary part; hence the RF-OSC can not fed the load, at the same time, with the nominal values of voltage and current estimated in 4.3.1.

To determine the real values of voltage and current supplied by the generator it must be considered the phase of the RF load impedance. The complex power $\boldsymbol{S}$ is expressed as

$$\boldsymbol{S} = \boldsymbol{V}\boldsymbol{I}^*$$

with "*" operation denoting complex conjugate and it can be rewritten considering the rms values of voltage and current and the phase displacement between them as

$$\boldsymbol{S} = VI\cos\phi + jVI\sin\phi.$$

The real term of this equation corresponds to the active power P and the imaginary part corresponds to the reactive power Q:

$$P = VI\cos\phi$$

$$Q = VI\sin\phi.$$

Since with a pure resistive impedance the phase is equal to zero, the complex power becomes equal to the active power P and, according to the requirements of the RF-OSC, on a pure resistive impedance of 50 Ω

$$\boldsymbol{S} = P = 200\ kW.$$

However, with the RF-Load $\phi \neq 0$ and then both P and Q are different from zero. Hence starting from the reference value of 200 kVA and considering that the phase displacement between voltage and current is equal to the phase of the impedance, it is possible to derive the real active and reactive power supplied by the RF-OSC as

$$P = \frac{S}{\cos\phi}$$

$$Q = \frac{S}{\sin\phi}.$$

Then, under the hypothesis of lossless line, the rms values of voltage and current are derived from the active power and the magnitude and phase of the impedance of the RF-Load evaluated in 4.1 as

$$I_s = \sqrt{\frac{P}{|\boldsymbol{Z_{RF-Load}}| \cos \phi}}$$

$$V_s = |\boldsymbol{Z_{RF-Load}}| I_s.$$

At this point, it has been introduced in the analysis a specific limitation of the output voltage and current of the RF-OSC to their nominal values (see 4.3.1). The output voltage and current of the RF-OSC vary with frequency. When, during frequency regulation, the voltage reaches its nominal value, the limit is triggered and the voltage is limited to this value. The current is then obtained by dividing the limited voltage value to the impedance of the RF load, frequency by frequency until the voltage becomes again lower than its nominal value. The same happens if the current reaches its nominal value, and the current limit is triggered. The resulting voltage is obtained by multiplying the limited current to the impedance of the RF load.

Once the controlled RF-OSC voltage and current outputs are defined, it is possible to start the measurement of the voltage and current distribution over the transmission line. At first, zero voltage phase is assumed, thus the phase of the current is equal to minus the phase of the impedance of the RF-Load

$$\phi = \phi_V - \phi_I = 0 - \phi_I = -\phi_I.$$

Hence, recalling the general equations of the voltage and current standing waves obtained in 4.3.1, since the values of voltage and current available are at the input port, it is necessary to elaborate them for their application. Adopting the same reference frame for the transmission line of the $x = 0$ point at the output port as in 4.1, the standing waves equations for $x = d$, where d is the line length, give the values of voltage and current at the input port, which correspond to the estimated output values of the RF-OSC

$$\boldsymbol{V_d} = \boldsymbol{V_1} e^{jk'' d} + \boldsymbol{V_2} e^{-jk'' d}$$

$$\boldsymbol{I_d} = \frac{\boldsymbol{V_1}}{\boldsymbol{z_0}} e^{jk'' d} - \frac{\boldsymbol{V_2}}{\boldsymbol{z_0}} e^{-jk'' d}.$$

It should be noted that the propagation constant $\boldsymbol{k}$ has been substituted with its imaginary part jk'', due to the specific lossless line hypothesis for which there is no attenuation ($k' = 0$). Therefore, rearranging the equations, it is possible to derive $\boldsymbol{V_1}$ and $\boldsymbol{V_2}$ as

$$\boldsymbol{V_1} = \frac{\boldsymbol{V_d} + \boldsymbol{z_0 I_d}}{2} e^{-jk'' d}$$

$$\boldsymbol{V_2} = \frac{\boldsymbol{V_d} - \boldsymbol{z_0 I_d}}{2} e^{jk'' d}$$

At this point it is possible to substitute these equations inside the progressive voltage wave and reflected voltage wave equations obtaining respectively

$$\boldsymbol{V_{progr}} = \boldsymbol{V_1} e^{jk''x}$$

$$\boldsymbol{V_{refl}} = \boldsymbol{V_2} e^{-jk''x}$$

and then, by adding up these equations, the voltage standing wave, $\boldsymbol{V_{st\_wv}}$, is obtained as

$$\boldsymbol{V_{st\_wv}} = \boldsymbol{V_{progr}} + \boldsymbol{V_{refl}}.$$

At this point, it is also easy to derive the current standing wave, $\boldsymbol{I_{st\_wv}}$, as

$$\boldsymbol{I_{st\_wv}} = \frac{\boldsymbol{V_{progr}} - \boldsymbol{V_{refl}}}{\boldsymbol{z_0}}.$$

This procedure has been implemented through a MATLAB code, considering the parameters of the driver in presence of plasma.

Figure 4. 9 and Figure 4. 10 show the behavior of the voltage standing wave, with plasma, through a 3D-plot. The former represents the behavior of voltage at the input port (RF-OSC output), while the latter represents the behavior of voltage at the output port (ion source side). For the voltage graph, the x-axis is the frequency in MHz, the y-axis is the line length in meters and the z-axis is the magnitude of the voltage in Volts.

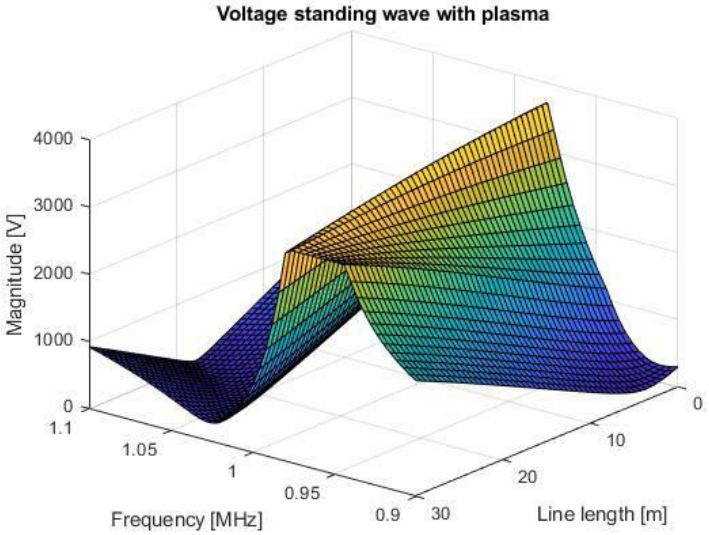

Figure 4. 9 *Voltage standing wave along the transmission line (input port point of view)*

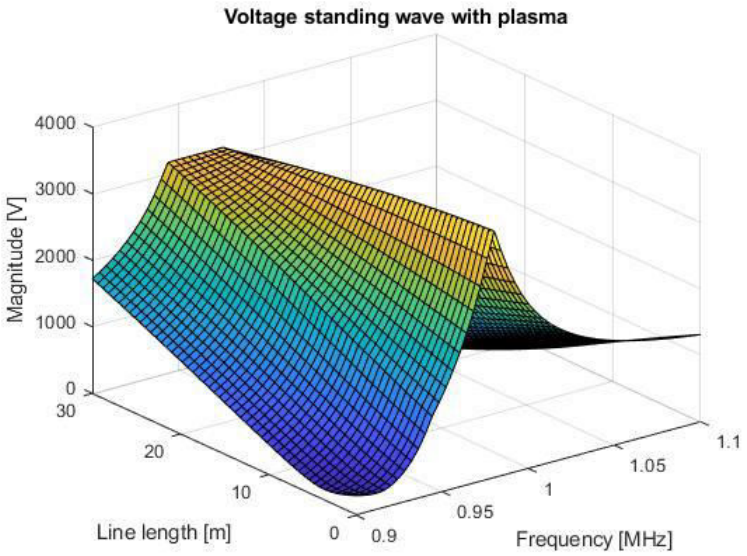

Figure 4. 10*Voltage standing wave along the transmission line (output port point of view)*

Figure 4. 11 and Figure 4. 12 show the 3D-plot of the current standing wave focusing respectively at the input port and at the output port with plasma. Even for the current graph, the x-axis is the frequency in MHz, the y-axis is the line length in meters and the z-axis is the magnitude of the current in Ampere.

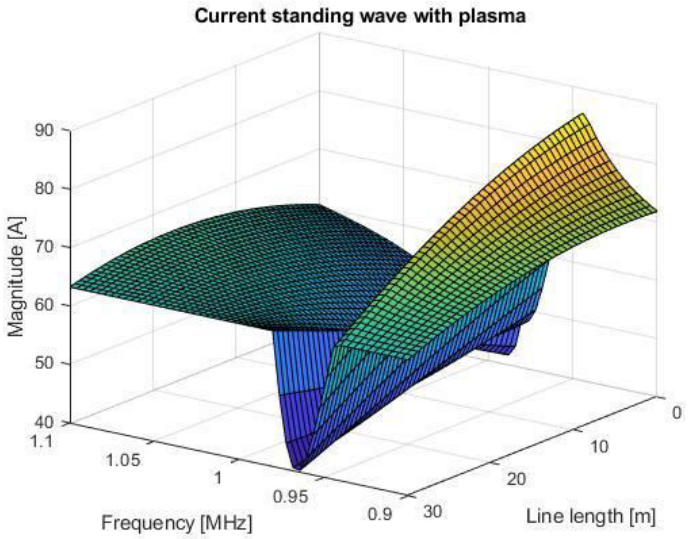

Figure 4. 11 *Current standing wave along the transmission line (input port point of view)*

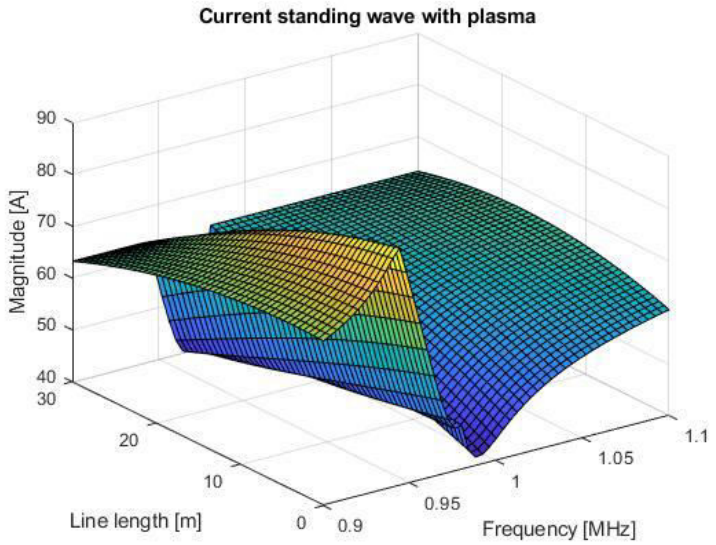

Figure 4. 12 *Current standing wave along the transmission line (output port point of view)*

Starting from the input port, which, according to the reference frame adopted, is in correspondence of 30 m, it is evident the effect of the voltage and current control of the RF-OSC. From 0.9 MHz to 0.944 MHz, the current is fixed at the value of 63.2 A which corresponds to the nominal value of the current of the generator supplying 200 kW on a resistive impedance of 50 Ω. This aspect highlights that, for these values of the frequency range, the current has exceeded the current limit, thus the output of the RF-OSC is limited to the nominal value. As regards the voltage standing wave at the input port, it starts growing from the value of 1723 V at 0.9 MHz, until 0.944 MHz. By this frequency value, the voltage, without control, would exceed the limit imposed by the control of the RF-OSC, and then it is fixed to the nominal value of 3162.3 V. At the same frequency of 0.944 MHz, the current starts to decrease until the minimum current value of 40.3 A at 0.964 MHz while, at this frequency, the voltage standing wave would show its peak. However, even in this case this value of voltage exceeds the control limit and so it is fixed to the nominal value. This is even clearer considering the graph of the magnitude of the impedance along the transmission line with plasma, focused on the input port, displayed in Figure 4. 13.

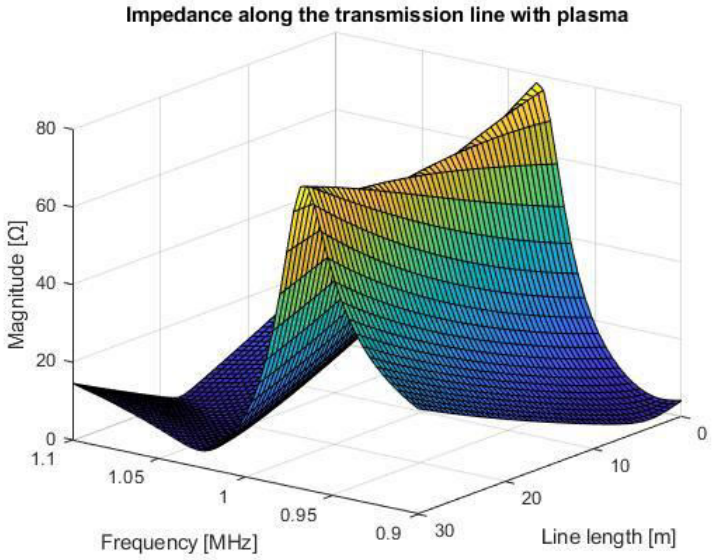

Figure 4. 13 *Magnitude of the impedance along the transmission line (input port point of view)*

Therefore frequency 0.964 MHz corresponds to the maximum magnitude of the impedance at the input port, so, for this value, the voltage would be at is maximum value, without the voltage control, and the current is at its minimum value. Then, from this minimum point, the current starts increasing until the frequency of 0.976 MHz for which it assumes the nominal value of 63.2 A and this value is kept until the higher edge of the frequency range. Instead, the voltage, from 0.976 MHz, starts to fall reaching its minimum of about 274.6 V at 1.028 MHz, which corresponds to the minimum of the impedance at the input port, equal to 4.3 Ω. The frequency value of 1.028 MHz would also correspond to the maximum of the current, which, however, is not shown due to the current control. Then voltage starts slightly to grow until the frequency of 1.1 MHz, for which it is equal to 920 V. Hence it is possible to notice that, as the impedance decreases, the voltage decreases too, while the current starts increasing, according to Ohm's law.

Considering the behavior of voltage and current from the input port to the output port, it is possible to observe that the voltage decreases within the frequency range 0.9÷0.974 MHz, while the current increases. From 0.972 MHz to 1.1 MHz, the opposite situation occurs: the voltage increases towards the output port, while the current decreases. This is proved by the behavior of the magnitude of the impedance along the transmission line: it decreases within 0.9÷0.974 MHz and it increases within 0.972÷1.1 MHz.

Considering the trends at the output port, it is possible to observe a shift of the characteristics of voltage and current towards higher frequency. Starting from 0.9 MHz, at which voltage is equal to 297.3 V, the voltage steadily increases until its maximum value of 3708 V at 0.98 MHz and then it decreases until 1310 V at 1.1 MHz. As regards the current, starting from 71.77 A at 0.9 MHz, it increases until 85.85 A, the maximum current value at the output port. Then it steadily decreases reaching the minimum current value at the output port of 41.7 A at 0.988 MHz. Finally, moving towards the highest value of the frequency range, the current increases until it reaches 60.4 A at 1.1 MHz. All of these trends are verified by the behavior of the magnitude of the impedance at the output port, portrayed in Figure 4. 14, which represents the same 3D-plot of the impedance, but focusing on the output port instead of the input port. It shows a peak of about 78 Ω at 0.984 MHz and then it decreases until the edges of the frequency range.

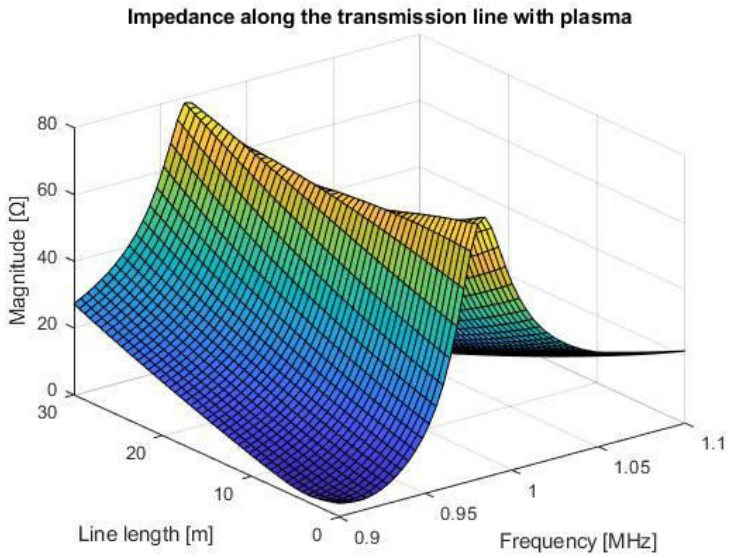

Figure 4. 14 *Magnitude of the impedance along the transmission line (output port point of view)*

4.3.3 Evaluation of voltage and current on the components downstream the transmission line

After the evaluation of the voltage and current distribution over the transmission line, it is possible to analyze their values on the components of the matching network and on the antennas of the two drivers.

The voltage applied to the parallel capacitor Cp is equal to the voltage seen at the output port in Figure 4. 10. The behavior of this voltage has been described in 4.3.2. However, for a clearer overview of the graph, Figure 4. 15 shows the magnitude of the voltage against frequency in a 2D-plot.

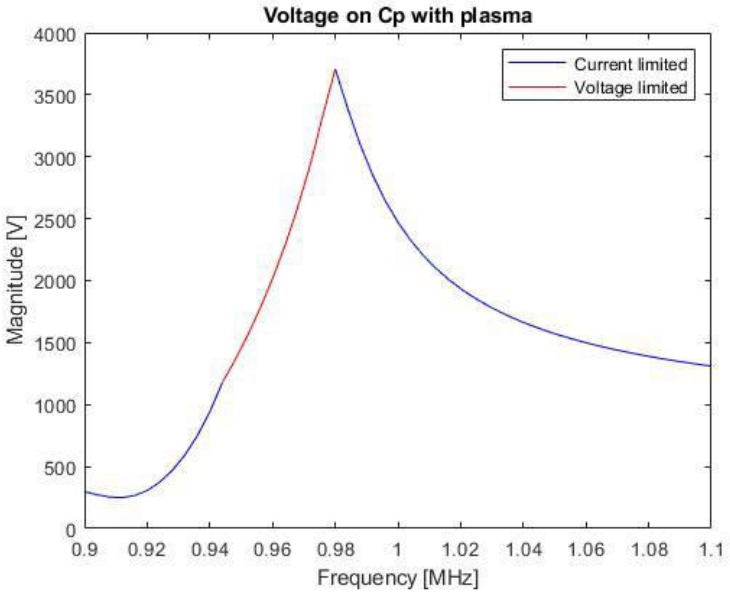

Figure 4. 15 *Magnitude of the voltage on Cp capacitor*

As a result, recalling the impedance of the parallel capacitor $\boldsymbol{Z_{Cp}}$, it is possibile to evaluate the current on Cp, as

$$\boldsymbol{I_{Cp}} = \frac{\boldsymbol{V_{Cp}}}{\boldsymbol{Z_{Cp}}}.$$

Figure 4. 16 shows the behavior of $\boldsymbol{I_{Cp}}$over the operating frequency range.

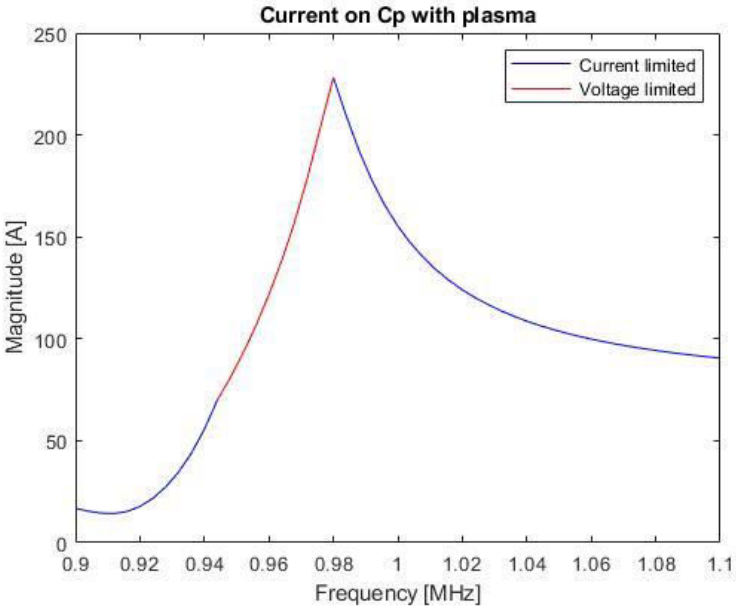

Figure 4. 16 *Magnitude of the current on Cp capacitor*

As expected, the current trend on Cp follows the voltage one and its magnitude is significant. Starting from 16.81 A at 0.9 MHz, the current decreases until its minimum value of 14.27 A at 0.9104 MHz. With increasing frequency, the current increases until its maximum of 228.3 A at 0.98 MHz, and then it steadily decreases to 90.54 A at 1.1 MHz.

At this point, it is possible to evaluate the distribution of voltage and current on the components of the series branch of the RF load. The current over the series branch can be evaluated by dividing the previously obtained voltage on Cp, $\boldsymbol{V_{cp}}$, by the equivalent impedance of the series branch, $\boldsymbol{Z_{series}}$, as

$$\boldsymbol{I_{series}} = \frac{\boldsymbol{V_{cp}}}{\boldsymbol{Z_{series}}}.$$

$\boldsymbol{Z_{series}}$ can be evaluated by summing the equivalent impedance of the antennas, $\boldsymbol{Z_d}$, and the equivalent impedance of the series capacitors, $\boldsymbol{Z_{cs}}$, obtained in 4.1. Figure 4. 17 shows the trend of $\boldsymbol{I_{series}}$against the frequency range of the RF-OSC.

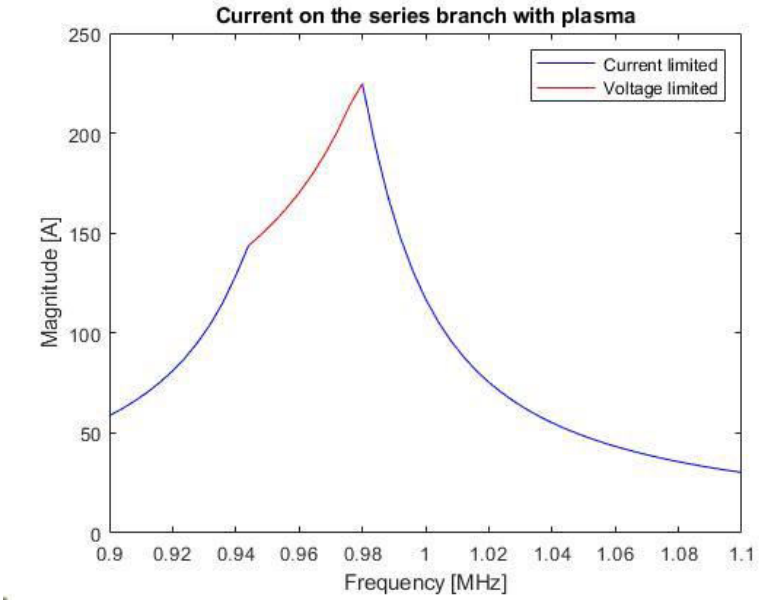

Figure 4. 17 *Magnitude of the current over the series branch*

Starting from the left edge of the graph, the current steadily increases, from 58.67 A, at 0.9 MHz, to the peak value of 224.9 A, at 0.98 MHz, and then it decreases, reaching 30.26 A at 1.1 MHz. It is interesting to note that the slope of the current graph changes at 0.94 MHz, where the current is equal to 143.7 A. This point corresponds to the frequency for which the RF-OSC changes from being limited in current to being limited in voltage, as it has been shown for all the voltage and current graphs of 4.3.2. Furthermore, the point where the RF-OSC returns to be limited in current corresponds to the peak of the graph (0.98 MHz).

Finally, by using$\boldsymbol{I_{series}}$, the voltage on the components of the series branch can be derived as follows:

- the voltage on the equivalent series capacitor, Cs, can be evaluated as $\boldsymbol{V_{cs}} = \boldsymbol{Z_{cs}}\boldsymbol{I_{series}}$. The magnitude of this voltage is shown in Figure 4. 18 against the frequency range.

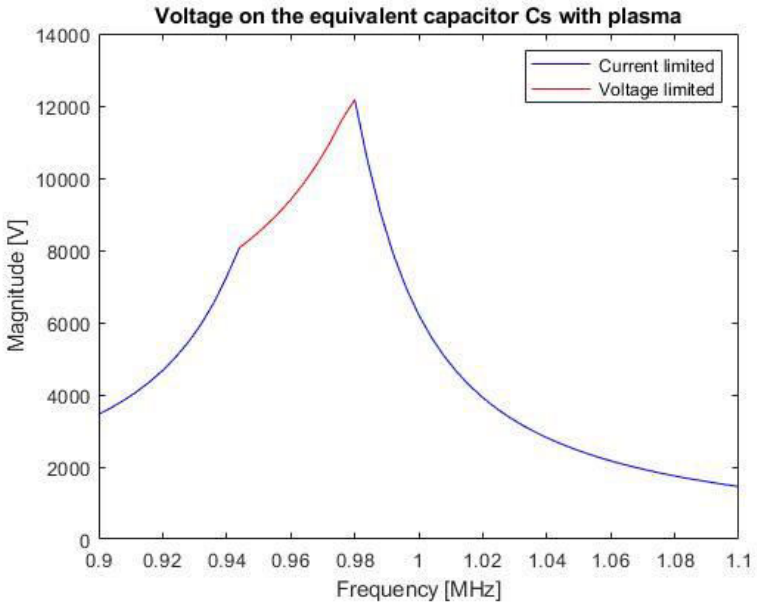

Figure 4. 18 *Magnitude of the voltage on the equivalent series capacitor Cs*

The behavior of the voltage follows the $\boldsymbol{I_{series}}$one: starting from 6917 V at 0.9 MHz, it reaches the peak of 24340 V at 0.98 MHz and then it decreases to 2919 V at 1.1 MHz. Even in this case it is evident the shift between current control mode and voltage control mode at 0.94 MHz, for which the voltage is equal to 16150 V, and the opposite shift is in correspondence of the peak. In order to obtain the voltage on a single series capacitor 2Cs (see Figure 3. 1), it is necessary to halve the voltage obtained in Figure 4. 18.

- the voltage on the equivalent resistance of the antennas of the two drivers, Rd, can be calculated as $\boldsymbol{V_{Rd}} = R_d \boldsymbol{I_{series}}$. Figure 4. 19 shows the magnitude of this voltage against frequency.

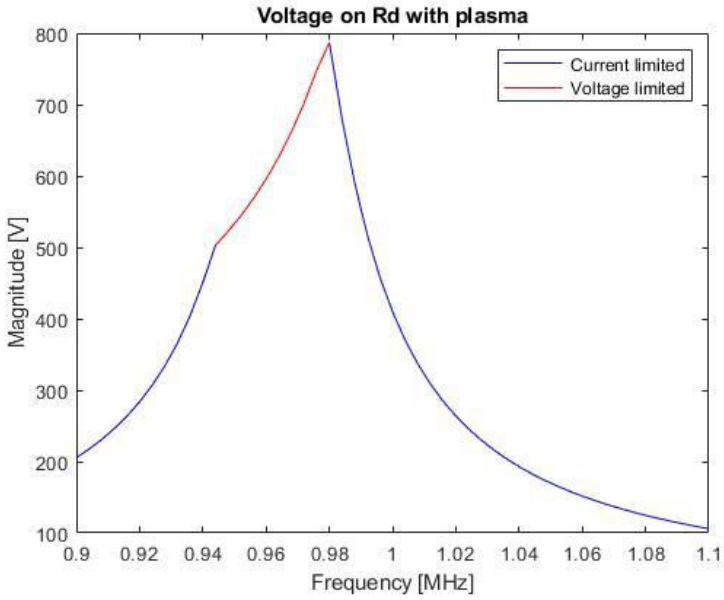

Figure 4. 19 *Magnitude of the voltage* $\boldsymbol{V_{Rd}}$

The voltage drop on Rd is equal to 205.3 V at 0.9 MHz, then it increases until the peak of 787 V at 0.98 MHz and, from this point onwards, it decreases until 105.9 V at 1.1 MHz. In this case, at 0.94 MHz, the voltage is equal to 502.9 V.

- the voltage on the equivalent inductance of the two antennas, can be obtained as $\boldsymbol{V_{Ld}} = \boldsymbol{Z_{Ld}} \boldsymbol{I_{series}}$. $\boldsymbol{Z_{Ld}}$ corresponds to the imaginary part of the equivalent impedance of the antennas of the two drivers, $\boldsymbol{Z_d}$, which has been obtained in 4.1. Figure 4. 20 shows the graph of the magnitude of $\boldsymbol{V_{Ld}}$ against the frequency range of the RF-OSC.

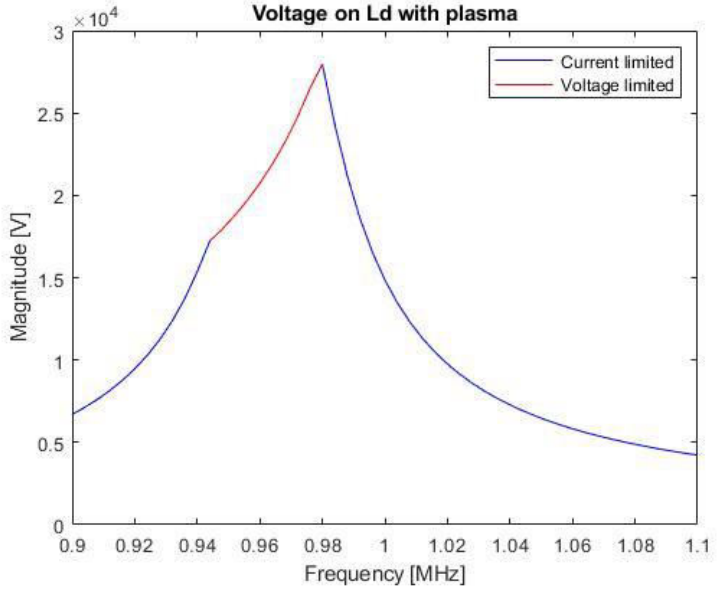

Figure 4. 20*Magnitude of the voltage* $\boldsymbol{V_{Ld}}$

Starting from 6702 V at 0.9 MHz, the voltage increases, reaching 17220 V at 0.94 MHz, up to the voltage peak of 27970 V at 0.98 MHz. This maximum voltage value confirms the expected value of $\boldsymbol{V_{Ld}}$, which was foreseen for being within within the range between 20 kV and 30 kV. Hence, starting from the peak, the voltage decreases until 4224 V at 1.1 MHz.

4.3.4 Active power analysis and evaluation of the results

Figure 4. 21 and Figure 4. 22, highlight respectively the active power delivered by the RF generator, with voltage and current limitations, the magnitude and the phase of the impedance of the RF load and the reflection coefficient, against frequency, without plasma (Rd=1.9 Ω and Ld=20.5 μH) and with plasma (Rd=3.5 Ω and Ld=20.2 μH), in order to compare the results also with respect to the active power transferred to the load.

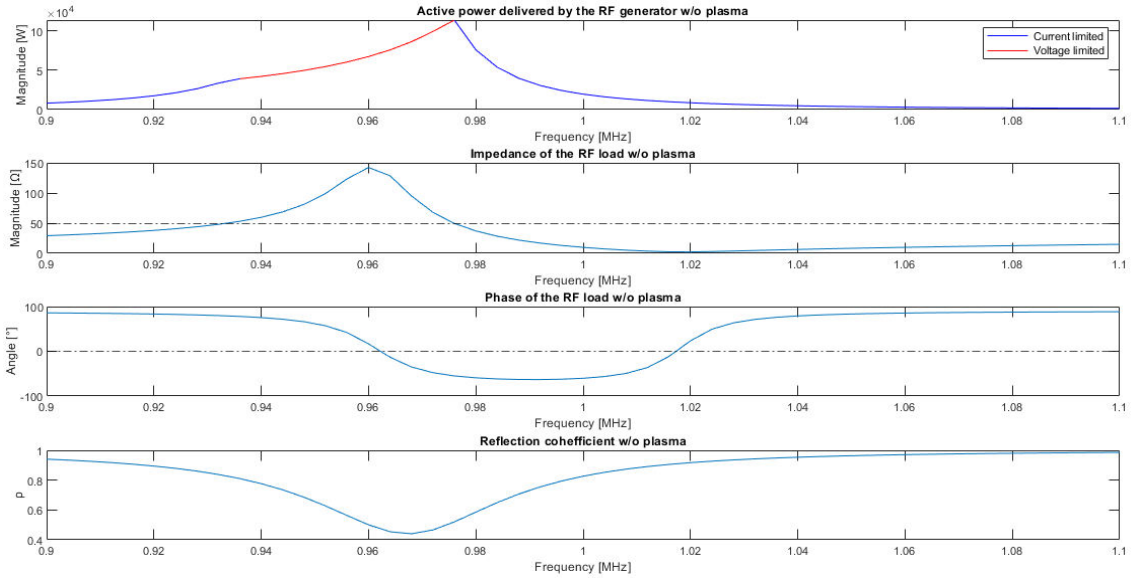

Figure 4. 21 *Active power (top), magnitude and phase of the impedance (middle) and reflection coefficient (bottom) against the frequency range of the RF generator, without plasma*

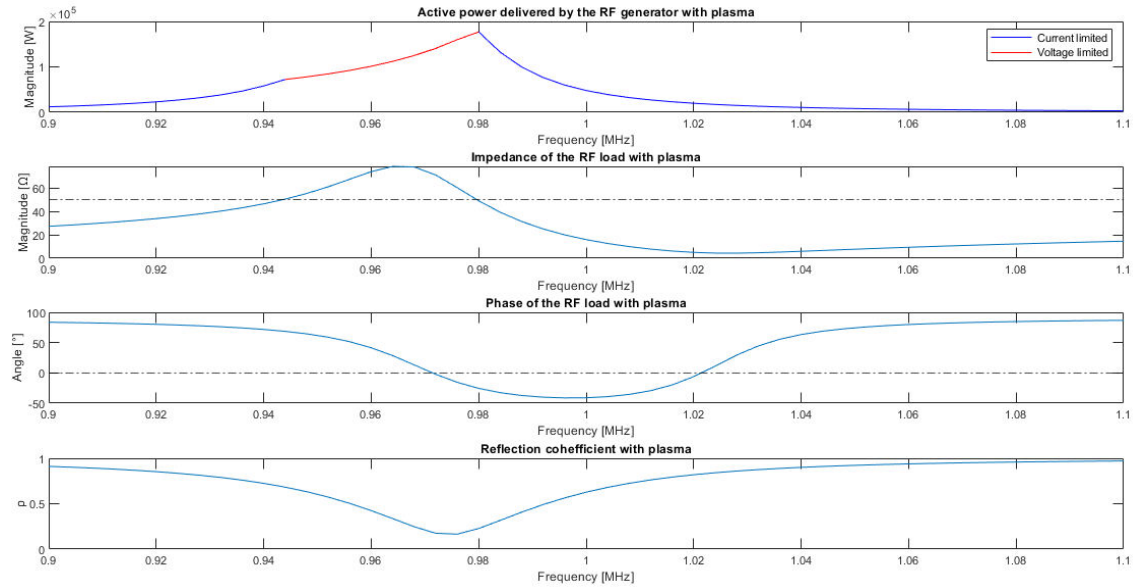

Figure 4. 22 *Active power (top), magnitude and phase of the impedance (middle) and reflection coefficient (bottom) against the frequency range of the RF generator, with plasma*

It is possible to observe that the maximum power delivered to the load, which is equal to 113 kW without plasma and 177.9 kW with plasma, is in correspondence of the frequency for which the impedance is about 50 Ω (0.9754 MHz without plasma and 0.9794 MHz with plasma). This frequency corresponds to a non-zero phase of the impedance of the RF load (-54.08° without plasma and -24.74° with plasma) and to a reflection coefficient equal to 0.5107 without plasma and 0.251 with plasma, which are different from the related minimum $\boldsymbol{\rho}$ values. The reflection coefficient is lower with plasma than without plasma, as discussed in 4.3.1, since the matching network is tuned for the operation with plasma. Nevertheless, it is away from the perfect matching condition, for which, at the same frequency, $\boldsymbol{\rho}$ should be equal to zero, the impedance should be equal to $50e^{j0}$ Ω and the RF generator should deliver the rated active power of 200 kW to the load.

As regard the overall active power delivered to the load, it is strictly related to the reflection coefficient of the system. Actually, the overall active power can be evaluated through the difference between the forward active power and the reflected active power, which are derived from the progressive and reflected voltage waves (see 4.3.2) as

$$P_{forw} = Re\{\boldsymbol{V_{progr}}(\boldsymbol{I_{progr}})^*\}$$
$$P_{refl} = Re\{\boldsymbol{V_{refl}}(\boldsymbol{I_{refl}})^*\}$$

where

$$\boldsymbol{I_{progr}} = \frac{\boldsymbol{V_{progr}}}{\boldsymbol{z_0}}$$

$$\boldsymbol{I_{refl}} = \frac{\boldsymbol{V_{refl}}}{\boldsymbol{z_0}}.$$

Hence, the overall active power can be obtained as

$$P_{load} = P_{forw} - P_{refl}$$

and the trends of P_{load}, P_{forw} and P_{refl} are shown in Figure 4. 23, considering the operation without plasma, and in Figure 4. 24, considering the operation with plasma.

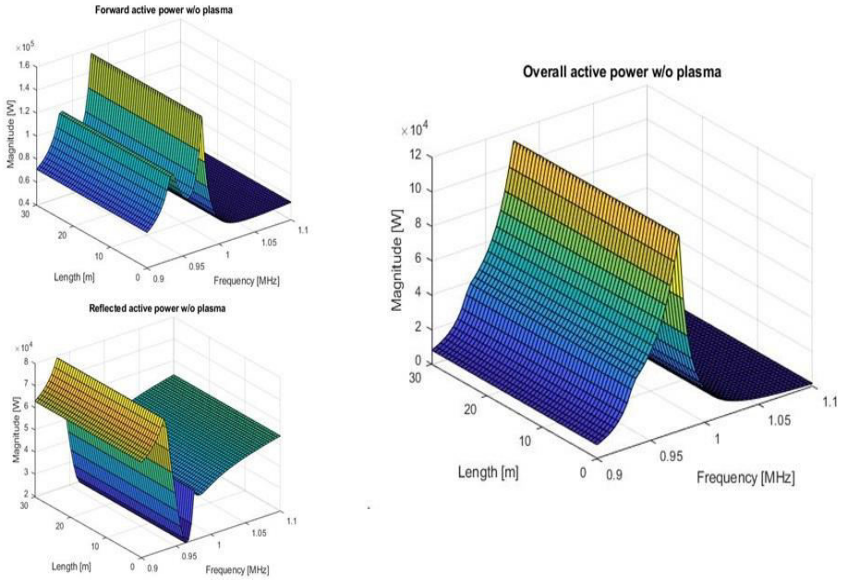

Figure 4. 23 *Forward active power (upper-left), reflected active power (lower-left) and the overall active power delivered to the load (right) against frequency and line length, without plasma*

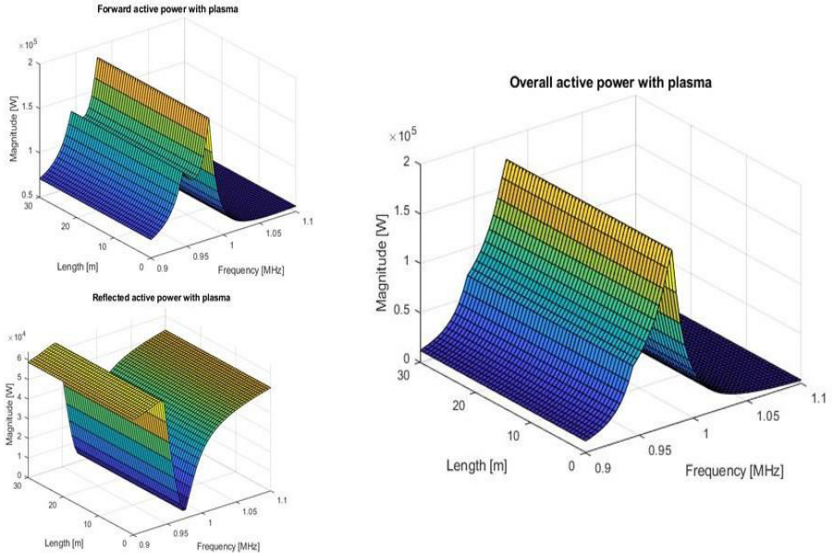

Figure 4. 24 *Forward active power (upper-left), reflected active power (lower-left) and the overall active power delivered to the load (right) against frequency and line length, with plasma*

The graphs show that the active power assumes the same values along the coaxial transmission line and this is due to the hypothesis of lossless line (see 4.1). For this reason the overall active power, both without and with plasma, varies with frequency but not with the line length, and its profiles against frequency is respectively the same portrayed in Figure 4. 21 and Figure 4. 22. Moreover, the forward power and the reflected power are linked together by the reflection coefficient as follows

$$|\boldsymbol{\rho}| = \sqrt{\frac{P_{refl}}{P_{forw}}}.$$

This is a fundamental aspect to take into account, since if ρ is equal to zero, there is no P_{refl} and then $P_{load} = P_{forw}$. For this reason the lower ρ is and the better the system works, reaching its best operation achieving the matching condition. However, as explained in 3.1.2 and 3.1.3, the matching condition is reachable only for a specific small frequency range and for a specific small range of values of the impedance of the antennas, after the ignition of plasma.

In order to provide a better explanation of the behavior of the system around the matching condition, Figure 4. 25 is given. It shows the same four graphs of Figure 4. 22 but considering three different combinations of the parameters of the impedance of the antennas:

1. Rd = 3.5 Ω and Ld = 20.2 μH (the same reference values adopted in chapter 4 for all the simulations with plasma);

2. Rd = 4.7 Ω and Ld = 20 μH;

3. Rd = 5 Ω and Ld = 19.5 μH.

Moving from the first combination, which has been previously analyzed, to the second one, it is possible to observe a slight shift towards higher frequency for all the four graphs characteristics. In addition, with this combination of parameters, the peak of the active power is equal to 198.3kW, the

impedance of the RF load has a magnitude of 50.43 Ω and a phase of -0.9274° and the reflection coefficient is equal to 0.0091. All of these results are obtained for the same frequency of 0.9794 MHz, highlighting that, with this hypothetical combination of the antennas parameters, the system should work next to the matching condition. Finally, with the third combination of parameters, there is a further frequency shift of the characteristics. The overall active power slightly decreases, compared to the previous combination of Rd and Ld, reaching 196 kW at 0.9905 MHz, and, at this frequency, the impedance assumes a magnitude of 49.22 Ω and a phase of 5.438° and the reflection coefficient is equal to 0.04817. This aspect shows that with a further increase in Rd and with a further decrease in Ld, the system moves away from the matching condition.

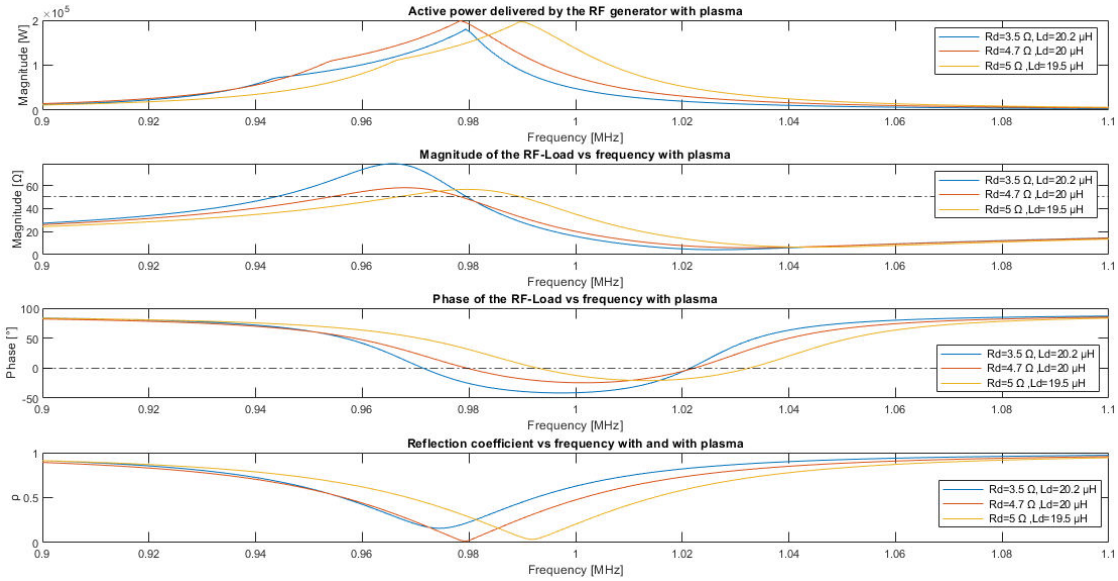

Figure 4. 25 *Overall Active power (top), magnitude and phase of the impedance of the RF load (middle) and the reflection coefficient (bottom) for three different combinations of the antennas parameters with plasma*

It is important to highlight that the process for achieving the matching condition is difficult since required to have a specific impedance of the antennas of the drivers. Even if it is the case, unfortunately, as aforementioned in 3.2.1, the frequency flip phenomenon prevents the RF-OSC from working under the matching condition, thus forcing the system to work mismatched to the load.

In the same way the relation of the overall active power from the reflection coefficient of the system is presented, it is possible to discuss the voltage and current distribution on the components of the RF load and along the coaxial transmission line. At first, the limitation on the output current and voltage of the RF generator is fundamental in order to prevent current and voltage from overcoming the maximum values tolerated by the components of the systems. Actually, since the system works mismatched delivering the rated 200 kW to the antennas would require a great increase in the output complex power of the RF generator. This, obviously, would lead to higher values of voltage and current on the components of the RF circuit, which may induce faults and breakdowns within the system. Actually, as it has been shown in Figure 4. 21, without plasma the reflection coefficient is very low and, for this reason, rising power to the operating levels, which would be firstly impossible due to the screen grid control fault[3]

[3]The SGCF is a relatively common fault which produce a limitation in the output power of the RF-OSC. The output power of the oscillator is increased by increasing the DC voltage applied to the screen grid of the tetrode, V_{screen} (see 3.1.1). The higher is the output power required to the RF-OSC, the higher isV_{screen}. When the difference between this voltage and the voltage of the anode of the tetrode is too small, the

(SGCF), would be overwhelming and disruptive for the components of the system. This is the reason why, the starting process is realize with low power levels, although sufficiently high in order to initiate the plasma. Hence, after its ignition, the output power of the RF generator is raised until it reaches the rated operating levels.

4.4 Accuracy in the evaluation of the antennas equivalent parameters

A fundamental aspect, in order to provide a complete characterization of the RF load in the context of substituting the tetrode based oscillators with solid-state amplifiers, is the proper measurement of the equivalent impedance of the antennas of the two drivers. In principle it is not a problem without plasma, since in this condition the impedance of the load can be evaluated offline with dedicated local measurement, with plasma the measurement of the antennas parameters is a critical issue, it can not be performed locally and has to rely on the measurement available at the RF generator and on the knowledge of the other parameters affecting the RF load impedance. It is in this context that an analysis of the effects of the errors introduced by the measurement system and by the components of the RF load is required, in order to have a better knowledge of the impedance of the antennas. In particular this section reports on: an evaluation of the accuracy on the estimation of the antennas parameters for a fixed frequency, an analysis of the distribution of their average values and their uncertainty ranges against frequency and a sensitivity analysis of the error components.

4.4.1 Accuracy analysis on the estimation of Rd and Ld

The evaluation of the impedance of the antennas is obtained from the voltage and current delivered by the generator, with their relative phase displacement, and these values are known only as measured ones. Furthermore, the line length and the capacitors of the matching network are provided by the manufacturers with specific uncertainties which also contribute to the evaluation of the antennas parameters. All of these error components contribute to the uncertainty on the estimation of the impedance of the antennas. The goal of this paragraph is to understand, thanks to a probability analysis, how the antennas parameters change considering uncertainty ranges for V, I, phase, Cs, Cp and line length. For this analysis, some assumptions have been made for the specific uncertainties of the different inputs. It has been considered an error of $\pm 10\%$ on the voltage and current measurement, an error of $\pm 10°$ on the phase displacement measurement and an uncertainty of $\pm 5\%$ on the values of Cs, Cp and line length. The idea behind the procedure is to impose the parameters of the antennas of the two drivers (the same values of Rd and Ld adopted 4.1), to solve the circuit and then to apply the uncertainty ranges to the estimated voltage, current and phase values, to the capacitors of the matching network and to the line length. After that, the procedure foresees to create a MATLAB model where, inside a loop, for a specific value of frequency (in this analysis, the frequency of 1 MHz has been chosen as reference value), the program takes a single random V, I, phase, Cs, Cp and line length value within their related uncertainty ranges. Hence, thanks to these values, it is possible to recalculate the parameters of the antennas of the two driver as follows: calling respectively V_{rnd}, I_{rnd}, ϕ_{rnd}, Cs_{rnd}, Cp_{rnd} and d_{rnd} the random values derived from the loop, the impedance of the RF load, $\boldsymbol{Z_{RF-Load}}$, has been evalueted as

$$\boldsymbol{Z_{RF-Load}} = \frac{V_{rnd}}{I_{rnd}} e^{j\phi_{rnd}}$$

and then Rd and Ld are derived backwards considering the reference circuit of Figure 3. 1. The equivalent impedance of the matching network and the antennas of the driver is equal to

---

SGCF occurs: the screen grid collects part of the secondary electrons emitted by the anode, and then some anode current is taken by the screen grid, thus reaching a saturation of the output power.

$$\boldsymbol{Z_a} = \frac{\boldsymbol{Z_{RF-Load}}\cosh(\boldsymbol{k}d_{rnd}) - \boldsymbol{z_0}\sinh(\boldsymbol{k}d_{rnd})}{\cosh(\boldsymbol{k}d_{rnd}) - \frac{\boldsymbol{Z_{RF-Load}}}{\boldsymbol{z_0}}\sinh(\boldsymbol{k}d_{rnd})}.$$

Hence, introducing the impedance of the equivalent series capacitors, Cs, and the impedance of the parallel capacitor, Cp, as $\boldsymbol{Z_{cp}} = \frac{1}{j\omega Cp_{rnd}}$ and $\boldsymbol{Z_{cs}} = \frac{1}{j\omega Cs_{rnd}}$, it is possibile to obtain the equivalent impedance of the series branch, $\boldsymbol{Z_{sb}}$, as

$$\boldsymbol{Z_{sb}} = \frac{\boldsymbol{Z_a Z_{cp}}}{\boldsymbol{Z_{cp}} - \boldsymbol{Z_a}}$$

and then, the equivalent impedance of the antennas of the two drivers, $\boldsymbol{Z_d}$, as

$$\boldsymbol{Z_d} = \boldsymbol{Z_{sb}} - \boldsymbol{Z_{cs}} = R_d + j\omega Ld.$$

By repeating this procedure for n=100000 times, it is possible to obtain the distribution of the values assumed by Rd and Ld. These results have been represented thanks to histogram graphs, where the values assumed by Rd and Ld are grouped into bins on the x-axis and their related counts are represented on the y-axis. Figure 4. 26 shows the histogram graphs of Rd and Ld without plasma, while Figure 4. 27 shows the same graphs, but with plasma.

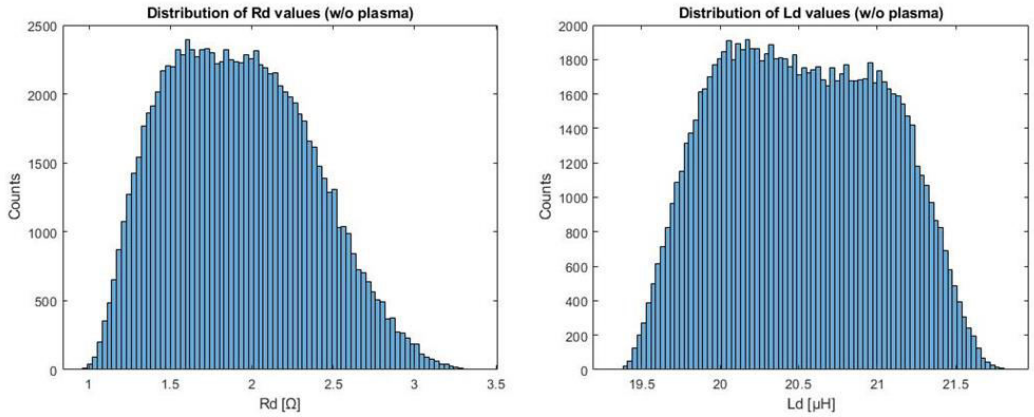

Figure 4. 26 *Histogram graphs of the distribution of the Rd values (left graph) and the Ld values (right graph), without plasma*

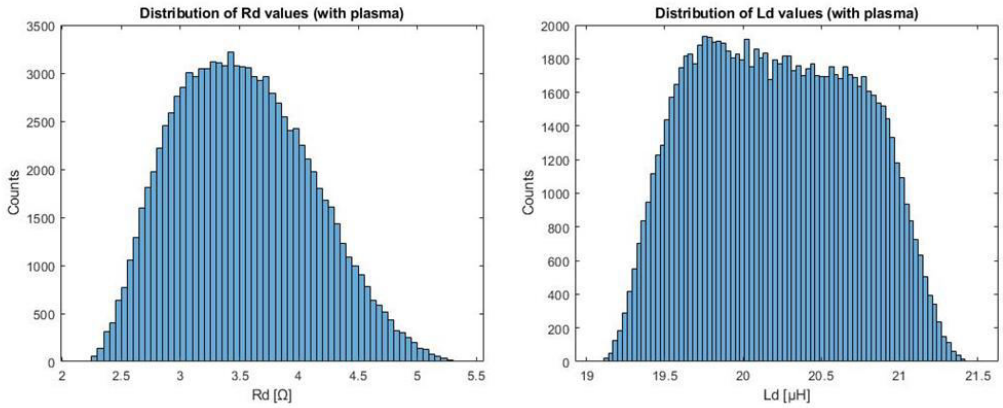

Figure 4. 27 *Histogram graphs of the distribution of the Rd values (left graph) and the Ld values (right graph), with plasma*

Hence, in order to complete the first step of the simulation process, it is required to evaluate the average value, μ, and the standard deviation, σ, of these distributions of values as

$$\mu = \frac{1}{n}\sum_{i=1}^{n} x_i \quad i = 1 \dots n$$

$$\sigma = \sqrt{\frac{\sum_{i=1}^{n} |x_i - \mu|^2}{n-1}} \quad i = 1 \dots n$$

where x_i is the i-th value of Rd or Ld. The results obtained applying these equations are shown in Table 4. 1, both without plasma and with plasma.

Table 4. 1 *Average value and standard deviation of the Rd and Ld distributions with and without plasma*

	Average value [μ]	**Standard deviation [σ]**
	without plasma	
Rd [Ω]	1.9179	0.4408
Ld [μH]	20.5218	0.5154
	with plasma	
Rd [Ω]	3.5255	0.5702
Ld [μH]	20.2186	0.5083

It is clearly evident that the average values of Rd and Ld are really close to the reference values adopted in the simulations, which without plasma are Rd = 1.9 Ω, Ld = 20.5 μH and with plasma are Rd = 3.5 Ω, Ld = 20.2 μH. The standard deviation is a statistical dispersion index that is representative of the dispersion of data around a measure of central tendency, which in this case is the average value of the distribution of Rd/Ld values. It plays a fundamental role inside the analysis of the effects of the errors on the evaluation of Rd and Ld, especially in the second step of the simulation process, allowing to define their interval of uncertainty. In order to complete the first step of the analysis, after the evaluation of μ and σ, it has been verified if the distributions of Rd and Ld, with and without plasma, approximate a normal distribution function or not. For this reason, it has been evaluated the normal probability density function (PDF) of the distribution of values of Rd and Ld achieved, based on their μ and σ, as

$$f(x,\mu,\sigma) = \frac{1}{\sigma\sqrt{2\pi}} e^{-\frac{(x-\mu)^2}{2\sigma^2}}.$$

The PDF, for a normal distribution, has been compared to the histogram graphs of Figure 4. 26, Figure 4. 27. In this context, the counts inside a bin i, c_i, is normalized as $v_i = \frac{c_i}{nw_i}$, where w_i is the width of the bin and n is the number of elements (in this case n=100000), in order to obtain the probability density function estimate. This comparison is shown in Figure 4. 28 and Figure 4. 29, respectively without and with plasma, where the normalized counts (PDF estimate) are on the y-axis and the Rd/Ld values are on the x-axis.

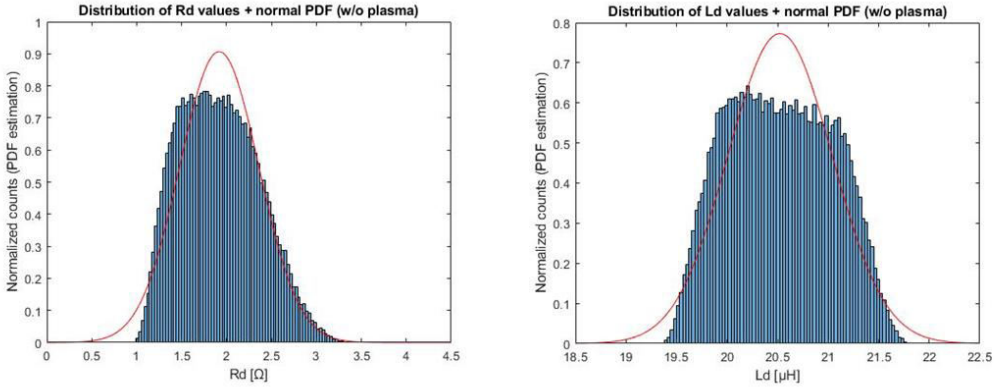

Figure 4. 28 *Histogram graphs of Rd (left graph) and Ld (right graph) compared to the PDF, for normal distribution, without plasma*

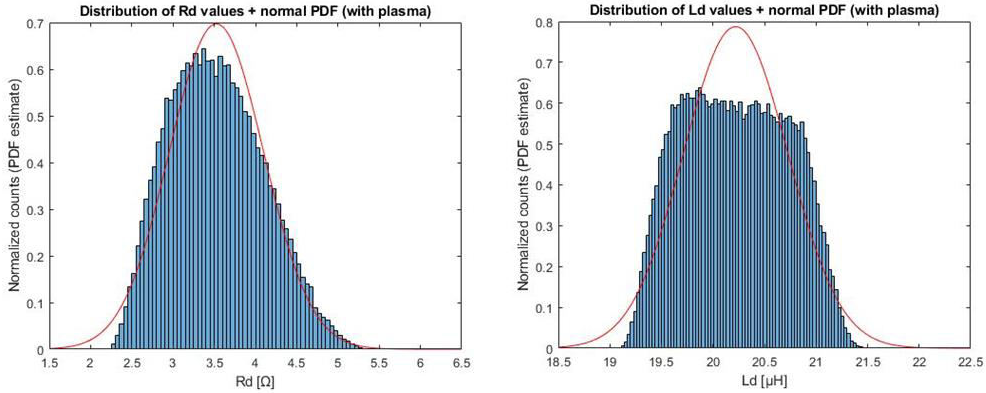

Figure 4. 29 *Histogram graphs of Rd (left graph) and Ld (right graph) compared to the PDF, for normal distribution, with plasma*

It is possible to observe that the histogram graphs, without and with plasma, do not match exactly to the normal probability density function, which has been calculated with the same values of μ and σ of the distributions of Rd and Ld. However, the histogram graphs of Rd, in both conditions, approximate the normal PDF better than the histogram graphs of Ld, which show a flatter top and it exceeds more the limits of the bell-like shape of the normal distribution.

4.4.2 Analysis of the distribution of μ and σ against frequency

In this section the behavior is presented of the average value and the standard deviation of the distribution of Rd and Ld values, without and with plasma, against frequency. This analysis is realized in order to find the frequency which allows to obtain the best measurement condition, thus, in other words, the frequency for which the dispersion of values around μ is lower. Since the index of dispersion of the values around μ can be represented by σ, as mentioned in 4.4.1, the task is to find the frequency for which σ is minimum. For this goal, it has been realized a model which repeats the same loop of the previous model, but varying frequency within the operative frequency range of the RF-OSC: 0.9÷1.1 MHz. In this case, μ and σ of the distribution of Rd and Ld values have been plotted against frequency and the results obtained are shown in Figure 4. 30, for the no-plasma case, and in Figure 4. 31, for the plasma case.

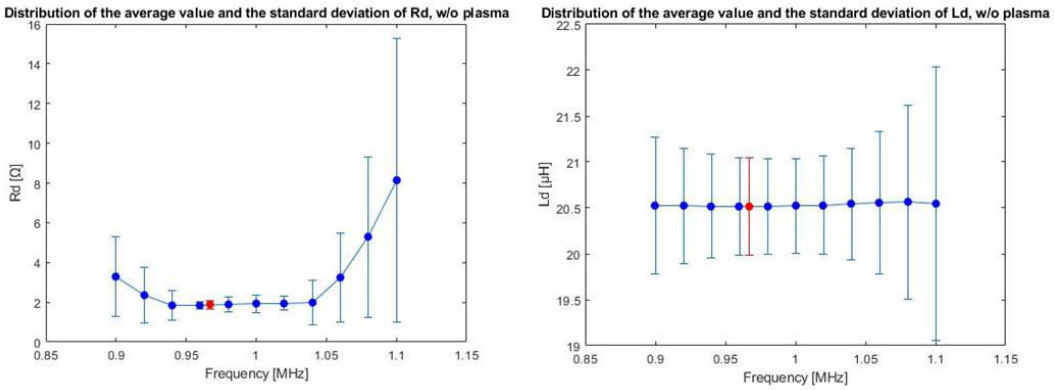

Figure 4. 30 *Distribution of the average value and the dispersion interval ($\pm\sigma$) of the Rd (left graph) and Ld (right graph) values against frequency, without plasma*

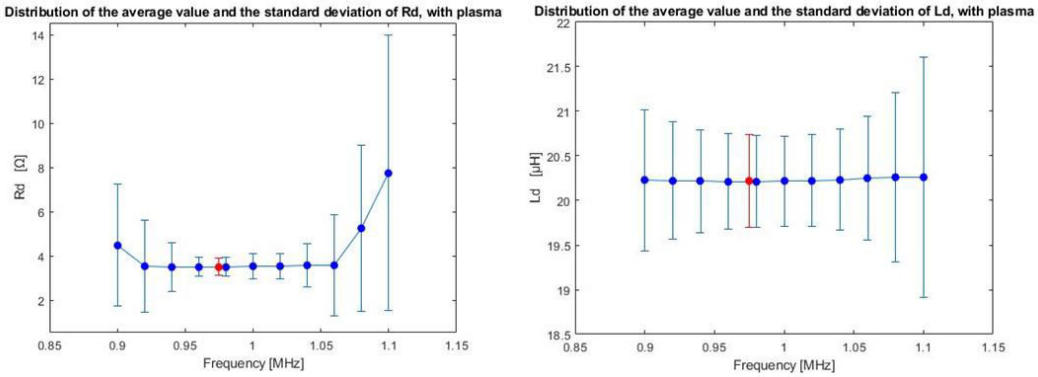

Figure 4. 31 *Distribution of the average value and the dispersion interval ($\pm\sigma$) of the Rd (left graph) and Ld (right graph) values against frequency, with plasma*

The blue circles represent the average values of Rd and Ld, while the vertical interval represents the related dispersion interval, or error bandwidth ($\pm\sigma$). It is clearly shown that the average values of the Ld graphs, both without and with plasma, are almost constant and equal the reference value of Ld = 20.5 μH, without plasma, and Ld = 20.2 μH, with plasma. As regard the error bandwidths, they are reduced towards 0.96 MHz, without plasma, and towards 0.98 MHz with plasma, while at the edges of the frequency range, they are really large for both conditions, highlighting that, for these frequencies, the measurement of Ld would be really inaccurate. As regard the Rd graphs, both without and with plasma,

similar trends are shown. However, it is possible to highlight some peculiar features, compared to the Ld graphs:

- there is a further reduction on the error bandwidths around the resonance frequency (0.962 MHz, without plasma and 0.971 MHz, with plasma) and, only for Rd, around the antiresonance frequency (1.017 MHz, without plasma and 1.021 MHz, with plasma) of the RF load;

- moving towards the edges of the frequency range, the average values of Rd grow, in contrast to the Ld graphs. This is due to the fact that, at these frequencies, the model has provided some Rd values which were in contrast to the reference circuit (Rd < 0). For this reason, these values were discarded. As a result, the related average values were increased and the same happens to the related error bandwidths, which are greatly higher than the Ld graphs ones. Hence, at these frequencies, the Rd measurement would produce wrong results.

In order to complete the analysis, it has been evaluated μ and σ at the frequency for which the reflection coefficient is at its minimum, adopting the results obtained in 4.3.1 (0.967 MHz without plasma and 0.975 MHz with plasma). The results are represented in Figure 4. 30 and Figure 4. 31 in red, showing that, for these frequencies, the measurements would be greatly reliable. All the results of this second step of the simulation process are shown in Table 4. 2 (without plasma) and in Table 4. 3 (with plasma).

Table 4. 2 *Average value, standard deviation and relative error of Rd and Ld, without plasma*

	Rd (without plasma)			Ld (without plasma)		
Frequency [MHz]	**Average value [Ω]**	**σ [Ω]**	**Relative error [%]**	**Average value [μH]**	**σ [μH]**	**Relative error [%]**
0.9	3.283102027	2.007462043	61.14528353	20.52757904	0.743762093	3.623233368
0.92	2.345633343	1.393425604	59.40509023	20.52315334	0.63078183	3.073513215
0.94	1.839074144	0.755544316	41.08286328	20.51949829	0.565136085	2.754141824
0.96	1.862668944	0.18262644	9.804557105	20.5178241	0.533770703	2.601497608
0.967	1.871371459	0.22380603	11.95946582	20.51995582	0.526978582	2.568127271
0.98	1.888672318	0.3956417	20.94813886	20.5190445	0.520074749	2.534595355
1	1.91700328	0.440563149	22.98186725	20.52381157	0.516172997	2.514995789
1.02	1.947226768	0.344315854	17.68237063	20.53244977	0.533217477	2.596950113
1.04	1.977623897	1.13220889	57.25097129	20.54460041	0.605127565	2.945433606
1.06	3.240460215	2.221164327	68.54471832	20.55814715	0.773562584	3.762803033
1.08	5.288232252	4.05037111	76.59215628	20.56645275	1.064714994	5.176950087
1.1	8.175314321	7.178639363	87.80872614	20.5526964	1.504397357	7.319707973

Table 4. 3 *Average value, standard deviation and relative error of Rd and Ld, with plasma*

	Rd (with plasma)			Ld (with plasma)		
Frequency [MHz]	**Average value [Ω]**	**σ [Ω]**	**Relative error [%]**	**Average value [μH]**	**σ [μH]**	**Relative error [%]**
0.9	4.485160389	2.741425625	61.12213137	20.22849254	0.795406947	3.932111824
0.92	3.516344567	2.075568614	59.02631481	20.22343657	0.663215064	3.279438002
0.94	3.484779275	1.102786744	31.64581333	20.21883221	0.579931688	2.868274895
0.96	3.495499069	0.430513976	12.31623776	20.21592241	0.536412021	2.653413533
0.975	3.506073899	0.372693024	10.62992496	20.21422036	0.520494053	2.574890566
0.98	3.509147048	0.424614659	12.10022416	20.21565468	0.516429727	2.554603029
1	3.525388124	0.572526337	16.24009378	20.21873754	0.507946503	2.512256276
1.02	3.543493125	0.574747848	16.21980987	20.2256333	0.514651741	2.544551921
1.04	3.561072404	0.982863109	27.60020011	20.23635423	0.563148392	2.782854982
1.06	3.570933413	2.26776323	63.50617521	20.2497714	0.695737633	3.435780183
1.08	5.258556745	3.757800404	71.46067992	20.2617262	0.946090557	4.669348247
1.1	7.751826989	6.229242257	80.35837572	20.26038786	1.334111221	6.584825673

Hence, it is possible to observe that there is a specific range of frequency (about 0.96÷1.02 MHz) for which σ is lower, thus highlighting a better measurements condition a more reliable values compare to the outer frequencies. For this reason, the measurement process should be focused on these frequencies, thus reaching the best accuracy of the results.

4.4.3 Sensitivity analysis

The final step of the evaluation of the effects of the errors on the measurements of Rd and Ld values, is a sensitivity analysis in order to comprehend what is the most influential error component. This is realized thanks to a MATLAB script which follows the same procedure of 4.4.2, but considering the error components individually: it is considered, in turn, a single error component while the other parameters are kept at their reference value. Figure 4. 32 and Figure 4. 33 show the results of this analysis thanks to bar graphs, respectively the former without plasma and the latter with plasma. Each error component is represented by a different color in order to provide a better view of the results.

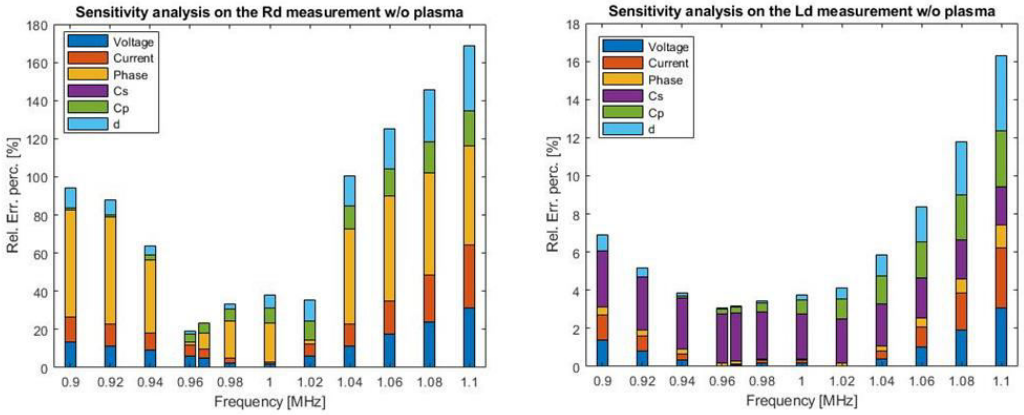

Figure 4. 32 *Sensitivity analysis on the effects of the error components on the Rd (left graph) and Ld (right graph) measurements, without plasma*

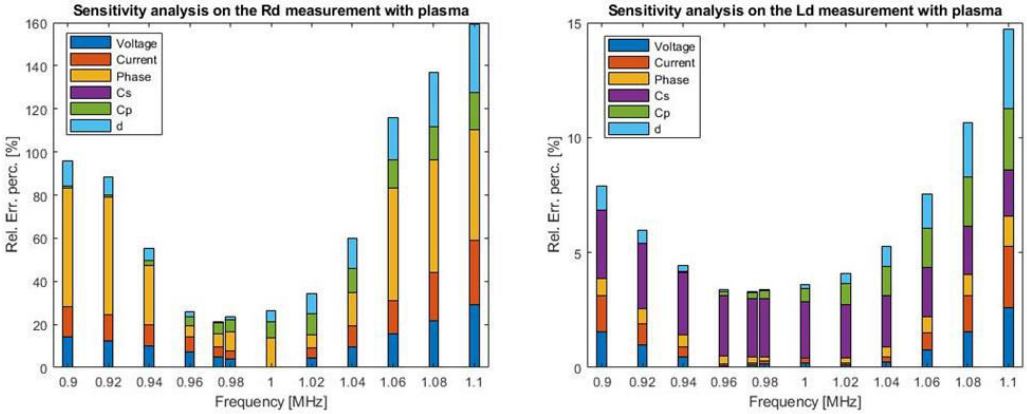

Figure 4. 33 *Sensitivity analysis on the effects of the error components on the Rd (left graph) and Ld (right graph) measurements, with plasma*

As regard the sensitivity analysis of the Rd graphs, both without and with plasma, it is clearly evident that the higher contribute to the error on the measurement of Rd is provided by the phase error. However, it is interesting to notice that, without plasma, at 0.96 MHz and at 1.02 MHz the phase error is much smaller and at 1 MHz the voltage error and the current error are almost zero. The Cs error is the less influential error component on the measurement of Rd and it is almost null at each frequency, while the other error components increase towards the edges of the frequency range (with the only exception of the Cp error which decreases towards 0.9 MHz). As regard the sensitivity analysis of the Ld graphs, the most influential error component is the Cs error, both without and with plasma. This is essentially due to the fact that Ld and Cs create a series resonance, so even a slight variation of Cs produces a great change on

the measurement of Ld. The other error components follow, more or less, the trends shown with the Rd graphs, with the exception of the phase error which has a much smaller impact on the Ld measurement. In order to complete the analysis, it is possible to observe that the Ld bar graphs, starting from the opposite edges of the frequency range, steadily decreases towards 0.96 MHz, for the no-plasma case, and towards 0.98 MHz, for the plasma case, following the behavior obtained in 4.4.3. As regard the Rd graphs, without plasma the bar graph shows the same behavior described in 4.4.3 with a decrease of the error on the measurement of Rd at the resonance and antiresonance frequencies. However, with plasma the bar graph decreases only in correspondence of the resonance frequency. The reduction of the error bar at the antiresonance frequency is probably masked by the increase of the phase error at 1.02 MHz and the reduction of the voltage and current errors at 1 MHz. The numerical results obtained thanks to the simulations are shown on Table 4. 4 and Table 4. 5, respectively without and with plasma.

Finally it is possible to assure that the best condition for the measurement of Rd and Ld is around the resonance frequency of the RF load, and, with plasma, even more reliable results can be obtained in correspondence of the frequency for which the reflection coefficient is at its minimum (0.975 MHz)

Table 4. 4 *Results of the sensitivity analysis of Rd (a) and Ld (b) measurements, without plasma*

Frequency [MHz]	Average value [Ω]	σ [Ω]	Relative error [%]	Average value [Ω]	σ [Ω]	Relative error [%]	Average value [Ω]	σ [Ω]	Relative error [%]
	V error effect			I error effect			Phase error effect		
0.9	1.832208892	0.246113431	13.43260762	1.816453508	0.240153752	13.22102387	3.169258866	1.781401228	56.20876372
0.92	1.844871815	0.212019909	11.49239243	1.831359336	0.207733322	11.34312191	2.284616193	1.282413326	56.13254996
0.94	1.856556777	0.167605919	9.027783122	1.845919869	0.165097341	8.94390615	1.811662634	0.696289486	38.43372786
0.96	1.872604946	0.11271714	6.033092792	1.861180357	0.111817186	6.007864069	1.851182112	0.021211518	1.145836359
0.967	1.86831437	0.091183718	4.869351525	1.867460908	0.090446127	4.843267483	1.862998478	0.152707413	8.196861926
0.98	1.881499237	0.047076522	2.502074996	1.878515124	0.047271926	2.516451727	1.884278851	0.36470525	19.35516337
1	1.897801253	0.029993407	1.580429279	1.899684592	0.029645768	1.560562648	1.905168225	0.382813414	20.09341794
1.02	1.919305819	0.119456928	6.223965308	1.926931533	0.120456095	6.251187095	1.907114306	0.033385256	1.750563994
1.04	1.948605619	0.223411603	11.46520365	1.963146438	0.228028735	11.61547254	1.883338952	0.930270711	49.39475763
1.06	1.988998831	0.345141374	17.35251767	2.012152848	0.356799801	17.73224146	2.960829184	1.62131665	54.75887157
1.08	2.044833488	0.490005238	23.96308751	2.079205639	0.513992399	24.72061396	4.557943608	2.437668245	53.48175525
1.1	2.122108705	0.666670679	31.41548202	2.171885725	0.711518105	32.76038408	6.518174926	3.39386038	52.06764806

Frequency [MHz]	Average value [Ω]	σ [Ω]	Relative error [%]	Average value [Ω]	σ [Ω]	Relative error [%]	Average value [Ω]	σ [Ω]	Relative error [%]
	Cs error effect			Cp error effect			Line length error effect		
0.9	1.802498266	8.97E-13	4.98E-11	1.802548017	0.011573598	0.642068776	1.817329131	0.189598134	10.43279012
0.92	1.822415979	1.98E-12	1.09E-10	1.822536066	0.019277954	1.057754304	1.830707436	0.140696332	7.685353168
0.94	1.842118346	1.09E-12	5.94E-11	1.843137212	0.051527405	2.795635863	1.845418277	0.085591388	4.63804813
0.96	1.861612205	1.12E-12	6.04E-11	1.864441496	0.085258003	4.57284408	1.862284209	0.023690318	1.27211078
0.967	1.868387005	8.29E-13	4.44E-11	1.87202193	0.097389198	5.202353464	1.868875262	0.000514425	0.027525892
0.98	1.880904038	2.65E-13	1.41E-11	1.886544536	0.12056552	6.390812262	1.882315818	0.045858492	2.436280435
1	1.9	1.10E-12	5.77E-11	1.909548349	0.157559799	8.251155257	1.906765144	0.124234965	6.515483331
1.02	1.918905938	1.61E-12	8.41E-11	1.933562289	0.196366524	10.1556865	1.937205408	0.213162793	11.00362367
1.04	1.937627415	2.14E-12	1.10E-10	1.958704132	0.237129292	12.10643753	1.975652373	0.315117998	15.95007311
1.06	1.956169727	1.25E-12	6.37E-11	1.985101327	0.280012048	14.10568037	2.024753303	0.433718051	21.42078495
1.08	1.974537921	2.62E-13	1.32E-11	2.012892447	0.325201962	16.15595321	2.088089429	0.574337944	27.50542846
1.1	1.992736812	1.77E-12	8.89E-11	2.042228887	0.372912833	18.26009001	2.170676993	0.745161406	34.32852554

(a)

Frequency [MHz]	Average value [μH]	σ [μH]	Relative error [%]	Average value [μH]	σ [μH]	Relative error [%]	Average value [μH]	σ [Ω]	Relative error [%]
	V error effect			I error effect			Phase error effect		
0.9	20.47391831	0.279415312	1.364737847	20.49129735	0.274790331	1.341009922	20.55375592	0.084875365	0.412943334
0.92	20.48636517	0.162941896	0.795367525	20.49647861	0.160655733	0.783821143	20.52698448	0.065095189	0.317120077
0.94	20.49513585	0.068812045	0.335748175	20.49939853	0.068077533	0.332095272	20.50885864	0.048562475	0.236787801
0.96	20.5000055	0.001766563	0.008617377	20.50011442	0.001780876	0.008687151	20.49988395	0.032242779	0.157282738
0.967	20.50082144	0.014539425	0.070921181	20.50010384	0.014429664	0.070388249	20.49861933	0.026015801	0.126914894
0.98	20.50143741	0.034044966	0.166061362	20.49933013	0.033929054	0.165512991	20.49856871	0.013490104	0.065809982
1	20.50067997	0.034884874	0.170164472	20.49851481	0.034967813	0.170587059	20.50092762	0.008367648	0.040815949
1.02	20.49986222	0.002791736	0.013618314	20.50003339	0.002776859	0.013545631	20.50012756	0.032403724	0.158065962
1.04	20.50210741	0.082687537	0.403312376	20.5073129	0.08384457	0.408852054	20.48649569	0.05887268	0.287373109
1.06	20.51169529	0.209183313	1.019824591	20.52508322	0.21382181	1.041758555	20.44813992	0.094131193	0.460341105
1.08	20.53432054	0.388014342	1.889589388	20.55975789	0.400209003	1.946564765	20.37232354	0.152249961	0.747337244
1.1	20.57752492	0.627334208	3.048637825	20.62007002	0.653862036	3.170998135	20.24744701	0.247133036	1.220563934

Frequency [MHz]	Average value [μH]	σ [μH]	Relative error [%]	Average value [μH]	σ [μH]	Relative error [%]	Average value [μH]	σ [μH]	Relative error [%]
	Cs error effect			Cp error effect			Line length error effect		
0.9	20.52072274	0.602446754	2.935796958	20.50000616	0.000179873	0.000877429	20.48986561	0.177985835	0.868653014
0.92	20.51983155	0.576538127	2.809663061	20.50000784	0.001943837	0.009482126	20.49590466	0.095436676	0.465637783
0.94	20.51899663	0.552265585	2.691484359	20.50030339	0.01843953	0.089947597	20.49890776	0.040427888	0.197219717
0.96	20.51821335	0.529494217	2.580605867	20.5012626	0.048802241	0.238045052	20.49984992	0.014188758	0.06921396
0.967	20.51662392	0.523582666	2.551992319	20.50149634	0.062404056	0.304387812	20.49995872	0.012062311	0.058840658
0.98	20.51747753	0.508102739	2.476438629	20.50324428	0.092287564	0.450112005	20.50005932	0.018110762	0.088344924
1	20.51678542	0.487981871	2.378451891	20.5065995	0.148261373	0.722993456	20.50128049	0.053861976	0.262724936
1.02	20.51613362	0.46903294	2.286166335	20.51167466	0.216191673	1.053993283	20.50575892	0.123550771	0.602517429
1.04	20.51551907	0.451166671	2.199148211	20.51881443	0.29564211	1.440834272	20.51635957	0.229960319	1.120863172
1.06	20.51493897	0.434302128	2.11700424	20.5283647	0.386266974	1.881625639	20.5367389	0.376890484	1.835201227
1.08	20.51439079	0.418365801	2.039377165	20.54067556	0.487807599	2.374837175	20.57160289	0.569671893	2.769214903
1.1	20.51387225	0.403290802	1.965941863	20.55610434	0.600090108	2.919279343	20.62710692	0.815968005	3.955804409

(b)

Table 4. 5 *Results of the sensitivity analysis of Rd (a) and Ld (b) measurements, with plasma*

Frequency [MHz]	Average value [Ω]	σ [Ω]	Relative error [%]	Average value [Ω]	σ [Ω]	Relative error [%]	Average value [Ω]	σ [Ω]	Relative error [%]
	V error effect			I error effect			Phase error effect		
0.9	3.560369919	0.505744574	14.20483224	3.532957463	0.492855833	13.95023399	4.342472668	2.389948245	55.03657543
0.92	3.546301226	0.438992251	12.37887655	3.522659366	0.429409285	12.18991791	3.438112139	1.881648752	54.72912681
0.94	3.5307632	0.354305152	10.03480359	3.511810684	0.348277578	9.917322116	3.436553201	0.942904949	27.43751933
0.96	3.515621705	0.25198153	7.167481352	3.502220827	0.249283503	7.117869351	3.470514547	0.180944688	5.2137712
0.975	3.507227423	0.163748878	4.668898188	3.496800624	0.163398343	4.672795513	3.49267316	0.221276986	6.335462147
0.98	3.503211816	0.132129099	3.771655999	3.496204591	0.131962462	3.77444909	3.497531343	0.314716478	8.998246118
1	3.496363539	0.006519834	0.186474723	3.496646342	0.005762635	0.164804617	3.508524644	0.46776415	13.33221787
1.02	3.498471008	0.162689809	4.650311774	3.507120037	0.16309004	4.650255428	3.492721442	0.2107405	6.033704756
1.04	3.513637582	0.341331401	9.71447375	3.532106825	0.346473962	9.809271893	3.438979667	0.516040917	15.00564023
1.06	3.546945293	0.54621747	15.39965871	3.577378727	0.561196689	15.68737146	3.338074718	1.740817597	52.15034846
1.08	3.604928594	0.784873655	21.77223859	3.650670013	0.817362354	22.38937925	4.680654651	2.447226724	52.28385572
1.1	3.69639706	1.06953128	28.93442621	3.76286992	1.131593973	30.07263066	6.423414604	3.281149686	51.08108207

Frequency [MHz]	Average value [Ω]	σ [Ω]	Relative error [%]	Average value [Ω]	σ [Ω]	Relative error [%]	Average value [Ω]	σ [Ω]	Relative error [%]
	Cs error effect			Cp error effect			Line length error effect		
0.9	3.5	0	0	3.50033671	0.041812274	1.194521494	3.532730402	0.403384172	11.41848164
0.92	3.5	8.88E-16	2.54E-14	3.499910669	0.016760197	0.478875001	3.519122886	0.308184609	8.757426741
0.94	3.5	2.22E-15	6.34E-14	3.500994491	0.076648347	2.189330702	3.508355932	0.203606528	5.80347411
0.96	3.5	0	0	3.503690288	0.137977624	3.938065672	3.501772687	0.088914414	2.539125798
0.975	3.5	0	0	3.506639948	0.185416612	5.287586261	3.500504087	0.004428292	0.126504413
0.98	3.5	0	0	3.508107226	0.200889101	5.726424187	3.500987322	0.037009747	1.05712315
1	3.5	0	0	3.514362564	0.265542678	7.555927224	3.507959063	0.175809163	5.011722208
1.02	3.5	2.22E-15	6.34E-14	3.52258285	0.332119079	9.428282964	3.525103432	0.329922091	9.359217321
1.04	3.5	4.44E-16	1.27E-14	3.532905284	0.400822394	11.34540446	3.555461664	0.502897081	14.14435392
1.06	3.5	0	0	3.545479299	0.471883087	13.30943005	3.602963196	0.69993417	19.42662559
1.08	3.5	4.44E-16	1.27E-14	3.56046837	0.545561551	15.32274675	3.672841914	0.92873061	25.2864303
1.1	3.5	1.33E-15	3.81E-14	3.578052129	0.62215232	17.3880172	3.77231662	1.200900094	31.83455196

(a)

Frequency [MHz]	Average value [µH]	σ [µH]	Relative error [%]	Average value [µH]	σ [µH]	Relative error [%]	Average value [µH]	σ [Ω]	Relative error [%]
	V error effect			I error effect			Phase error effect		
0.9	20.17164544	0.317369543	1.573344844	20.1886554	0.31175725	1.544219977	20.26336018	0.154295956	0.761452962
0.92	20.1845279	0.194838469	0.965286231	20.19493491	0.19189072	0.950192317	20.23374197	0.128090493	0.633053901
0.94	20.19392811	0.093110213	0.461080245	20.1988829	0.092037814	0.45565794	20.21255762	0.101233247	0.500843333
0.96	20.19948058	0.016936977	0.083848575	20.20037692	0.016888981	0.083607256	20.20081232	0.071651537	0.354696315
0.975	20.201428	0.020924727	0.103580436	20.20009723	0.020747548	0.10271014	20.19760863	0.04670845	0.231257328
0.98	20.20146366	0.029544246	0.146248048	20.19989555	0.02932044	0.145151441	20.19770519	0.037574301	0.186032524
1	20.20089379	0.042640119	0.21108036	20.19862955	0.042621937	0.211014004	20.20012528	0.001484942	0.007351152
1.02	20.19961424	0.01894613	0.093794514	20.19859911	0.019135254	0.094735551	20.20223201	0.044420289	0.219878125
1.04	20.20039483	0.045013616	0.222835327	20.20279654	0.045329183	0.224370832	20.19531667	0.089408496	0.442718961
1.06	20.20706852	0.153154955	0.757927626	20.21538632	0.155712146	0.770265496	20.16819942	0.136491027	0.676763571
1.08	20.22474388	0.310504566	1.535270694	20.24201463	0.318525778	1.57358733	20.10836118	0.191436987	0.952026796
1.1	20.2601562	0.524034306	2.586526486	20.29031795	0.542973973	2.676024959	20.00377018	0.267093214	1.335214368

Frequency [MHz]	Average value [µH]	σ [µH]	Relative error [%]	Average value [µH]	σ [µH]	Relative error [%]	Average value [µH]	σ [µH]	Relative error [%]
	Cs error effect			Cp error effect			Line length error effect		
0.9	20.2187513	0.603428307	2.984498392	20.20003955	0.000340088	0.001683598	20.19010128	0.205530465	1.017976395
0.92	20.21794489	0.577477468	2.856261956	20.1999814	0.002935888	0.014534115	20.19614344	0.114943015	0.569133483
0.94	20.2171894	0.553165379	2.736114146	20.19999918	0.008382339	0.041496728	20.19917863	0.05096097	0.252292287
0.96	20.21648064	0.530356911	2.623388909	20.20045764	0.033415223	0.165418146	20.20006804	0.014739097	0.072965579
0.975	20.21623777	0.513086411	2.537991572	20.20123475	0.060863224	0.301284673	20.19997036	0.006572253	0.032535953
0.98	20.21581482	0.50893058	2.517487346	20.20170931	0.071405228	0.353461318	20.19999982	0.007559797	0.037424736
1	20.21518855	0.488776929	2.41786975	20.20409758	0.121702902	0.602367425	20.20054519	0.030933593	0.153132465
1.02	20.21459876	0.469797125	2.324048727	20.20795979	0.18375904	0.909339894	20.20373254	0.086732208	0.429288045
1.04	20.21404267	0.451901746	2.235583222	20.21363004	0.25711791	1.272002649	20.21214958	0.177398312	0.877681571
1.06	20.21351776	0.435009727	2.15207334	20.22144203	0.34141197	1.688366089	20.22908986	0.306230245	1.513811282
1.08	20.21302174	0.419047436	2.073155816	20.2317319	0.436357936	2.156799717	20.2587695	0.477811345	2.358540803
1.1	20.21255252	0.403947875	1.998500064	20.24484104	0.541754115	2.676010711	20.30665843	0.698667708	3.440584331

(b)

5 Common mode current analysis with the RF-OSC

One crucial issue related to the operation of SPIDER, as aforementioned in 0, is the existence of RF common mode (CM) currents within the system. These currents, at the working frequency for which the RF circuits have been designed for (1 ± 0.1 MHz), are allowed to circulate in low equivalent impedance loop, see Figure 5. 1, which involves $C_{protect}$(which has been designed in order to keep the potential of the ion source body and the PG as similar as possible in case of breakdown between the extraction and PG or grounding grids) (see 0) RF lines, PG busbars, the output filter of ISEG, the HVD and the CVD.

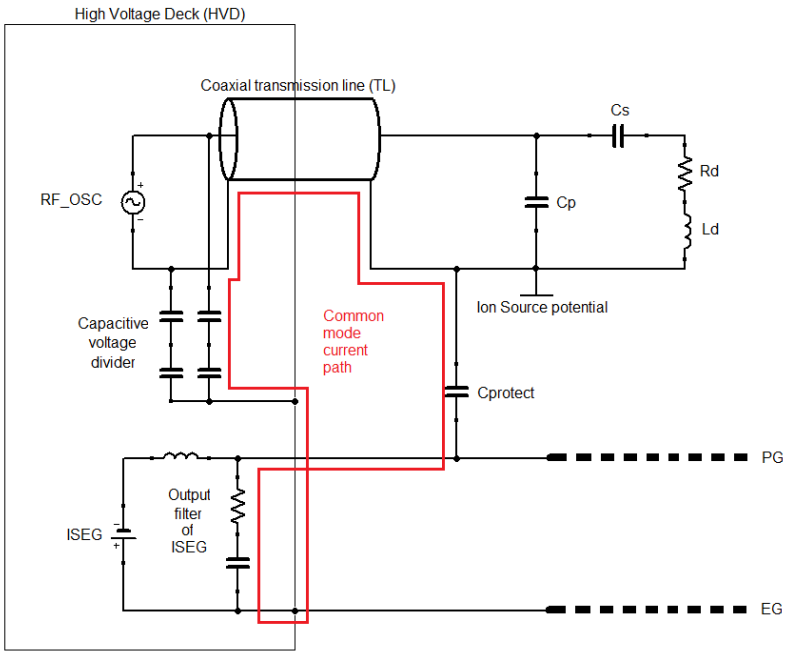

Figure 5. 1 *Simplified scheme of the common mode currents (CMC) path*

Several experimental tests have been carried out at SPIDER in order to analyze the phenomenon and the effects of these currents, highlighting overheating issues on the ISEG filter and noise signals over the diagnostic devices (see 0). For these reasons, many efforts have been devoted to the study of possible solutions for reducing the CM currents to acceptable values.

In the context of substituting the RF-OSC with solid-state RF amplifiers, the analysis of the RF CM currents plays a fundamental role. In fact, it is necessary to understand the current situation with the oscillators and define a model for the evaluation of these currents. Hence, the goal is to identify the RF CM currents with the RF-OSC model as an issue, and then trying to predict if it will be an issue even with the amplifiers.

For this reason, this chapter has been focused on the analysis of the CM currents in the current configuration of the ISRF, with the RF oscillators. It is important to highlight that the oscillators work at a frequency different from the optimal one (minimum ρ frequency) due to the Frequency Flip phenomenon. In fact, the real operating frequencies are ranging from 946 kHz and 956 kHz, depending on the specific

RF-OSC, considering the 4 RF-OSC operating at 100 kW with the CVD on the secondary winding of the output transformer,. This analysis has been realized through circuital and numerical simulations both in frequency domain, by interfacing MATLAB and QucsStudio [24] (a free software for circuit simulations in different regimes) and in time domain, through MATLAB Simulink [25]. The simulation process has to take into account the overall RF system of SPIDER, which consists of four different operating RF circuits each supplied by a dedicated RF-OSC and for this reason a circuital model of the system has been developed.

5.1 Definition of the circuital model for the RF CM currents analysis

The electrical scheme for the analysis of the RF CM currents has been developed on the basis of the single RF circuit of Figure 5. 2: an RF-OSC feeding the antennas of the two drivers of the ion source (with an equivalent impedance $Z_d = R_d + j\omega L_d$) through a coaxial transmission line (TL) and a capacitive matching network (2Cs and Cp).

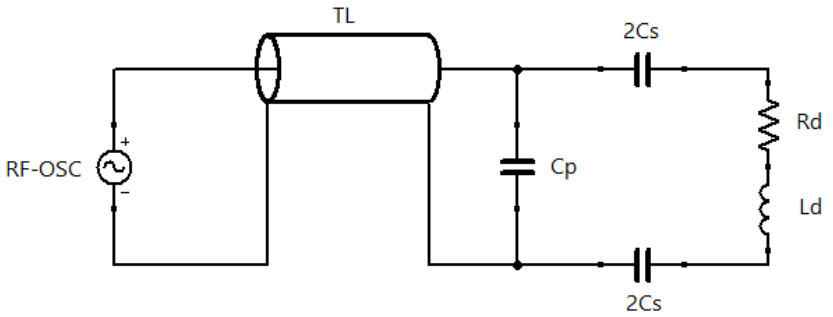

Figure 5. 2 *Single RF circuit*

This pattern has been repeated four times in order to represent the four RF circuits of SPIDER. However, since the probability for Rd and Ld of being perfectly equal within every RF circuit is almost zero, the values of Rd and Ld have been introduced in the model are shown in Table 5. 1. This consideration can be verified by considering the analysis of4.4, which highlights the uncertainty related to the estimation of Rd and Ld, for a single RF circuit, and its dependence on frequency.

Table 5. 1 *Values of Rd and Ld adopted in the model*

	Rd	Ld
RF circuit #1	3.5 Ω	20.2 µH
RF circuit #2	3.4Ω	19.8 µH
RF circuit #3	3.6 Ω	20.6 µH
RF circuit #4	3.3 Ω	20 µH

A crucial aspect in the definition of the electrical scheme for the simulation has been the characterization of the model of the transmission line. In fact, the four coaxial transmission lines of the four RF circuits are mutually coupled between them and to the others conductors which are included within the TL of SPIDER which connects the power supplies contained within the HVD to the ion source (see THT1 in Figure 2. 8). In addition, it is necessary to take into account also the stray capacitances between all the conductors (which have been assumed in the transmission line): the RF inner conductor and outer conductor, and the PG busbar. All these conductors are potentially involved for the return of the RF CM currents from the ion source to the HVD. In the first evaluations, most of current flows through the PG busbars. For this reason, it has been taken into account only the PG busbars in the TL model for the return of the RF CM currents. Differently from chapter 4, where the focus was to highlight the influence of the transmission line on the

impedance of the RF load and for this reason a 30 m, lossless line model has been assumed, for the analysis of the RF CM current it has been considered a line model closer to the SPIDER TL, in order to obtain results which can approximate the experimental ones. For this reason, it has been considered a 40 m (see 3.1.2) lossy transmission line model. Furthermore, in order to take into account all the mutual couplings and the stray capacitances of the transmission line, it has been adopted a lumped components transmission line model by splitting the overall transmission line in a specific number of sections. In order to apply this model, each section must be electrically short at the highest frequency of interest. This means that it must respects the condition of quasi-stationariety for which the dimension of the circuit l (in this case the length of the section) must be much smaller than the wavelength, λ, at the operating frequency of the system. In order to respect this condition and to have good accuracy, it has been adopted the criteria for the selection of the number of sections (N) suggested in [26] for which

$$N \gg 50\frac{d}{\lambda}$$

where d is the overall line length and the λ is equal to

$$\lambda = \frac{v}{f}$$

where v is the propagation velocity of the wave (in this case it is equal to the speed of light c = 3×10^8m/s) and f is the operating frequency. Considering f = 1 MHz and d = 40 m it is possible to obtain

$$N \gg 50\frac{40 \cdot 1 \times 10^6}{3 \times 10^8} \approx 7.$$

For this reason, the overall transmission line has been splitted in 8 sections of 5 m length. The input port and the first section of the resulting lumped components model of the transmission line, which has been adopted for the RF CM currents analysis is portrayed in Figure 5. 3 (the conductances have been neglected).

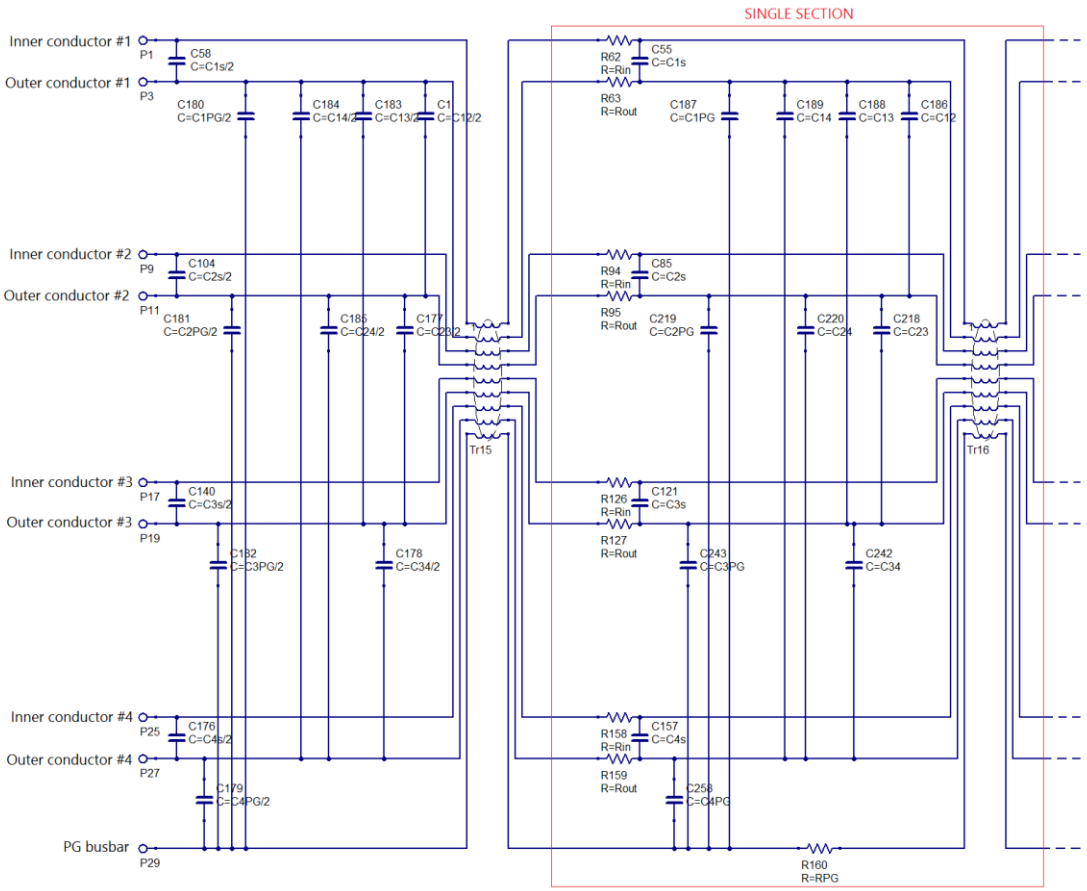

Figure 5. 3 *Input port and first section of the lumped components model of the transmission line*

The values of the inductances and the capacitances per unit length have been obtained by estimating the inductances matrix and the stray capacitances between the conductors of the TL through Finite Element Method Magnetics (FEMM), a free 2D finite element solver [27]. The inductances matrix is an NxN matrix with N equal to the number of conductors of the system. It is characterized by the following features: on the main diagonal there are the self inductances (L_{ii}) while the outer terms are respectively the mutual inductances (L_{ij}) and they are simmetrical with respect to the main diagonal (for i = 1...N and j = 1...N). Its structure is the following:

$$\begin{bmatrix} L_{11} & L_{21} & \cdots & L_{N1} \\ L_{12} & L_{22} & \cdots & L_{N2} \\ \vdots & \vdots & \ddots & \vdots \\ L_{1N} & L_{2N} & \cdots & L_{NN} \end{bmatrix}$$

The resulting inductances matrix and the stray capacitances between conductors are shown in Table 5. 2 and Table 5. 3.

Table 5. 2 *Inductances matrix of the transmission line model per meter*

	In. Cond. #1	Out. Cond. #1	In. Cond. #2	Out. Cond. #2	In. Cond. #3	Out. Cond. #3	In. Cond. #4	Out. Cond. #4	PG busbar
In. Cond. #1	7.11E-07	5.32E-07	1.47E-07	1.47E-07	1.49E-07	1.49E-07	3.14E-07	3.14E-07	2.38E-07
Out. Cond. #1	5.32E-07	5.30E-07	1.47E-07	1.47E-07	1.49E-07	1.49E-07	3.14E-07	3.14E-07	2.38E-07
In. Cond. #2	1.47E-07	1.47E-07	7.10E-07	5.32E-07	3.14E-07	3.14E-07	1.49E-07	1.49E-07	3.13E-07
Out. Cond. #2	1.47E-07	1.47E-07	5.32E-07	5.30E-07	3.14E-07	3.14E-07	1.49E-07	1.49E-07	3.13E-07
In. Cond. #3	1.49E-07	1.49E-07	3.14E-07	3.14E-07	7.08E-07	5.30E-07	1.78E-07	1.78E-07	2.77E-07
Out. Cond. #3	1.49E-07	1.49E-07	3.14E-07	3.14E-07	5.30E-07	5.28E-07	1.78E-07	1.78E-07	2.77E-07
In. Cond. #4	3.14E-07	3.14E-07	1.49E-07	1.49E-07	1.78E-07	1.78E-07	7.09E-07	5.30E-07	2.29E-07
Out. Cond. #4	3.14E-07	3.14E-07	1.49E-07	1.49E-07	1.78E-07	1.78E-07	5.30E-07	5.28E-07	2.29E-07
PG busbar	2.38E-07	2.38E-07	3.13E-07	3.13E-07	2.77E-07	2.77E-07	2.29E-07	2.29E-07	6.44E-07

Table 5. 3 *Stray capacitances between the conductors of the transmission line model per meter*

Stray capacitance	C [F]
Inner conductor #1 - Outer conductor #1	6.64E-11
Outer conductor #1 - Outer conductor #2	1.30E-13
Outer conductor #1 - Outer conductor #3	8.72E-14
Outer conductor #1 - Outer conductor #4	1.58E-11
Outer conductor #1 - PG busbar	6.72E-13
Inner conductor #2 - Outer conductor #2	6.64E-11
Outer conductor #2 - Outer conductor #1	1.30E-13
Outer conductor #2 - Outer conductor #3	1.58E-11
Outer conductor #2 - Outer conductor #4	8.69E-14
Outer conductor #2 - PG busbar	1.16E-11
Inner conductor #3 - Outer conductor #3	6.64E-11
Outer conductor #3 - Outer conductor #1	8.72E-14
Outer conductor #3 - Outer conductor #2	1.58E-11
Outer conductor #3 - Outer conductor #4	1.74E-12
Outer conductor #3 - PG busbar	6.25E-12
Inner conductor #4 - Outer conductor #4	6.64E-11
Outer conductor #4 - Outer conductor #1	1.58E-11
Outer conductor #4 - Outer conductor #2	8.69E-14
Outer conductor #4 - Outer conductor #3	1.74E-12
Outer conductor #4 - PG busbar	1.39E-12

As regards the resistance per unit length of the inner conductors, the screens and the PG busbar, the following values have been assumed:

- resistance of the inner conductor of each coaxial transmission line: 0.0024 Ω/m;
- resistance of the screen of each coaxial transmission line: 0.001 Ω/m;
- resistance of the PG busbar: 0.001 Ω/m.

Hence, in order to obtain the values of the inductances, capacitances and resistances in each section of the TL model, the parameters obtained have been multiplied by the length of each section (5 m).

The resulting model of the ISRF system and relevant ISEPS components for the analysis of the RF CM currents is represented in Figure 5. 4. The transmission line has been integrated within the scheme through the subcircuit TL1.

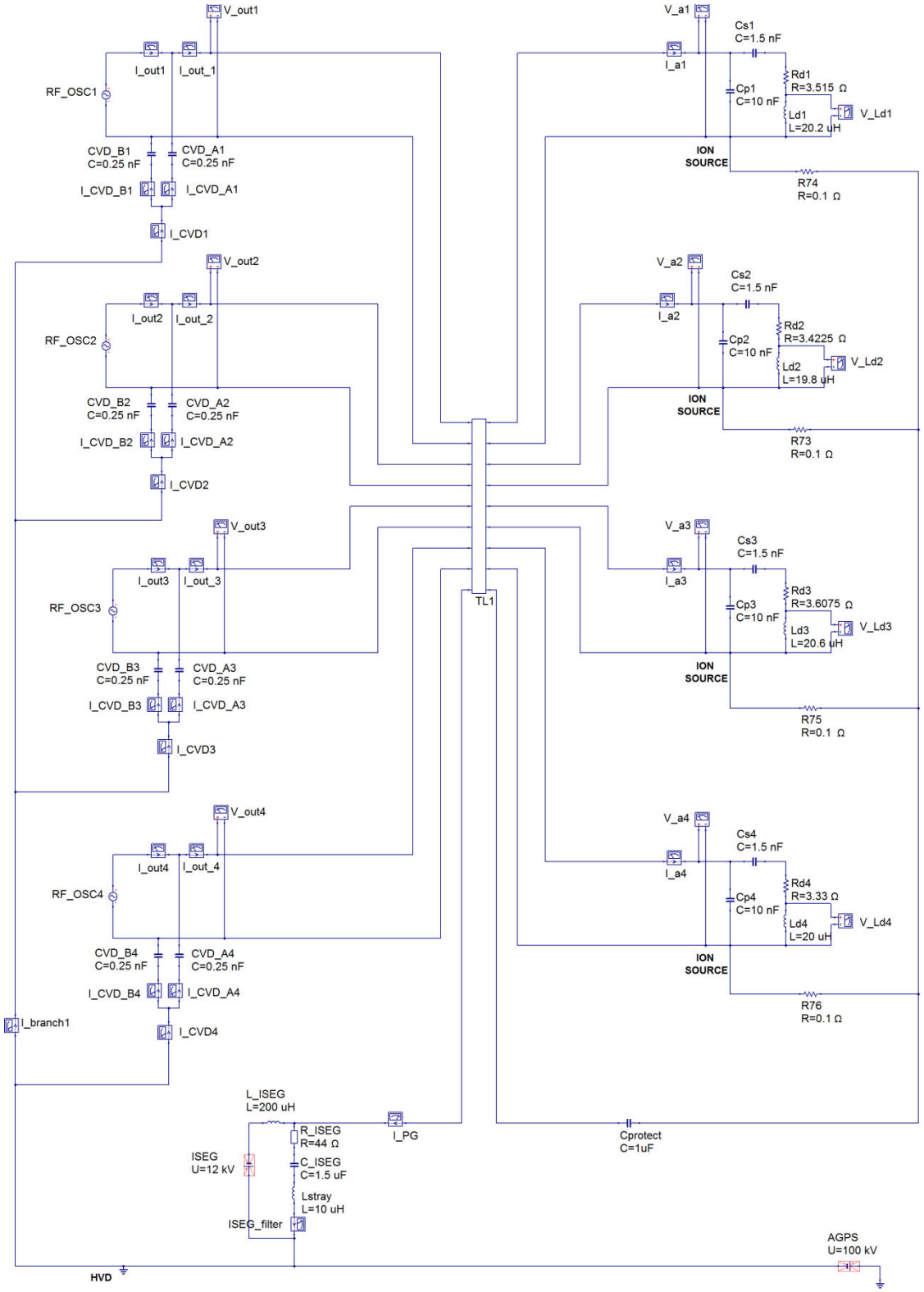

Figure 5. 4 *Electrical scheme for the analysis of the RF common mode currents with the actual configuration of SPIDER with the RF-OSC*

The CVD of each RF circuit is represented through two parallel capacitors of 250 pF connected between the HVD and the output terminal of the related RF-OSC. In particular, the CVD_A is connected to the inner conductor of the coaxial transmission line, while the CVD_B is connected to the outer conductor of the coaxial transmission line. The ISEG output filter, which is connected between the PG busbar and the HVD, is represented through the series connection of a resistance of 44 Ω, a capacitance of 1.5 μF and an inductance of 10 μH. The protection capacitor ($C_{protect}$), is equal to 1μF and the resistor of 0.1 Ω represents the connection between the RF load of each circuit and the PG busbar (the inductances of these connections have been neglected). Furthermore, the components marked with the red cross are disabled during the simulation of the model and they act as an open circuit (this notation has been adopted for all the simulation with QucsStudio).

5.2 Frequency domain analysis

The RF CM currents analysis in the frequency domain aims to evaluate the trends and the values of these currents over the frequency range of the RF-OSC (0.9 ÷ 1.1 MHz). It is important to highlight that the analysis over the entire frequency range is not representative of the real operational condition: not all frequencies represent real operating condition, and the Frequency Flip phenomenon it is not considered. The analysis is focused on the RF return currents from the ion source to the HVD through the PG busbar, I_{PG}, and the ISEG output filter, I_{ISEG}. In order to start the AC simulation procedure, the electrical scheme of Figure 5. 4 has been implemented in QucsStudio, imposing the starting frequency of the simulation at 0.9 MHz and the end at 1.1 MHz, for an overall of 10^5 sampling points. By introducing in the circuit the measurement blocks (Voltage probes and Current probes) available in the Qucsstudio directory and then running the simulation, it is possible to obtain the desired results in magnitude and phase. However, QucsStudio does not allow to limit the output of the AC voltage generator and for this reason, in order to ensure the assumptions of limiting output voltage and current to the RF-OSC nominal values (see 4.3.2), a specific procedure involving MATLAB has been developed. The procedure starts by imposing an output voltage of 1 V (phase zero) to the AC voltage generators (representing the RF-OSC) of each RF circuit. Hence, the simulation is started with only one generator ON and the other three OFF (for example RF-OSC #1 ON). With this solution, the resulting RF CM currents measurements are referred to 1 V. At this point, the output voltage and current of the generator and all the required measurements have been imported to MATLAB where the limitation process is realized. Starting from 0.9 MHz, the output voltage and current of the generator are increased until the voltage limit (3162 V) or the current limit (63.25 A) is reached. The resulting limited voltage is used for scaling the RF CM currents values derived from QucsStudio, which are referred to 1 V. This procedure is repeated for all the frequencies of the RF-OSC operating frequency range. At this point the RF-OSC #1 is turned OFF and the RF-OSC #2 is turned ON and the simulation is started again. This procedure has been repeated for all the four RF-OSC.

For the RF CM currents analysis it is necessary to evaluate also the combined operation of the RF-OSC, especially with the four RF-OSC ON at the same time since it is the worst condition in which the currents reach the higher values. However, this procedure does not allow to evaluate it, since it is impossible to distinguish, at a specific frequency the effect of one RF-OSC from another for scaling the specific RF CM current value. For this reason, the evaluation of the effects of the combined operation of all the four RF-OSC will be discussed in the time domain analysis (see 5.3).

5.2.1 RF-OSC operating parameters

Figure 5. 5, Figure 5. 6, Figure 5. 7 and Figure 5. 8 show the output voltage, the output current and the output active power respectively of the four RF-OSCs derived from the limitation procedure. In addition it has been provided the reflection coefficient of the four RF circuits.

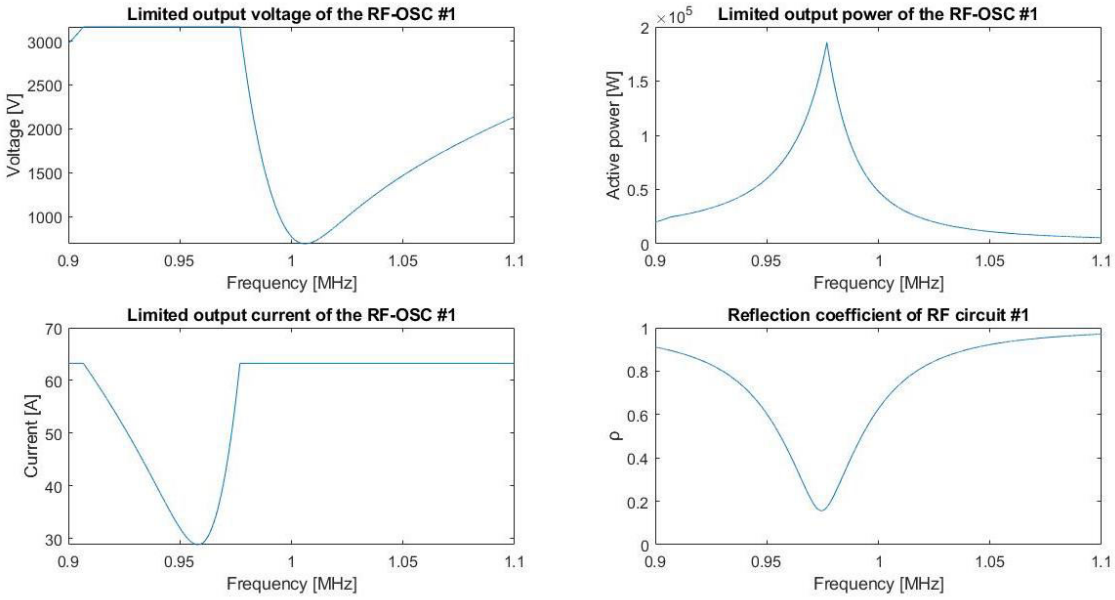

Figure 5. 5 *Output voltage, output current, output power of the RF-OSC #1 and the reflection coefficient of RF circuit #1*

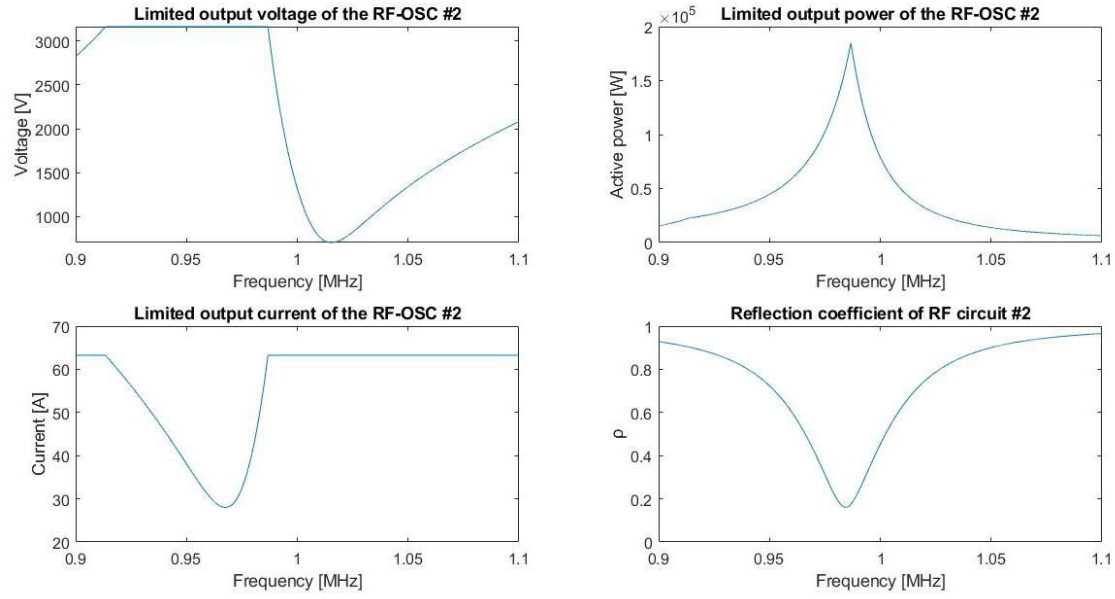

Figure 5. 6 *Output voltage, output current, output power of the RF-OSC #2 and the reflection coefficient of RF circuit #2*

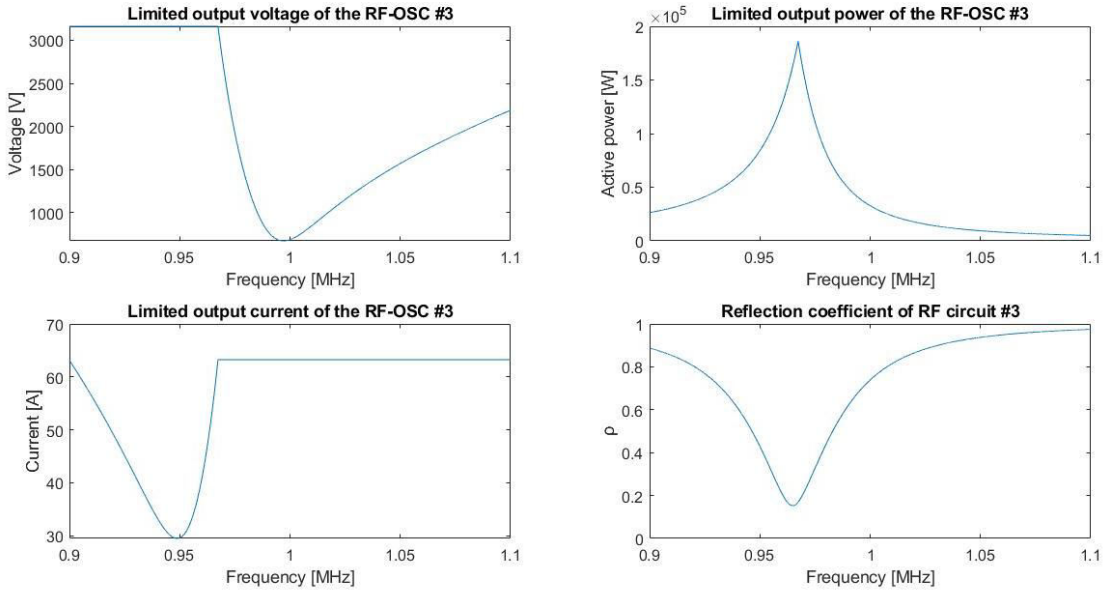

Figure 5. 7 *Output voltage, output current, output power of the RF-OSC #3 and the reflection coefficient of RF circuit #3*

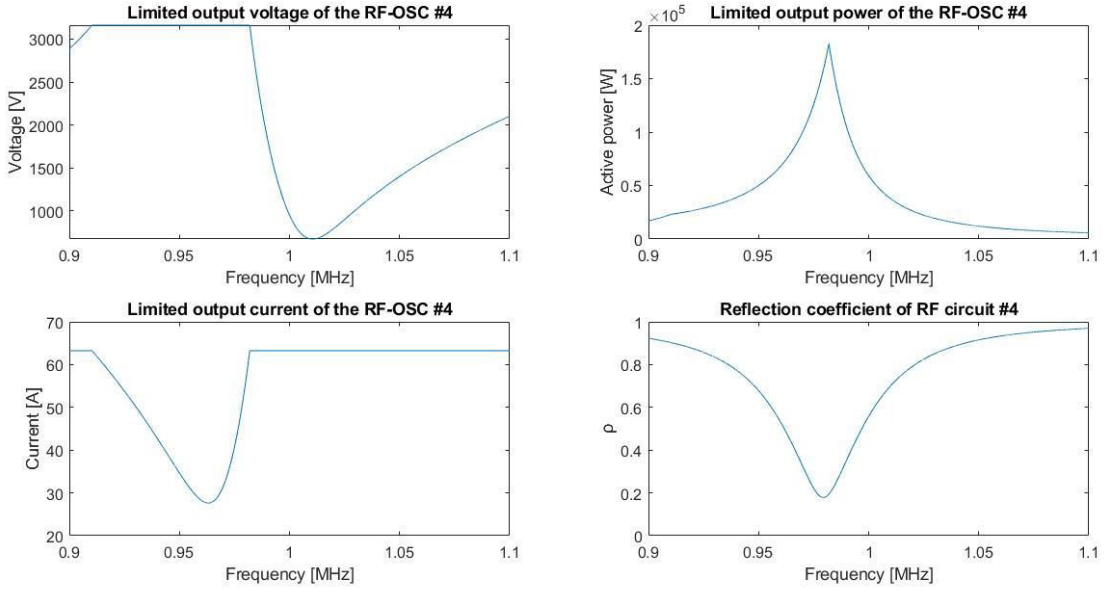

Figure 5. 8 *Output voltage, output current, output power of the RF-OSC #4 and the reflection coefficient of RF circuit #4*

It is important to highlight that the four RF-OSCs have different trends and this is due to the asymmetry introduced between the antennas parameters of the drivers of the RF load of the four RF circuits. Furthermore these differences are also due to the mutual coupling effect between the transmission lines. The effect of the voltage and current limitation in the output voltage and current plots is also evident. The main features derived from the plots of the RF-OSC operating parameters are the following:

- the RF-OSC #1 is limited in voltage within 0.907÷0.976 MHz and in current within 0.9÷0.906 MHz and 0.977÷1.1 MHz. The peak of the output power is equal to 185.7 kW at ~0.977 MHz

and the minimum of the reflection coefficient of the RF circuit #1 is equal to 0.157 at 0.975 MHz;

- the RF-OSC #2 is limited in voltage within 0.913÷0.986 MHz and in current within 0.9÷0.914 MHz and 0.987÷1.1 MHz. The peak of the output power is equal to 184.9 kW at ~0.987 MHz and the minimum of the reflection coefficient of the RF circuit #1 is equal to 0.161 at 0.985MHz;

- the RF-OSC #3 is limited in voltage within 0.9 ÷ 0.967 MHz and in current within 0.968÷1.1MHz. The peak of the output power is equal to 186.1 kW at ~0.967 MHz and the minimum of the reflection coefficient of the RF circuit #1 is equal to 0.153 at 0.965 MHz;

- the RF-OSC #4 is limited in voltage within 0.911÷0.982 MHz and in current within 0.9÷0.91 MHz and 0.983÷1.1 MHz. The peak of the output power is equal to 182.6 kW at ~0.982 MHz and the minimum of the reflection coefficient of the RF circuit #1 is equal to 0.179 at 0.979 MHz;

In this analysis it is interesting to consider also the results that could be reached from the RF-OSC if they could operate at the matching condition (minimum ρ frequency). Obviously, in real operation this condition is unreachable due to the frequency flip phenomenon (see 3.2.1).

5.2.2 Results of the RF common mode current analysis

Considering the reference electrical scheme of Figure 5. 4, it is possible to highlight that the current circulating on the PG busbar, I_{PG}, corresponds to the current circulating on the ISEG output filter, I_{ISEG}. Figure 5. 9 shows the trends of the magnitude of I_{ISEG} for a single RF-OSC ON at time, while the other ones are OFF (four different conditions have been represented with different colors).

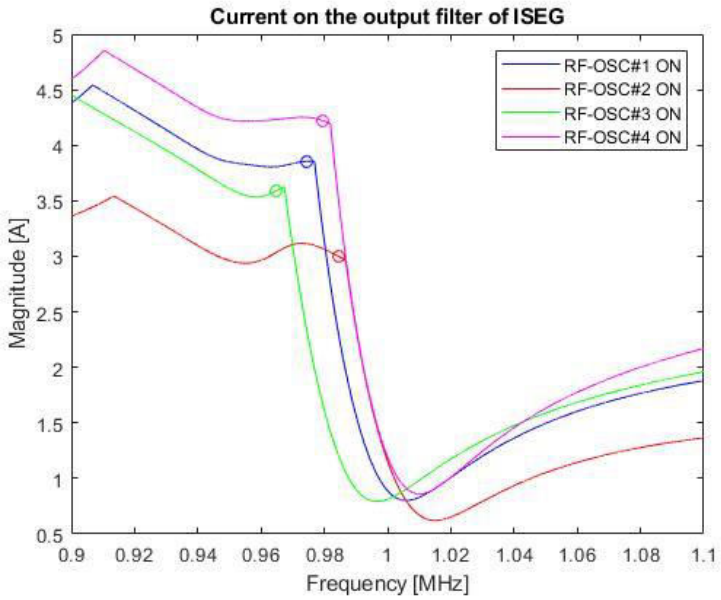

Figure 5. 9 *Current on the ISEG output filter with each RF-OSC operating independently (the markers highlight the* $\boldsymbol{I_{ISEG}}$*value at the minimum ρ frequency for each specific RF circuit)*

I_{ISEG}, in each condition, show similar magnitude trends: the higher values are obtained at low frequencies while towards ~1 MHz, it is possible to observe a strong reduction in magnitude, reaching minimum values lower than 1 A. From these points onwards, I_{ISEG} magnitude values start to increase until reaching 1.1 MHz. Among all trends, the worst results have been obtained when RF-OSC #4 is on and the others oscillators are OFF, reaching the maximum current value of about 4.9 A at ~0.91 MHz. In Figure 5. 9, circular markers have been introduced in correspondence of the minimum ρ frequency of each RF circuit in order to provide the hypotetical magnitude value of I_{ISEG} with the RF-OSC working in matching condition. Considering the RF-OSC #4 ON, the current on the ISEG output filter at 0.979 MHz would be equal to 4.2 A.

It is interesting to consider also how the RF CM currents are distributed within the circuit, in particular how I_{ISEG}, after exiting the ISEG output filter and reaching the HVD, is distributed among the capacitive voltage dividers (CVD) of each RF circuit. For this reason, referring to Figure 5. 10, it has been verified the distribution of the currents at node A by considering, for each of the three branch currents, its related magnitude and phase. In particular, the current reaching node A are I_{ISEG}, the current flowing towards the CVD of the RF circuit #4, I_{CVD4}, and the sum of the currents circulating on the HVD towards the other three CVD, which have been represented through $I_{branch1}$.

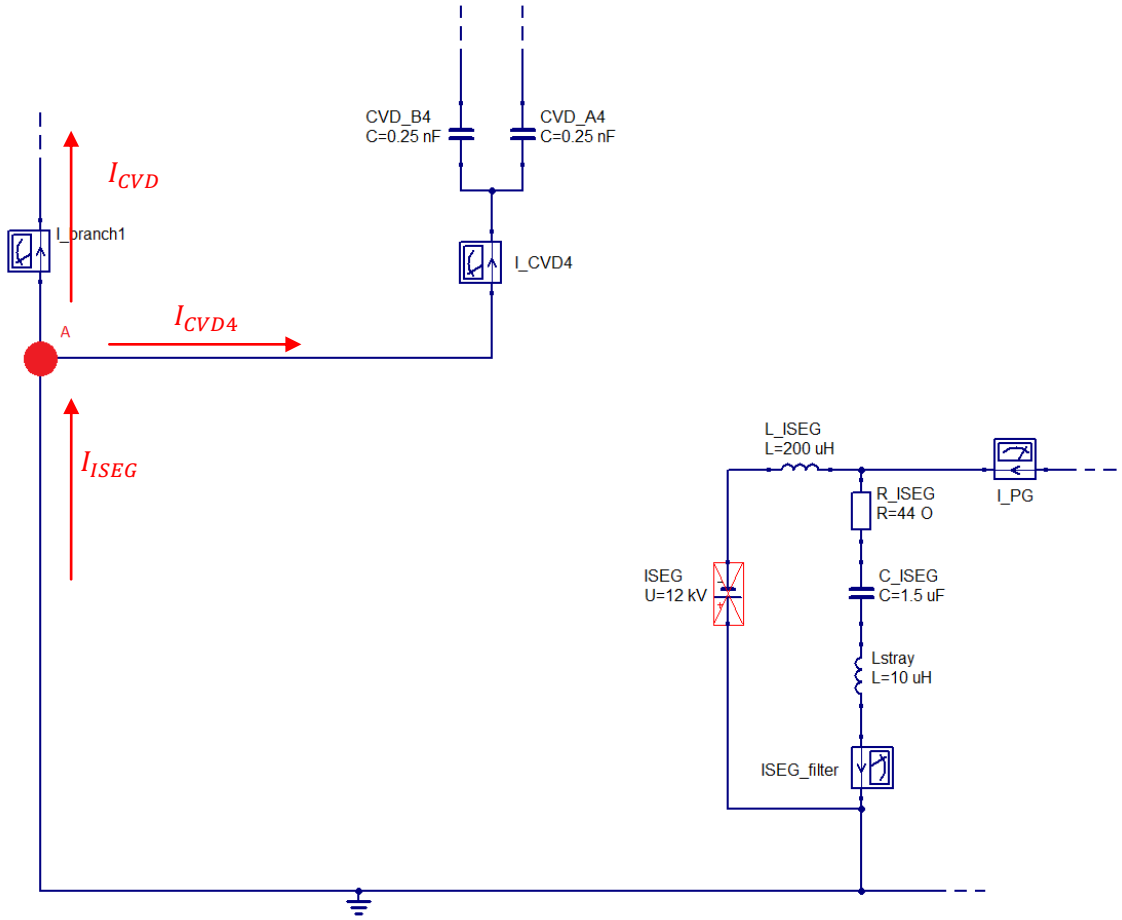

Figure 5. 10 *Zoom of the electrical scheme for the evaluation of the distribution of* $\boldsymbol{I_{ISEG}}$ *at node A*

Focusing on the worst condition for which RF-OSC #4 is ON, the Figure 5. 11 shows the magnitude and the phase of I_{ISEG}, I_{CVD4} and I_{CVD}.

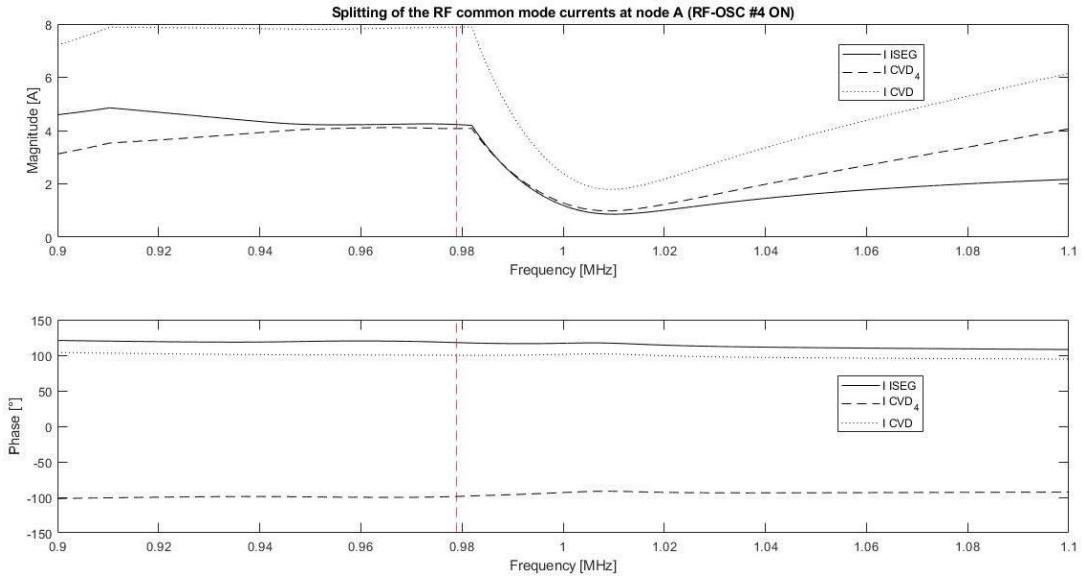

Figure 5. 11 *Magnitude (upper plot) and phase (bottom plot) of* $\boldsymbol{I_{ISEG}}$ *,* $\boldsymbol{I_{CVD4}}$ *and* $\boldsymbol{I_{CVD}}$ *with RF-OSC #4 ON*

By applying the Kirchoff current law (KCL) with phasors at node A, the sum of the currents flowing into node A must be equal to the sum of the current exiting the node:

$$\boldsymbol{I_{ISEG} = I_{CVD4} + I_{CVD}}.$$

It is interesting to highlight also how the current $I_{CVD4}$is distributed between the two CVD of the RF circuit #4 (CVD_A4 and CVD_B4 in Figure 5. 10), even in this case considering the RF-OSC #4 ON and the others OFF. Defining I_{CVDA4} and I_{CVDB4} respectively the current on the CVDA_4 and CVD_B4, Figure 5. 12 shows the magnitude and the phase of these two currents, along with I_{CVD4}. The results provided by the model can be compared to the ones obtained experimentally at SPIDER: at ~0.95 MHz, it has been measured that about the 90% of the current flows through the CVD connected to the inner conductor of the coaxial transmission line (CVD_A), while the 10% flows through the CVD connected to the outer conductor of the coaxial transmission line (CVD_B). The resulting currents of Figure 5. 12 reflect this aspect, highlighting also that the distribution of current between the CVD_A and CVD_B depends on frequency.

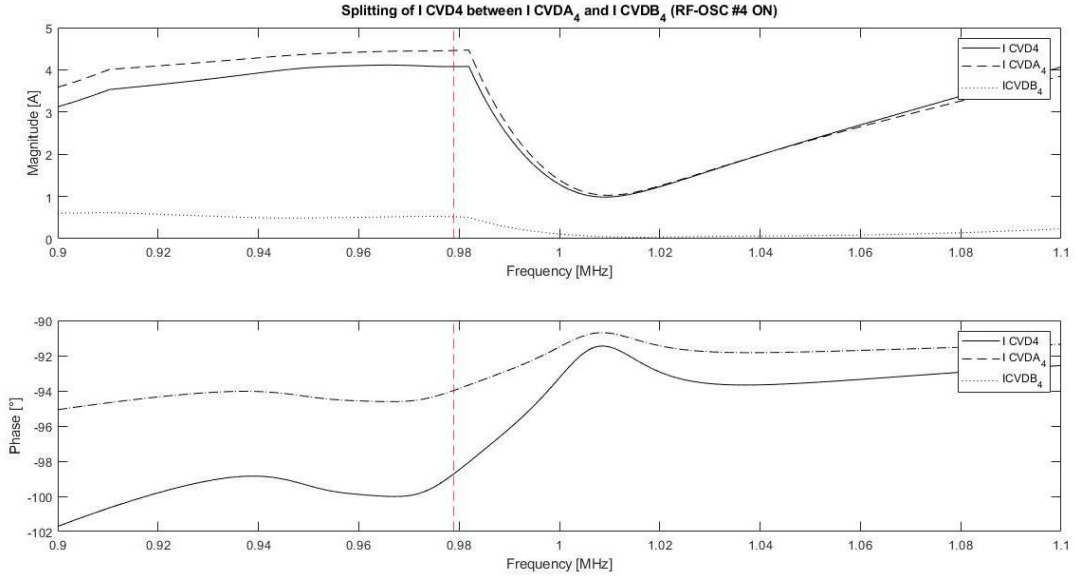

Figure 5. 12 *Magnitude (upper plot) and phase (bottom plot) of* $\boldsymbol{I_{CVD4}}$, $\boldsymbol{I_{CVDA4}}$ *and* $\boldsymbol{I_{CVDB4}}$ *with RF-OSC #4 ON*

5.3 Time domain analysis

The time domain analysis of the scheme reported in Figure 5. 4 has been realized through MATLAB Simulink in order to have an idea of the evolution of the CM currents over time, allowing to estimate their RMS value which is a key parameter in the dimensioning of the components of the overall circuit, especially the passive components of the ISEG output filter. In the time domain analysis, each RF-OSC has been operated at the minimum ρ frequency of the related RF circuit, hence in matching condition. As aforementioned in 5.2, this is not a real operating condition for the oscillators but it will be useful to analyze these results in the perspective of a comparison on the RF CM currents between the RF-OSC and the RF amplifiers (see 6.4.4), since the latter are able to ensure stable operation within the overall frequency range of SPIDER (0.9÷1.1 MHz). The time domain analysis has been initially dedicated to simulate the circuit with a single operating RF-OSC at time, at the minimum ρ frequency, at full power. After that, the analysis has been focused on the simulation of the circuit with all the four RF-OSC operating at the same time[4], even in this case, each one at the related minimum ρ frequency, at full power. This corresponds to the worst condition in terms of RF CM currents, and consequently the most interesting one: more power is delivered to the circuit, voltage and current increase and the same happens to the RF CM currents. The parameters of the RF-OSC which has been adopted in time domain analysis are summarized in Table 5. 4.

Table 5. 4 *Output voltage, current and active power of the RF-OSC of each RF circuit, at the minimum ρ frequency, at full power*

	ρ minimum frequency [MHz]	Output voltage [V]	Output current [A]	Output active power [W]
RF-OSC #1	0.975	3162	54.9	164.6
RF-OSC #2	0.985	3162	55.2	163.5
RF-OSC #3	0.965	3162	54.1	162.8
RF-OSC #4	0.979	3162	53.5	158.8

[4] The frequency domain analysis could be used for the sum of these currents just in the case of the four RF-OSC operating at the same frequency (taking into account their phases). In frequency domain it is not possible to sum signals with different frequencies since it would correspond to sum phasors with different angular velocities.

5.3.1 Results of the RF common mode current analysis

For the RF CM currents analysis in time domain, it has been implemented a discrete simulation considering a time interval of 1 ms with a sampling time of 1 ns. MATLAB Simulink allows to select the initial state of the simulation and, in order to have an idea of the the initial transient, it has been set to 0 s.

Figure 5. 13 shows the evolution of I_{ISEG} over time for each of the four operating condition with just one RF-OSC ON at time.

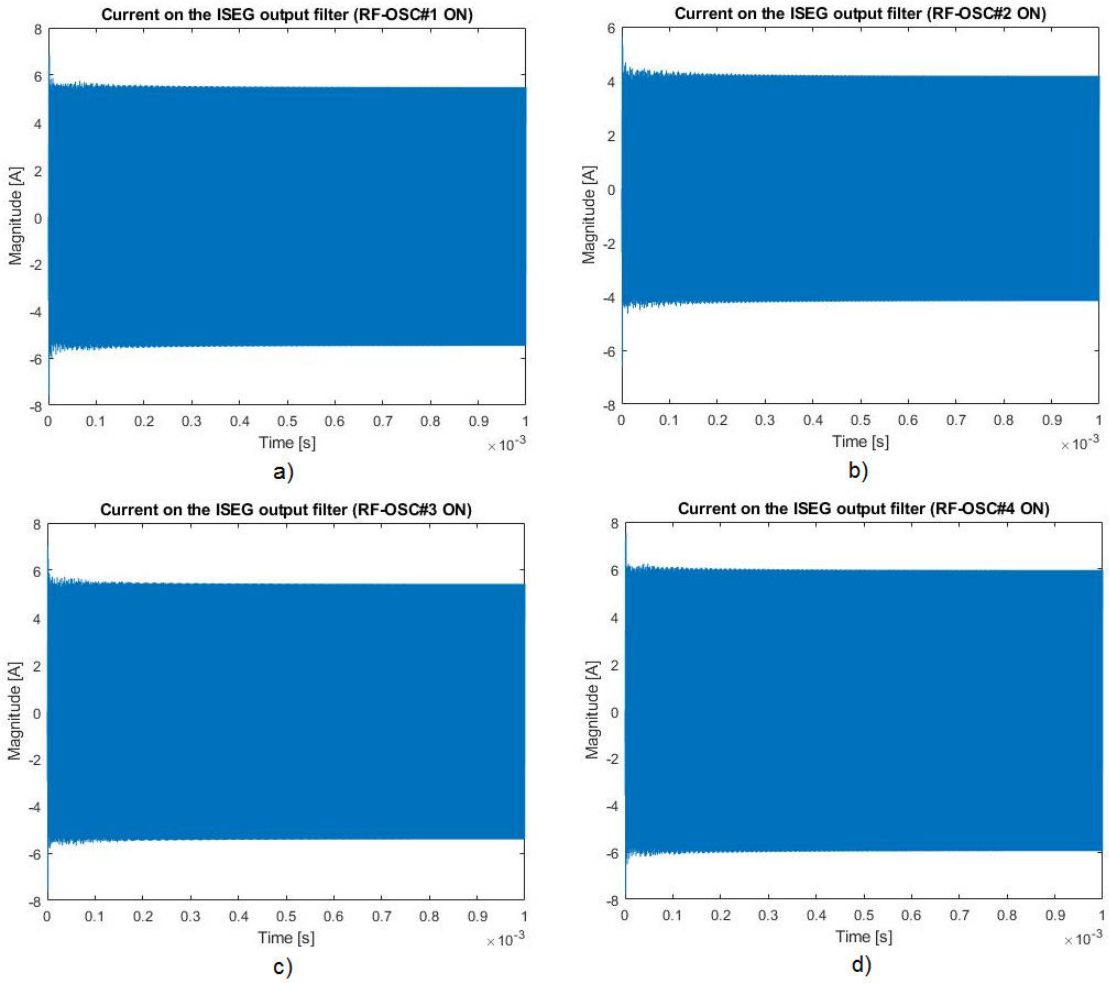

Figure 5. 13 *Current on the ISEG output filter with RF-OSC #1 ON, others OFF (a), RF-OSC #2 ON, others OFF (b), RF-OSC #3 ON, others OFF (c) and RF-OSC #4 ON, others OFF (d)*

Each of the four plots of I_{ISEG} represents a sinusoidal waveform oscillating at the specific frequency imposed for each RF-OSC. Furthermore it is possible to observe that the initial transient is quite short in each operating condition and it ends in about 0.3 ms. The features of the resulting waveform of each simulation, in steady state, are the following:

a) RF-OSC#1 ON: sinusoidal waveform oscillating at 0.975 MHz, which corresponds to a period of 1.03 μs, and with an amplitude of 5.49 A;

b) RF-OSC #2 ON: sinusoidal waveform oscillating at 0.985 MHz, which corresponds to a period of 1.015μs, and with an amplitude of 4.18 A;

c) RF-OSC #3 ON: sinusoidal waveform oscillating at 0.965 MHz, which corresponds to a period of 1.04 μs, and with an amplitude of 5.42 A;

d) RF-OSC #4 ON: sinusoidal waveform oscillating at 0.979 MHz, which corresponds to a period of 1.02 μs, and with an amplitude of 5.96 A.

In order to identify the frequency spectrum components of each waveform obtained from the simulation, it is possible to estimate the Discrete Fourier Transform (DFT) (in the form of Fast Fourier Transform (FFT)) [28] of the I_{ISEG} signal in steady state condition. What is expected, for each condition, is to obtain a single harmonic which corresponds to the operating frequency imposed to each RF-OSC. Figure 5. 14 shows the spectrum of the signal obtained for each of the four conditions.

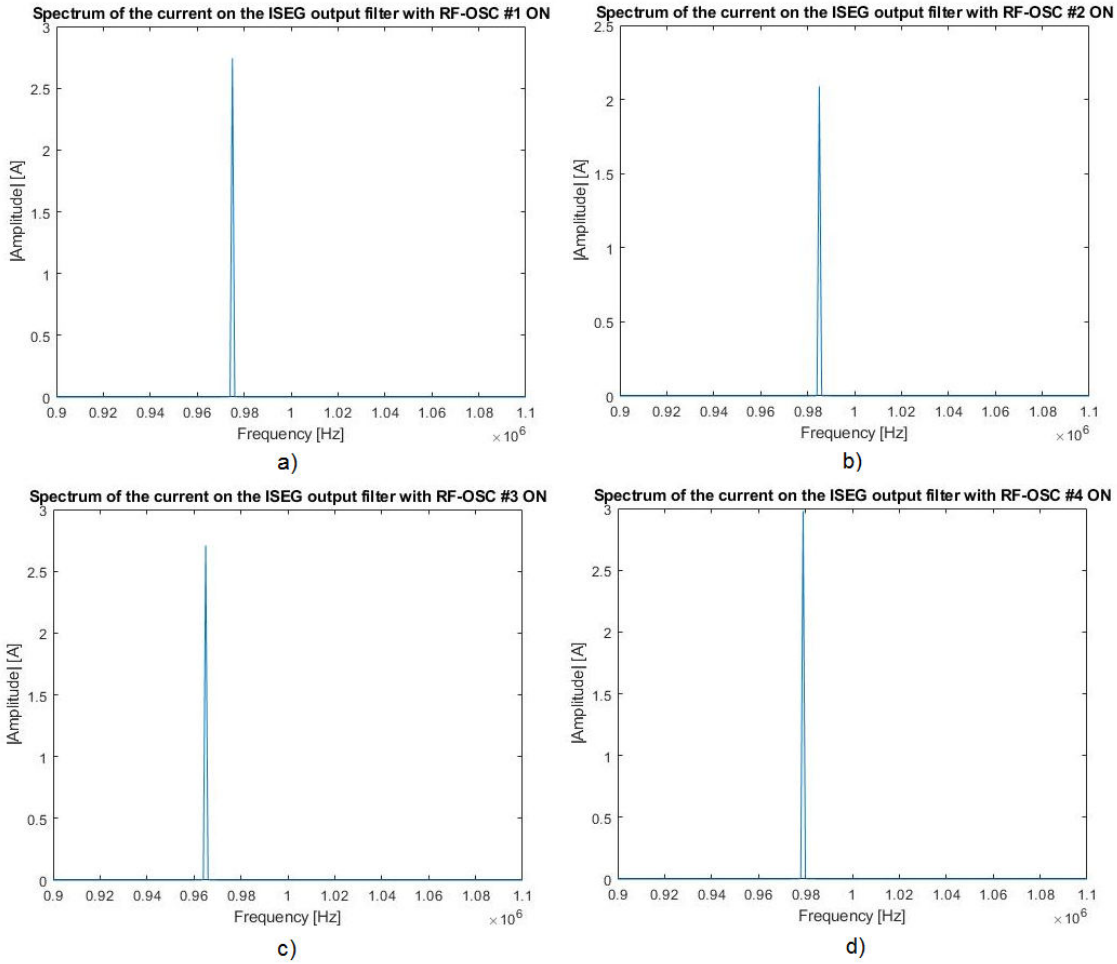

Figure 5. 14 *Spectrum of the current on the ISEG output filter with RF-OSC #1 ON (a), RF-OSC #2 ON (b), RF-OSC #3 ON (c), RF-OSC #4 ON (d)*

The result corresponds to the foreseen one: with RF-OSC #1 ON there is only the harmonic at 0.975 MHz, with RF-OSC #2 ON the harmonic at 0.985 MHz, with RF-OSC #3 ON the harmonic at 0.965 MHz and with RF-OSC #4 ON the harmonic at 0.979 MHz.

Furthermore, for each of the four conditions, a time range is identified after the initial transient where the waveforms reach the steady state, and the RMS value of I_{ISEG} has been estimated. The results are shown in Table 5. 5.

Table 5. 5 *RMS value of the current on the ISEG output filter for each of the four RF-OSC conditions*

RF-OSC ON	RMS current value on the ISEG output filter [A]
RF-OSC#1	3.88
RF-OSC#2	2.95
RF-OSC#3	3.83
RF-OSC#4	4.21
RF-OSC#1-#2-#3-#4	7.56

It is possible to highlight that the current on the ISEG output filter is particularly high, reaching ~4.2 A when RF-OSC #4 is ON. The I_{ISEG} RMS value limit, in order to prevent overheating on the passive components of the ISEG output filter, is in the order of 500 mA which is far from the values obtained in the simulation.

At this point it is possible to evaluate the evolution of the current on the ISEG output filter over time with the combined operation of the four RF-OSC together at their minimum ρ frequency, at full power. Figure 5. 15 shows the waveform obtained through the simulation.

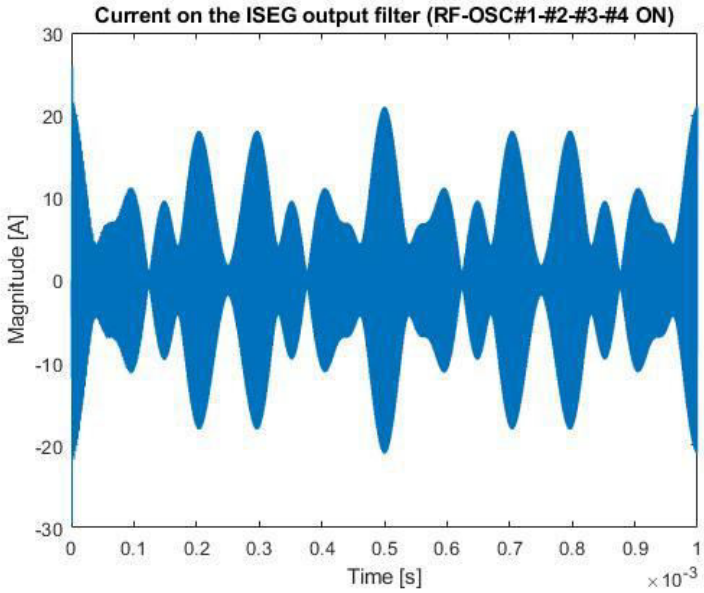

Figure 5. 15 *Evolution of the current on the ISEG output filter when all the RF-OSC are operating at the same time*

In order to prove the presence of the four harmonics corresponding to the four frequencies imposed by the RF-OSCs, it has been estimated the FFT of the I_{ISEG} signal. The spectrum of the signal is shown in Figure 5. 16 and it is interesting to note the greatest contribute is due to the harmonic related to the frequency of the RF-OSC #4 (0.979 MHz).

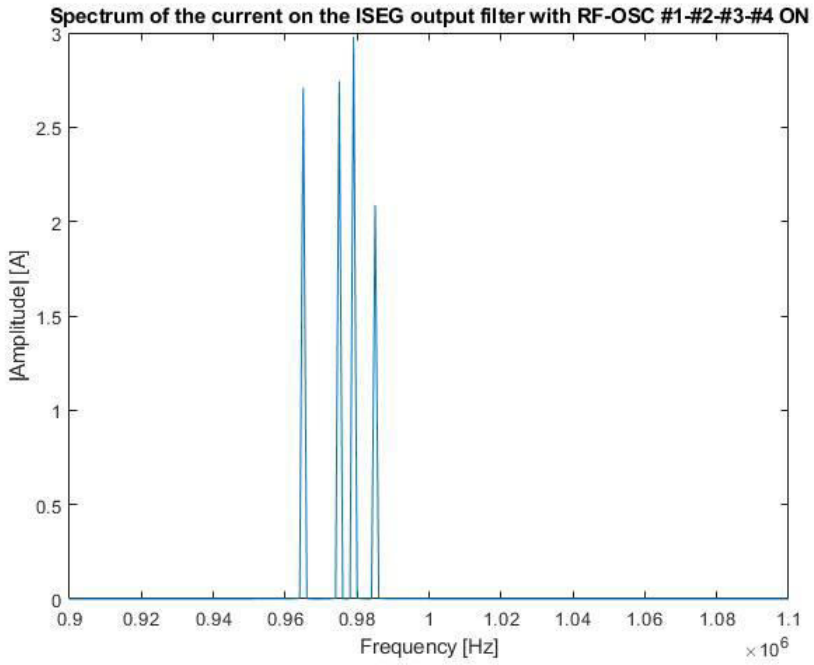

Figure 5. 16 *Spectrum of the current on the ISEG output filter when all the RF-OSC are operating at the same time*

The I_{ISEG} RMS value, in this operating condition, results in ~7.6 A, at ~1 MHz. This is the worst case and it represents a critical condition for the passive components of the ISEG output filter. This is further evidence that the present configuration of the RF circuit with the CVD downstream the output transformer of each RF-OSC it is not the right solution. Currently several alternative solutions are being investigated in order to mitigate the effects of these currents, essentially focusing on the typology of voltage divider and on its positioning, as described in 3.3.2 (these analyses have been focused on the CVD since it is an accessible component of the circuit). All the foreseen solutions have the aim to increase the impedance of the RF CM current circuit. Between them, moving the CVD on the primary side of the output transformer of the RF-OSC has provided great results, preserving the functionality of the CVD.

6 Study of the solid-state amplifier solution for the SPIDER ion source

The exploitation of the self-excited oscillator technology, as the RF power supply of SPIDER, shows several issues related to the operation of the overall system of the NBI. The occurrence of the frequency flip phenomenon (see 3.2.1) prevents from reaching the optimal matching condition and affects the maximum power level delivered to the RF load. The RF-OSC output power measurements are not reliable (see 3.3.1) due to the introduction of a systematic error on the phase shift between the TA and the CVD output signals which varies with frequency. Then, the circulation of RF common mode currents from the ion source to the CVDs (see 0) overwhelms noise to the useful signal of the diagnostic devices and overheats the passive components of the ISEG output filter. To these issues related to the operation of SPIDER follows the risk of obsolescence of the self-excited oscillator technology, thus adding the further issue of future procurements and replacements of high power tubes components. It is precisely in this context that the idea of substituting the tetrode based oscillators with solid-state amplifiers, as the power supply for the RF negative ion source of NBI, will be a fundamental step in order to reduce and, if possible, eliminate the issues related to the self-excited oscillators technology, thus allowing improvements in the operation of the overall NBI system. For this reason, in the last few years several efforts have been devoted to the study of possible implementation of solid-state amplifiers in the community of high power ion sources similar to SPIDER have already been tested with beneficial results. The verification of the feasibility and applicability of this technology would be crucial for SPIDER operation, and then for ITER. In addition, it would become the baseline technology for future experimental fusion power plants, i.e. DTT and DEMO. The goal of this chapter is to provide a conceptual design of a solid-state RF amplifier meeting the requirements of SPIDER, and a subsequent analysis of the effects of its integration on the ISEPS system.

6.1 RF generator requirements

Following the reference scheme of Figure 2. 8, the plasma source requires four different feeding RF circuits for the production of plasma within its 8 drivers. Hence, each RF circuit requires a dedicated RF generator rated for delivering the required power to the RF load. In the analysis, for each of the four solid-state RF amplifiers, the same requirements of the RF oscillator regarding the output power, the control and the measurements (see Table 3. 1) signals, have been assumed. The requirements of the RF amplifier are summarized in Table 6. 1.

Table 6. 1 *Requirements of the solid-state RF amplifier*

Frequency range	0.9 - 1.1 MHz
Frequency accuracy	± 1 kHz
RF harmonic distortion	< 1 % at full power on 50 Ω
Rated output power	20 - 200 kW on 50 Ω
Power control accuracy	1 % of rated power
Output voltage accuracy	± 1% of rated voltage
Output current accuracy	± 1% of rated current

6.2 Design of the solid-state RF amplifier

For the solid-state RF amplifier module it has been decided to employ an H-bridge, Class D voltage-switching[5] topology module with MOSFETs (Metal-Oxide-Semiconductor Field-Effect Transistor) as switching devices (the general scheme is shown in Figure 6. 1[29]). The module is fed by a proper DC voltage source in order to provide the required power to the load.

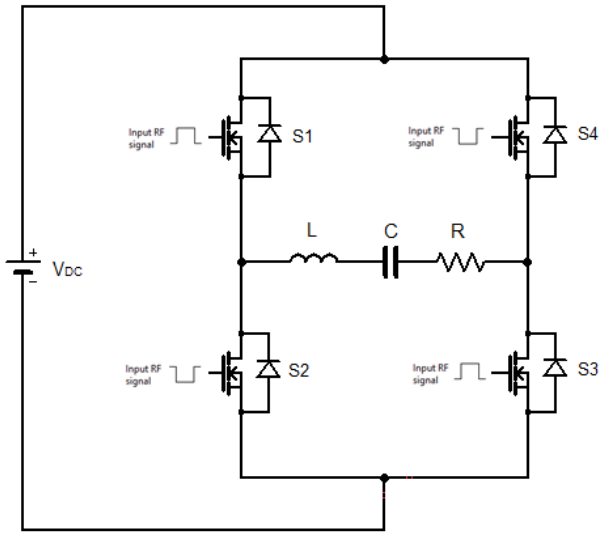

Figure 6. 1 *General scheme of an H-bridge class D power amplifier*

In a Class D amplifier topology, differently from the linear amplifier topology (Class A, B, C, AB) where the active devices are operated in their active region, the active devices are operated as switches, thus they are alternatively switched either completely ON or completely OFF. The linear amplifiers are distinguished through their *conduction angle*, $2\vartheta_c$ [30], which corresponds to the fraction of the period the active device spends in its active region during an RF cycle:

- Class A RF amplifier: $2\vartheta_c$ is equal to 360° (the active device is in its active region for all the RF cycle);
- Class B RF amplifier: $2\vartheta_c$ is equal to 180°;
- Class AB RF amplifier: $180° < 2\vartheta_c < 360°$;
- Class C RF amplifier: $2\vartheta_c < 180°$.

Since a switching device is not required to operate in its active region, a Class D power amplifier has lower power losses, allowing to reach an overall efficiency (η) > 90% (the theoretical efficiency of several amplifier classes are shown in Figure 6. 2).

[5] A Class D voltage-switching power amplifier is a Class D RF power amplifier which is fed by a DC voltage source, which is distinguished from a Class D current-switching power amplifier which is fed by a DC current source (not analyzed in this thesis work).

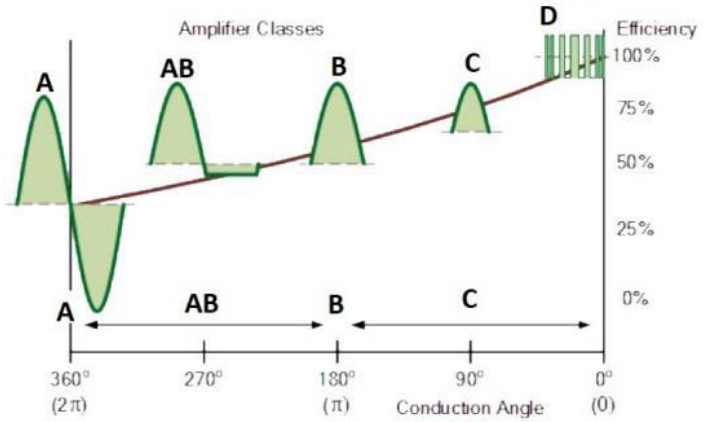

Figure 6. 2 *Theoretical efficiencies of several amplifier classes* [31]

The solid-state RF amplifiers required to be implemented in SPIDER are rated for delivering 200 kW on a resistive impedance of 50 Ω, at 1 ± 0.1 MHz. The conceptual design of the RF amplifier (ISRF-AMP), in order to deliver the rated output power to the load, foresees to implement a modular scheme by splitting the total RF power among several solid state low power amplifier modules. The frequency of the output signal must be equal to the switching frequency with which the switching devices are driven. For this reason they must be rated for operating at switching frequencies in the order of 1 MHz. As it is shown in Figure 6. 3, MOSFETs have the highest switching speed compared to the others semiconductor power devices, being compliant with the required switching frequency of the system, but their power performances are the lowest [32]. However, considering a modular design for the ISRF-AMP, this problem can be manage since each module has to deal with low power (in the order of $1 \div 2$ kW). Following these considerations, this modular concept employing a MOSFET bridge has been adopted for the conceptual design of the RF amplifier for SPIDER. This is a common design for the RF power amplifiers and it has been also adopted for the 200 kW solid-state RF amplifier prototype which has been developed by ITER-India [33].

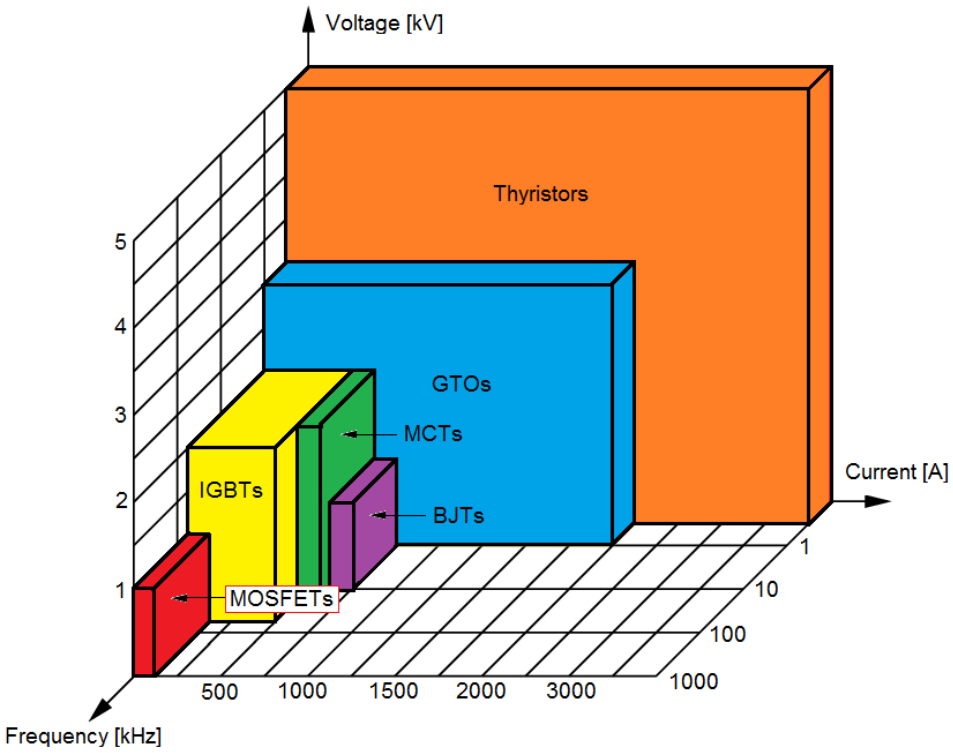

Figure 6. 3 *Performances of the semiconductor power devices*

The circuit symbol of a n-MOSFET is represented in Figure 6. 4.

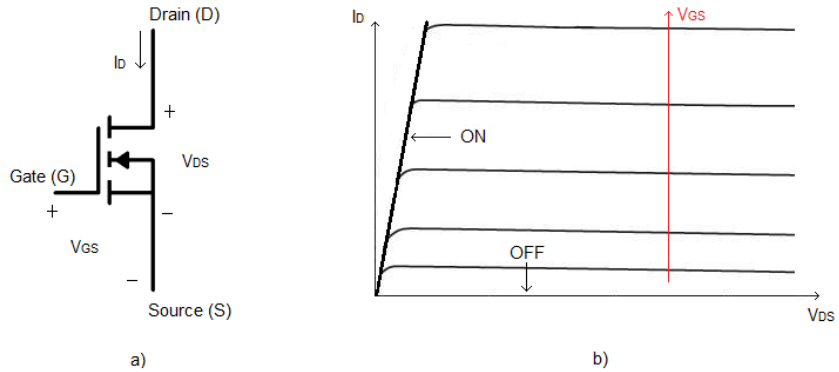

Figure 6. 4 *Circuit symbol of an n-MOSFET (a) and i-v characteristics (b)*

It is a voltage-controlled device characterized by three terminals: the *Gate* (G), the control terminal, and the *Drain* (D) and the *Source* (S), the power terminals. As it is shown in Figure 6. 4 [32], it acts like a completely ON switch when the voltage between the *Gate* and the *Source* (V_{GS}) overcomes the treshold value of V_{GS} (V_{GSth}), which is typical for the design of the specific component, and the voltage between D and S (V_{DS}) is positive. Hence, the transition between ON and OFF state must be produced by an adequate driving circuit. The ON-resistance of the device, between the Drain and Source terminals (r_{DS}), is proportional to V_{DSS} ,the maximum voltage that can be applied across Drain and Source when the

MOSFET is in OFF state ($r_{DS} \propto {V_{DSS}}^{2.5\div2.7}$) [32]. For this reason, the lower is V_{DSS}, the lower is r_{DS} and then the ON-losses.

6.2.1 Generation of the MOSFETs control signal

Figure 6. 5, highlights the driving circuit of the MOSFETs focusing on a single H-bridge amplifier module.

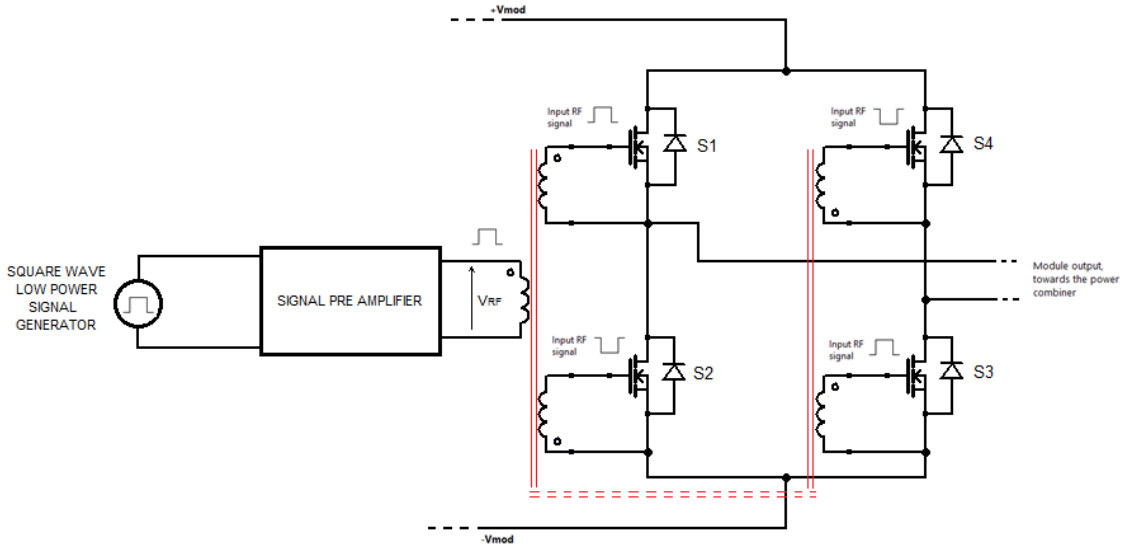

Figure 6. 5 *Driving circuit of the MOSFETs of the H-bridge, Class D RF power amplifier modules (focus on a single amplifier module)*

For the design of SPIDER RF amplifier, a voltage square waveform is used in order to drive the MOSFETs of the module. The driving voltage signal is produced by a square wave low power signal generator. The square waveform could be obtained through a Pulse Width Modulation technique (PWM) which consists of comparing a repetitive signal (for example a saw-tooth signal) to a control signal. The principle behind the PWM technique is described in Figure 6. 6: when the control signal is higher than the saw-tooth one, the resulting signal is high, otherwise it is low. In this case, in order to obtain the desired output square waveform for controlling the MOSFETs of the amplifier modules, the control signal has been kept constant, in order to have a duty cycle equal to 50%. The duty cycle is the ratio between the ON-time (t_{ON}) and the overall switching period (T_S).

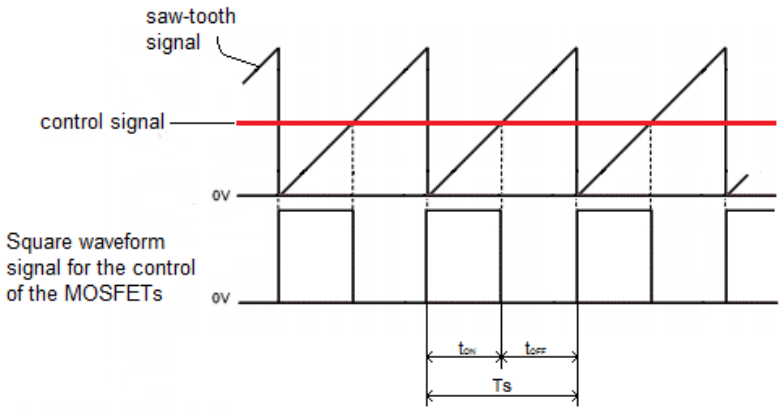

Figure 6. 6 *Square waveform generation with PWM (duty cycle equal to 50%)*

It is important to highlight that the switching frequency (f_S) of the MOSFETs is imposed by the square waveform and it is equal to the saw-tooth signal one. For this reason the saw-tooth signal must be produced at 1 MHz. The resulting low power square waveform signal is then amplified by a pre-amplifier stage in order to reach a voltage value (V_{RF}) able to trigger the MOSFET switching ($V_{RF} > V_{GSth}$). In order to apply the resulting signal to all the amplifier modules, an adequate driving circuit has been introduced downstream the pre-amplifier stage. It can be represented by a single-primary multi-secondary transformer which distributes the square waveform signal to all the amplifier modules. Hence, each signal is used for driving the four MOSFETs of each H-bridge amplifier module.

6.2.2 Operating principle of the RF amplifier module

For the operation of the H-bridge Class D amplifier module, a sort of bipolar PWM, where the MOSFETs are driven in pairs (S1, S3 and S2, S4), has been implemented: when a pair is in ON-state, the other one is in OFF-state and vice versa. What is important is that the two MOSFETs on the same leg of the amplifier module must not be ON at the same time in order to prevent shoot-through. For this reason, within the switching transition, a specific *dead time* during which both the two MOSFETs are OFF shall be foreseen. When S1, S3 are ON and S2, S4 are OFF, the voltage at the output of the module is equal to $+V_{mod}$, while when S1, S3 are OFF and S2, S4 are ON, it is equal to $-V_{mod}$. In order to properly trigger the MOSFETs, as it is shown in Figure 6. 5, the secondary windings of the splitter related to the MOSFETs on the same leg (S1, S2 and S3, S4) are opposite polarized while S1, S3 and S2, S4 are equally polarized. Thanks to this choice, when V_{RF} is at high potential for S1 and S3, it is at low potential for S2 and S4, thus S1 and S3 are triggered ON while S2 and S4 are kept OFF. The opposite happens on the second half of the period of the voltage square waveform, when V_{RF} is at high potential for S2 and S4 and at low potential for S1 and S3. With this solution, the resulting voltage at the output of the module is a square waveform ranging from $+V_{mod}$ to $-V_{mod}$ at f_s.

6.2.3 Output stage of the RF amplifier

In order to deliver the rated power to the RF load, a combiner at the output of the RF power amplifier modules has been foreseen. The combiner[6], which is shown in Figure 6. 7, is a multi-primary single-

[6]Combiners and splitters (the complementary devices of the combiners) are fundamental components for modular solution and they are commonly used for high power modular solid-state RF amplifier solutions (see for example [33] and [34]).

secondary transformer able to add the output power of the RF amplifier modules in order to provide the required power at the output of the ISRF-AMP.

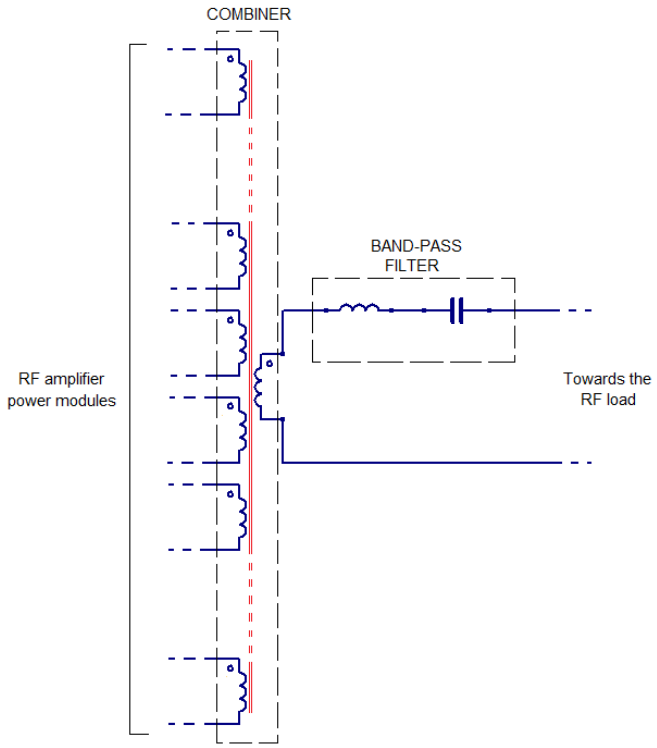

Figure 6. 7 *Output stage of the RF amplifier: power combiner and band-pass filter*

Downstream the combiner, the resulting power signal is still represented by a square waveform and for this reason it must be properly filtered in order to obtain a sinusoidal waveform towards the RF load. Since SPIDER operating frequency range is 1 ± 0.1 MHz, a properly designed band-pass filter is required. In the analysis, it has been considered a simple series RLC band-pass filter. Considering the cutting frequencies at -3 dB equal to f_M = 1.2 MHz (upper frequency) and f_m = 0.8 MHz (bottom frequency), the *Bandwidth* (B) for the tuning of the filter is equal to B = 0.4 MHz. B can be expressed as

$$B = \frac{f_0}{Q}$$

where f_0 is the *central frequency* of the bandwidth (corresponding to the resonance frequency), which can be approximate through the arithmetic mean of f_M and f_m as

$$f_0 = \frac{f_M + f_m}{2} = \frac{1.2 \times 10^6 + 0.8 \times 10^6}{2} = 1\ MHz$$

and Q is the *quality factor*, which is a dimensionless index of the selectivity of the filter: higher is Q and higher is the selectivity of the filter. By rearranging the equation, it is possible to derive the value of Q as

$$Q = \frac{f_0}{B} = \frac{1 \times 10^6}{0.4 \times 10^6} \approx 2.5.$$

The Q factor can be also expressed as

$$Q = \frac{\omega_0 L}{R} = \frac{1}{\omega_0 RC}$$

where $\omega_0 = 2\pi f_0$ and R, in this case, is equal to 50 Ω. At this point, it is possible to derive the required values of the inductance and capacitance of the band-pass filter as

$$L = \frac{QR}{2\pi f_0} \approx 20\ \mu H$$

$$C = \frac{1}{2\pi f_0 RQ} \approx 1273\ pF$$

Figure 6. 7 shows the resulting output stage of the RF amplifier.

6.2.4 Estimation of the ratings of the RF amplifier module

In order to provide the rated 200 kW on a resistive impedance of 50 Ω, each amplifier module has been foreseen for delivering 1.1 kW (this choice has been realized considering the ratings of the modules of the RF amplifiers on the market, such as TRAM 50 [35]). With this solution, an overall of $\frac{200\ kW}{1.1\ kW} \approx 180$ amplifier modules are required. Starting from the equation of the output active power of an H-bridge Class D power amplifier, for $f = f_0$, which can be derived from [29] as,

$$P_{out} \approx \frac{8{V_{mod}}^2}{\pi^2 R}$$

where$R$ is equal to the rated resistive impedance of the load (50 Ω) (this assumption has been realized on the basis of the analysis realized in [33]). It is possible to estimate the DC power supply voltage of the module (V_{mod}) as

$$V_{mod} = \sqrt{\frac{P_{out}\pi^2 R}{8}}.$$

Considering the foreseen output power of 1.1 kW, it is possible to obtain

$$V_{mod} = \sqrt{\frac{1100 \cdot \pi^2 \cdot 50}{8}} \approx 260\ V.$$

This is a key parameter in the dimensioning of the power amplifier module since each MOSFET of the H-bridge, when in OFF-state, has to withstand the overall V_{mod} between its *Drain* and *Source* terminals. For example a MOSFET rated for V_{DS} = 500 V could be a good candidate, but further verification shall be realized in terms of conduction resistance (r_{DS}), drain current (I_D), input capacitance (C_{ISS}), etc.

6.2.4.1.1 Verification of the ratings of the RF amplifier module

For the verification of the ratings of the RF amplifier module, a simple circuital model has been developed through MATLAB Simulink. The features of the model, following the results of the previous paragraphs are summarized in Table 6. 2.

Table 6. 2 *Parameters for the simulation of the RF amplifier module*

Frequency range	0.9 - 1.1 MHz
DC power supply	260 V
L band-pass filter	20 µH
C band-pass filter	1273 pF
Equivalent resistive load	50 Ω
Switching component	MOSFET

The electrical scheme implemented for the simulation is the same of Figure 6. 1, with just one single module feeding the 50 Ω resistive load, series connected to the band-pass filter defined in 6.2.3. For the simulation, it has been considered the default parameters of the MOSFET block provided by Simulink (the ON resistance is equal to 130 mΩ). The driving circuit of the MOSFETs has been realized through a pulse generator with a frequency of 1 MHz and a duty cycle of 50%. Figure 6. 8 shows the resulting current across the MOSFETs, the voltage across the MOSFETs and the voltage at the output of the H-bridge, focusing on steady state condition.

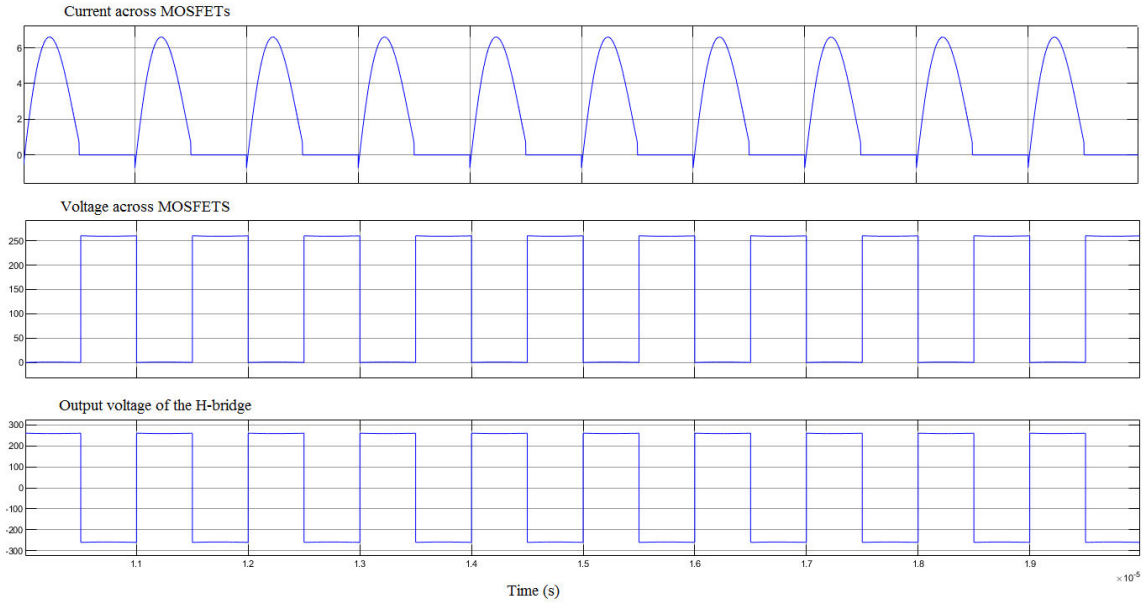

Figure 6. 8 *Current across the MOSFETS (upper plot), voltage across the MOSFETs (medium plot) and output voltage of the H-bridge (bottom plot) for a switching frequency of 1 MHz, in steady state condition*

Figure 6. 9 shows the voltage, current and active power on the 50 Ω load (R).

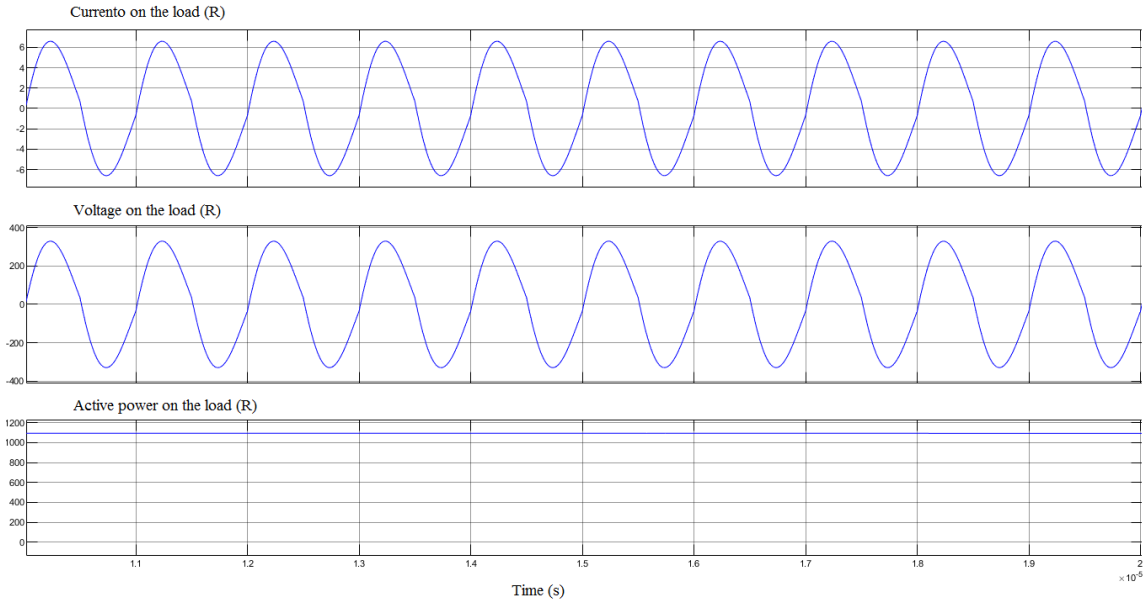

Figure 6. 9 *Current (upper plot), voltage (medium plot) and active power (bottom plot) on the 50 Ω load*

It is possible to observe that the simulation verifies the results of 6.2.4 by providing an output active power on the 50 Ω load of about 1100 W. Furthermore, it is possible to observe that the band-pass filter (see 6.2.3) cuts the harmonic components of the voltage square waveform, exiting the H-bridge, which are external to the operating frequency range. This filtering effect produces a sinusoidal voltage and current waveforms on the load, with a certain amount of distortion. Finally, it is interesting to notice also that the current across the MOSFETS, when the MOSFET is switched from ON-state to OFF-state, is not equal to zero. This is due to the effect of the inductance of the filter which delays the current decrease. Moreover, during the transition from OFF-state to ON-state, for a short time interval, the current across the MOSFET is negative. Even in this case this is due to the inductance of the filter which prevents the negative current from reaching the zero value before the MOSFET is switched ON. In this case, since the MOSFET is not able to conduct negative current, the conduction is provided by the anti-parallel diode of the MOSFET. Once the current becomes positive, it starts flowing through the MOSFET.

6.2.5 RF amplifier power supply

In order to provide the 260 V DC to each RF amplifier module, a proper power supply system is required. Referring to the ISEPS electrical scheme of Figure 2. 8, the three-phase AC power supply is derived from the 6.6 kV bar, as for the actual RF-OSC solution, and then it must be rectified in order to obtain the required DC voltage. The rectification stage required for the RF amplifiers solution is different from the oscillator's one: each oscillator is fed by an AC/DC modular converter rated for delivering 12 kV DC (ISRF-TE) (see 3.1.1); each RF amplifier module requires only 260 V DC. For this reason a three-phase diode rectifier [32] for one AC/DC conversion and a step-down DC/DC converter (Buck converter) [32] have been foreseen feeding all the RF modules. Assuming an efficiency of the overall RF amplifier of about 90% (η_{AMP}) (on the basis of Figure 6. 2) and considering the rated output power of the RF amplifier (P_{outAMP} = 200 kW), it is possible to have an estimation of the output power of the Buck converter (P_{DC}), which is approximately equal to

$$P_{DC} = \frac{P_{outAMP}}{\eta_{AMP}} = \frac{200000}{0.9} \approx 220\ kW.$$

At this point, by assuming an efficiency of the Buck converter of about 85% (η_{Buck}) (this value has been assumed on the basis of the efficiency values of [36]) it is possible to derive an estimate of the output power of the three-phase diode rectifier (P_{Diode}), thus obtaining

$$P_{Diode} = \frac{P_{DC}}{\eta_{Buck}} = \frac{220000}{0.85} \approx 260\ kW.$$

Finally by assuming an input power factor[7] of the three-phase rectifier equal to 90% (PF) (this value has been defined on the basis of the information derived from [32]), it is possible to define the rated power of the three-phase transformer (S_{transf}) as

$$S_{transf} = \frac{P_{Diode}}{PF} = \frac{260000}{0.9} \approx 290\ kVA.$$

Following these considerations, for the power supply of the RF amplifier, a 6.6 kV/210 V, 300 kVA three-phase, three-windings transformer (Y-Δ) has been assumed. The choice of a three-windings transformer has been foreseen in order to reduce the harmonic content by realizing a 12 pulse rectifier [32].

6.2.6 Control system of the RF amplifier

In order to ensure a proper operation of the RF amplifier, it has been foreseen an adequate control system of the output power and frequency. It consists of: a negative feedback active power control loop and an open loop frequency control.

6.2.6.1 Negative feedback active power control loop

The output power of the RF amplifier, must be properly controlled in order to face the impedance variation of the RF load due to the effect of plasma and a negative feedback power control approach is provided. The block diagram of the output power control is shown in Figure 6. 10.

[7]The power factor (PF) is a dimensionless index, ranging between -1 and 1, equal to the ratio between the active power (P) and the apparent power (S):

$$PF = \frac{P}{S}.$$

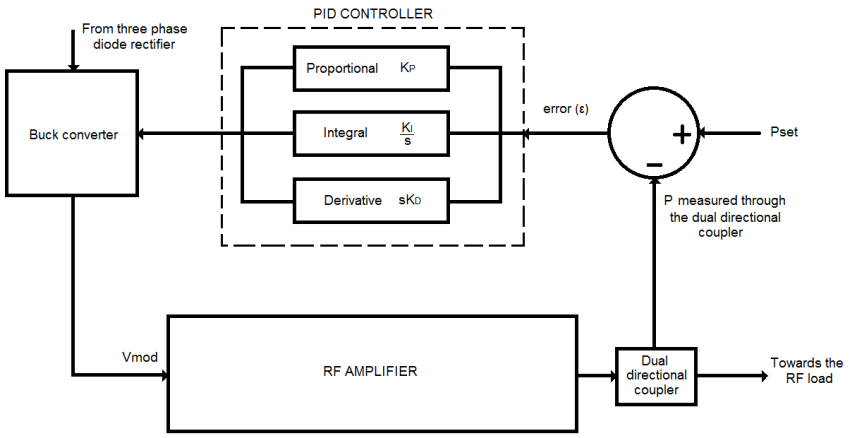

Figure 6. 10 *Negative feedback active power control loop*

A key element of the scheme is a dual directional coupler installed downstream (the output filter of) the RF amplifier. It measures both the forward and reflected power at this port (the features of the dual directional coupler are described in Appendix C). By comparing the measured output power to a reference value, it is possible to obtain an error signal which is applied to a PID controller. The PID (Proportional-Integral-Derivative) acts in order to correct the error (ε) until it reaches the zero value. This effect can be obtained by properly tuning the PID by changing the gain of its three terms: Proportional term (K_P), Integral term (K_I) and derivative term (K_D). The proportional term provide an overall control action proportional to the error, the integral term allows reducing steady-state errors through low-frequency compensation and the derivative term improves transient response through high-frequency compensation [37]. Once the PID is properly tuned, it automatically acts for providing at its output the adequate reference for the Buck converter in order to change its duty cycle and then the DC voltage applied to the RF amplifier modules (V_{mod}). By changing V_{mod}, the output power of the RF amplifier changes (see 6.2.4).

6.2.6.2 Open loop frequency control

The RF amplifier, differently from the RF-OSC, is not affect by frequency instabilities during operation and for this reason it does not require a negative feedback frequency control loop. For this reason the output frequency of the RF amplifier, which is equal to the switching frequency of the MOSFETs of the H-bridge of each module, is controlled in open loop with the f_{set} signal. The output frequency is changed by changing the frequency of the saw-tooth signal of the PWM adopted for the generation of the driving signal of the MOSFETs of the RF power amplifier module (see 6.2.1). The block diagram of the open loop frequency control is shown in Figure 6. 11.

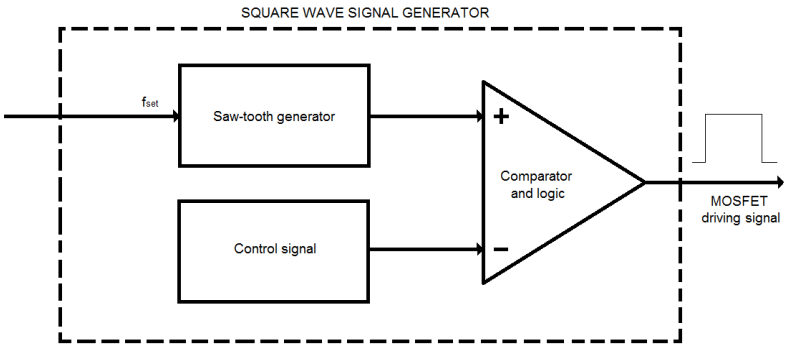

Figure 6. 11 *Open loop frequency control*

6.2.7 Block diagram of the RF amplifier and its integration within the HVD

Figure 6. 12 shows the conceptual block diagram which has been developed for the integration of the ISRF-AMP within the SPIDER HVD. The block diagram summarizes all the components and the systems which have been described in the previous paragraphs. In particular, different colors have been adopted for different systems: cyan for the RF system, green for the control system and red and black respectively for the MV AC power supply and LV power supply and purple for the DC power supply. The components of the block diagram are the following:

- 6.6 kV/210 V, 300 kVA three-phase three-windings transformer insulated for 12 kV DC (ISRFT);
- three-phase diode rectifier with an input power factor of 90% and a DC/DC converter (Buck converter) with an efficiency of 85%;
- RF amplifier rated for delivering 200 kW on a resistive impedance of 50 Ω, with an efficiency of 90% characterized by:
    - 180 power amplifier modules (H-bridge, Class D with MOSFETs as switching devices) rated for delivering 1.1 kW;
    - Square wave signal generator for the production of the driving signal of the MOSFETs of each module in the range of frequencies 0.9÷1.1 MHz;
    - Signal pre-amplifier;
    - Single primary, multi-secondary transformer for the distribution of the driving signal of the 4 MOSFETs of the H-bridge to each module (Driving circuit);
    - Combiner;
    - RLC series Band-pass filter tuned to 0.8÷1.2 MHz, with L = 20 μH, C = 1273 pF, R = 50 Ω;
    - Dual directional coupler for the output power measurement;

- Negative feedback active power control loop;
- Open loop frequency control.

In the block diagram also the auxiliary power supply has been included which is fed through a 6.6 kV/400 V three-phase transformer (ISGNT).

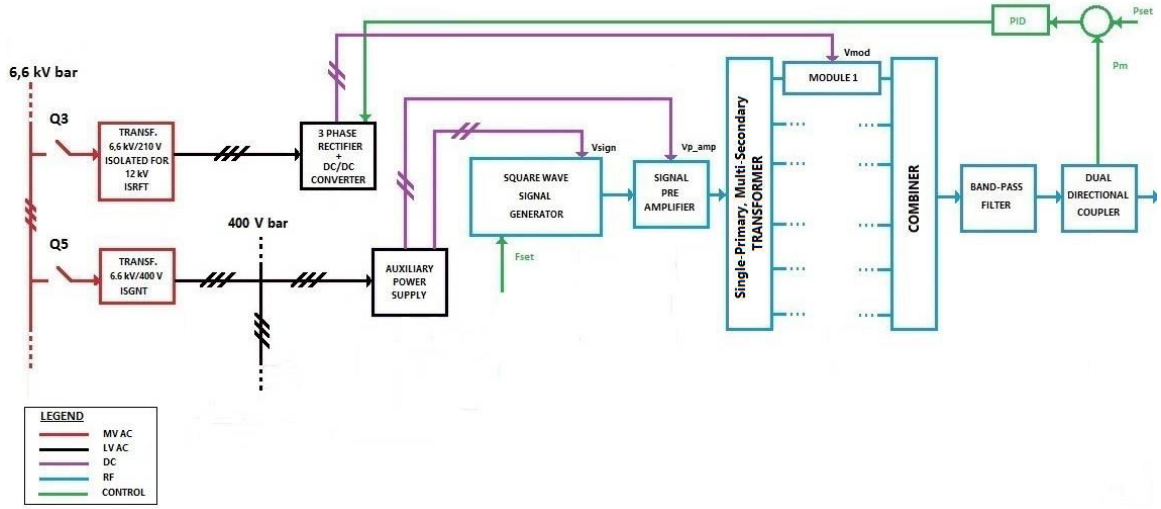

Figure 6. 12 *Block diagram of the RF amplifier*

6.3 Insulation of the RF amplifiers from the HVD potential

A crucial aspect in the study of the implementation of the RF amplifiers within the framework of SPIDER is the evaluation of their electrical insulation from the HVD, which is at the EG potential of -100 kV to ground. In fact since the RF load is locally referred to the ion source body potential which is (approximately) at the PG potential of -112 kV to ground, a local connection of the RF amplifier output to the HVD is not possible to allow the 12 kV DC (see 2.1.2.1) applied between PG and EG. The information and measurements about the operation of the amplifier, referred to the HVD, are collected and elaborated by the Control and Data Acquisition System (CODAS) through proper fiber optic connections.

The characterization of the RF amplifier insulation involves the RF amplifier output stage and the amplifier case to the HVD floor:

- as regards the insulation of the output stage of the RF amplifier from the HVD, the implementation of an insulating transformer downstream the RF amplifier has been foreseen in order to block the DC component coming from ISEG;
- the insulation of the case of the RF amplifier from the HVD can be ensure by mounting it on platform raised from the HVD floor and properly insulated through insulating beams.

The former solution has been neglected since it is easier to realize an insulating transformer on the 50 Hz side than on the RF side, as regards the power involved (need for the use of ferrites, higher power dissipation, etc.). In fact, the former solution is "conventional", while the latter should be properly developed.

The ISRF requires 4 different RF amplifiers for the supply of the eight driver of SPIDER. Each one of these must be insulated from the HVD on the 50 Hz mains power supply side through an adequate insulating transformer properly designed for sustaining the 12 kV DC. For this purpose, two different configurations have been taken into account in this analysis: the first one with an insulating transformer for each RF amplifier, the second one where a single insulating transformer feeds 4 (industrial) transformers each at the input of a RF amplifier. The selection of one solution over the other will be detailed in 6.4 since the effects of the RF common mode currents will be crucial in order to define the recommend configuration.

6.3.1 Single insulating transformer for each RF amplifier solution

Directly following the results of 6.2.5 and the block diagram of Figure 6. 12, this solution is designed to have four different 6.6 kV/210 V, 300 kVA three-phase, three-winding transformers to feed each RF amplifier (ISRF-AMP). These transformers must be insulated for 12 kV DC (ISRF-T) (see 6.3). In addition it has been introduced four 400 V/ 400 V transformers insulated for 12 kV DC (ISLCC-T) within the ISGN, from which are derived the power supply of the local control cubicle of the four ISRF-AMP (AMPL LCC). The configuration described above is portrayed in Figure 6. 13 and it has been realized thanks to AutoCAD Electrical [38] (the three-phase diode rectifier and the Buck converter are included within the RF amplifier and for this reason they are not represented in Figure 6. 13).

6.3.2 Single transformer for all RF amplifiers solution

This second solution foresees, for each circuit, a 400 V/210 V, 300 kVA three-phase, three-winding transformer feeding the three-phase diode rectifier which, in turn, feeds the Buck converter and then the ISRF-AMP. The LV/LV transformers of the four circuits of the ISRF are fed by a main 6.6 kV/400 V three-phase transformer insulated for 12 kV DC (ISRF-T), with a rated power of 1.2 MVA (4×300 kVA). Even in this case it has been adopted the same solution for the supply of the AMP LCC. The electrical scheme of this second solution proposed, which has been in turn realized through Autodesk Electrical, is shown in Figure 6. 14 (even in this case the three phase diode rectifier and the Buck converter of each circuit are not shown).

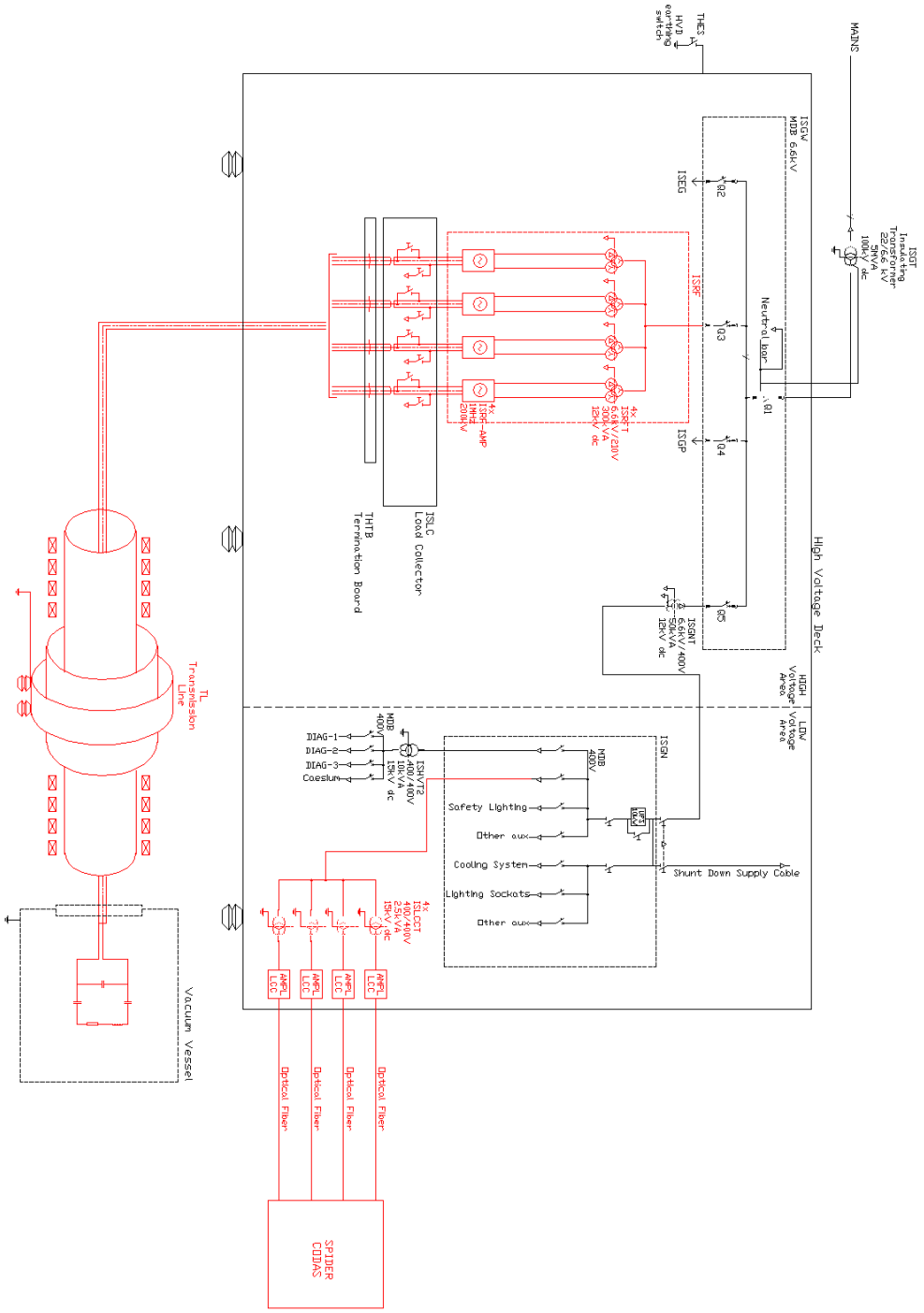

Figure 6. 13 *Electrical scheme of the "single insulating transformer for each RF amplifier configuration within ISEPS framework*

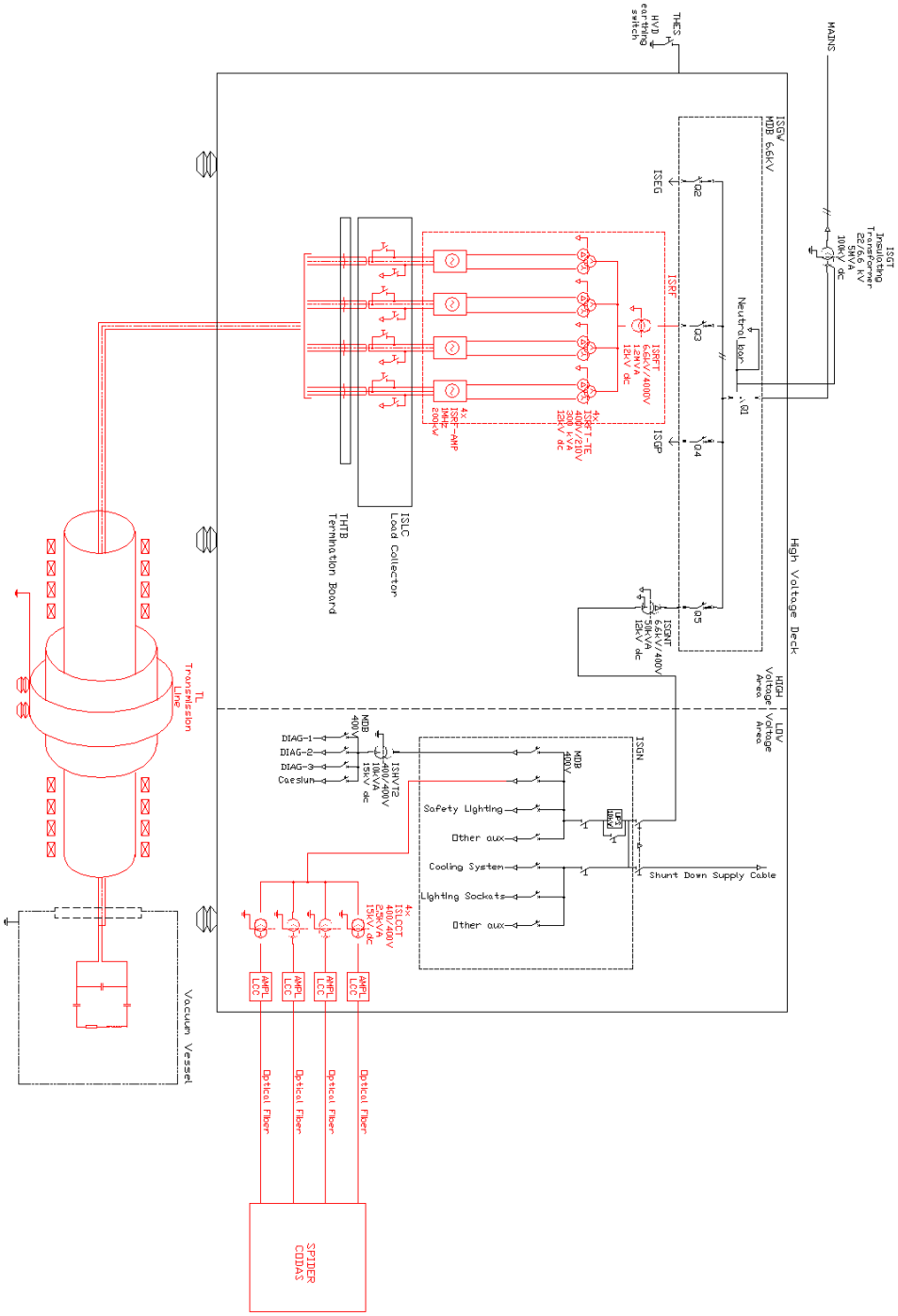

Figure 6. 14 *Electrical scheme of the "single transformer for all RF amplifiers configuration within ISEPS framework*

6.4 RF Common mode current analysis

The analysis of the RF CM current is the core of the study on the feasibility of the integration of a solid-state RF amplifiers solution within SPIDER system. In fact, the circulation of these currents is a critical issue for the actual oscillators solution and it is necessary to consider this aspect in the design of a proper solution with the amplifiers.

The analysis, starting from the same model of the RF load developed in chapter 5 (transmission line, matching network and drivers equivalent impedance), will be focused on the verification of the two configurations proposed in 6.3:

- Configuration 1#: single 6.6 kV/210 V three-phase, three-windings transformer for each RF amplifier solution (see 6.3.1);

- Configuration 2#: single 6.6 kV/400 V insulating transformer feeding four additional 400 V/210 V three-phase, three-winding transformers, one for each of the four RF amplifiers (see 6.3.2);

The RF CM current of these two configurations will be simulated both in frequency and time domain, following the simulation process adopted in chapter 5. The results of these two simulations will be compared to the oscillators one and to each other in order to define which of them is less affected by the RF CM current issue, thus choosing the optimal solution to be implemented in SPIDER.

6.4.1 Configuration #1: single MV/LV transformer for each RF amplifier

The electrical scheme for the simulation of Configuration #1 is represented in Figure 6. 15. The subcircuit TL1 represents the transmission line model shown in Figure 5. 3 and it has been considered the same asymmetry in the parameters of the antennas of the drivers, coupled with plasma, between the four RF circuits as in the analysis of the RF-OSC circuits in chapter 5 (see Table 5. 1).

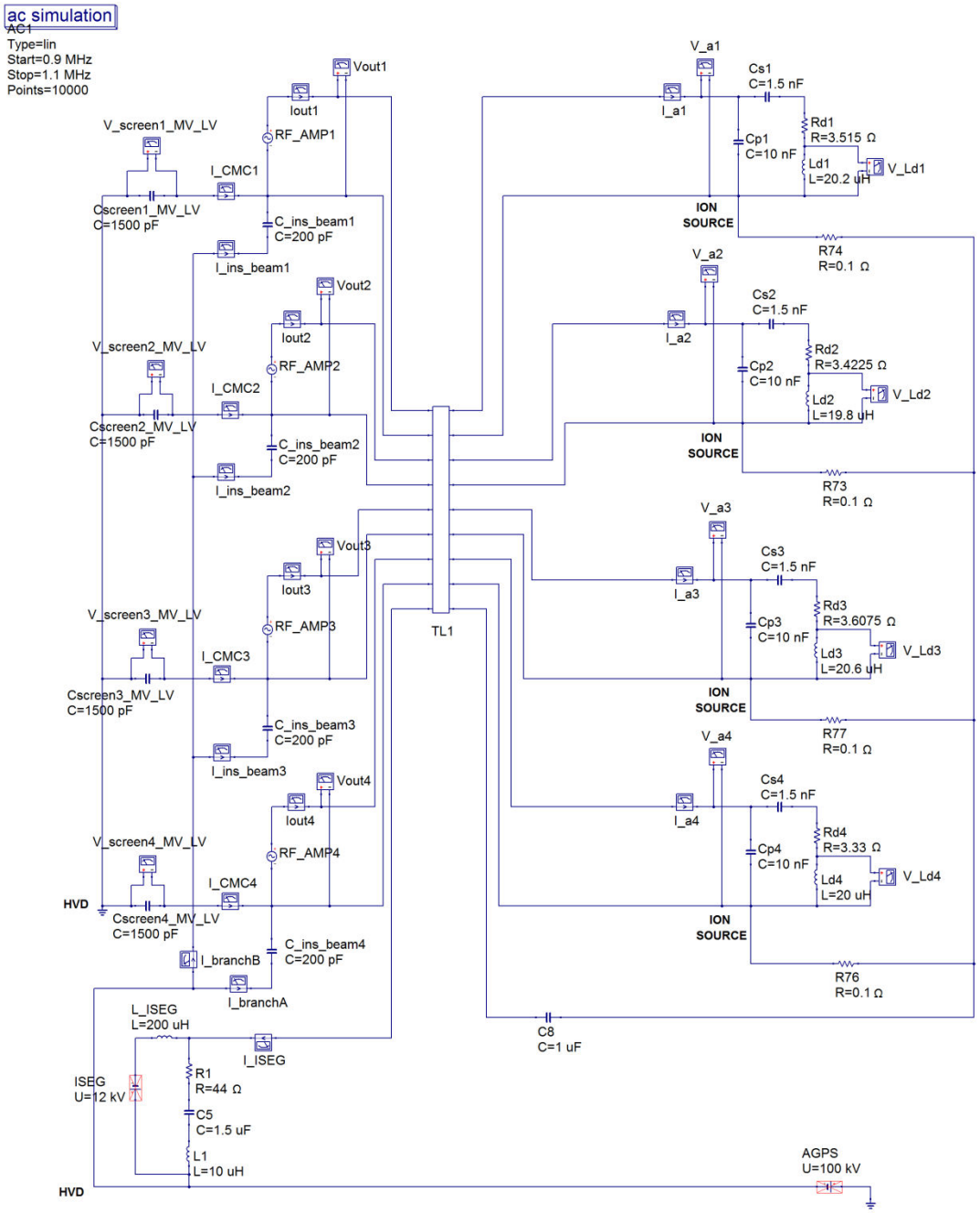

Figure 6. 15 *Electrical scheme for the analysis of the RF common mode current (Configuration #1)*

The RF-AMP has been simplified as an ideal voltage source. What changes, compared to the oscillators electrical scheme, is the power supply side, while the TL and the matching network and the antennas parameters of each RF circuit are exactly the same of Figure 5. 4 (also for the parameters of the output filter of ISEG are the same of Figure 5. 4). As aforementioned in 6.3, the amplifiers are mounted on insulating beams in order to be insulated from the HVD potential and they are insulated on the 50 Hz side through a MV/LV insulating transformer. These insulating solutions affect the system by introducing stray capacitances which, at the operating frequency of 1 ± 0.1 MHz, allow the circulation of RF CM current, as it is shown in Figure 6. 16. In particular these capacitances are the stray capacitances between the

insulating beams and the floor of the HVD, C_{ins}, and the stray capacitances between the screens of the 6.6 kV/210 V three-phases, three-windings transformers, $C_{stray_{MV/LV}}$, which have been estimated to be respectively 200 pF for each insulating beam and 1500 pF for each MV/LV transformer. The estimation of these values has been realized through geometric considerations and it is discussed in Appendix D. In the scheme reported in Figure 6. 15 the MV/LV transformers have been represented through the stray capacitance between their screens.

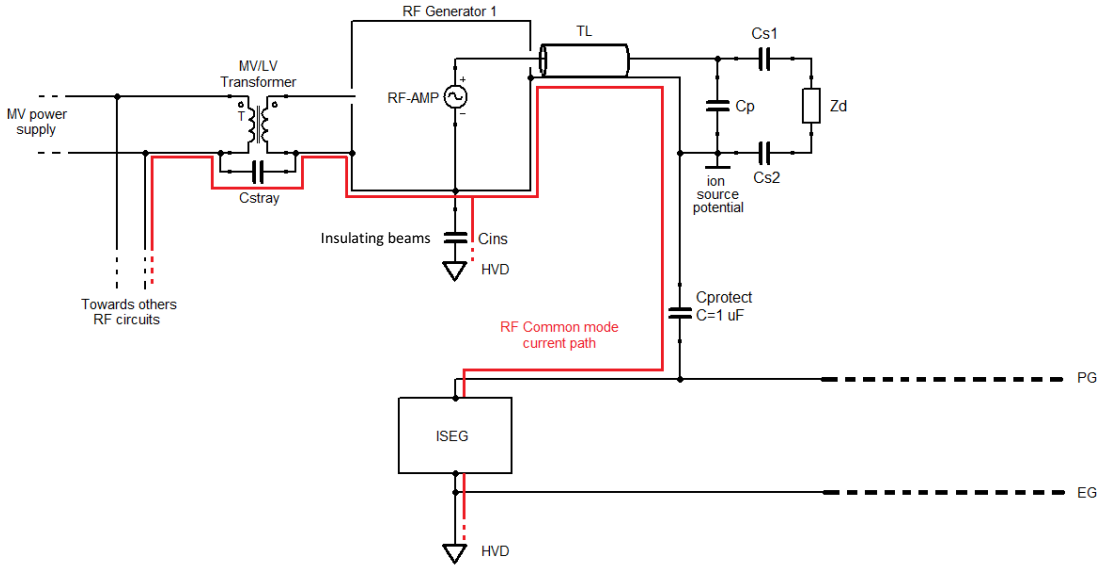

Figure 6. 16 *RF common mode current path in the electrical circuit of Configuration #1 (a single RF circuit is shown)*

6.4.1.1 Frequency domain analysis

The analysis in the frequency domain of the circuit in Figure 6. 15 is focused on evaluating the evolution of the RF CM currents over the frequency range, 0.9 ÷ 1.1 MHz, when just one RF amplifier is operating at time at full power. The simulation in the frequency domain has been realized with Qucsstudio and MATLAB, following the same procedure described in 5.2, highlighting also the optimal operating condition (minimum ρ frequency) for each RF-AMP.

6.4.1.1.1 RF-AMP operating parameters

Figure 6. 17, Figure 6. 18, Figure 6. 19 and Figure 6. 20 show respectively the output voltage (V_{out}), the output current (I_{out}), the output power (P_{out}) of the four RF amplifiers and the reflection coefficient (ρ) of their related RF circuits. Even for the RF amplifiers it has been assumed the hypothesis of output voltage and current limitation to their nominal values (see 4.3.2)

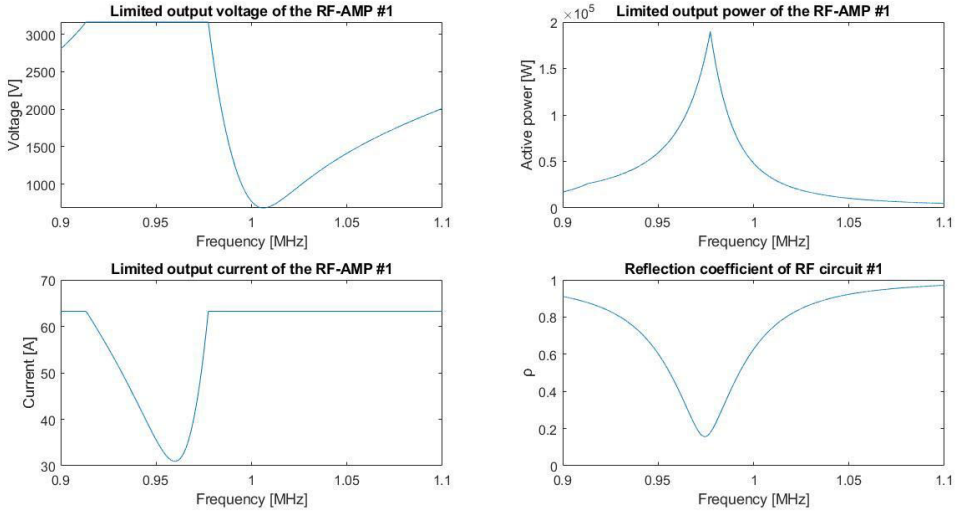

Figure 6. 17 *Output voltage, output current, output power of the RF-AMP #1 and the reflection coefficient of RF circuit #1*

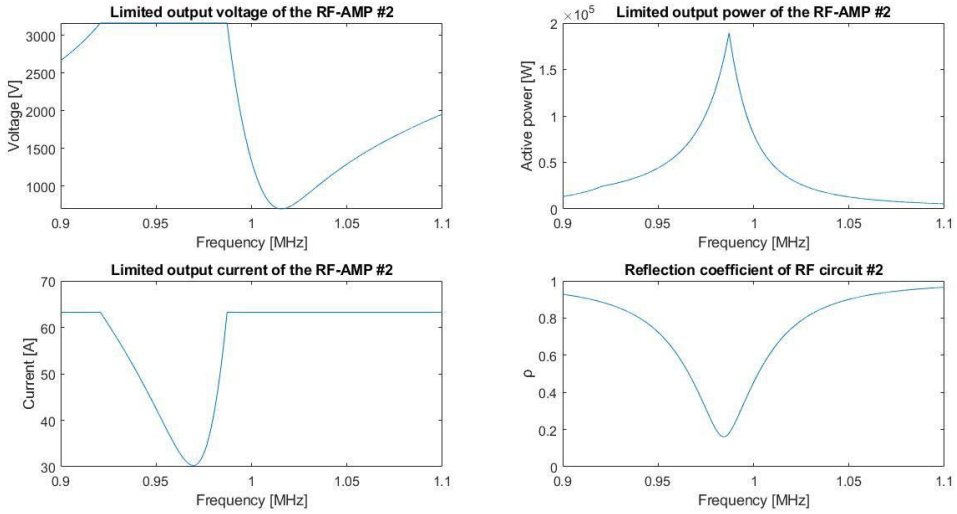

Figure 6. 18 *Output voltage, output current, output power of the RF-AMP #2 and the reflection coefficient of RF circuit #2*

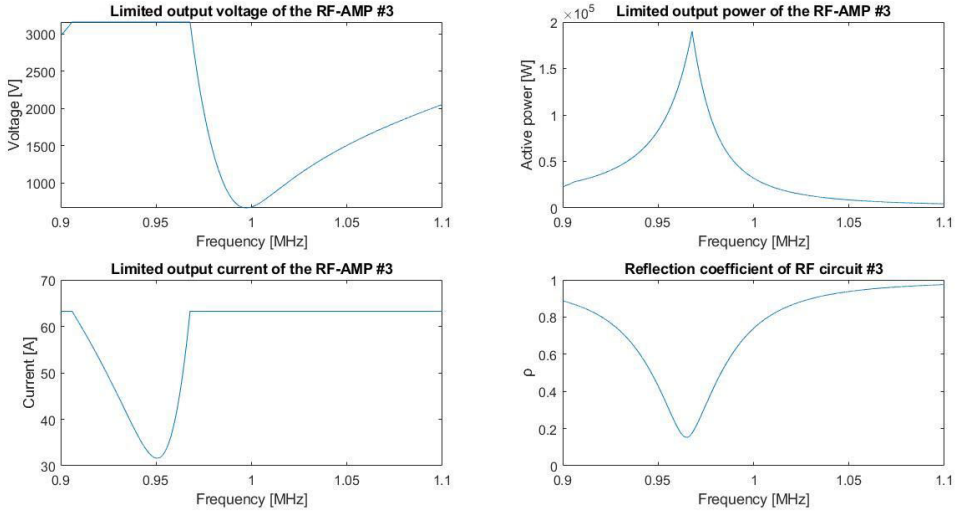

Figure 6. 19 *Output voltage, output current, output power of the RF-AMP #3 and the reflection coefficient of RF circuit #3*

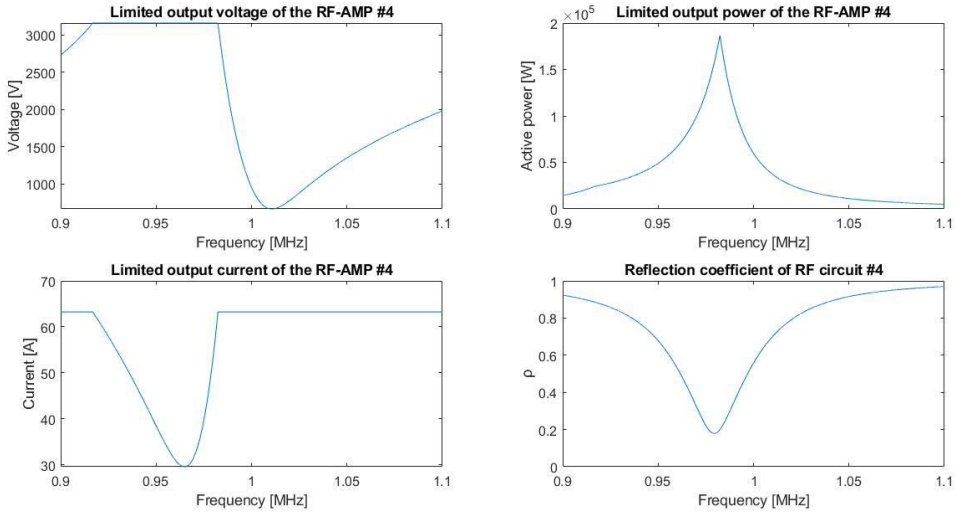

Figure 6. 20 *Output voltage, output current, output power of the RF-AMP #4 and the reflection coefficient of RF circuit #4*

Due to the asymmetry in the RF load and the inductive and capacitive coupling between the coaxial line and the PG busbar, the four parameters are different for each RF circuit. In particular it is possible to highlight that:

- the RF-AMP #1 is limited in voltage within 0.91÷0.977 MHz and in current within 0.9÷0.913 MHz and 0.978÷1.1 MHz. The peak of the output power is equal to 189.6 kW at ~0.977 MHz and the minimum of the reflection coefficient of the RF circuit #1 is equal to 0.157 at 0.975 MHz;

- the RF-AMP #2 is limited in voltage within 0.921÷0.986 MHz and in current between 0.9÷0.92 MHz and 0.987÷1.1 MHz. The peak of the output power is equal to 189.4 kW at 0.987 MHz.The minimum of the reflection coefficient of the RF circuit #2 is equal to 0.161 at 0.985 MHz;

- the RF-OSC #3 is limited in voltage within 0.906÷0.967 MHz and in current within 0.9÷0.905 MHz and 0.968÷1.1 MHz. The peak of the output power is equal to 190.1 kW at ~0.968 MHz.The minimum of the reflection coefficientof the RF circuit #3 is equal to 0.153 at 0.965 MHz;

- the RF-OSC #4 is limited in voltage within 0.917÷0.982 MHz and in current within 0.9÷0.916 MHz and 0.983÷1.1 MHz. The peak of the output power is equal to 186.9 kW at ~0.982 MHz.The minimum of the reflection coefficientof the RF circuit #4 is equal to 0.179 at 0.979 MHz.

6.4.1.1.2 Results of the RF common mode current analysis

The focus of the analysis is the estimation of the value of the RF CM current that from ion source through the PG busbar reaches ISEG, I_{PG}. Along with this current, the focus is also to estimate the value of the current circulating on the ISEG output filter, I_{ISEG}. The latter is crucial for the power dimensioning of the ISEG output filter itself, as aforementioned in chapter 5. With the circuital solution of Configuration #1, the value of I_{PG} corresponds to the I_{ISEG} one.

As in chapter 5, the frequency domain analysis has been realized by simulating the overall circuit with a single RF-AMP ON and the others OFF and this procedure has been repeated for all the amplifiers. The trends of the four resulting currents on the ISEG output filter have been portrayed in Figure 6. 21, highlighting the magnitude of I_{ISEG} at the minimum ρ frequency of the related RF circuit through a circular marker (this representation has been adopted for all the plots of 6.4, in the frequency domain). The different conditions are highlighted with different colors in order to have a better comprehension of the results.

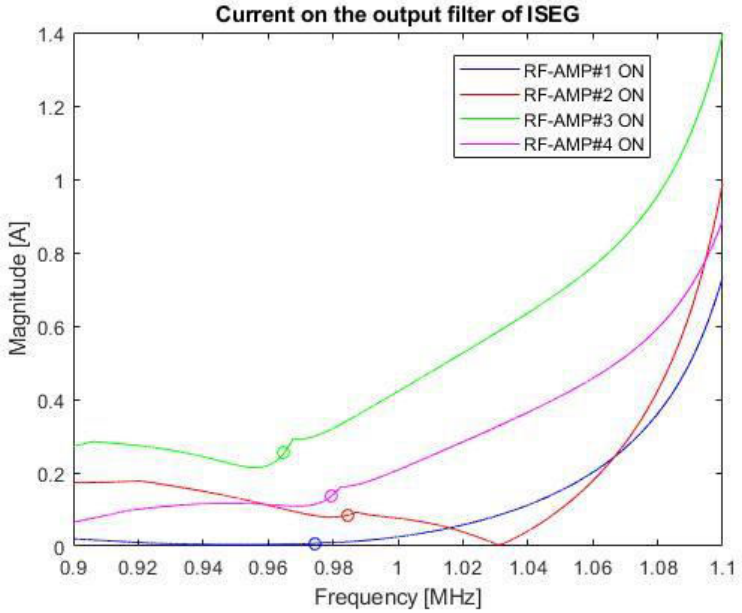

Figure 6. 21 *Current on the ISEG output filter with each RF-AMP operating independently (Configuration #1) (the markers highlight the* $\boldsymbol{I_{ISEG}}$*value at the minimum ρ frequency for each specific RF circuit)*

It is possible to observe that there is a common trend in the four currents: at 0.9 MHz they show low magnitude current values which strongly increase at 1.1 MHz. It is interesting to notice that with the RF-

AMP #2 ON (red curve) there is a minimum point at about 1.03 MHz (45 kHz away from the minimum ρ frequency of the RF circuit #2) at which the current is almost negligible. The best results are obtained when there is only the RF-AMP #1 ON, for which, at the operating frequency, I_{ISEG} is equal to~7 mA. The worst case is when the RF-AMP #3 is ON: at its optimal operating frequency (0.965 MHz) it produces a current on the output filter of ISEG equal to 0.253 A, almost twice the value of I_{ISEG} produced by the RF-AMP #4 at its optimal operating frequency (0.136 A at 0.979 MHz).

Considering Figure 6. 22, which represents a zoom of Figure 6. 15 close to ISEG output filter, it is possible to evaluate how I_{ISEG} is splitted, in correspondance of node A, into I_{Beam4} and I_{Beams}. The former represents the current on the stray capacitance of the insulating beam of RF-AMP #4, while the latter represents the overall current circulating towards the insulating beams of the other three RF-AMP.

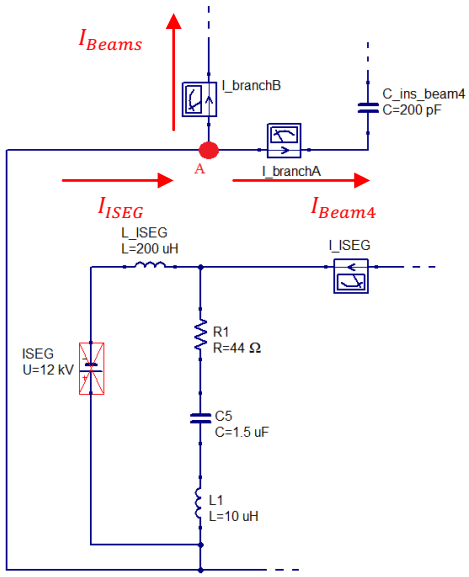

Figure 6. 22 *Zoom of the electrical scheme of simulation #1 for the evaluation of the distribution of* $\boldsymbol{I_{ISEG}}$ *at node A (Configuration #1)*

For the evaluation of the current distribution at node A, it has been taken into account the worst condition observed in Figure 6. 21, which corresponds to RF-AMP #3 ON (green curve). Figure 6. 23 shows the magnitude (upper plot) and the phase (bottom plot) of I_{ISEG}, I_{Beam4} and I_{Beams}. The vertical red dashed line crosses the values of magnitude and phase of these currents in correspondance of the minimum ρ frequency of the RF circuit #3.

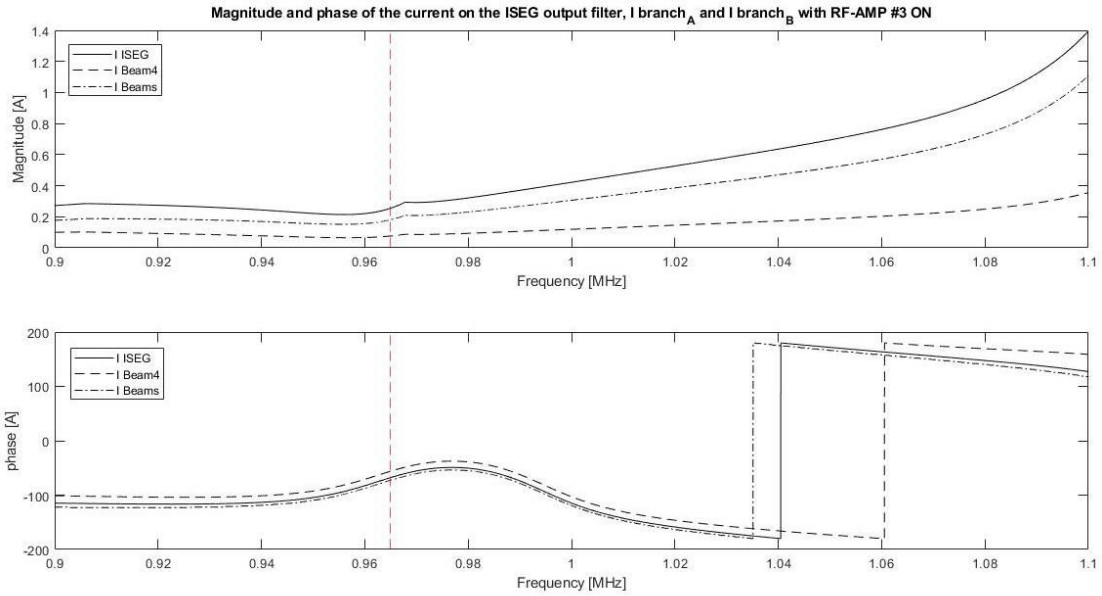

Figure 6. 23 *Magnitude (upper plot) and phase (bottom plot) of* $\boldsymbol{I_{ISEG}}$, $\boldsymbol{I_{Beam4}}$ *and* $\boldsymbol{I_{Beams}}$ *with RF-AMP #3 ON (Configuration #1)*

6.4.1.2 Time domain analysis

The analysis of the RF CM current of the electrical scheme of Figure 6. 15, in time domain, has been realized with each amplifier operating at its optimal operating frequency at full power, as it has been done for the oscillators in 5.3. (the parameters of the four RF-AMP adopted for this analysis are summarize in Table 6. 3).

Table 6. 3 *Output voltage, current and active power of the RF-AMP of each RF circuit, at the minimum ρ frequency, at full power for Configuration #1*

	ρ minimum frequency [MHz]	Output voltage [V]	Output current [A]	Output active power [kW]
RF-AMP #1	0.975	3162	52.9	162.9
RF-AMP #2	0.985	3162	53.6	163.9
RF-AMP #3	0.965	3162	52.4	160.9
RF-AMP #4	0.979	3162	52.3	158.3

6.4.1.2.1 Results of the RF common mode current analysis

For each of the analysis of this paragraph, as in 5.3, it has been implemented a discrete simulation with a sampling time of 1 ns with a time interval equal to 1 ms. Furthermore, it has been considered the initial state equal to 0 s, thus showing the initial transient.

Figure 6. 24 shows the evolution of I_{ISEG} over time where, in turn, each RF-AMP is operating alone with the others OFF, following the analysis in the frequency domain.

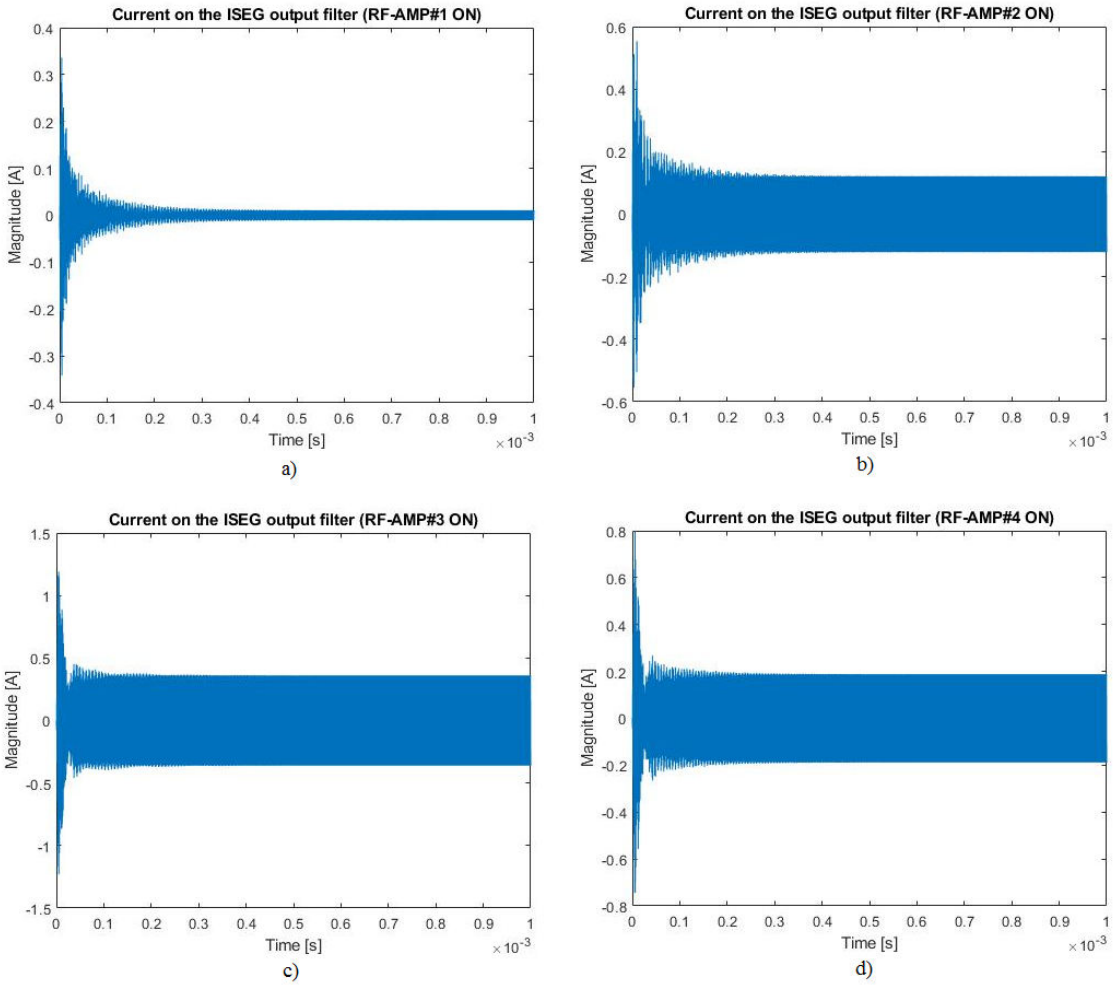

Figure 6. 24 *Current on the ISEG output filter with RF-AMP #1 ON, others OFF (a), RF-AMP #2 ON, others OFF (b), RF-AMP #3 ON, others OFF (c) and RF-AMP #4 ON, others OFF (d) (Configuration #1)*

The four plots represent a sinusoidal waveform oscillating at the optimal operating frequency of each of the four RF-AMP. In steady state condition (the initial transient can be considered over after ~0.4 ms), the four plots show the following features:

a) RF-AMP #1 ON, others OFF: sinusoidal waveform oscillating at 0.975 MHz (T = 1.03 μs) with an amplitude of the current on the ISEG output filter of about 0.01 A;

b) RF-AMP #2 ON, others OFF: sinusoidal waveform oscillating at 0.985 MHz (T = 1.015μs) with an amplitude of the current on the ISEG output filter of about 0.12 A;

c) RF-AMP #3 ON, others OFF: sinusoidal waveform oscillating at 0.965 MHz (T = 1.04 μs) with an amplitude of the current on the ISEG output filter of about 0.36 A;

d) RF-AMP #4 ON, others OFF: sinusoidal waveform oscillating at 0.979 MHz (T = 1.02 μs) with an amplitude of the current on the ISEG output filter of about 0.19 A;

As for the RF-OSC analysis, it is possible to identify the frequency spectrum components of the sinusoidal waveform by calculating the FFT (see 5.3.1). The results are shown in Figure 6. 25, highlighting that, as expected, there is only one harmonic for each condition, which corresponds to the related minimum ρ frequency.

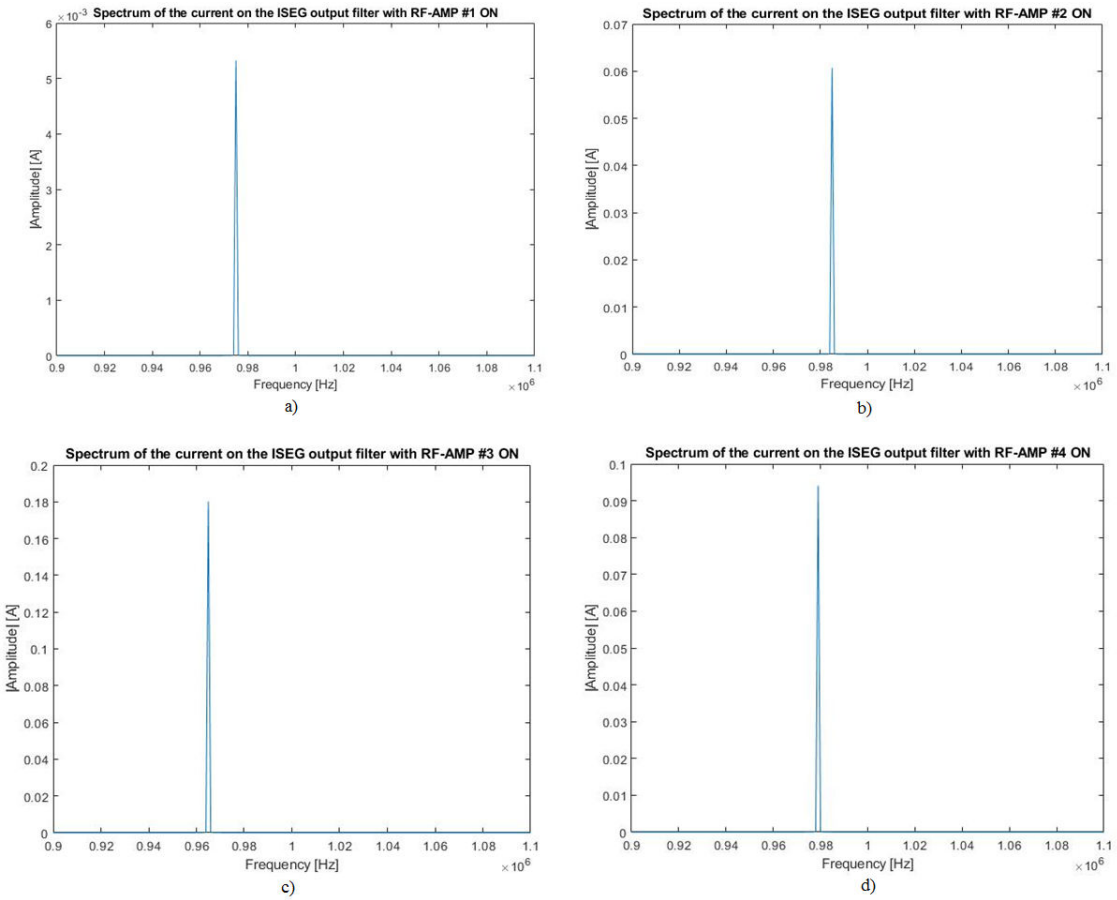

Figure 6. 25 *Spectrum of the current on the ISEG output filter with RF-AMP #1 ON (a), RF-AMP #2 ON (b), RF-AMP #3 ON (c), RF-AMP #4 ON (d) (Configuration #1)*

For each of these currents, it has been estimated the RMS value, in steady state condition, and the resulting values are shown in Table 6. 4. As aforementioned in 5.3, the current RMS value is a fundamental parameter in the analysis since it is representative of the heating on the passive components of the ISEG output filter, thus affecting the dimensioning of the filter itself.

Table 6. 4 *RMS value of the current on the ISEG output filter for each of the four RF-AMP conditions (Configuration #1)*

RF-AMP ON	Current on the ISEG output filter [A]
RF-AMP#1	0.008
RF-AMP#2	0.086
RF-AMP#3	0.255
RF-AMP#4	0.133

As expected, the highest RMS value of the current on the ISEG output filter is obtained when the RF-AMP #3 is ON, reflecting the results obtained in the frequency domain (the magnitude of the phasor corresponds to the RMS value).

As discussed in chapter 5, the time domain analysis allows studying the operation of more than one RF-AMP at time. This analysis has been done for all the 4 operating condition of the amplifiers but it is interesting to consider the results obtained when all the RF-AMP are ON at the same time, they operate at their optimal frequency and they deliver the maximum output active power. Figure 6. 26 shows the waveform of the current on the ISEG output filter for these specific conditions.

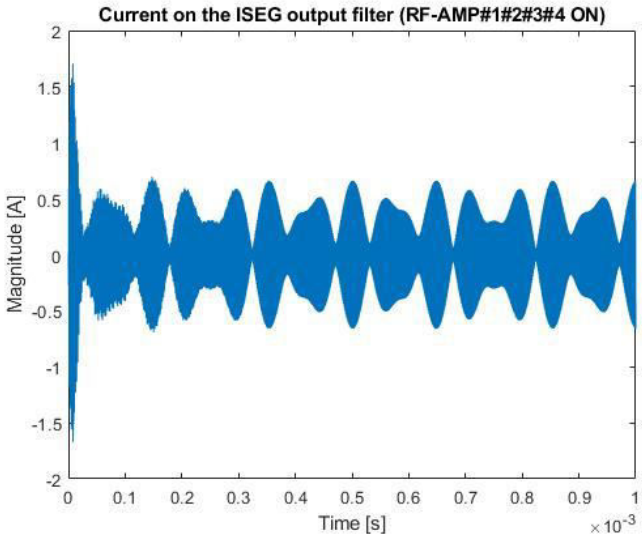

Figure 6. 26 *Evolution of the current on the ISEG output filter when all the RF-AMP are operating at the same time (Configuration #1)*

The resulting current waveform is the superposition of the current waveform produced by the four RF-AMP, each one operating at a different frequency (its optimal operating frequency). In fact, by applying the FFT to the signal it is possible to obtain four harmonic components corresponding to the operating frequency of each RF-AMP, as it is shown in Figure 6. 27: 0.975 MHz (RF-AMP #1), 0.985 MHz (RF-AMP #2), 0.965 MHz (RF-AMP #3) and 0.979 MHz (RF-AMP #4). Figure 6. 27 highlights also that, as expected, the greatest contribute is due to the harmonic related to the RF-AMP #3.

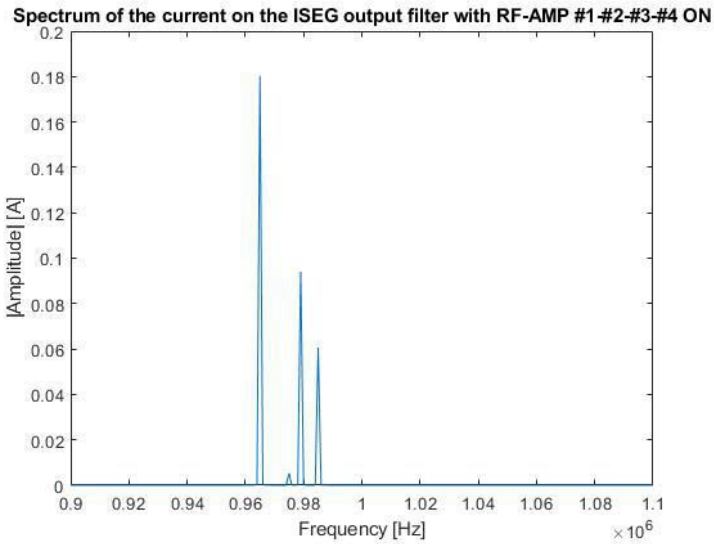

Figure 6. 27 *Spectrum of the current on the ISEG output filter when all the RF-AMP are operating at the same time (Configuration #1)*

The RMS value of I_{ISEG}, in this operating condition, is equal to ~300 mA (at ~1 MHz) and this value must be taken into account for the dimensioning of the ISEG output filter. This is an acceptable value since, as aforementioned in 5.3.1, to prevent overheating of the passive components of the filter, I_{ISEG} should be in the order of 500 mA or lower.

In order to complete the analysis of the RF CM current, in time domain, the RMS values of the voltage on the stray capacitances between the screens of the MV/LV transformer and on the stray capacitances between the insulating beam of each RF-AMP and the floor of the HVD have been evaluated. The results have been estimated for the worst condition, which corresponds to the combined operation of the four RF-AMP and they are shown in Table 6. 5.

Table 6. 5 *Voltage RMS value on the stray capacitance of the insulating beams and the MV/LV transformers (Configuration #1)*

	Voltage RMS value [V]
stray capacitance insulting beam #1	75.05
stray capacitance insulting beam #2	70.12
stray capacitance insulting beam #3	100.62
stray capacitance insulting beam #4	94.58
stray capacitance between screens of MV/LV transformer #1	56.26
stray capacitance between screens of MV/LV transformer #2	61.37
stray capacitance between screens of MV/LV transformer #3	66.23
stray capacitance between screens of MV/LV transformer #4	56.27

The RF voltage applied between the screens of the MV/LV transformer it's a peculiar aspect of the application on SPIDER and its effects should be carefully analyzed to properly design a transformer with suitable RF isolation material. A RF voltage of tens of Volt may not be an issue for the industrial transformer, while a RF voltage of several kV should require further attention. In this case the simulation results show that the RMS voltage is about 70 V in all the cases, showing the higher value on the stray capacitance of the MV/LV transformer #3. The maximum RMS value of the voltage on the stray capacitances of the insulating beams is about 101 V for the insulating beam #3. These results must be taken into account during the dimensioning, respectively of the MV/LV transformers and the insulating beams of the amplifiers.

6.4.2 Configuration #2: single MV/LV transformer + LV/LV transformer for each RF amplifier

The electrical scheme implemented for this second configuration is shown in Figure 6. 28. The scheme is identical to the one of the Configuration #1 as regard the RF load, while, on the power supply side, the four 6.6 kV/210 V transformers have been substituted with four 400 V/210 V three-phases, three-winding transformers, which are fed by an additional 6.6 kV/400 V three-phases transformer.

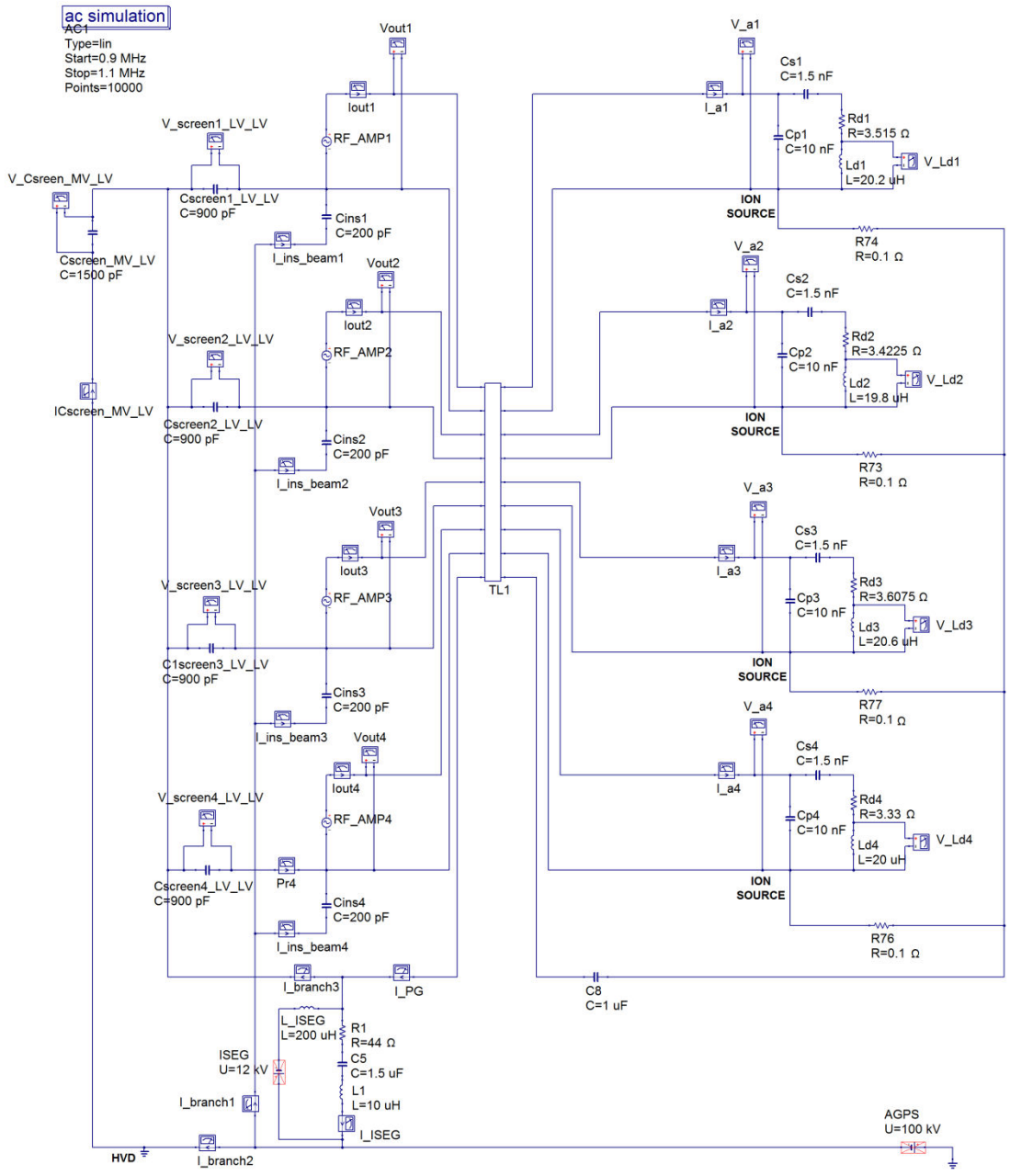

Figure 6. 28 *Electrical scheme for the analysis of the RF common mode current (Configuration #2)*

As in 6.4.1, in the electrical scheme the transformers are represented through the stray capacitance between their screens. In this configuration, the primary screen of the MV/LV transformer is connected to the HVD, thus providing a further path for the circulation of the RF common mode currents through the stray capacitance between the screens of the MV/LV transformer itself (see Figure 6. 29).

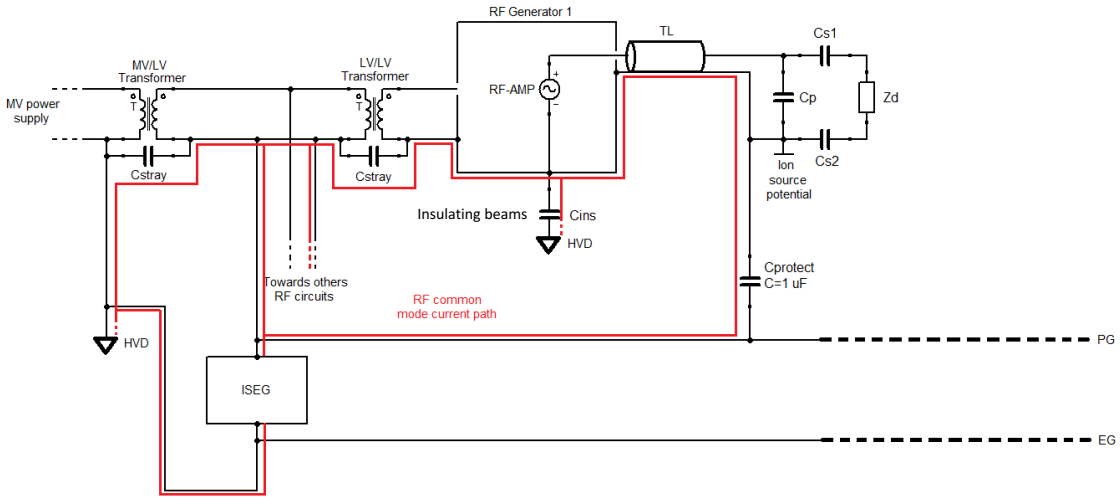

Figure 6. 29 *RF common mode current path in the electrical circuit of Configuration #2 (a single RF circuit is shown)*

6.4.2.1 Frequency domain analysis

The assumptions of the frequency domain analysis of the electrical scheme of Figure 6. 28, for Configuration #2, are the same of Configuration #1. Furthermore, RF-AMP operating parameters are essentially equal to the ones estimated in 6.4.1.1.1, showing the same trends, since the variations in the electrical scheme from Configuration #1 to Configuration #2 produce negligible effects on them.

6.4.2.1.1 Results of the RF common mode current analysis

The core of the analysis, even in Solution #2, is the estimation of the RF CM current circulating through the PG busbar, I_{PG}, towards ISEG, and the current on the ISEG output filter, I_{ISEG}. However, differently from Configuration #1, these two currents are different due to the specific electrical connection of the output filter of ISEG, which has the terminal connected to the PG busbar also connected between the secondary screen of the MV/LV transformer and the primary screen of each LV/LV transformer.

Figure 6. 30 shows the trend of I_{PG} for each of the four conditions with just one RF-AMP ON and others OFF.

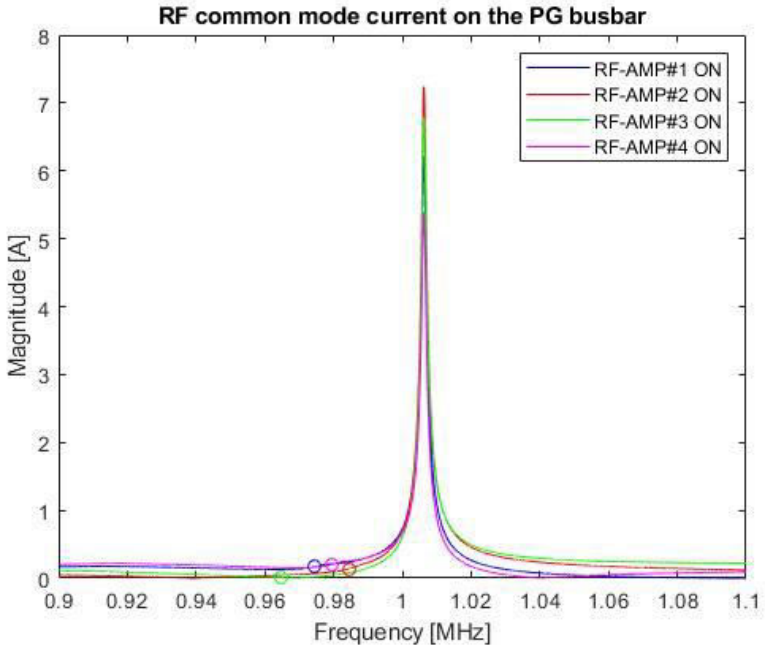

Figure 6. 30 *RF common mode current on the PG busbar (Configuration #2)*

It is possible to highlight the presence of a resonant point at 1.006 MHz for which the current reaches extremely high current values, assuming ~7.2 A when RF-AMP #2 is ON. Further verifications have shown that this resonance is triggered by the equivalent impedance of the stray capacitances between the screens of the LV/LV transformers and the equivalent impedance of the inductance of the transmission line. Focusing on the optimal operating condition for each RF-AMP (highlighted by circular markers), they all have this one quite distant from the resonance frequency, thus showing low current values, especially for RF-AMP #3 ON condition (0.011 A), which in Configuration #1 provided the worst results. Between the four RF-AMP, although their low current values, RF-AMP #4 represents the worst condition showing a current value equal to ~0.2 A at the minimum ρ frequency of the RF circuit #4 (0.979 MHz).

The effects of this resonance on the current circulating on the ISEG output filter, for the four conditions where a single RF-AMP is ON and the others are OFF, are shown in Figure 6. 31.

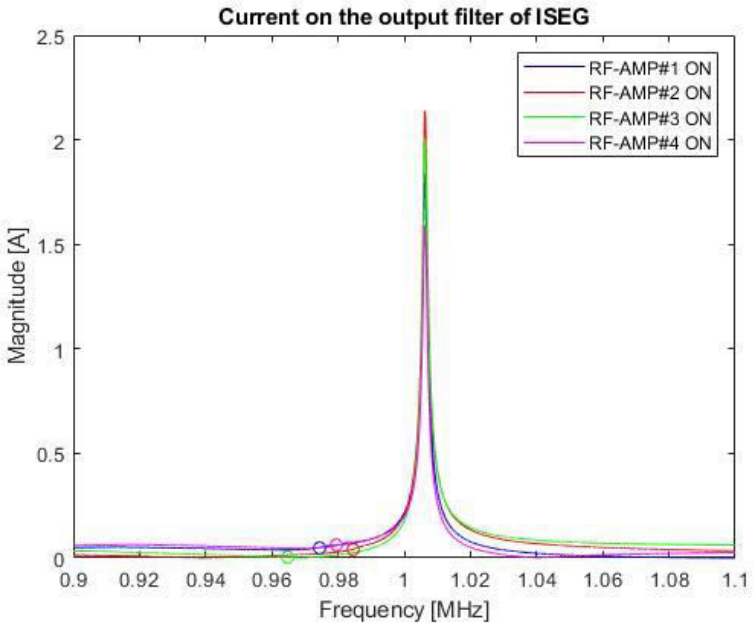

Figure 6. 31 *Current on the output filter of ISEG (Configuration #2)*

The trend of I_{ISEG} reflects the I_{PG} one, reaching a current value of ~2.1 A at the resonance frequency when RF-AMP #2 is ON. Considering the current values achieved when each RF-AMP works at its optimal frequency, the worst result is provided again when RF-AMP #4 is ON (~0.06 A).

As in Configuration #1, it is interesting to evaluate how I_{PG} and I_{ISEG} are distributed in the circuit, especially focusing on the two nodes at the exit of the ISEG output filter, which are shown in Figure 6. 32 (node A and node B).

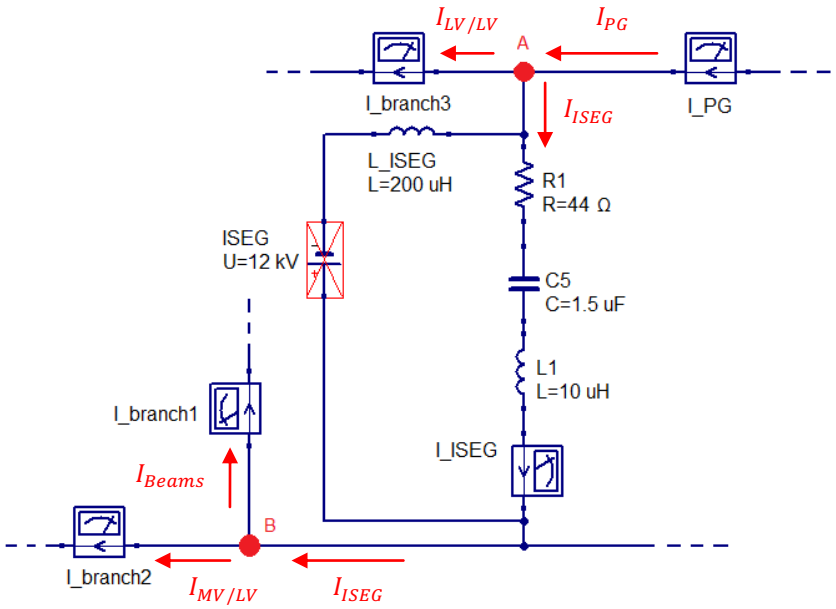

Figure 6. 32*Zoom of the electrical scheme of Configuration #2 for the evaluation of the distribution of* $\boldsymbol{I_{PG}}$ *and* $\boldsymbol{I_{ISEG}}$ *at node A and node B*

The currents reaching node A are: I_{PG}, I_{ISEG} and the current on the branch electrically connected between the secondary screen of the MV/LV transformer and the primary screen of the LV/LV transformers, $I_{LV/LV}$. Considering the worst case (RF-AMP #4 ON), Figure 6. 33 shows the magnitude and the phase of I_{PG}, I_{ISEG} and $I_{LV/LV}$in this specific condition (the trend of the magnitude of $I_{LV/LV}$ is almost completely masked by the trend of the magnitude of I_{PG}). The red dashed line represents the optimal operating condition of the RF-AMP #4 (0.979 MHz).

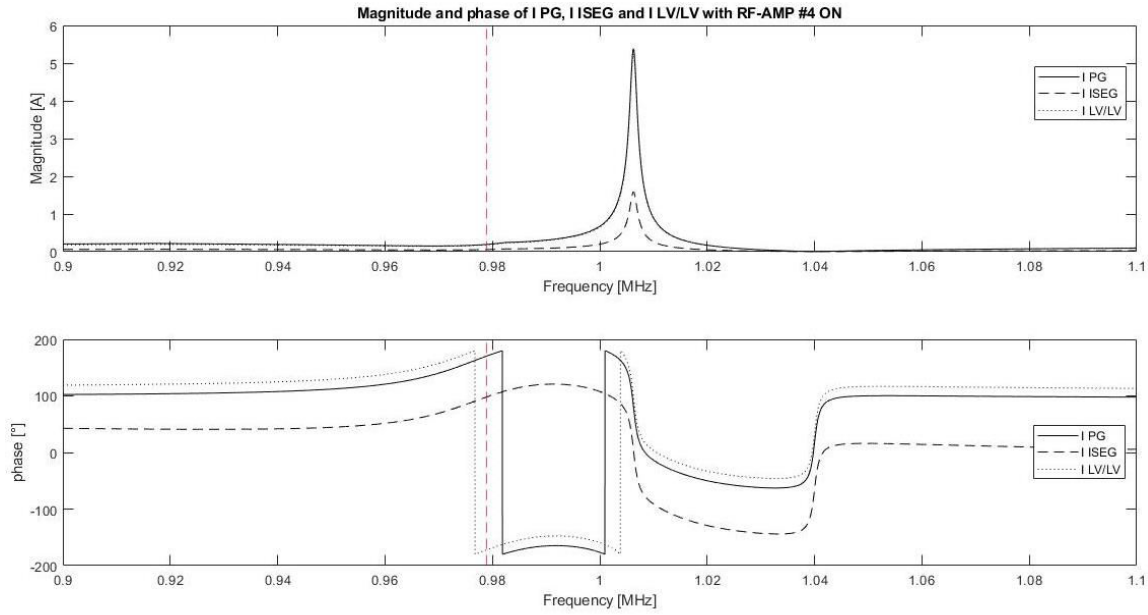

Figure 6. 33 *Magnitude (upper plot) and phase (bottom plot) of* $\boldsymbol{I_{PG}}$, $\boldsymbol{I_{ISEG}}$ *and* $\boldsymbol{I_{LV/LV}}$ *with RF-AMP #4 ON (Configuration #2)*

The same analysis has been applied to node B. Figure 6. 34 shows the magnitude and the phase of I_{ISEG}, of the current reaching the stray capacitance of the MV/LV transformer through the HVD, $I_{MV/LV}$,and the current reaching the insulating beams of the four RF-AMP, I_{Beams}.

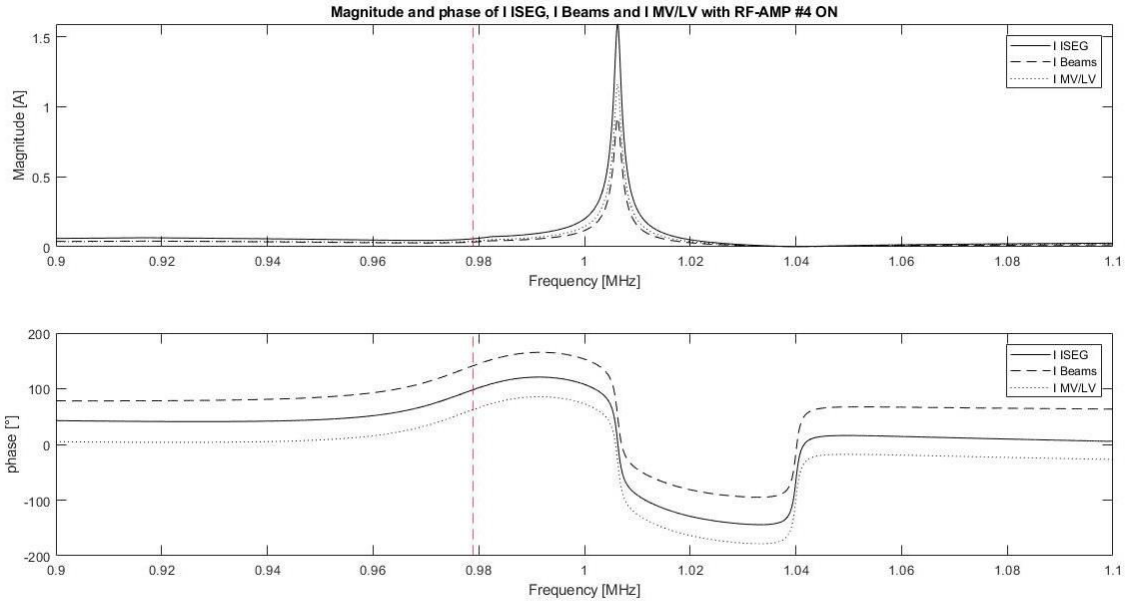

Figure 6. 34 *Magnitude (upper plot) and phase (bottom plot) of* $\boldsymbol{I_{ISEG}}$,$\boldsymbol{I_{Beams}}$ *and* $\boldsymbol{I_{MV/LV}}$ *with RF-AMP #4 ON (Configuration #2)*

6.4.2.2 Time domain analysis

The analysis of $I_{PG}$and I_{ISEG} of the electrical scheme of Figure 6. 28, in the time domain shows, as in Configuration #1, similar trends for each of the four conditions when, in turn, a single RF-AMP works at its optimal operating frequency at full power. For this reason, the first section of the time domain analysis will be focused only on the discussion of the plots obtained with the RF-AMP #4 ON (the worst case for a single operating amplifier). The RMS values of I_{PG} and I_{ISEG} for each other conditions will still be provided. The parameters of the RF-AMP considered for the time domain analysis are summarized in Table 6. 6. As aforementioned in 6.4.2.1, these parameters are similar to the ones of Table 6. 3.

Table 6. 6 *Output voltage, current and active power of the RF-AMP of each RF circuit, at the minimum ρ frequency, at full power for Configuration #2*

	ρ minimum frequency [MHz]	Output voltage [V]	Output current [A]	Output active power [kW]
RF-AMP#1	0.975	3162	52.8	162.2
RF-AMP#2	0.985	3162	53.9	164.1
RF-AMP#3	0.965	3162	52.5	161.6
RF-AMP#4	0.979	3162	52.2	158.1

6.4.2.2.1 Results of the RF common mode current analysis

Figure 6. 35 shows the evolution of the current on the PG busbar when RF-AMP #4 is ON (others OFF), and the related FFT.

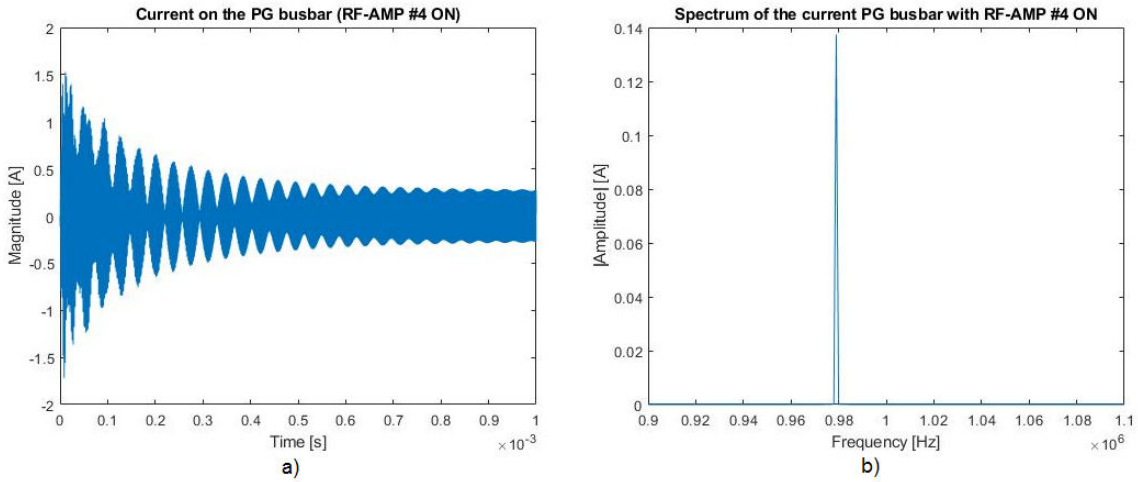

Figure 6. 35 *Evolution of the current on the PG busbar over time (a) and related FFT (b) with RF-AMP #4 ON (Configuration #2)*

It is possible to observe that, differently from the results obtained in Solution #1, the initial transient of the current is longer due to the higher overall capacity of the electrical circuit. Furthermore, the FFT of I_{PG} produces a single harmonic in correspondance of 0.979 MHz (RF-AMP #4 imposed operating frequency).

The same features can be observed in Figure 6. 36, which shows the evolution of the current on the ISEG output filter over time and the related FFT.

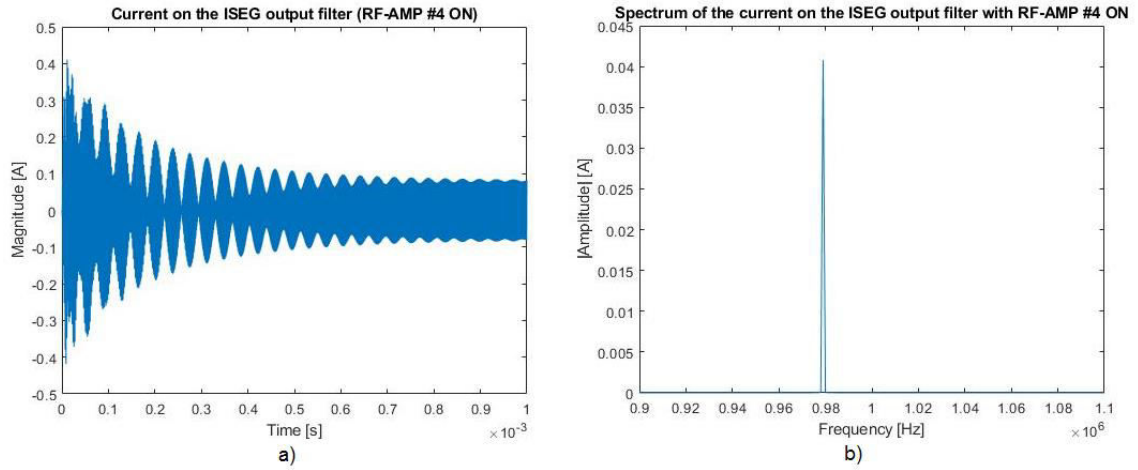

Figure 6. 36 *Evolution of the current on the ISEG output filter over time (a) and related FFT (b) with RF-AMP #4 ON (Configuration #2)*

The RMS current values of I_{PG} and I_{ISEG}, estimated after the initial transient, in steady state condition, are shown in Table 6. 7, for all the four conditions with one RF-AMP ON (others OFF). The results prove that the worst case is when RF-AMP #4 is ON. It is interesting also to notice that the RMS values of the current on the ISEG output filter are greatly lower than the ones evaluated in Configuration #1, especially when the RF-AMP #3 is ON (see Table 6. 4).

Table 6. 7 *RMS value of the current on the ISEG output filter for each of the four RF-AMP conditions (Configuration #2)*

RF-AMP ON	RMS value of the current on the PG busbar [A]	RMS current value on the ISEG output filter [A]
RF-AMP#1	0.172	0.0512
RF-AMP#2	0.147	0.0438
RF-AMP#3	0.01	0.003
RF-AMP#4	0.194	0.058

At this point, as in Configuration #1, it is possible to discuss the trend of I_{PG} and I_{ISEG} when all the four RF-AMP are operating together, each one at its optimal operating frequency, at full power. The evolution of the two currents and the related FFT are portrayed respectively in Figure 6. 37 (I_{PG}) and in Figure 6. 38 (I_{ISEG}).

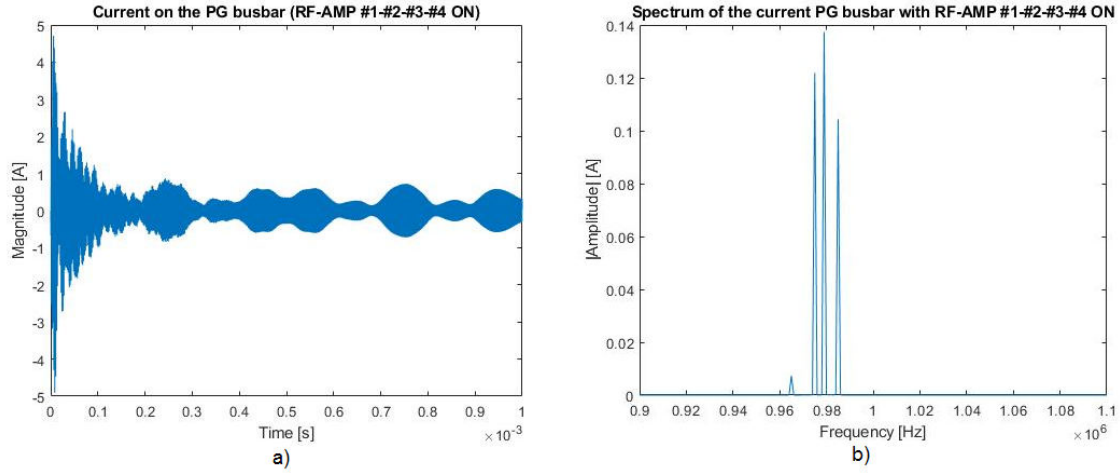

Figure 6. 37 *Evolution of the current on the PG busbar when all the RF-AMPs are operating at the same time (a) and FFT (b) (Configuration #2)*

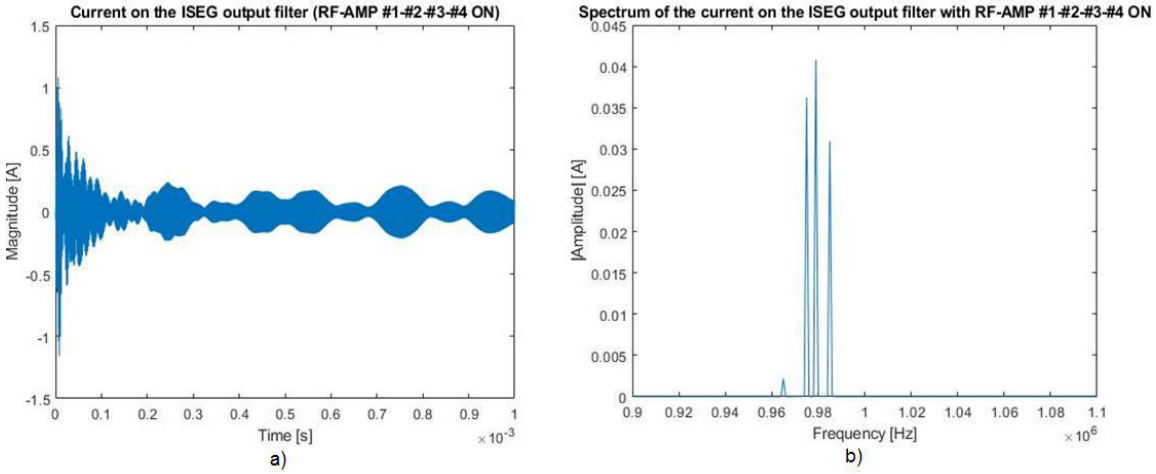

Figure 6. 38 *Evolution of the current on the ISEG output filter when all the RF-AMPs are operating at the same time (a) and FFT (b) (Configuration #2)*

The spectrum of the waveform of the two currents highlights the presence of four harmonic corresponding to the imposed operating frequency of the four RF-AMP. The harmonic associated to the frequency of the RF-AMP #3 (0.965MHz) is barely visible since is the most distant from the resonance frequency of the circuit. The other three harmonics, associated to the optimal operating frequencies of the RF-AMP #1, RF-AMP #2 and RF-AMP #4 produce the largest contribute, both to I_{PG} and I_{ISEG}. In particular, the most

relevant component, as aforementioned in 6.4.2.1.1, is the one associated to the condition for which RF-AMP #4 is ON. The RMS values of I_{PG} and I_{ISEG}, at ~1 MHz, are respectively equal to 305 mA and 91 mA. It is also interesting to evaluate the RMS value of the voltage on the stray capacitances of the circuit when the four RF-AMP are operating at the same time at their optimal operating frequency, whose values are shown in Table 6. 8. With Configuration #2, the resulting RMS voltage value on the stray capacitance between the screens of the MV/LV transformer should not be an issue (following the considerations of on the RMS voltage value of 6.4.1.2.1). However, on the stray capacitance of the insulating beams and on the stray capacitance between the screens of the LV/LV transformers the RMS voltage value is quite high and this aspect must be taken into account during the dimensioning of these components.

Table 6. 8 *Voltage RMS value on the stray capacitance of the insulating beams, the four LV/LV transformers and the MV/LV transformer (Configuration #2)*

	Voltage RMS value [V]
stray capacitance insulating beam #1	203.55
stray capacitance insulating beam #2	229.63
stray capacitance insulating beam #3	190.65
stray capacitance insulating beam #4	183.34
stray capacitance between screens of LV/LV transformer #1	201.79
stray capacitance between screens of LV/LV transformer #2	231.29
stray capacitance between screens of LV/LV transformer #3	192.15
stray capacitance between screens of LV/LV transformer #4	181.82
stray capacitance between screens of MV/LV transformer	6.84

These aspects (in particular the RMS CM current values), at a first glance, would demonstrate that the configuration with the MV/LV transformer and the four LV/LV transformer is the best configuration to implement from a RF CM current point of view. In fact, at the minimum ρ frequency the RMS values of I_{PG} and I_{ISEG} are low. However, moving away from this optimal condition, towards ~1 MHz, the currents rapidly increase since there is a really close resonant point. In particular, the current on the ISEG output filter, by approaching the resonant frequency, would reach critical values, thus producing unsustainable overheating on the passive components of the filter. For this reason, a possible solution for moving the resonance frequency away from the operating frequency range of SPIDER (0.9÷1.1 MHz) has been studied: the idea is to introduce a filter in parallel to the stray capacitance of each LV/LV transformer, properly tuned for producing an antiresonance at 1 MHz. In order to verify this solution, a third simulation has been performed.

6.4.3 Configuration #2 + filter in parallel to the stray capacitance of each LV/LV transformer

Figure 6. 39 shows the electrical scheme which has been implemented for the analysis of Configuration #2 + filter.

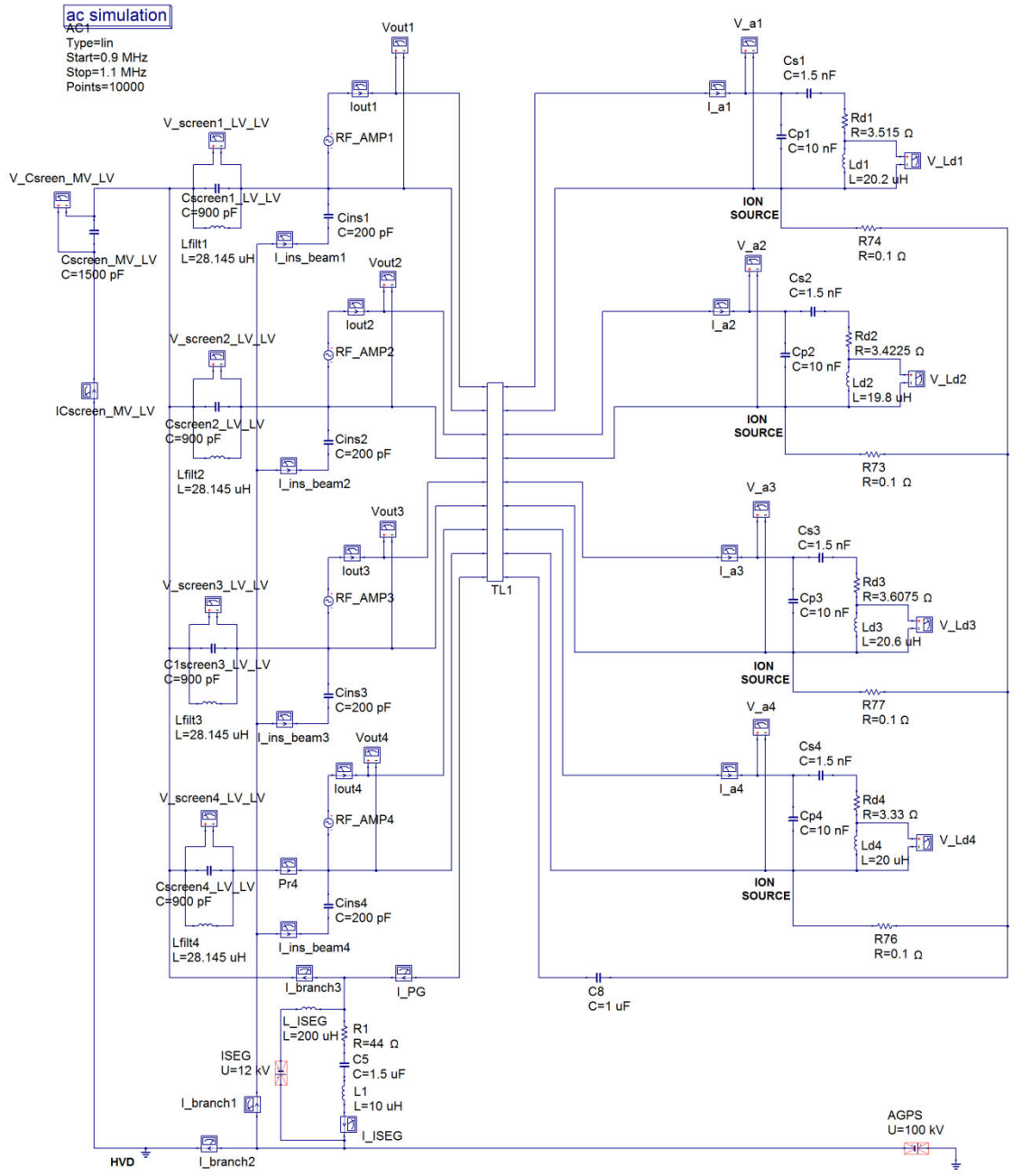

Figure 6. 39 *Electrical scheme for the analysis of the RF common mode current (Configuration #2 + filter)*

The filter placed in parallel to the equivalent stray capacitance of each LV/LV transformer (900 pF), properly tuned for producing an antiresonance at 1 MHz, is represented through an equivalent inductor. Figure 6. 40 shows the path of the RF CM currents for the Configuration #2 + filter.

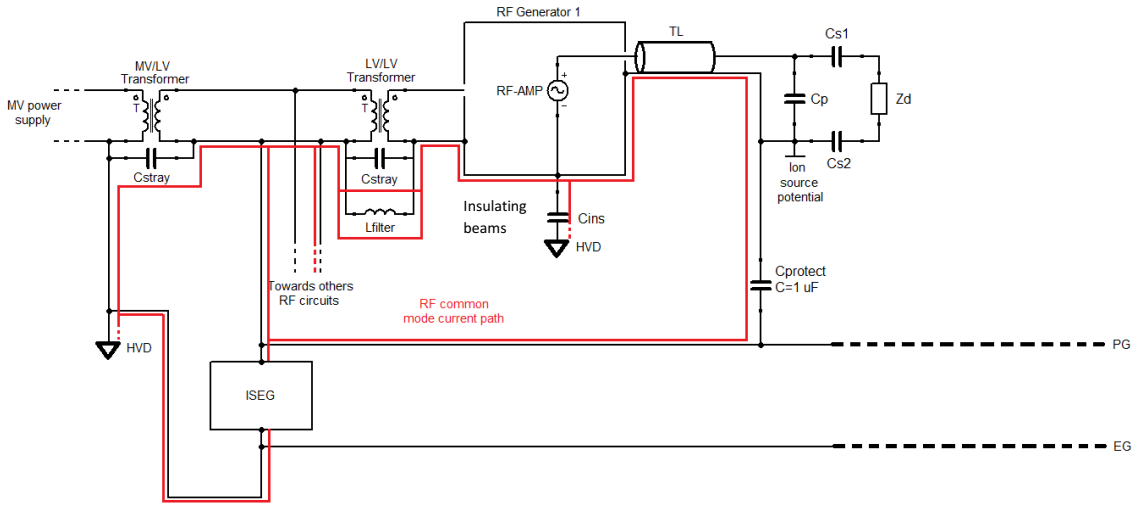

Figure 6. 40 *RF common mode current path in the electrical circuit of Configuration #2 + filter (a single RF circuit is shown)*

The value of the inductance of the filter has been estimated from the resonance condition of an LC circuit

$$\omega L = \frac{1}{\omega C}.$$

By rearranging the relation and considering a resonance frequency of 1 MHz (f_0), it is possible to derive the value of the equivalent inductance of the filter as

$$L_{filter} = \frac{1}{4\pi^2 {f_0}^2 C_{stray_{LV/LV}}} = \frac{1}{4\pi^2 (1 \cdot 10^6)^2 900 \cdot 10^{-12}} \approx 28.145\ \mu H.$$

Since the electrical configuration of Configuration #2 + filter is equal to the one of Configuration #2, with the exception of the filters, the RF CM currents show the same path of Configuration #2. However, at 1 MHz the filter and the stray capacitance of each LV/LV transformer, parallel connected, show an antiresonant behavior, resulting in a strong increase of their equivalent impedance. For this reason, the currents which in Configuration #2 circulated through each $C_{stray_{LV/LV}}$ in Solution #3 are strongly reduced.

6.4.3.1 Frequency domain

The analysis in the frequency domain of the electrical scheme of Figure 6. 39 follows the same procedure of Configuration #2, focusing on the most relevant aspects that the introduction of the filter produces in the system, especially considering the worst case in which I_{PG} and I_{ISEG} assume the higher value. As in Configuration #2, the RF-AMP operating parameters are approximately equal to the 6.4.1.1.1 estimated ones.

6.4.3.1.1 Results of the RF common mode current analysis

Figure 6. 41 and Figure 6. 42 show respectively the trend of I_{PG} and I_{ISEG} in the four operating conditions considered in 6.4.1.1.2 and in 6.4.2.1.1 (single RF-AMP ON, others OFF).

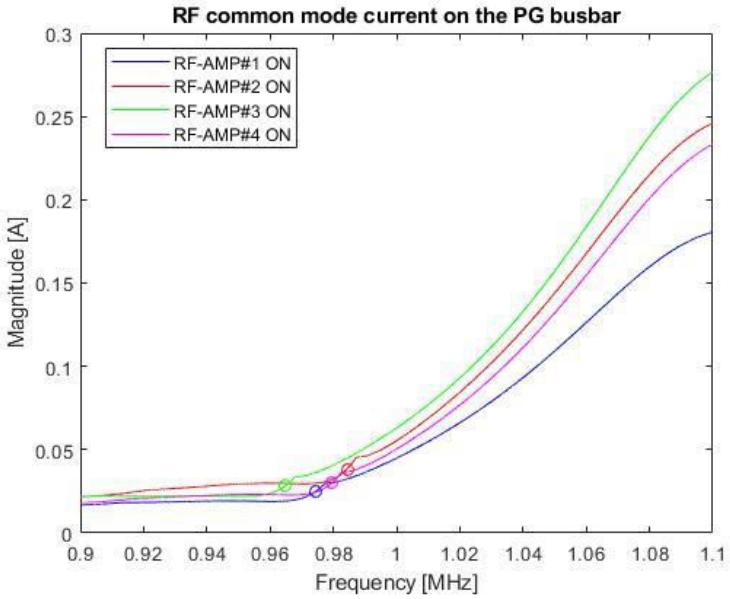

Figure 6. 41 *RF common mode current on the PG busbar (Configuration #2 + filter)*

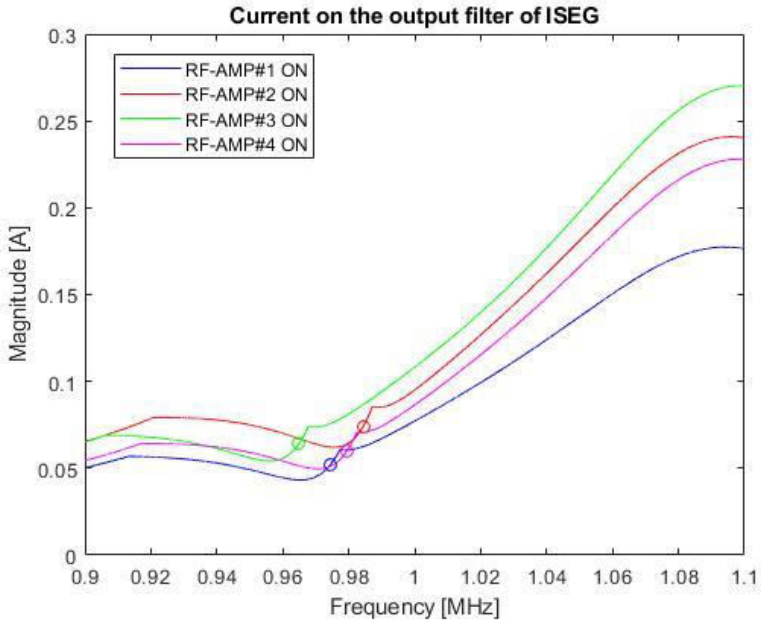

Figure 6. 42 *Current on the output filter of ISEG (Configuration #2 + filter)*

The two figures clearly highlight the beneficial effect resulting from the introduction of the filter: the resonant peak in the magnitude of both I_{PG} and I_{ISEG}(at ~1 MHz) isremoved. In particular, the trends of I_{PG} and I_{ISEG} show, for all the four RF-AMP, the lowest values between 0.9 MHz and~0.98 MHz (except for the RF-AMP #3 for which the lowest values are obtained between 0.9 MHz and 0.96 MHz). Then, they start to increase until 1.1 MHz. The maximum values of I_{PG} and I_{ISEG} are obtained at 1.1 MHz, when RF-AMP #3 is ON and the others are OFF, and they are respectively equal to ~0.28 A and ~0.27 A. These maximum values are extremely lower than the ones of Configuration #2, respectively equal to ~7.2 A and ~2.1 A, reached in correspondence of the resonance peak (~1 MHz), when the RF-AMP #2 is ON (see 6.4.2.1.1)

The interesting aspect is that, with Configuration #2 + filter the maximum values are even lower than the ones estimated in Configuration #1, since I_{ISEG} (which in Configuration #1 corresponds to I_{PG}) reaches ~1.39 A at 1.1 MHz when RF-AMP #3 is ON. However, considering the optimal operating frequency of each RF-AMP (circular markers in Figure 6. 41 and Figure 6. 42), the worst condition is achieved when the RF-AMP #2 is ON (the next analysis will be referred to this condition). In particular, I_{PG} has a magnitude of ~0.04 A and I_{ISEG} has a magnitude of ~0.07 A, at the optimal operating frequency of RF-AMP #2 (0.985 MHz). It is interesting to notice that with the introduction of the filters, the magnitude of the RF CM current circulating on the PG busbar is lower than the magnitude of the current on the ISEG output filter.

At this point it is possible to evaluate the distribution of the current at node A and node B of the electrical circuit of Configuration #2 + filter (these nodes corresponds to the ones represented in Figure 6. 32 for Configuration #2). Figure 6. 43 shows the trends of the three currents reaching node A, with RF-AMP #2 ON: I_{PG}, I_{ISEG} and $I_{LV/LV}$ (the same currents described in Configuration #2). The red dashed line highlights the magnitude and the phase of the three currents in correspondence of the optimal operating frequency of RF-AMP #2 (0.985 MHz).

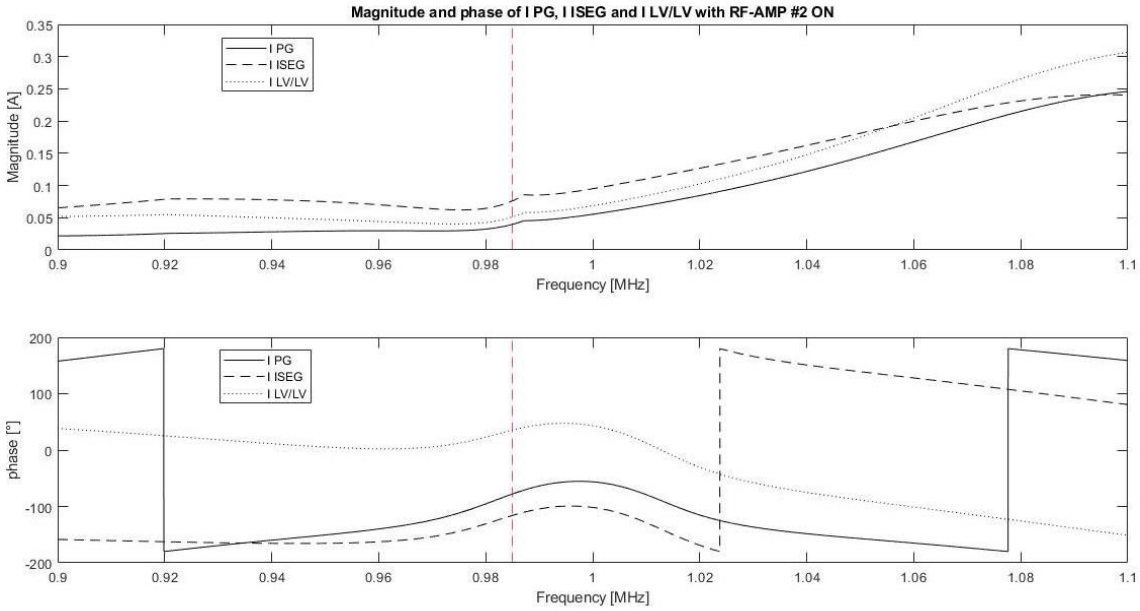

Figure 6. 43 *Magnitude (upper plot) and phase (bottom plot) of* $\boldsymbol{I_{PG}}$, $\boldsymbol{I_{ISEG}}$ *and* $\boldsymbol{I_{LV/LV}}$ *with RF-AMP #2 ON (Configuration #2 + filter)*

In the same way, the magnitude and the phase of the currents reaching node B, I_{Beams}, $I_{MV/LV}$ and I_{ISEG} (the same currents described in Configuration #2), when RF-AMP #2 is ON, are shown in Figure 6. 44.

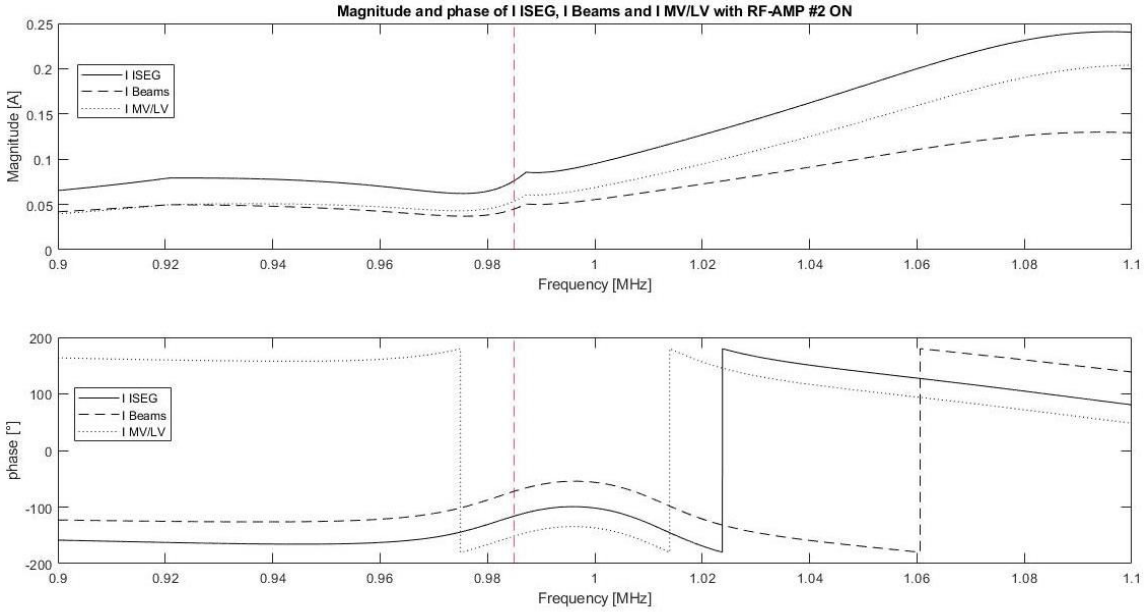

Figure 6. 44 *Magnitude (upper plot) and phase (bottom plot) of* $\boldsymbol{I_{ISEG}}$, $\boldsymbol{I_{Beams}}$ *and* $\boldsymbol{I_{MV/LV}}$ *with RF-AMP #2 ON (Configuration #2 + filter)*

6.4.3.2 Time domain analysis

The time domain analysis of the RF CM currents of the electrical scheme of Figure 6. 39, for Configuration #2 + filter, follows the same steps of Configuration #2. Since, as in Configuration #1 and #2, the evolution of I_{PG} and I_{ISEG} over time show the same pattern in the four conditions when a single RF-AMP works at its optimal operating frequency, at full power, the analysis will be focused on the worst condition, which corresponds to RF-AMP #2 ON. Then will be discussed the condition for which all the RF-AMP are operating together at their optimal frequency, at full power, which corresponds to the most severe condition for the system, from a RF CM currents point of view. In Table 6. 9 are portrayed the RF-AMP operating parameters for the Configuration #2 + filter which are essentially equal to the previous simulations ones.

Table 6. 9 *Output voltage, current and active power of the RF-AMP of each RF circuit, at the minimum ρ frequency, at full power for Configuration #2 + filter*

	ρ minimum frequency [MHz]	Output voltage [V]	Output current [A]	Output active power [kW]
RF-AMP #1	0.975	3162	52.8	162
RF-AMP #2	0.985	3162	53.6	163.9
RF-AMP #3	0.965	3162	52.7	161.9
RF-AMP #4	0.979	3162	52.1	157.9

6.4.3.2.1 Results of the RF common mode current analysis

Figure 6. 45 and Figure 6. 46 show respectively the evolution of I_{PG} and I_{ISEG} over time when RF-AMP #2 works at it optimal operating frequency (0.985 MHz) at full power and their spectrum in frequency obtained by applying the FFT to the signals.

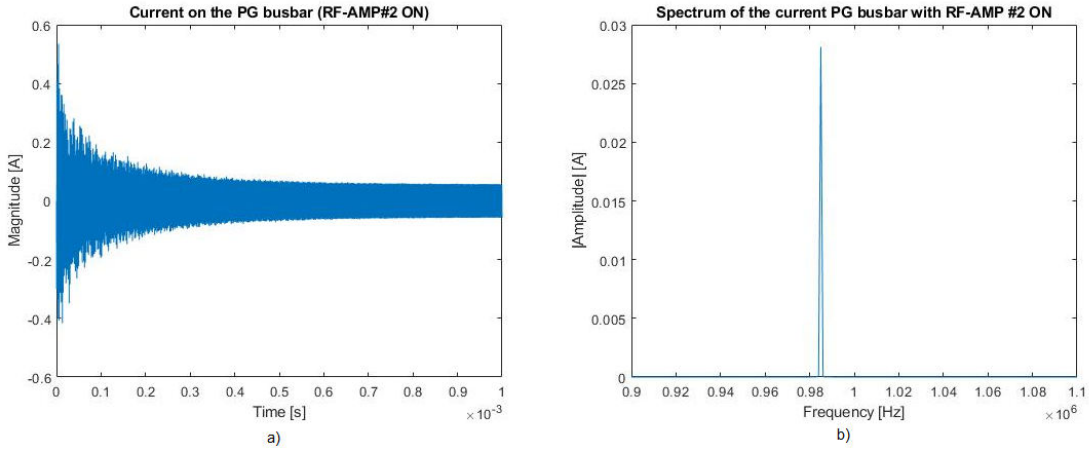

Figure 6. 45 *Evolution of the current on the PG busbar over time (a) and related FFT (b) with RF-AMP #2 ON (Configuration #2 + filter)*

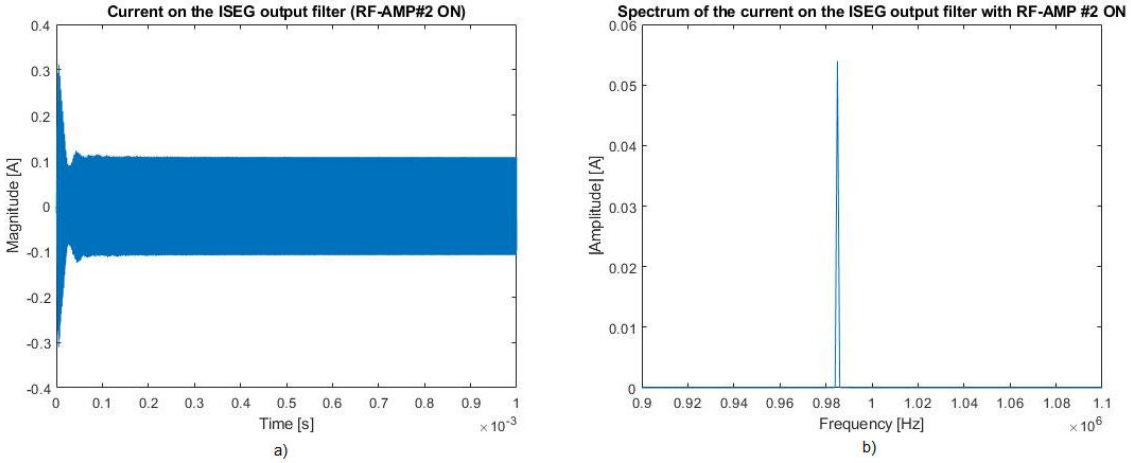

Figure 6. 46 *Evolution of the current on the ISEG output filter over time (a) and related FFT (b) with RF-AMP #2 ON (Configuration #2 + filter)*

It is possible to observe that, with the introduction of the filter, the duration of the initial transient has been reduced compared to Configuration #2, since the overall capacitance of the electrical circuit is partially compensated by the inductance of the filter. As expected, the FFT of I_{PG} and I_{ISEG} shows the presence of a single harmonic at 0.985 MHz, which corresponds to the operating frequency of the RF-AMP #2. In Table 6. 10 are provided the RMS values of I_{PG} and I_{ISEG}, which has been estimated after the initial transient, in steady state condition, for all the operating condition with just one RF-AMP on at time. The results underline that, as aforementioned, the worst condition is when RF-AMP #2 is ON. Furthermore, they highlight that, in Configuration #2 + filter, the RMS values of I_{PG} are lower than Configuration #2 ones, while the RMS values of I_{ISEG} are slighty higher. This is valid for all the RF-AMP conditions, except for the condition for which RF-AMP #3 is ON: in this case the I_{PG} RMS value in Configuration #2 + filter is higher than Configuration #2 one and the I_{ISEG} RMS value of Configuration #2 + filter is distinctly higher than the Configuration #2 one (see Table 6. 7). However, the RMS value of I_{ISEG} when RF-AMP #3 is ON is lower than the one measured in Configuration #1 (see Table 6. 4).

Table 6. 10 *RMS value of the current on the ISEG output filter for each of the four RF-AMP conditions (Configuration #2 + filter)*

RF-AMP ON	RMS value of the current on the PG busbar [A]	RMS current value on the ISEG output filter [A]
RF-AMP#1	0.026	0.053
RF-AMP#2	0.04	0.076
RF-AMP#3	0.029	0.064
RF-AMP#4	0.029	0.059

The same analysis has been provided for the combined operation of the four RF-AMP, at their specific operating frequency, at full power. The results, represented in Figure 6. 47 (I_{PG}) and Figure 6. 48 (I_{ISEG}).

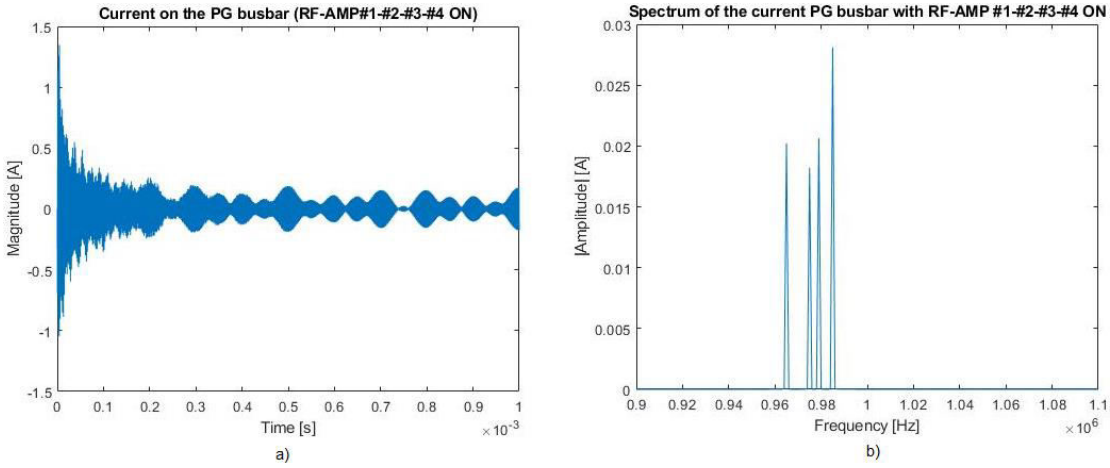

Figure 6. 47 *Evolution of the current on the PG busbar when all the RF-AMPs are operating at the same time (a) and FFT (b) (Configuration #2 + filter)*

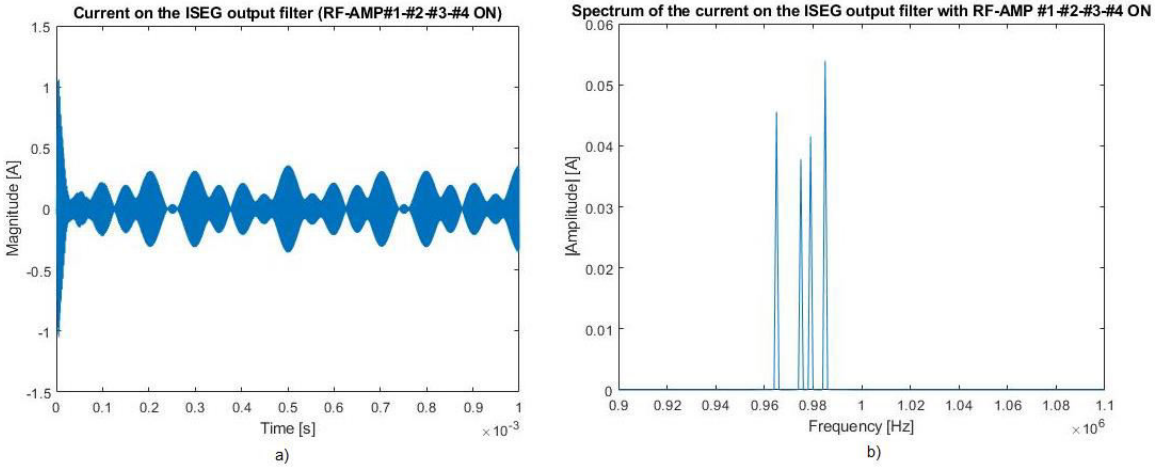

Figure 6. 48 *Evolution of the current on the ISEG output filter when all the RF-AMPs are operating at the same time (a) and FFT (b) (Configuration #2 + filter)*

By comparing these results to the ones obtained in Configuration #2 (Figure 6. 37 and Figure 6. 38), it is possible to observe a reduction in the initial transient of I_{PG} and I_{ISEG}, as observed in the analysis of Figure 6. 45 and Figure 6. 46. The FFT, as expected, shows the presence of just four harmonic corresponding to the operating frequency of each RF-AMP. The estimation of the RMS value of these two currents, in steady state condition, at ~1 MHz, provides ~63 mA for I_{PG} and ~128 mA for I_{ISEG}. In particular I_{ISEG} is significantly lower than the targeted limit of 500 mA required for preventing overheating on the passive components of the ISEG output filter.

Finally, even for this simulation, it has been estimated the RMS values of the voltage on the stray capacitances between the screens of the MV/LV transformer and of each LV/LV transformer and also on the stray capacitances between the insulating beams of each RF-AMP and the floor of the HVD. The results are shown in Table 6. 11.

Table 6. 11 *Voltage RMS value on the stray capacitance of the insulating beams, the four LV/LV transformers and the MV/LV transformer (Configuration #2 + filter)*

	Voltage RMS value [V]
stray capacitance insulating beam #1	26.15
stray capacitance insulating beam #2	29.43
stray capacitance insulating beam #3	27.65
stray capacitance insulating beam #4	26.73
stray capacitance between screens of LV/LV transformer #1	26.48
stray capacitance between screens of LV/LV transformer #2	30.95
stray capacitance between screens of LV/LV transformer #3	28.21
stray capacitance between screens of LV/LV transformer #4	26.65
stray capacitance between screens of MV/LV transformer	9.63

It is possible to highlight a strong reduction in the RMS voltage values on all the stray capacitances, especially with respect to Configuration #2 (except for the RMS value of the voltage on the stray capacitance of the MV/LV transformer which is slightly higher than the Configuration #2 one). In particular, it is interesting to focus on the voltage on the stray capacitance of the LV/LV transformer. In fact, the antiresonance obtained by introducing the filter in parallel to the stray capacitance, tuned to 1 MHz, would be expected to induce an extremely high voltage value on the equivalent impedance of L_{filter} and $C_{stray_{LV/LV}}$. On the contrary, the effect of the introduction of the filter has proved to be the opposite, thus limiting the voltage RMS to quite low values.

6.4.4 Comparison of the simulations results

In order to complete the analysis, a comparison between the results of the three configurations explored with all the RF-AMP operating together have been provided in Table 6. 12 (I_{PG} and I_{ISEG} RMS values) and in Table 6. 13 (voltage RMS values on the stray capacitance of the circuit), taking into account also the results of the common mode current analysis obtained with the RF-OSC, in chapter 5.

Table 6. 12 *Comparison on the RF CM currents RMS values*

	Current RMS value [A]			
	RF-OSC	CONFIG. #1	CONFIG. #2	CONFIG. #2 + FILTER
Current on the PG busbar	7.56	0.3	0.305	0.063
Current on the ISEG output filter	7.56	0.3	0.091	0.128

Table 6. 13 *Comparison on the voltage RMS values on the stray capacitance of the circuit*

	Voltage RMS value [V]		
	CONFIG. #1	CONFIG. #2	CONFIG. #2 + FILTER
Stray capacitance insulating beam #1	75.05	203.55	26.15
Stray capacitance insulating beam #2	70.12	229.63	29.43
Stray capacitance insulating beam #3	100.62	190.65	27.65
Stray capacitance insulating beam #4	94.58	183.34	26.73
Stray capacitance between screens of 400V/210V transformer #1	\	201.79	26.48
Stray capacitance between screens of 400V/210V transformer #2	\	231.29	30.95
Stray capacitance between screens of 400V/210V transformer #3	\	192.15	28.21
Stray capacitance between screens of 400V/210V transformer #4	\	181.82	26.65
Stray capacitance between screens of 6.6kV/210V transformer #1	56.26	\	\
Stray capacitance between screens of 6.6kV/210V transformer #2	61.37	\	\
Stray capacitance between screens of 6.6kV/210V transformer #3	66.23	\	\
Stray capacitance between screens of 6.6kV/210V transformer #4	56.27	\	\
Stray capacitance between screens of 6.6kV/400V transformer	\	6.84	9.63

The results obtained with the RF-OSC are extremely higher compared to the RF-AMP ones, for all the simulations. As aforementioned in chapter 5, the solution with the CVD on the secondary side of the RF-OSC output transformer is not the right solution and the RF CM currents RMS values could be reduced by shifting the CVD on the primary side, but further verification are under investigation. Differently from the oscillators, where the optimal operating frequency is in practice unreachable due to the frequency flip phenomenon, the amplifiers are able to operate at this frequency. For this reason, the results obtained through the simulations of 6.4 could be directly compared to the future experimental ones. By observing the results obtained through the simulations of the three configurations with the RF-AMP, it is possible to highlight that the best results corresponds to the ones of Configuration #2 + filter, both as regard the RF CM currents and the voltage on the stray capacitances of the insulating beams with respect to the HVD and between the transformers screens. Even if the lowest RMS value of the current on the ISEG output filter has been obtained with Configuration #2, the presence of the resonance at ~1 MHz prevents from selecting this solution for the integration of the RF-AMP in the HVD. Furthermore, Configuration #2 produces the highest voltage RMS values on the stray capacitances of the insulating beams and on the stray capacitances between the screens of the LV/LV transformers. For this reason the Configuration #2 + filter is the better solution for the integration of the RF-AMP in the SPIDER system. However, further analysis especially as regard the sizes and the weights of the components of the system (especially MV/LV transformers, LV/LV transformers and the RF amplifiers) must be realized in order to verify the feasibility of the integration in the HVD.

7 Conclusion

Currently, the RF system for heating the plasma within the ion source of SPIDER is based on tetrodes oscillators. This solution revealed several issues, especially in terms of frequency instability, thus requiring the study of alternative solutions. In this thesis, an RF system based on solid-state RF amplifiers solution has been studied and a conceptual design of the RF power generation based on amplifiers for the ion source of SPIDER has been proposed.

An initial analysis has been dedicated to the characterization of the RF load in order to understand its nature and its behavior against frequency. The results of the characterization of the RF load highlight a resonant behavior and the importance of operating in matching condition (at the minimum ρ frequency) in order to deliver the rated RF power to the antennas of the drivers with low stress on the components of the circuit. Furthermore, in this condition, it has been verified that the uncertainties on the estimation of the parameters of the antennas of the drivers, with plasma, are minimum. These results highlight the need for a RF power generator stable in frequency and they are useful for the definition of its requirements.

The goal of the study is to provide an RF amplifier able to provide the rated 200 kW on a resistive impedance of 50 Ω, required for the proper operation of the ion source of SPIDER. The solution proposed in this thesis is based on a modular scheme for the RF amplifier implementing H-bridge, Class D voltage-switching topology modules with MOSFETs. This solution is resulting from the need for working at the high frequency of ~1 MHz with an high efficiency of about 90%. This is allowed by the switching topology and by the implementation of MOSFETs as switching devices. The latter ensure the high switching speed required by the operating frequency of the system but they have low power performances. For this reason, each module is foreseen for delivering about 1.1 kW, so that an overall of 180 modules is required, thus reducing the overall power handled by each MOSFET. The MOSFETs of each H-bridge module are driven through bipolar PWM and their control signal is provided by a specific circuit consisting of a square waveform signal generator and a pre-amplifying stage. In order to provide this signal to all the modules, a single-primary, multi-secondary transformer is foreseen. Special attention was given also to the output stage of the RF amplifier which is interfacing with the transmission line and then the load of the RF circuit. In order to add the output power of each module for producing the rated 200 kW, a combiner is foreseen. Moreover, a pass-band filter properly tuned in the range 0.8÷1.2 MHz has been designed in order to obtain a similar sinusoidal waveform in all the operating frequency range of SPIDER (0.9÷1.1 MHz). In order to provide an output power of 1.1 kW, each module has to be fed by 260 V DC from a proper power supply system, derived from the 6.6 kV bar of the Ion Source and Extraction Grid Power Supplies (ISEPS). For this reason a three-phase transforming stage from 6.6 kV to 210 V AC and a rectification stage consisting of a three-phase diode rectifier and a Buck converter have been foreseen.

It has been developed also the conceptual design of an active power and frequency control loop. The former has been realized through a negative feedback control loop by deriving the output power measurement from a dual directional coupler. The active power error, obtained by comparing the measurement to the reference active power value, is provided to a PID in order to obtain correction signal which is applied to the driving circuit of the MOSFET of the Buck converter, thus changing the duty cycle, and then the DC output voltage of the Buck converter and the output power of the RF amplifier modules. For the frequency control loop, instead, thanks to the intrinsic frequency stability of the amplifier, an open loop control is foreseen. It acts by changing the frequency of the output square waveform signal for the control of the MOSFET, thus controlling the switching frequency of the amplifier modules.

In addition, the integration of the RF amplifier solution within the system of SPIDER has been studied. The amplifiers shall be integrated within a system of power supplies (ISEPS) inside the HVD and several alternative electrical schemes for their implementation are discuss also considering the insulation requirement with respect to the HVD. In this thesis, two different solutions have been considered, especially in order to evaluate the impact of the RF common mode currents: the former is consisting of four 6.6 kV/210 V three-phase, three-windings transformers, each feeding the rectification stage of the amplifier of each of the four RF circuits; the latter is consisting of a single 6.6 kV/400 V three-phase transformer feeding four 400 V/210 V three-phase, three-windings transformers dedicated to the power supply of the rectification stage of the amplifier of the 4 RF circuits.

These two solutions have been simulated in frequency and time domain in order to study the RF common mode currents in the SPIDER ion source power circuit and their impacts on the components of the circuit. The former solution shows good results with low values of the current circulating on the output filter of ISEG (∼300 mA), quite below the estimated limit of 500 mA for preventing the overheating of the passive components of the filter. In addition, also the voltage on the stray capacitances of the main components of the circuit (MV/LV transformers electrostatic screen and insulating beams) are quite low (about 60÷70 V). The second solution has shown critical values for the RF common mode currents since, at ∼1 MHz, a resonance phenomenon between the stray capacitances of the LV/LV transformers and the equivalent inductance of the transmission line appeared. In order to solve this issue, a filter properly tuned to 1 MHz has been inserted parallel to the stray capacitance between the screens of each LV/LV transformer. This solution has provided the best results in terms of RF common mode currents circulations (∼140 mA on the ISEG output filter) and very low voltage RMS values have been estimated between the screens of the LV/LV transformers (∼30 V). This is an interesting result since a high increase in voltage was expected due to the anti-resonance between the stray capacitance between the screens of the LV/LV transformer and the filter. This last solution is the most suitable alternative for the integration of the RF amplifiers in SPIDER, from an RF common mode currents point of view. However further analysis in terms of weight, layout and cooling requirements shall be done in order to validate this solution.

In summary, solid-state RF amplifier can provide several benefits with respect to the actual tetrodes based oscillator technology since it has an higher efficiency, over 90%, it allows to work at the desired frequency, without running into frequency flips and allowing to work at the matching condition, ensuring also a secure availability of its components in future. The experimental demonstration of the applicability of this technology will be a fundamental step in the path towards energy production based on thermonuclear fusion, with the possibility to be already implemented in ITER NBI, in the perspective of being integrated in the new NBI which will be studied for DTT, and then DEMO.

APPENDIX

A. Derivation of the RF load impedance

Assuming a distributed parameter line's model and the hypothesis of a lossless line, which is a good approximation of the real RF line, the characteristic impedance $\boldsymbol{z_0}$ and the propagation constant $\boldsymbol{k}$arecalculated from the following transmission line parameters per unit length for a coaxial cable:

- $r = \frac{1}{\sigma_m \delta}\left(\frac{1}{2\pi a} + \frac{1}{2\pi b}\right)$resistance per unit length
- $l = \frac{\mu_0}{2\pi} ln\left(\frac{b}{a}\right)$ inductance per unit length
- $g = \frac{2\pi\sigma_d}{ln\left(\frac{b}{a}\right)}$ conductance per unit length
- $c = \frac{2\pi\varepsilon_0\varepsilon_r}{ln\left(\frac{b}{a}\right)}$capacitance per unit length

where a is the outer diameter of the inner conductor, b is the inner diameter of the shield, σ_{Cu} is the conductivity of copper, σ_d is the conductivity of dielectric (in this case air), ε_0 is the vacuum permittivity,ε_r is the relative permittivity andδ is the skin depth.

For a copper air filled 3" 1/8 rigid coaxial transmission line, a = 33.4 mm and b = 76.9 mm. Furthermore, since the dielectric is air, the conductivity σ_d is approximately equal to zero, thus g≈0 and considering the assumption of a lossless transmission line r≈0.

At this point, introducing the kilometric impedance z and the kilometric admittance y as:

- $\boldsymbol{z} = r + j\omega l$ kilometric impedance
- $\boldsymbol{y} = g + j\omega c$ kilometric admittance

which in this specific case will become

$$\boldsymbol{z} = 0 + j\omega l$$

$$\boldsymbol{y} = 0 + j\omega c$$

where $\omega = 2\pi f$ is the angular frequency

finally, it is possible to calculate

- $\boldsymbol{z_0} = \sqrt{\frac{z}{y}}$ characteristic impedance

- $\boldsymbol{k} = \sqrt{\boldsymbol{zy}}$ propagation constant

that under the hypothesis of lossless line become scalars

$$z_0 = \sqrt{\frac{l}{c}}$$

$$k = \sqrt{lc}.$$

At this point, it is possible to evaluate the RF-Load using the Telegrapher's Equation. As already mentioned, considering a distributed parameter line's model and assuming that x is the reference axis along the line length, it is possible to focus on an infinitesimal line segment in the x direction, between a generic x position and its infinitesimal increment x + dx. This section of the line can be described by the aforementioned parameters per unit length and the equivalent circuit shown in Figure A. 1, where the subscript 's' stands for the start of the line, the subscript '*a*' stands for the arrive of the line and the origin of the x-axis system is at the output port.

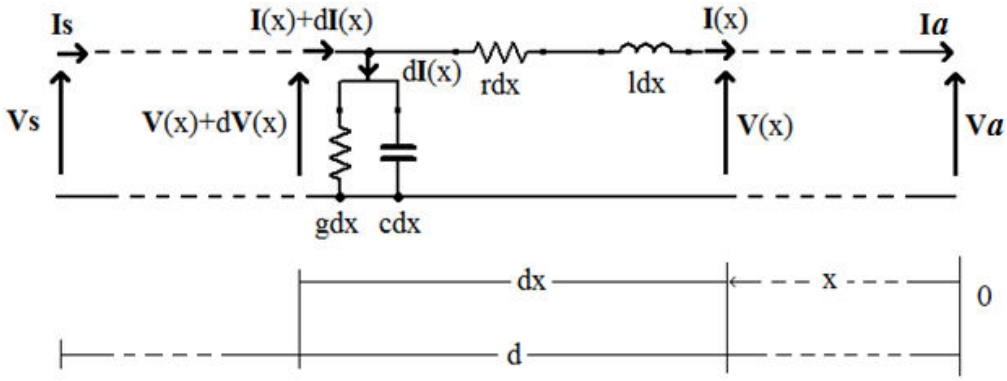

Figure A. 1*Transmission line's reference scheme per unit length*

According to this scheme, the longitudinal impedance and the transversal admittance are:

$$\boldsymbol{z}dx = (r + j\omega l)dx$$

$$\boldsymbol{y}dx = (g + j\omega c)dx.$$

The voltage drop and the current increment on the infinitesimal line segment are respectively

$$d\boldsymbol{V}(x) = \boldsymbol{I}(x)\boldsymbol{z}dx$$

$$d\boldsymbol{I}(x) = [\boldsymbol{V}(x) + d\boldsymbol{V}(x)]\boldsymbol{y}dx$$

and, neglecting the term $d\boldsymbol{V}(\boldsymbol{x})\boldsymbol{y}dx$ as a higher order infinitesimal, they can be rewrite as the so called telegrapher's equations:

$$\frac{d\boldsymbol{V_x}}{dx} = \boldsymbol{zI_x}$$

$$\frac{d\boldsymbol{I_x}}{dx} = \boldsymbol{yV_x}$$

The solution of these equations can be written as

$$\boldsymbol{V_x} = \boldsymbol{V_a}\, cosh\, \boldsymbol{kx} + \boldsymbol{I_a z_0}\, sinh\, \boldsymbol{kx}$$

$$\boldsymbol{I_x} = \boldsymbol{V_a}\frac{sinh\, \boldsymbol{kx}}{\boldsymbol{z_0}} + \boldsymbol{I_a}\, cosh\, \boldsymbol{kx}$$

introducing the hyperbolic functions and recalling $\boldsymbol{z_0}$ and $\boldsymbol{k}$ (that in this specific case are scalars, as mentioned before).

This result is fundamental for the evaluation of the RF-Load impedance: through these equations it is possible to define the impedance $\boldsymbol{Z_x}$ as it is seen from a generic section at distance x from the output port. So the situation must be like the one highlighted in Figure A. 2, considering a generic load at the end of the line.

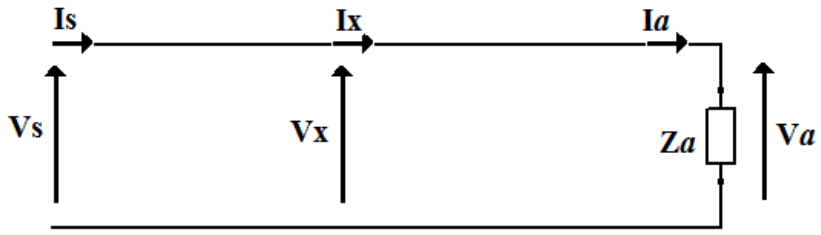

Figure A. 2*Transmission line ending on a generic load* $\boldsymbol{Z_a}$

In the RF circuit, downstream the coaxial transmission line, there is not a generic load but the sum of the matching network and the drivers impedance (Figure A. 3). Therefore, it is necessary to define the equivalent impedance of the drivers and the matching networks.

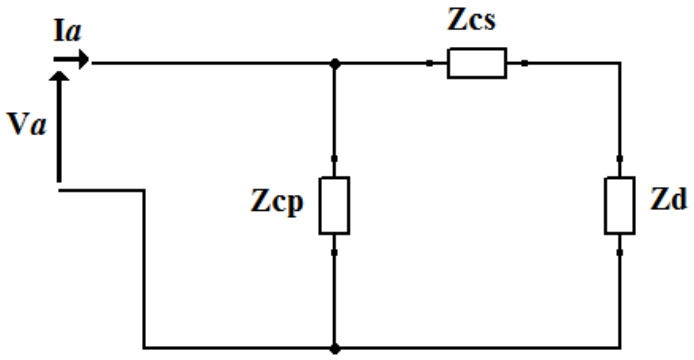

Figure A. 3*Scheme of the matching network and driver impedances at the output port*

According to this scheme:

- $\boldsymbol{Z_{cs}} = \frac{1}{j\omega Cs}$ equivalent impedance of the series capacitors
- $\boldsymbol{Z_{cp}} = \frac{1}{j\omega Cp}$ impedance of the parallel capacitor
- $\boldsymbol{Z_d} = 2R_d + 2j\omega L_d$ equivalent impedance of the two drivers

At this point, it is possible to evaluate the series impedance of $\boldsymbol{Z_{cs}}$ and $\boldsymbol{Z_d}$ and then the parallel impedance, obtaining the equivalent impedance as it seen at the end of the coaxial transmission line

$$\boldsymbol{Z_a} = \frac{(\boldsymbol{Z_{cp}})(\boldsymbol{Z_{cs}} + \boldsymbol{Z_d})}{\boldsymbol{Z_{cp}} + \boldsymbol{Z_{cs}} + \boldsymbol{Z_d}}$$

Finally, considering that the impedance $\boldsymbol{Z_x} = \frac{\boldsymbol{V_x}}{\boldsymbol{I_x}}$ of the generic section at distance x from the output port of the line is equal to

$$\boldsymbol{Z_x} = \boldsymbol{z_0}\frac{\boldsymbol{Z_a}\cosh \boldsymbol{k}x + \boldsymbol{z_0}\sinh \boldsymbol{k}x}{\boldsymbol{Z_a}\sinh \boldsymbol{k}x + \boldsymbol{z_0}\cosh \boldsymbol{k}x}$$

substituting the entire length of the line, d, instead of the generic x position provides the expression of the impedance as it is seen by the RF-Generator

$$\boldsymbol{Z_{RF-Load}} = \boldsymbol{z_0}\frac{\boldsymbol{Z_a}\cosh \boldsymbol{k}d + \boldsymbol{z_0}\sinh \boldsymbol{k}d}{\boldsymbol{Z_a}\sinh \boldsymbol{k}d + \boldsymbol{z_0}\cosh \boldsymbol{k}d}$$

B. Derivation of the reflection coefficient equation

Starting from the solutions of the Telegrapher's equation obtained in appendix A, and substituting the Euler-Lambert's relations

$$\cosh \boldsymbol{kx} = \frac{e^{\boldsymbol{kx}} + e^{-\boldsymbol{kx}}}{2}$$

$$\sinh \boldsymbol{kx} = \frac{e^{\boldsymbol{kx}} - e^{-\boldsymbol{kx}}}{2}$$

it is possible to obtain

$$\boldsymbol{V_x} = \boldsymbol{V_a}\frac{e^{\boldsymbol{kx}} + e^{-\boldsymbol{kx}}}{2} + \boldsymbol{I_a z_0}\frac{e^{\boldsymbol{kx}} - e^{-\boldsymbol{kx}}}{2}$$

$$\boldsymbol{I_x} = \frac{\boldsymbol{V_a}}{\boldsymbol{z_0}}\frac{e^{\boldsymbol{kx}} - e^{-\boldsymbol{kx}}}{2} + \boldsymbol{I_a}\frac{e^{\boldsymbol{kx}} + e^{-\boldsymbol{kx}}}{2}$$

which can be rewrite as

$$\boldsymbol{V_x} = \frac{\boldsymbol{V_a} + \boldsymbol{z_0 I_a}}{2}e^{\boldsymbol{kx}} + \frac{\boldsymbol{V_a} - \boldsymbol{z_0 I_a}}{2}e^{-\boldsymbol{kx}}$$

$$\boldsymbol{I_x} = \frac{\boldsymbol{V_a} + \boldsymbol{z_0 I_a}}{2\boldsymbol{z_0}}e^{\boldsymbol{kx}} - \frac{\boldsymbol{V_a} - \boldsymbol{z_0 I_a}}{2\boldsymbol{z_0}}e^{-\boldsymbol{kx}}.$$

It is clear that these two equations completely describe the sinusoidal regime in every point of the transmission line, once the voltage and current at the output port are known. Hence, defining $\boldsymbol{V_1} = \frac{\boldsymbol{V_a + z_0 I_a}}{2}$ and $\boldsymbol{V_2} = \frac{\boldsymbol{V_a - z_0 I_a}}{2}$ it is possible to obtain the simplified form of these equations

$$\boldsymbol{V_x} = \boldsymbol{V_1}e^{\boldsymbol{kx}} + \boldsymbol{V_2}e^{-\boldsymbol{kx}} = \boldsymbol{V_{1x}} + \boldsymbol{V_{2x}}$$

$$\boldsymbol{I_x} = \frac{\boldsymbol{V_1}}{\boldsymbol{z_0}}e^{\boldsymbol{kx}} - \frac{\boldsymbol{V_2}}{\boldsymbol{z_0}}e^{-\boldsymbol{kx}} = \frac{\boldsymbol{V_{1x}} - \boldsymbol{V_{2x}}}{\boldsymbol{z_0}}.$$

recalling the propagation constant as $\boldsymbol{k} = k' + jk'$, highligthing the real and imaginary part. Increasing x, the vector $\boldsymbol{V_{1x}} = \boldsymbol{V_1}e^{k'x} + \boldsymbol{V_1}e^{jk''x}$ is progressively anticipated in phase compared to $\boldsymbol{V_1}$ due to the effect of jk'' (k'' is called phase constant) and attenuated towards the output port due to the effect of k' (attenuation constant). Figure B. 1 shows that the effect of the anticipation of the phase of vectors $\boldsymbol{V_{1x}}$ with the increase of x. These vectors $\boldsymbol{V_{1x}}$can be imagined as vectors rigidly rotating around x-axis at the same angular velocity, which corresponds to the angular frequency ω. The projections of these vectors towards the z-axis, perpendicular to the x-axis, describe a sinusoidal distribution of the instantaneous values of voltage. This aspect, over time, produces a motion of this sinusoidal distribution towards the output port (in Figure B. 1 the attenuation effect is neglected). For this reason $\boldsymbol{V_{1x}}$is called progressive wave (V_{progr}). Following the same logic, $\boldsymbol{V_{2x}}$is a wave that attenuates towards the input port and it moves

from the output port to the input port, so it is called reflected wave (V_{refl}). The superposition of the progressive wave and the reflected wave, $\boldsymbol{V_x}$ provides the values of voltage in every point of the transmission line, and finally the voltage standing wave. Dividing $\boldsymbol{V_x}$ by $\boldsymbol{z_0}$, the current in every point of the trasmission line $\boldsymbol{I_x}$ is obtained as well.

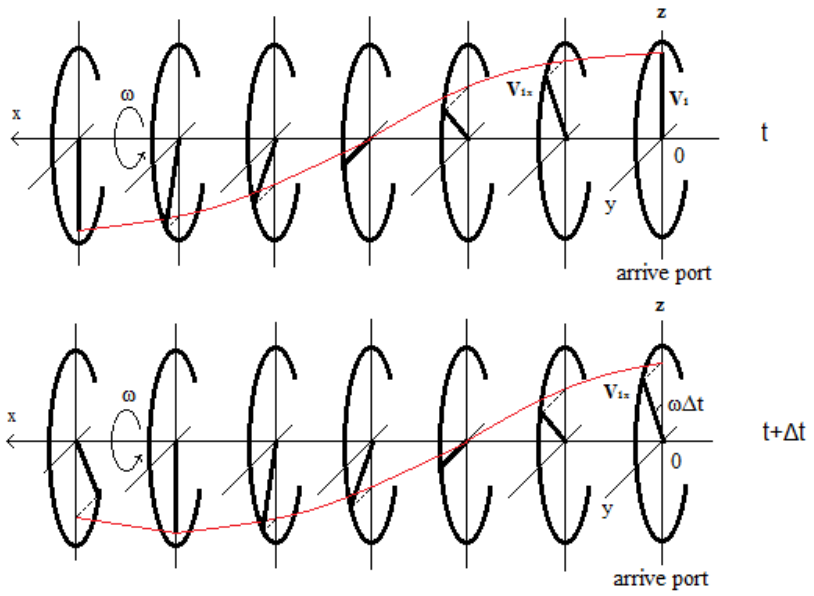

Figure B. 1*Scheme of the propagation of a progressive wave, neglecting the attenuation constant*

At this point, it is possible to determine the reflection coefficient as the ratio between the reflected wave $\boldsymbol{V_{2x}}$and the progressive wave $\boldsymbol{V_{1x}}$

$$\boldsymbol{\rho = \frac{V_{2x}}{V_{1x}} = \frac{V_2 e^{-kx}}{V_1 e^{kx}} = \frac{V_a - z_0 I_a}{V_a + z_0 I_a} e^{-2kx}}$$

and, considering $x = 0$ and substituting $\boldsymbol{V_a = Z_a I_a}$ inside the equation, it can be write only as a function of the characteristic impedance $\boldsymbol{z_0}$ and the generic impedance at the output port as

$$\boldsymbol{\rho = \frac{Z_a - z_0}{Z_a + z_0}}.$$

C. Measurement device: Dual directional coupler

A dual directional coupler is a 4 port passive device typically implemented as RF power measurement of travelling waves in transmission line [39]. Its diagram is represented in Figure C. 1 .

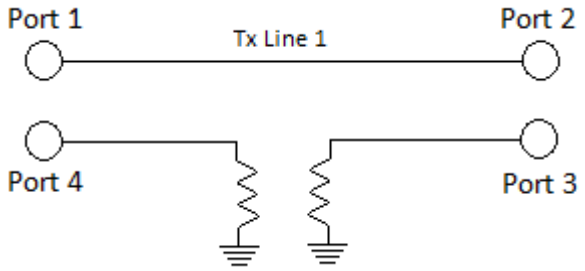

Figure C. 1*Dual directional coupler*

Port 1 and Port 2 are connected to the main transmission line, while Port 4 and Port 3, the coupled port, are terminated to an internal matched load (typically of 50 Ω). This configuration results in a forward coupled port (Port 4) and in a reverse coupled port (Port 3): the former allows to measuring the progressive voltage wave, V_{progr}, while the latter allows measuring the reflected voltage wave, V_{refl}, on the transmission line (see appendix B). Thanks to V_{prog} and V_{refl}, through a power sensor, the forward power, P_{forw}, and the reflected power, P_{refl} are obtained and then it is possible to derive the overall active power (see 4.3.4). The characteristics of a dual directional coupler [40] are defined considering Figure C. 1:

- the coupling factor (C), for the forward power measurement, C_{13}, is the ratio of the input power at port 1, P_1, to the power at the coupled port 3, P_3 (the same could be written for the coupling factor C_{24} for the reflected power measurement). It is an index of the amount of power that is collected by the coupled port compared to the overall power which moves towards the output port, and it can be express as

$$C_{13} = 10\log\left(\frac{P_1}{P_3}\right);$$

- the directivity (D) is the ratio of the power at the two coupled ports, P_3 and P_4, and it highlights the capability of the device of separating the opposite-travelling wave (forward and reflected ones) at the coupled ports. It is described as

$$D = 10\log\left(\frac{P_3}{P_4}\right);$$

- the isolation (I) is the ratio of the power at the input/output port (respectively port 1 and port 2) and the power at the opposite coupled port (respectively port 4 and port 3). It is an index of the power delivered to the specific uncoupled port and it is expressed as

$$I_{14} = 10\log\left(\frac{P_1}{P_4}\right);$$

- the Voltage Standing Wave Ratio (VSWR) is the key parameters for the definition of the matching condition of the system. It can be express through the reflection coefficient (see 4.3.1) as

$$VSWR = \frac{1 + |\boldsymbol{\rho}|}{1 - |\boldsymbol{\rho}|}.$$

  A VSWR = 1 implies that the system is perfectly matched and there is no reflected power.

The quality of the measurements is strongly relied upon the directivity and isolation factors and, thanks to dual directional coupler inherent structure, it is possible to achieve high values of these two parameters. In addition, the high directivity and high coupling factor are key features in order to derive reliable measurements of V_{forw} and V_{refl} for the negative feedback power control.

D. Estimation of the stray capacitance

The estimation of the stray capacitances which allows the circulation of the RF CM currents within the system has been realized through geometrical consideration.

Stray capacitance between the insulating beam and the HVD floor: it can be represented as a parallel plate capacitor with a surface A at distance d, with a dielectric between them with a dielectric constant ε, as it is shown in Figure D. 1. The capacitance value of this type of capacitor can be estimated as

$$C = \varepsilon \frac{A}{d} = \varepsilon_0 \varepsilon_r \frac{A}{d}$$

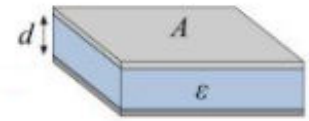

Figure D. 1*Parallel plate capacitor*

The insulating beams have been estimated to have a surface of 3.6 m^2, a height of 0.15 m and considering that the dielectric is air ($\varepsilon_r = 1$) it is possible to obtain a capacity of

$$C = (8.85 \times 10^{-12}) \cdot \frac{3.6}{0.15} \approx 200\ pF.$$

Stray capacitance between the screens of the three-phase, three-windings insulating transformer: by considering the height of the transformer column and the distance between its screens, it is possible to represents this stray capacitance as the capacitance of a cylindrical capacitor. It can be schematized as it is shown in Figure D. 2 where l is the height of the transformer, R_1 and R_2 are respectively the radius of the inner and outer screen and ε is the dielectric constant. The capacitance of this type of capacitor can be expressed as

$$C = 2\pi\varepsilon \frac{l}{\ln\left(\frac{R_2}{R_1}\right)} = 2\pi\varepsilon_0\varepsilon_r \frac{l}{\ln\left(\frac{R_2}{R_1}\right)}.$$

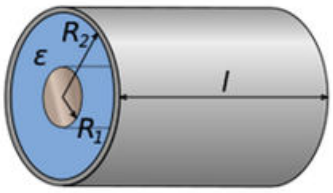

Figure D. 2*Cylindric capacitor*

This relation allows estimating the stray capacitance of the MV/LV and the LV/LV three-phase, three-windings insulating transformers implemented in the two RF amplifier power supply solutions discussed in 6.3.1 and 6.3.2. As regard the MV/LV transformer, which is epoxy resin insulated (ε_r = 3.25 at 1 kHz), it has been measured to have a column height of 1 m, a gap between the two screens of 0.1 m with an inner screen diameter of 0.35 m. The resulting stray capacitance between the screens, considering a single phase, is equal to

$$C = 2\pi \cdot 8.85 \times 10^{-12} \frac{1}{\ln\left(\frac{0.175}{0.125}\right)} \approx 500 \frac{pF}{phase}.$$

Hence, the overall stray capacitance of the MV/LV three-phase, three-winding transformer is equal to $3{\times}500\ \frac{pF}{phase}$ = 1500 pF. As regard the LV/LV tranformer, which is also epoxy resin insulated, it has been measured to have a column height of 0.4 m and gap between the screens of 0.05 m with a diameter of the inner screen of 0.2 m. The resulting stray capacitance between the screens is estimated to be $\approx 300\ \frac{pF}{phase}$, thus resulting in an overall stray capacitance of 900 pF.

8 References

[1] International energy outlook, 2019

[2] Oliver J.G.J and Peters J.A.H.W. (2019), "Trends in global C02 and total greenhouse gas emissions: 2019 report". PBL Netherlands Environmental Assessment Agency, The Hague. (Last updated 26 May 2020)

[3] Garry McCracken, Peter Stott, "Chapter 7 - Inertial-Confinement Fusion, Fusion (Second Edition)", Academic Press, pp. 67-81, 2013

[4] Fisenko Stanislav, Fisenko Igor. "The Conception of Thermonuclear Reactor on the Principle of Gravitational Confinement of Dense High-temperature Plasma", *Applied Physics Researc*h, vol. 2, 2010

[5] Samuel J. Ling, Jeff Sanny and William Moebs, "University Physics Volume 3", OpenStax, 1 September 2016

[6] Freidberg, "Plasma Physics and fusion energy", CAMBRIDGE UNIVERSITY PRESS, 2007

[7] John Wesson, "Tokamaks" , Clarendon Press, Oxford, 2004

[8] Peter Donnel, "Impurity transport in tokamak plasmas: gyrokinetic study of neoclassical and turbulent transport" in Plasma Physics [physics.plasm-ph], Aix Marseille Université, 2018

[9] P. Vincenzi, "Interaction between neutral beam fast particles and plasma in fusion experiments", Ph.D thesis, Padova 2016

[10] «https://www.ipp.mpg.de/en» (consulted 20 October 2020)

[11] «https://www.iter.org/» (consulted 25 October 2020)

[12] «https://www.euro-fusion.org/» (consulted 26 October 2020)

[13] «https://www.dtt-project.it/» (consulted 26 October 2020)

[14] R. S. Hemsworth *et al.,New J. Phys.,* vol19, no.025005, 2017

[15] R. S. Hemsworth and T. Inoue, "Positive and negative ion sources for magnetic fusion," in *IEEE Transactions on Plasma Science*, vol. 33, no. 6, pp. 1799-1813, Dec. 2005

[16] V. Toigo *et al.,New J. Phys.*, vol19, no.085004, 2017

[17] D. Marcuzzi *et al*. "Detail design of the beam source for the SPIDER experiment" in *Fusion Engineering and Design*, vol. 85, pp. 1792-1797, 2010

[18] A. Masiello *et al*. "The fabrication and assembly of the beam source for the SPIDER experiment" in *Fusion Engineering and Design*, vol. 146, Part A, pp. 839-844, 2019

[19] M. Bigi *etal*."Design, manufacture and factory testing of the Ion Source andExtraction Power Supplies for the SPIDER experiment", in *Fusion Engineering and Design*, vol. 96-97, pp. 405-410, 2015

[20] F. Gasparini *et al*. "Investigation on stable operational regions for SPIDER RF oscillators", in *Fusion Engineering and Design,* vol. 146, pp. 2172-2175, 2019

[21] A. Zamengo *et al*. "Electrical and thermal analyses for the radio-frequency circuit of ITER NBI ion source" *Fusion Engineering and Design,*vol. 84, pp. 2025-2030, 2009

[22] A. Maistrello *et al*. " Improvements in the SPIDER RF system", *Fusion Engineering and Design,* 2021 (to be published)

[23] «https://it.mathworks.com/products/matlab.html»

[24] «http://dd6um.darc.de/QucsStudio/download.html»

[25] «https://it.mathworks.com/products/simulink.html»

[26] W. Cui *et al*., "Lumped-element sections for modeling coupling between high-speed digital and I/O lines," *IEEE 1997, EMC, Austin Style. IEEE 1997 International Symposium on Electromagnetic Compatibility. Symposium Record (Cat. No.97CH36113)*, Austin, TX, USA, 1997, pp. 260-265

[27] «https://www.femm.info/wiki/Download»

[28] A.C. Fischer-Cripps, "3.5 - Digital signal processing", A.C. Fischer-Cripps, Newnes Interfacing Companion, Newnes, 2002, pp. 269-283

[29] Marian K. Kazimierczuk, "RF Power Amplifiers" (2nd ed.), John Wiley and Sons Ltd, Wright State University, Dayton, Ohio, USA, 2015

[30] Mihai Albulet, "Rf Power Amplifiers", Noble Publishing Company, Atlanta, 2001

[31] «https://www.electronics-tutorials.ws/amplifier/amplifier-classes.html»(consulted 15 December 2020)

[32] N. Mohan, T. M. Undeland, W. P. Robbins, "Power Electronics: converters, applications and design", John Wiley and Sons, Inc., New York, 2003

[33] Darshan Parmar *et al*., *J. Phys.: Conf. Ser*., vol. 823, no. 012037, 2017

[34] Jain, Akhilesh & Hannurkar, P. & Sharma, Deepak & Gupta, Alok & Tiwari, Ashish & Lad, Mahendra & Kumar, R. & Gupta, P.D. "Design and Characterization of 50 kW Solid-State RF Amplifier", *International Journal of Microwave and Wireless Technologies* (2012)

[35] «https://elsyscom.de/wp-content/uploads/2019/11/Datasheet_TRAM-50AN_ELS.pdf»

[36] «https://datasheet.lcsc.com/szlcsc/Texas-Instruments-TI-TPS62748YFPT_C133949.pdf»

[37] Kiam Heong Ang, G. Chong and Yun Li, "PID control system analysis, design, and technology," in *IEEE Transactions on Control Systems Technology*, vol. 13, no. 4, pp. 559-576, July 2005

[38] «https://www.autodesk.it/products» (consulted 20 December 2020)

[39] Zhong Chen and D. Lewis, "Evaluating uncertainties in net power delivery using dual directional couplers," *2005 International Symposium on Electromagnetic Compatibility, 2005. EMC 2005.*, Chicago, IL, 2005, pp. 782-786 Vol. 3

[40] Rohde & Schwarz. (2015). "Influence of a directional coupler's parameters on the results of forward and reflected power measurements" [White paper]. Available: https://scdn.rohde-schwarz.com/ur/pws/dl_downloads/dl_common_library/dl_brochures_and_datasheets/pdf_1/service_support_30/White_Paper_Parameters_Directional_Coupler.pdf